Coupling Road Vehicle Aerodynamics and Dynamics in Simulation

by

David C. Forbes

Doctoral Thesis

Submitted in partial fulfilment of the requirements

for the award of

Doctor of Philosophy of Loughborough University

March 2017

ABSTRACT

A fully coupled system in which a vehicle's aerodynamic and handling responses can be simulated has been designed and evaluated using a severe crosswind test. Simulations of this type provide vehicle manufacturers with a useful alternative to on road tests, which are usually performed at a late stage in the development process with a prototype vehicle. The proposed simulations could be performed much earlier and help to identify and resolve any aerodynamic sensitivities and safety concerns before significant resources are place in the design.

It was shown that for the simulation of an artificial, on-track crosswind event, the use of the fully coupled system was unnecessary. A simplified, one-way coupled system, in which there is no feedback from the vehicle's dynamics to the aerodynamic simulation was sufficient in order to capture the vehicle's path deviation. The realistic properties of the vehicle and accurately calibrated driver model prevented any large attitude changes whilst immersed in the gust, from which variations to the aerodynamics could arise. It was suggested that this system may be more suited to other vehicle geometries more sensitive to yaw motions or applications where a high positional accuracy of the vehicle is required.

ACKNOWLEDGEMENTS

Thank you to my Mum, Dad and brother Tom, for their support and generosity. To my family and friends, for offering escape. And finally to Ghilly, for understanding.

For Johanna

Publications

Work for this thesis has also been published in the following:

- A. Wood, M. Passmore, D. Forbes, D. Wood, A. Gaylard, "Base Pressure and Flow-Field Measurements on a Generic SUV Model", *SAE International Journal of Passenger Cars - Mechanical Systems* Volume 8, Issue 1, Pages 233 - 241, 2015.

- D. Forbes, G. Page, M. Passmore, A. Gaylard, "Computational study of wake structure and base pressure on a generic SUV model", The International Vehicle Aerodynamics Conference, Oct 2014.

- D. Forbes, G. Page, M. Passmore, A. Gaylard, "A Fully Coupled, 6 Degree-of-Freedom, Aerodynamic and Vehicle Handling Crosswind Simulation using the DrivAer Model", *SAE International Journal of Passenger Cars - Mechanical Systems* Volume 9, Issue 2, Pages 710 - 722, 2016.

- D. Forbes, G. Page, M. Passmore, A. Gaylard, "A study of computational methods for wake structure and base pressure prediction of a generic SUV model with fixed and rotating wheels", *Proceedings of the Institution of Mechanical Engineers, Part D: Journal of Automobile Engineering*, 2017.

- J. Howell, D. Forbes, M. Passmore, G. Page, "The Effect of a Sheared Crosswind Flow on Car Aerodynamics," *SAE International Journal of Passenger Cars - Mechanical Systems*, Volume 10, Issue 1, Pages 278 - 285, 2017.

Contents

LIST OF FIGURES

LIST OF TABLES

Nomenclature

All variables defined using SI base units unless otherwise stated.

Definitions

Count	0.001

Symbols

a	Side area
A	Frontal area
A'	Ratio of model frontal area to working section cross-sectional area
b	Spring moment arm
C_D	Drag coefficient
C_{D_F}	Front drag coefficient
C_{D_R}	Rear drag coefficient
C_L	Lift coefficient
C_{L_F}	Front lift coefficient
C_{L_R}	Rear lift coefficient
C_{MX}	Roll moment coefficient
C_{MZ}	Yaw moment coefficient
C_p	Pressure coefficient
$C_{P_{total}}$	Total pressure coefficient
C_r	Mechanical damping
C_Y	Side force coefficient
C_{Y_F}	Front side force coefficient
C_{Y_R}	Rear side force coefficient
d	Height of zero-displacement plane
$f_{d_{on}}$	Damped frequency with wind on
$f_{d_{off}}$	Damped frequency with wind off
f_i	Probability density of wind speed for components $i = u, v, w$
H	Height of obstacle
H	Height
$I_{u,v,w}$	Components of turbulence intensity
I_{zz}	Yaw moment of inertia
J_i	Predicted turbulence intensity for components $i = u, v, w$

k	Von Karman constant
K	Reduced frequency
K_r	Linear mechanical stiffness
K_s	Torsional mechanical stiffness
K_{lat}	Lateral gain
K_{ug}	Understeer gradient gain
$\mathbf{L}$	Length
$\mathrm{L_W}$	Wheelbase length
$\mathrm{M_Z}$	Aerodynamic yaw moment
Q	Volume flow rate
$S_i(n)$	Spectral density with gust frequency n for $i = u, v, w$
t_{lag}	Driver reaction time
t_p	Driver preview time
T	Time
u, v, w	Velocity components in cartesian coordinate system
$\overline{U}_{10}$	Wind speed at height $10\,\mathrm{m}$
u_*	Friction velocity
u_∞	Freestream velocity
$\overline{U}_g$	Gradient wind speed
U_R	Resultant velocity
U_{veh}	Vehicle velocity
U_w	Wind velocity
u'_z	Fluctuation of wind velocity from mean
U_z	Wind speed at height z
$\overline{U}_z$	Average wind speed at height z
v_{max}	Maximum crosswind velocity
$\mathbf{W}$	Width
^xL_i	Turbulent length scale of ith velocity component in x direction
X_{ML}	Width of gust mixing layer
y^+	Non-dimensional near wall spacing
z_0	Local terrain roughness coefficient
z_g	Height of gradient wind

Greek Symbols

α	Surface roughness best-fit constant
β	Yaw angle

$\dot{\beta}$	Yaw rate
$\ddot{\beta}$	Yaw accleration
β_0	Initial yaw angle
Δ	Change in
Δt	Time-step
$\oslash$	Diameter
λ	Plan area density of surface roughness
ω_n	Natural frequency
Φ	Angle of wind velocity vector
ρ	Air density
$\sigma_{u,v,w}$	Components of standard deviation
τ_0	Surface shear stress
ζ	Damping ratio

Subscripts

Shear+Turb	With sheared and turbulent velocity profile
Unshear	Unsheared velocity profile
Windward	On windward side of the vehicle
Leeward	On leeward side of the vehicle
cor	Corrected for blockage

Abbreviations and Acronyms

ALE	Arbitrary Lagrangian-Eulerian
API	Application Programming Interface
CFD	Computational Fluid Dynamics
CFL	Courant-Friedrichs-Lewy
CoG	Centre of Gravity
DES	Detached Eddy Simulation
DOF	Degrees of Freedom
ESDU	Engineering Sciences Data Unit
Exp	Experiment
FFT	Fast Fourier Transform
HPC	High Performance Computer
IDDES	Improved Delayed Detached Eddy Simulation
IDIADA	Institut d'Investigaci Aplicada de l'Autombil
ISO	International Organization for Standardization

LBM	Lattice-Boltzmann Method
LES	Large Eddy Simulation
LHS	Left Hand Side
LUMS	Loughborough University Model Scale
MIRA	Motor Industry Research Association
MRF	Moving Reference Frame
NRC	National Research Council Canada
OEM	Original Equipment Manufacturer
PIV	Particle Image Velocimetry
RANS	Reynolds Averaged Navier Stokes
Re	Reynolds Number
RHS	Right Hand Side
RMS	Root Mean Square
SAE	Society of Automotive Engineers
SDR	Specific Dissipation Rate
SEM	Synthetic Eddy Method
SS	Steady Static
SUV	Sports Utility Vehicle
TGS	Turbulence Generation System
TKE	Turbulent Kinetic Energy
UD	Unsteady Dynamic
UNECE	United Nations Economic Commission for Europe
URANS	Unsteady Reynolds Averaged Navier Stokes
US	Unsteady Static
WLTP	Worldwide harmonized Light vehicles Test Procedure

CHAPTER 1

INTRODUCTION

Contents

Aerodynamic performance is an important attribute to consider during a vehicle's design and testing processes. Of leading interest is a vehicle's aerodynamic drag, as this force has a direct impact on fuel consumption and journey range. Obtaining the value of the force requires a replication of the flow environment through which the vehicle travels, and is usually generated artificially using experimental wind tunnel facilities and complementary computational fluid dynamics simulations. The onset flow is normally smooth, quasi-steady and aligned with the the vehicle's forward direction. Such conditions provide the best environment for acquisition of repeatable data, making it possible to reliably resolve the effects of detailed shape changes through a vehicle's design phase, however these conditions are rarely met on the road. Velocity variations can arise from numerous sources such as atmospheric winds, the wakes of other vehicles and gaps in road side obstacles, all of which can significantly alter the drag acting on the vehicle when compared to the value obtained in the 'ideal' conditions of a wind tunnel.

In addition to drag, a realistic environment can also affect other important metrics of vehicle performance, such as handling and stability. Surprisingly, given the importance

of this performance metric in terms of vehicle quality, refinement and even safety, this impact has received much less attention. A vehicle that is sensitive to typical wind fluctuations under normal driving conditions will be unpleasant to drive and felt by any passengers within the vehicle. Whereas under more extreme events such as high speed gusts and prolonged crosswinds, it is vital that the vehicle is stable and does not behave unexpectedly. In both cases, quasi-steady loads obtained under ideal wind tunnel conditions will not pick up the frequencies and instantaneous peaks that are associated with these events. This is becoming more important due to the trends in low-drag, lighter vehicles with highly curved features and sloped fastback rear ends that are more susceptible to large aerodynamic loads. The current methods of assessing handling and stability issues due to unsteady aerodynamics, are on-road tests or vehicle dynamics simulations using the simplification of quasi-steady aerodynamics loads of the vehicle at yaw. The first of these methods requires a prototype vehicle, and hence occurs at a late stage in the development process where shape modifications are usually an expensive process. Whereas in simulation, there is little evidence to suggest that using quasi-steady loads to assess an unsteady event is an acceptable simplification.

The purpose of this thesis is to present and document the results of a fully coupled simulation method in which a vehicle's unsteady aerodynamics and multi-body, 6 degree of freedom motion including a typical driver's response can be predicted simultaneously. This will require an appropriate meshing technique such that geometry is free to move within the computational fluid domain alongside a system in which aerodynamic loads and vehicle positional data can be exchanged. The thesis will start by collating existing knowledge and evaluating appropriate techniques. The simulation method will be used to determine the response to an unsteady crosswind event whilst comparing to the existing simplified quasi-steady method.

1.1 The Natural Wind

The natural wind is unsteady, continuously changing in speed and direction. In an attempt to understand what appears to be random behaviour, wind engineers have and continue to measure the natural wind's velocity at locations all over the world. A

generic sample of instantaneous wind speed $U_z(t)$ at height z is shown in Figure 1.1.
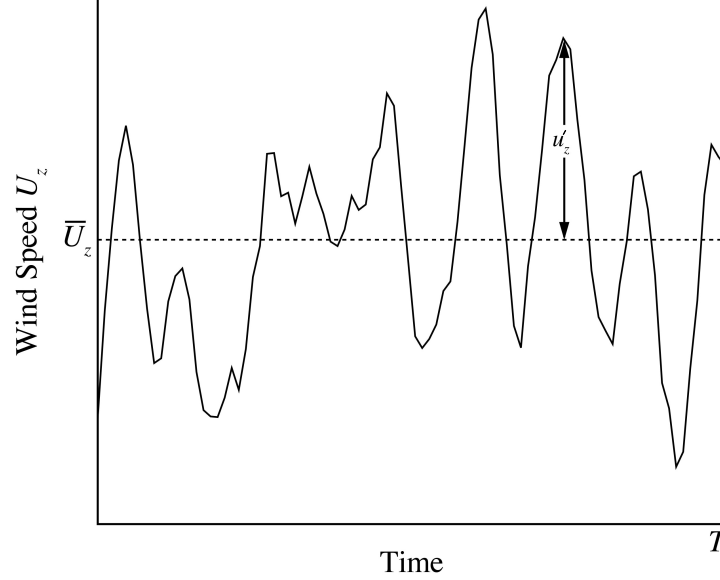
Figure 1.1: Wind speed data sample.

Databases usually do not contain complete samples of measured instantaneous speeds as per Figure 1.1, but rather consist of mean values $\overline{U}_z$, calculated over a period of time T using Equation 1.1, published by the Engineering Sciences Data Unit ESDU 82026 [1].

$$\overline{U}_z = \frac{1}{T} \int_0^T U_z(t)dt, \qquad U_z(t) = \overline{U}_z + u_z'(t). \qquad (1.1)$$

The period over which wind speeds are averaged is chosen to ensure a stable average, typically one hour. Spectral analysis of annually measured wind speed data obtained by Van der Hoven [2] confirms the suitability of this period length. Figure 1.2 shows how this value falls within a spectral gap between two peak energy spectrum values associated with the passage of large, synoptic-scale pressure systems and the high frequency, small scale fluctuations in the natural wind. Although the data used in Figure 1.2 refers only to a single location at a height of $100\,\mathrm{m}$, similar spectral gaps have been measured at different locations and heights from as low as $30\,\mathrm{m}$ over North America [2, 3]. It is proposed that the reason for this spectral gap is the lack of a physical process that

supports wind fluctuations in the frequency range from approximately 10 minutes to 1 hour, inferring the suitably of this averaging period.
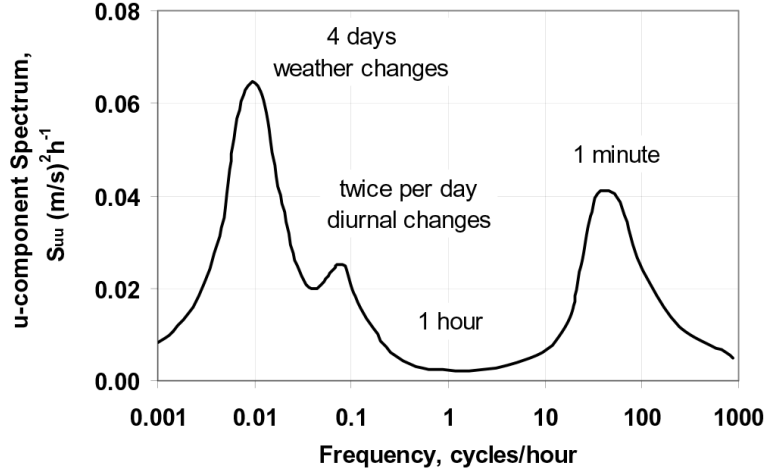
Figure 1.2: Spectrum of wind fluctuations at 100m taken from Cooper based on Van der Hoven [4, 2]

.

1.1.1 The Natural Wind's Velocity Profile

Measurements at different heights and locations are key in understanding the behaviour of the natural wind. Close to the Earth's surface, the wind is more strongly influenced by local terrain features, where drag forces induced by obstacles on the ground, lead to a reduction in wind speed. In contrast, moving far above the surface, the wind eventually becomes unaffected by these shear forces, a state referred to as the gradient wind. As a result, the atmosphere is commonly divided into three regions: the free atmosphere, atmospheric boundary layer and surface boundary layer. The gradient wind defines the start of free atmosphere, where wind speed is determined by pressure gradient, Coriolis and inertial forces [5]. Under the free atmosphere is the atmospheric boundary layer where the viscosity of the air has an influence on the wind speed. The height of this layer has been quoted anywhere between $300\,\text{m}$ up to $3000\,\text{m}$, depending on the specific roughness of the terrain upstream and strength of the gradient wind [5, 6, 7]. The surface boundary layer is a low-level sub-layer of the atmospheric boundary layer extending from the ground up to approximately $60\,\text{m}$, within which a constant shear

4

stress and lack of Coriolis forces are assumed. Again the height of this layer is dependent on surface conditions.

As shown by Watkins [6], the profile of the atmospheric boundary layer can be approximated using a logarithmic law, Equation 1.2, along with a numerical interpretation of the local terrain roughness z_0, for which typical values are shown in Table 1.1.

$$\overline{U}_z = \frac{u_*}{k} \ln \left(\frac{z}{z_0} \right), \qquad u_* = \sqrt{\left(\frac{\tau_0}{\rho} \right)}. \qquad (1.2)$$

Terrain	z_g (m)	α	k	z_0 (m)
Open Terrain	300	0.16	0.005	0.03
Woodland Suburbs	430	0.28	0.015	0.20
City Centre	560	0.40	0.050	1.00

Table 1.1: Characteristics of the natural wind for different terrain [7].

In Equation 1.2, $\overline{U}_z$ is the average wind speed at height z, u_* is friction velocity calculated from the density of the air ρ and surface shear stress τ_0 and k is the von Karman constant. This expression was originally derived by Prandtl for turbulent boundary layers on flat plates [8] and as shown by Flay [9], this expression only applies to the entire boundary layer in flat, open, homogeneous terrain, conditions which are rarely met in the real world. In areas of significant surface roughness, the accuracy of the prediction from the ground up to the height of the roughness-producing obstacle breaks down, due to the complexity of the flow in this region. Therefore it is common to define a displacement plane, known as the zero-plane displacement, to which the bottom of the boundary layer profile is shifted and all heights used in the calculations are referred. Consequently this shift mathematically invalidates the logarithmic law under the zero-plane as z takes a negative value. The height of this plane d, is usually less than the height of the roughness-producing obstacle H, Holmes suggests 75% of H, and is a function of the surface roughness z_0 and its plan-area density λ [1, 10].

For $0.2 < \lambda < 0.8$,

$$d = H - (4.3\ z_0\ (1 - \lambda)).$$ (1.3)

An alternative expression for the boundary layer profile is the power law

$$\overline{U}_z = \overline{U}_g \left(\frac{z}{z_g} \right)^{\alpha},$$ (1.4)

where $\overline{U}_g$ and z_g are the gradient wind speed and height, and α is a best-fit constant that takes into account surface roughness, typical values for which can be found in Table 1.1 [6].

In practice, the values for the gradient wind and height required in the power law are often hard to measure, so for convenience it is common for these values to be replaced by values of U_{10} and $z_g = 10\,\mathrm{m}$, as this is a typical height of anemometer measurements [6].

$$\overline{U}_z = \overline{U}_{10} \left(\frac{z}{10} \right)^{\alpha}.$$ (1.5)

Although the power law is mathematically valid for heights under the zero-plane displacement, the accuracy of the expression for the velocity profile in this region is still questionable, especially for heights under $10\,\mathrm{m}$. This low-level region of the surface boundary layer is of minimal importance to civil engineers and meteorologists and hence, has received little attention. One exception is the work by Flay [9], where measurements suggest that the power law is only suitable in this low-level region for smooth, open terrain. For lack of a more suitable alternative, the power law is still being used to model this region for all terrain conditions.

1.1.2   Average and Maximum Wind Speeds

With an appropriate averaging method established and a general understanding of the influence of shear forces in the majority of the atmospheric boundary layer, analysis

of the natural wind data can be performed. Figure 1.3 shows the results of a study by Archer and Jacobson [11], used to assess the potential of renewable global wind power. Wind speeds were recorded at an elevation of 10 m at over 8000 weather stations worldwide and global averages for the year 2000 were calculated: 6.64 m/s over oceans and 3.28 m/s over land. In their study, these measurements were used along with the power law to approximate the average wind speeds at a height of 80 m, the typical hub height of modern wind turbines, and placement of such were suggested.
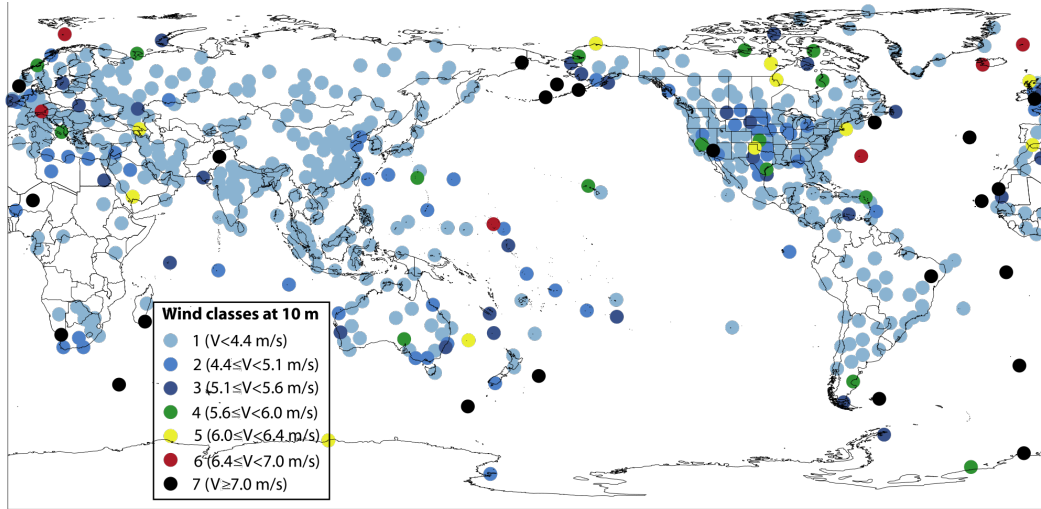
Figure 1.3: Average global wind speed at a height of 10 m for the year 2000 [11].

In the UK wind speeds are typically larger than the global average, with an average for 2001, measured by the Met Office [12] at 4.42 m/s and over the last 15 years the average wind speed has raised to 4.53 m/s. Whilst long period averages give a good indication of the typical wind speed in a particular geographical location, extreme wind speeds are generally a deeper concern, due to the added risk that accompanies them. Figure 1.4 shows the extreme hourly-mean and 3-second gust speeds for the UK, with a chance of reaching the quoted value being a once in fifty year occurrence. All values assume uniform open country terrain ($z_0 = 0.03$) but do not account for local topography changes such as speed up effects over hills and through valleys. The velocity is referenced at a height of 10 m and is increased by 10% for every 100 m above sea level. Much like the yearly averages, the hourly-mean values still veil the true extremes of the gust, with the three second gust almost double the mean-hourly value over most parts of the UK. The ratio of the instantaneous gust to the mean-hourly speed is know as the

gust factor. Sachs [13] suggests that where no instantaneous gust records are available, gust factors can be applied to the mean-hourly measurements for an approximation of the maximum gust speed, and these are presented for a range of terrains in Table 1.2.

(a) Mean-hourly speed [14]

(b) 3 second gust speed [15]
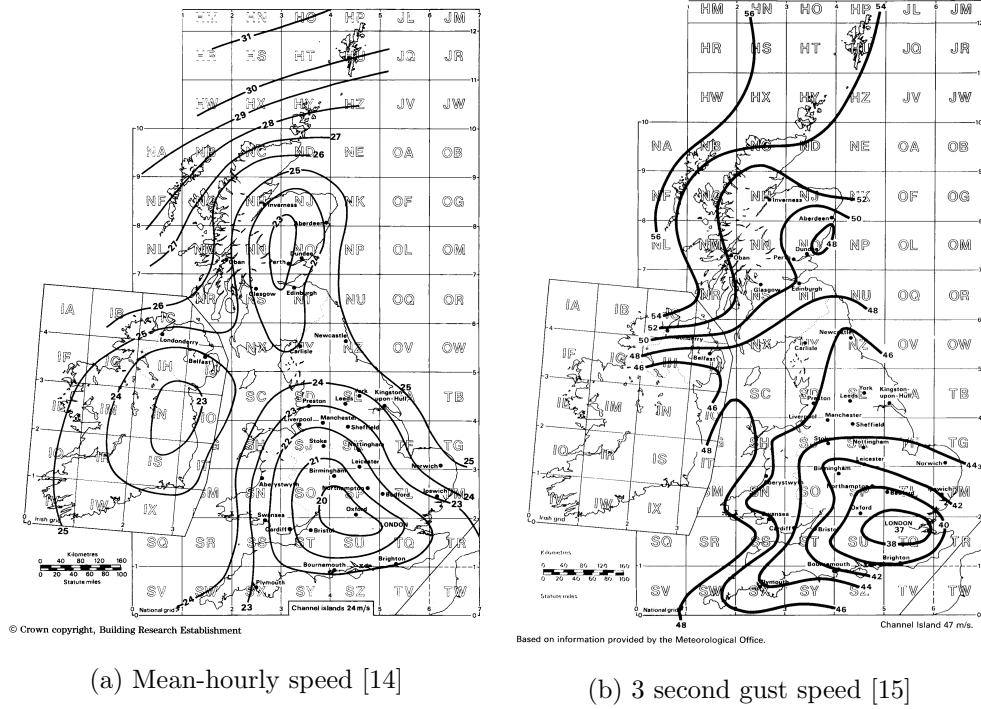
Figure 1.4: Maximum wind speeds at 10 m, once in 50 year occurrence.

Terrain	Maximum Gust Factor
Open Terrain	1.59
Woodland Suburbs	1.91
City Centre	2.22

Table 1.2: Maximum gust factors for different terrain [13].

1.1.3 Turbulence in the Natural Wind

'The variation of gusts in the natural wind is known as turbulence and emerge as a result of exchanges in momentum due to the vertical movement of air; a secondary effect of the retarding forces generated by the Earth's surface and obstructions upon

8

it' [13]. Turbulence can be quantified using two parameters: turbulence intensity and length scale.

Turbulence intensity, is a measure of the magnitude of the fluctuating velocity component, compared to the mean wind speed at the same height. Referring back to Figure 1.1, the fluctuation to the mean at any given time, in the direction of the mean wind, is given by the value $u'_z(t)$. By definition of the average wind speed, the average of this fluctuation over the period T is zero, however the mean square, also known as variance over this period has value and is calculated as follows,

$$\sigma_u^2 = \frac{1}{T} \int_0^T (u'_z(t))^2 dt. \tag{1.6}$$

The longitudinal component of the turbulence intensity, denoted by I_u, is then calculated by taking the square root of the variance, otherwise know as the standard deviation, and dividing through by the mean wind speed. Components of velocity are defined by u, v, w,

$$I_u = \frac{\sigma_u}{\overline{U}_z}. \tag{1.7}$$

Similarly for the other components of turbulence intensity,

$$I_v = \frac{\sigma_v}{\overline{U}_z}, \qquad I_w = \frac{\sigma_w}{\overline{U}_z}. \tag{1.8}$$

Both Harris and Davenport [16, 17] suggest that as the variance of turbulence is proportional to the shear stress (assumed constant in the surface boundary layer) a modification to the power law can yield an expression for the longitudinal component of turbulence intensity at any given height .

$$\frac{\sigma_u}{\overline{U}_z} = 2.5k^{\frac{1}{2}} \left(\frac{\overline{U}_{10}}{\overline{U}_z} \right)^\alpha. \tag{1.9}$$

In a similar fashion, Flay [9] showed that the logarithmic law can be used to express

turbulence intensity,

$$\frac{\sigma_u}{\overline{U}_z} = \frac{1}{\ln\left(\frac{z}{z_0}\right)}. \tag{1.10}$$

It is generally agreed that up to a height of 20 m, the components of turbulent intensity can be approximated relative to each other, as shown in Equation 1.11, although there is slight variation on the specific values of this ratio within the literature [5, 10].

$$\sigma_u = \sigma_v = \sigma_w = 1 : 0.8 : 0.5. \tag{1.11}$$

Studies that measure the behaviour of turbulence in the lowest level of the atmospheric boundary layer are limited, making validation of these laws difficult. One exception is the study performed by Flay [9], who obtained turbulence intensity measurements from a stationary tower situated near Christchurch, New Zealand over a height range from 3.3 m to 20 m metres. The test site was situated in open grassland and terrain conditions were maintained for the surrounding area ($z_0 = 0.03$), ensuring an equilibrium boundary layer at the measurement site. Measurements correlated well with theoretical data obtained using Equations 1.9 and 1.10, and confirmed that larger longitudinal and lateral intensities are found closer to the ground increasing from $I_u = 16\%$ and $I_v = 12\%$ at 20 m to $I_u = 19\%$ and $I_v = 15\%$ at 3.3 m. Vertical intensities behaved slightly differently, decreasing linearly towards the ground from $I_w = 8.5\%$ at 13 m to $I_w = 7\%$ at 3.3 m. It is claimed by ESDU 83045 [18], that theoretical methods such as Equations 1.9 and 1.10, should hold true for any equilibrium boundary layer, even in areas of substantial roughness ($z_0 > 0.1$) and ESDU 85020 [19] provides theoretical data for turbulence intensity with respect to height at a range of surface roughness values, Figure 1.5. This measurements by Flay [9] agree well with this theoretical data for a comparable roughness value. Intuitively, the theoretical data shows how added surface roughness increases turbulence intensity, and the subplot of Figure 1.5 shows how an increase in wind speed can reduce the turbulence intensity at low heights ($\leq$ 10m), whilst the opposite is true for heights greater than 60m.
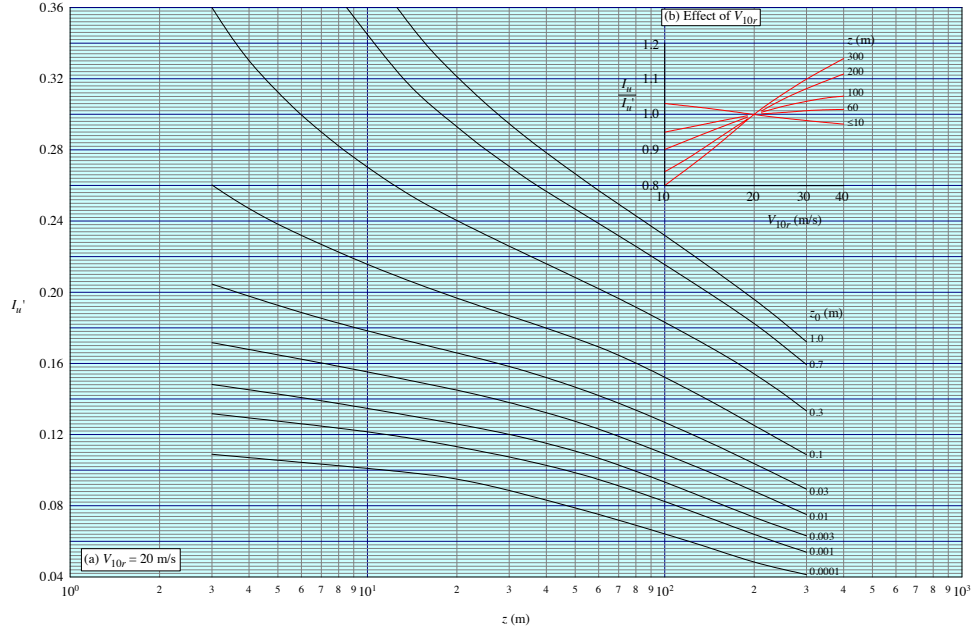
Figure 1.5: Turbulence intensities for equilibrium conditions [19].

Turbulence is only partly defined by intensity as these values give no information on the probability of a specific gust occurring. Statistical methods are used to define the proportion of time that a wind velocity U_z spends in a specific range $U_z + \delta U_z$, otherwise know as the probability density $f_i(U_z)$ for each wind component $i = u, v, w$ [19].

$$f_i(U_z) = \frac{1}{\sigma_i \sqrt{2\pi}} \exp \left[-\frac{1}{2} \left(\frac{U_z - \overline{U_z}}{\sigma_i} \right)^2 \right]. \qquad (1.12)$$

However, this function alone is still not sufficient to define the random nature of gusts, as it only provides information about the magnitude of a specific wind velocity and does not describe how slowly or quickly it varies in time. This is done by a function called the spectral density or spectrum $S_i(n)$, where n is a specific gust frequency [19].

$$\sigma_i^2 = \int_0^\infty S_i(n) dn \qquad i = u, v, w. \qquad (1.13)$$

As already shown, Figure 1.2 shows the spectrum of wind fluctuations from measured data. Although no details on the equations used in the calculation of spectral density were provided by Van der Hoven [2], it is reasonable to a assume that the value was

11

calculated using the model developed by von Karman [19], in which the spectral density takes on the non-dimensional form $\frac{n \cdot S_u(n)}{\sigma_i^2}$.

$$\frac{n \cdot S_u(n)}{\sigma_u^2} = \frac{4n_u}{(1 + 70.8n_u^2)^{5/6}} \qquad n_u = \frac{n\,{}^xL_u}{\overline{U}_z}, \qquad (1.14)$$

$$\frac{n \cdot S_i(n)}{\sigma_i^2} = \frac{4n_i(1 + 755.2n_i^2)}{(1 + 283.2n_i^2)^{11/6}} \qquad n_i = \frac{n\,{}^xL_i}{\overline{U}_z}, \qquad i = v, w. \qquad (1.15)$$

In Equation 1.15, ${}^xL_i$ is known as the turbulent length scale of the ith velocity component in the x direction (the direction of the wind). It is a measure of the physical size of the eddies constituting the turbulence and is dependent on height and surface roughness. ESDU 85020 [19] shows how the value of the longitudinal length scale increases with height, Figure 1.6. This trend was also confirmed by the measurements of Flay [9] up to a height of 20m.
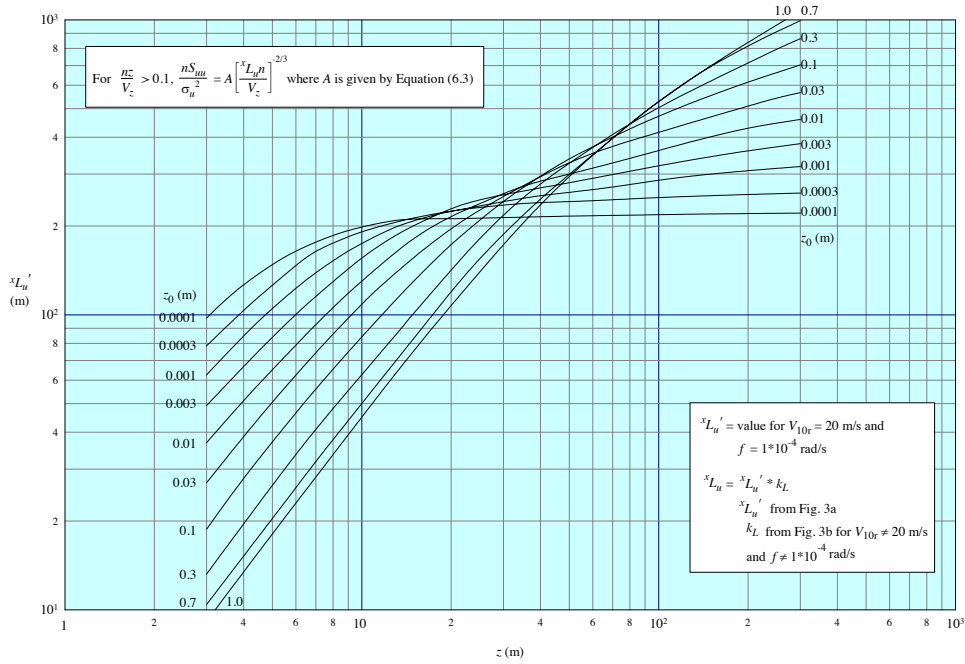
Figure 1.6: Integral length scales for equilibrium conditions [19].

In his attempts to derive a mathematical model of the atmospheric boundary layer, Flay [9] states that when considering the boundary layer as a whole, length scales can

be approximated using the following relations,

$$^xL_u = 20\sqrt{z},$$
$$^xL_v = {}^xL_w = 0.4z,$$

(1.16)

and when considering the surface layer alone the following modifications are suggested,

$$^xL_u = 4.2z^{0.73},$$
$$^xL_u = 2\,{}^xL_v = 2\,{}^xL_w.$$

(1.17)

Although these relations provide a useful approximation of the turbulent length scale components, they should be used with caution as they are primarily based on a single, smooth, uniform terrain condition under which Flay [9] obtained his results.

It is clear that there is a good understanding of the natural wind's behaviour and several theoretical laws can be used to predict its defining parameters. Measurements of the wind speed at a height of 10m are most common, and these laws can be adapted for use with such measurements to gain a reasonable understanding of the wind's profile and fluctuations throughout the majority of the atmospheric boundary layer. The main difficultly is predicting the wind's behaviour in close proximity to the Earth's surface. Variations in terrain roughness and its plan area density result in a highly complex flow and a lack of measurements have restricted the advancement of knowledge of the wind's behaviour within this region.

1.2   The Flow Seen By a Road Vehicle

Throughout a journey on the road, a vehicle will be subjected to a range of yaw angles since the flow seen by the vehicle is the combination of the wind velocity vector and the inverse of the vehicle's velocity vector, both of which are time dependent. This is shown in Figure 1.7 as angle β and is calculated along with the value of resultant velocity U_R using the Equations 1.18 and 1.19.

$$U_{\mathrm{R}}{}^2 = U_{\mathrm{veh}}{}^2 + U_{\mathrm{w}}{}^2 + 2U_{\mathrm{veh}}U_{\mathrm{w}}\cos\Phi.$$

(1.18)

$$\beta = \tan^{-1}\left(\frac{U_{\mathrm{w}}\sin\Phi}{U_{\mathrm{veh}} + U_{\mathrm{w}}\cos\Phi}\right).$$

(1.19)
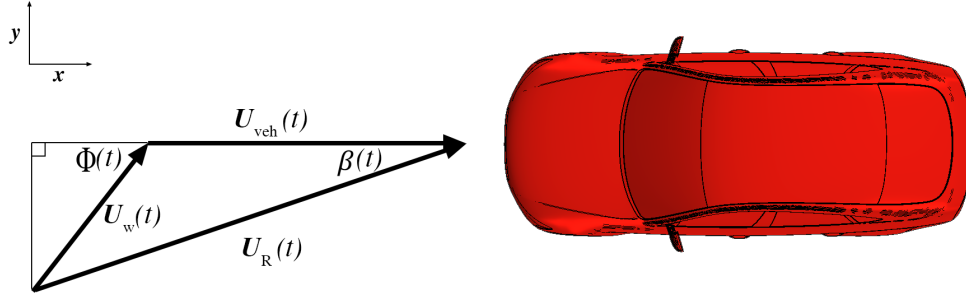
Figure 1.7: Yaw angle of resultant flow velocity.

1.2.1 A Sheared Velocity Profile

Shear in the natural wind results in a velocity profile and thus flow yaw angle profile which varies over the height of the vehicle, as shown in Figure 1.8. As already discussed, an approximation of this wind profile over typical vehicle heights can be provided by the power law, Equation 1.5.
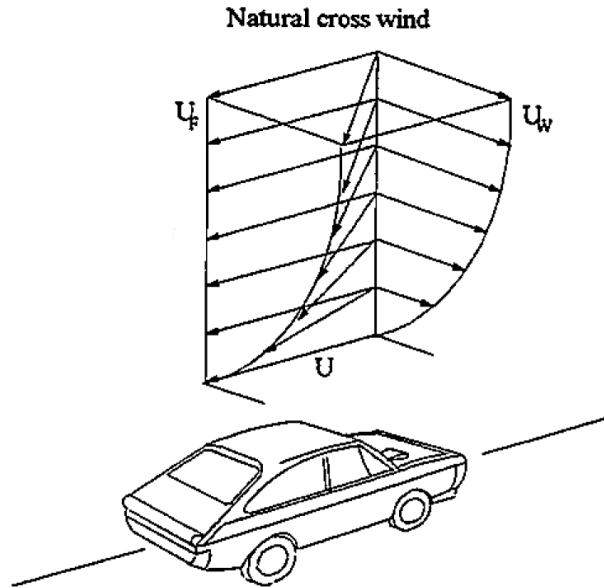
Figure 1.8: The effect of shear on the flow seen by a vehicle [20].

A typical on-road scenario is described as follows: a truck of standard height $4\,\mathrm{m}$ is travelling at $25\,\mathrm{m/s}$. A prolonged gust or crosswind acts perpendicular to the direction of travel, the speed of which at a height of $10\,\mathrm{m}$ is measured at the global average of

4.5 m/s. Using the power law (Equation 1.5) and assuming an α value of 0.16 (indicative of smooth, open terrain) the wind speed at the top of the cabin can be calculated at approximately 3.9 m/s. Furthermore, the wind speed at typical bumper height of 0.5 m can be found to be approximately 2.8 m/s. Whilst this difference may seem small, Equation 1.19 can be used to show how the flow yaw angle seen by the truck varies from 8.9° at the top of the cabin to 4.4° at bumper height and 0° at the ground, and stronger wind speeds will increase this yaw angle difference. As increases in flow yaw angle can be associated with larger aerodynamic drag forces and stability issues, this effect can be of particular interest to vehicle aerodynamicists. However the effect is typically ignored and a constant wind speed and yaw angle is assumed to act over the height of the vehicle.

1.2.2 Wind Speed and Flow Yaw Angle Probability

Figure 1.9 shows the probability distribution of this assumed constant flow yaw angle, taken from on-road measurements by Lawson et al. [21]. Although the distribution is centred around zero degrees, there is still good probability of the flow yaw angle falling in ±10°. Their results also imply that the most probable wind speed encountered by vehicle in the UK is < 5 m/s and this agrees well with annual averages over the last fifteen years [12].

Measurements during more gusty periods have been recorded Wojciak [22] in Germany. Wind speeds from 6 m/s to 14 m/s were taken in an attempt to classify gusts into profiles and determine their probability. Figure 1.10 shows an extract from their wind samples, with a gust event identified by a disturbance in u and v velocities as well as turbulence intensity and length scale. Maximum intensity and length scale values for the gusts were calculated at 7% and 80 m respectively. By applying a low pass filter to the complete dataset, the gusts were classified into three categories, where it was found that the single peak gust was the most likely profile to occur with a probability of 63%. Furthermore, it was found that 75% of all gusts feature a zero-crossing in yaw angle. It has been found by Theissen [23] that the switch between windward and leeward sides on the vehicle leads to increases in unsteady phenomena.
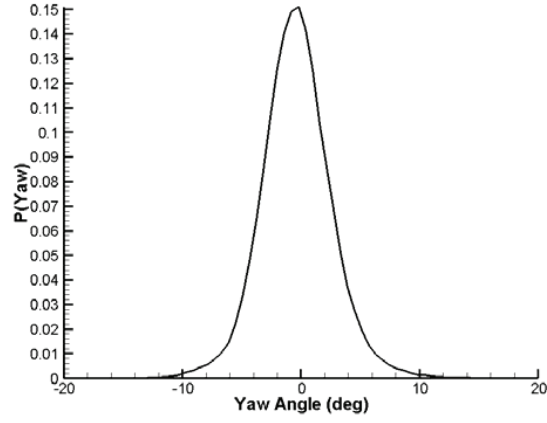
Figure 1.9: On-road probability of flow yaw angle [21].
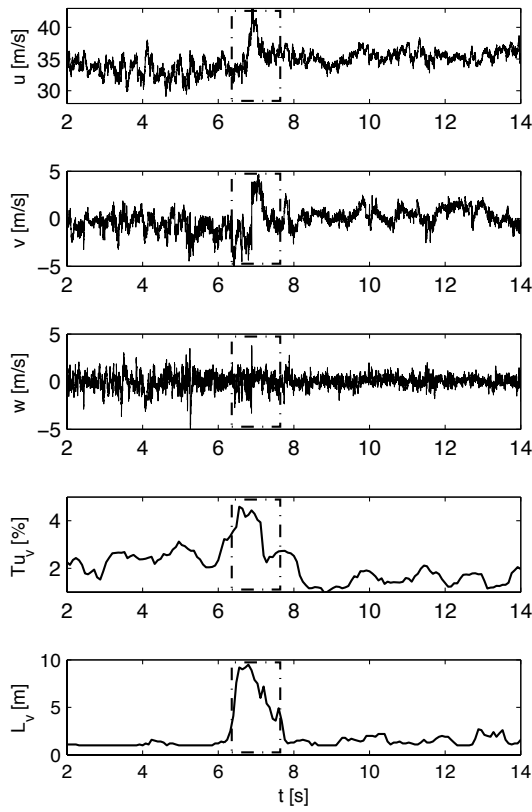
(a) Wind speed sample with gust event.
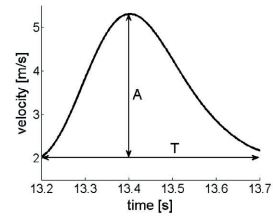
(b) Single peak, $P = 63\%$
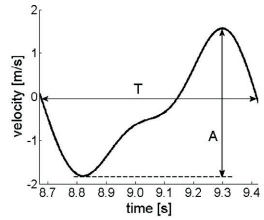
(c) Double peak, $P = 9\%$
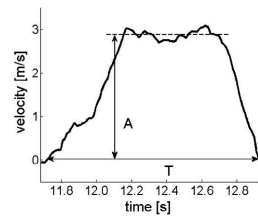
(d) Trapeze peak, $P = 28\%$

Figure 1.10: Wind speed sample and gust classification with probabilities P by Wojciak [22].

1.2.3 Turbulence Seen By a Moving Vehicle

The turbulence parameter values calculated Wojciak [22] are only relevant for gusty and similar road conditions. Studies which measure the behaviour of turbulence at vehicle heights and in more typical conditions are limited. In the study by Flay [9], turbulence intensity measurements were obtained from 20m down to 3m which although useful, is a height range above that of the majority of road vehicles. In addition, measurements were obtained from stationary apparatus, whereas on the road, the speed of the vehicle will invoke a different range of intensities. This was shown by Watkins and Saunders [24] in their attempt to derive a model capable of predicting the flow seen by a moving vehicle based on stationary measurements. Using the stationary data obtained by Flay [9] at a height of $3.3\,\mathrm{m}$, intensities were predicted for a range of wind speed and yaw angles at a vehicle speed of $30\,\mathrm{m/s}$, Figure 1.11.
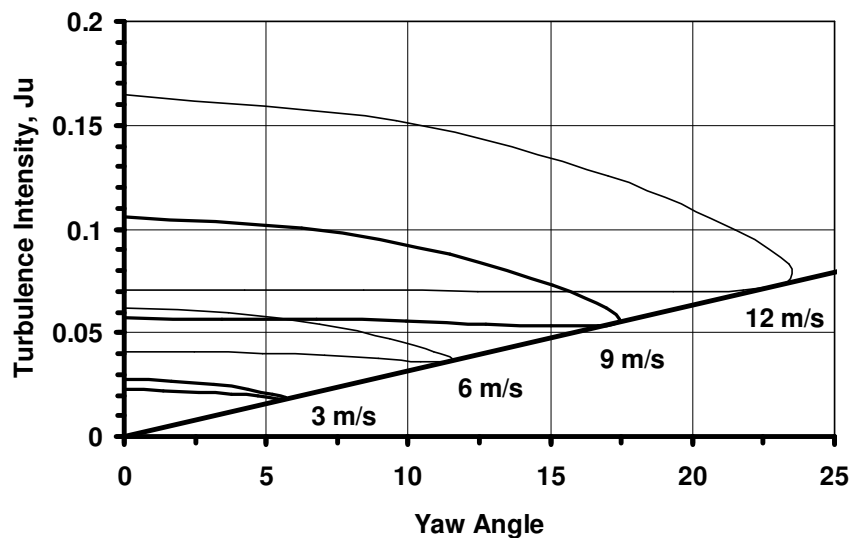
Figure 1.11: Predicted longitudinal turbulence intensity experienced by a moving vehicle [24, 25].

For each wind speed at zero yaw angle, there are two values for turbulence intensity due to head and tailwind arrangements, with a higher intensity for the tailwind due to the lower resultant velocity. It was shown by Watkins and Saunders [24] through comparisons to measured moving data that the prediction method developed could be used reliably in smooth, open terrain, however in the presence of roadside obstructions,

these predictions were inaccurate and moving data was required.

On road measurements such as those obtained by Watkins and Saunders [24] are generally recorded using a test rig of pressure tappings mounted to the front of the vehicle. Wordley and Saunders [26] used similar apparatus to measure the wind environment along roads in Australia at a height of 0.5 metres. The test locations were carefully chosen to ensure a variety of terrain conditions: open terrain, tree lined roads, city buildings and freeway traffic. In general, their results agree with the observations of Flay [9], with added surface roughness leading to higher turbulence intensities as shown in Figure 1.12a. The freeway driving conditions generated the largest intensity values due to the wakes of upstream vehicles, with a maximum longitudinal value of 16% and an average of 9%. Average values for road side obstacles and open terrain were measured at 4.4% and 4.2% respectively. The exception to this trend is the city terrain with an average intensity value of 2.4%. Although the low value is counter-intuitive based on the high surface roughness value this terrain invokes, it occurs due to the sheltering effect of the buildings on the ambient wind. This is a clear indication of the inadequacy of the surface roughness parameter, for describing the wind conditions at heights relevant to road vehicles.

The most surprising result was a high correlation and consistency in the ratio between
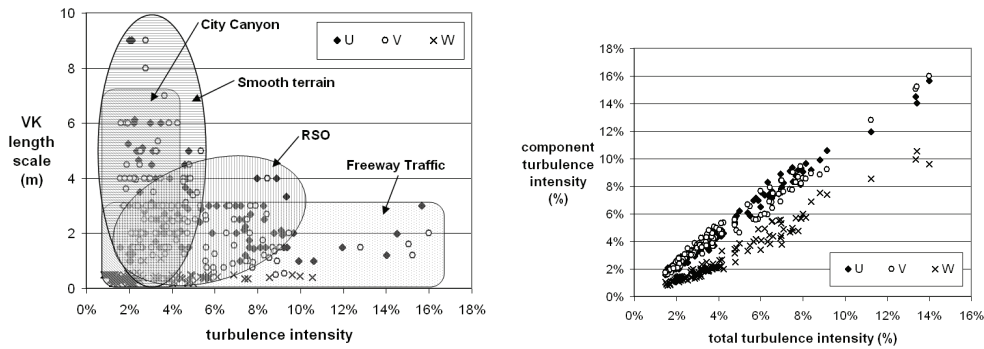
(a) Intensity versus von Karman Length Scale (b) Component versus total intensity for all terrain conditions

Figure 1.12: Turbulence intensities at a height of 0.5m, taken from a moving car $U_{\text{veh}} = 100$km/h [26].

the turbulence intensity components, despite the range of terrain and traffic conditions tested, Figure 1.12b. The specific values of the ratio are quoted in Equation 1.20, and differ to those theoretically determined, most noticeably in the lateral component, Equation 1.11. This is consistent with the results of Watkins and Saunders [24], which displayed lateral components up to 30% larger than the predicted values. In a follow-up study using the same test sites and modified measurement apparatus [27], this ratio was still found to apply over the height range of 0.25m to 1m.

$$I_u = I_v = I_w = 1 : 1.01 : 0.61. \qquad (1.20)$$

A similar study by McAuliffe et al. [28] measured the turbulence experienced by a moving vehicle in Eastern Canada over the height range of heavy duty trucks, 0.5m to 4m, and in a wide range of terrain, traffic and wind conditions. The values of intensity components appear to follow the updated, experimentally determined ratio, but more generally, their results agree with the wider trend of increases in intensity with roughness, with measured values typically $< 8\%$ in heavy traffic compared to 9% measured by Wordley and Saunders, [27]. Their measurements also suggest that within the range tested, traffic density and in particular the wakes of heavy duty vehicles have a much stronger effect on turbulence intensity than either wind speed or terrain type. With this in mind a modification or redefinition of the surface roughness parameter to incorporate this effect may help in providing more accurate predictions of intensity values seen by a moving vehicle.

Values of turbulent length scale across all studies and terrain conditions are found to be less than 6m on average. Unlike the relationship between the measured intensities, the lateral length scale is smaller than the longitudinal, in some cases by as much as 50%. Vertical scales are substantially lower, typically less than 0.5m, most likely due to the close proximity of the ground. Over the range of typical vehicle heights $0 - 4\text{m}$, length scales are seen to decrease towards the ground, with traffic density being a crucial determining factor. Saunders and Mansour [29] showed that upstream vehicles reduced the longitudinal length scale component to below $1\,\text{m}$, although this seems to be an extreme case with the average from the majority of traffic studies below 3m.

In obtaining a generalisation of on-road turbulence and comparing flows of varying intensities and length scales, the wind energy spectrum is considered a more appropriate metric [27, 28]. Figure 1.13 shows the way in which the frequency distribution of on-road wind energy changes with turbulence intensity and length scale, taken from the measurements of Wordley and Saunders [27].
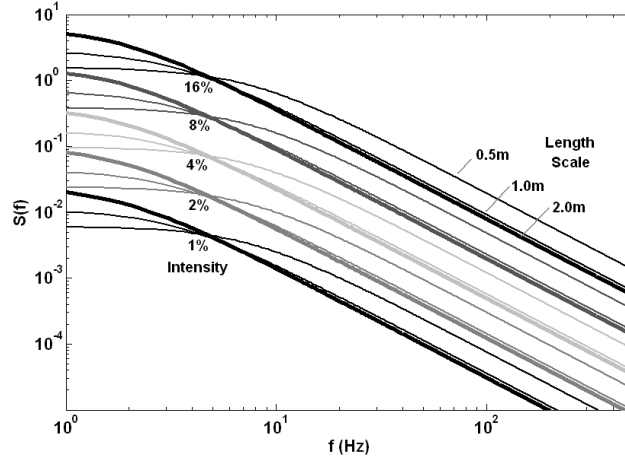
Figure 1.13: Variation of power spectra with turbulence intensity and length scale [27].

Initial observations reveal that high spectrum values are associated with lower frequencies, with a roll off to lower energy content as the frequency increases beyond 1Hz. High values of intensity result in the greatest spectral values and for frequencies below 5Hz, large length scales also lead to large spectral values. Above this frequency, larger length scales are found to reduce the energy content. Using this wind spectrum metric, Wordley and Saunders [27] measured the turbulence properties of the Monash full scale wind tunnel and compared these value to the range of on-road spectra. It was shown that the wind tunnel was unable to replicate the on-road turbulence low frequency energy content, most noticeably in reproducing highway traffic conditions and road-side obstacle terrains. As a result, wind tunnel target length scale and intensity values were suggested to shift the spectral range and provide a reasonable compromise in simulating a typical on-road environment, as shown in Figure 1.14.

From the limited on-road measurements of wind speed at vehicle heights, the complexity of the wind's behaviour has been shown. Turbulence intensity measurements have been shown to lie within a range from 1% for city terrain up to 16% for heavy traffic

conditions with longitudinal and lateral components of similar magnitude. Turbulent length scale values were found to vary drastically depending on the terrain and traffic conditions but were on average, found to be less than 6m. These ranges can be combined in a single wind energy spectrum metric, to provide an indication of how the wind energy content varies with frequency. The resulting band of energy spectra can be used to assess the methods of simulating these real-world conditions.
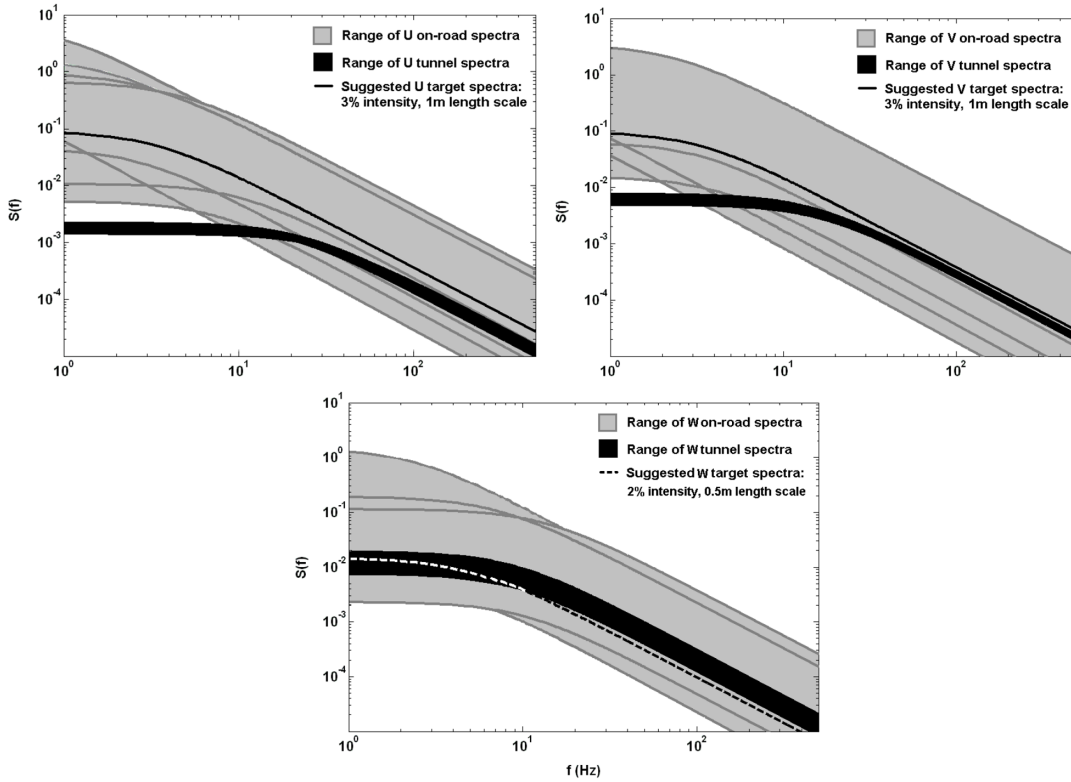
Figure 1.14: Comparison of component on-road power spectra (grey), to Monash wind tunnel (black) and suggested wind tunnel target (dashed) [27].

1.3 Simulating Typical On-Road Conditions

Simulating the flow around a vehicle is crucial for vehicle aerodynamicists who would otherwise rely solely on on-road tests. Simulation of the flow, either experimental or computational, offers control over the flow's properties, providing a level of repeatability necessary to monitor the effect of shape modifications and aerodynamic devices on a

vehicle's design. In addition, simulation offers a vast array of flow field and force measurements, properties that are often limited or not possible to record during on road tests.

1.3.1 Experimental Simulation

The flow produced by the majority of wind tunnels is deemed smooth due to its low turbulence properties, with typical values of intensity $< 0.5\%$. These flow conditions fulfil the repeatability requirement whilst also widening the potential applications of the facility, although as already shown, they are not a correct replication of the conditions found on the road. To be able to use wind tunnels to simulate a typical on-road environment, turbulence has to be added to the flow through turbulence generation systems (TGS). These systems generally fall into one of three categories: passive, active drag based or active lift based devices [30].

Passive devices are defined as static objects place upstream to generate controllable disturbances. Purpose built turbulence grids are an example of this, where turbulence properties can be varied through the design and placement of such a device, as shown in Figure 1.15a. The disturbance scales generated by these devices are generally an order of magnitude smaller than the vehicle and thus only represent the high frequency end of the on-road wind spectra. One example of such a device is the NRC Road Turbulence System designed by McAuliffe et al. [31, 32] and calibrated using their measured on-road data discussed previously [28]. The spectra of their generated turbulence was shown to match to on-road values during moderate traffic conditions only at high frequencies, with an under prediction of the highest energy content at low frequencies. Although high frequencies are associated with low energy content, it was shown by Howell et al. [33] and Newnham [34] that the introduction of such small scale turbulence at post-critical Reynolds numbers increases the turbulence inside the vehicle's boundary layer, consequently delaying flow separation and increasing skin friction and base suction. This led to increases in the drag coefficient with freestream turbulence intensity, suggesting that the drag of a vehicle on the road will be greater than the value obtained in the smooth flow of the wind tunnel.
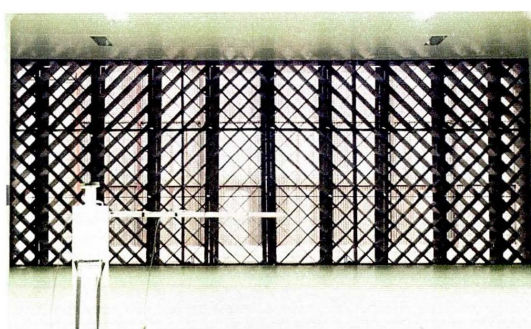
(a) Turbulence grid in MIRA wind tunnel [34].

(b) Upstream vehicle arrangement used by Cogotti [35].

Figure 1.15: Examples of passive TGS.

Placement of a second vehicle upstream can also be used as a passive device, an arrangement shown in Figure 1.15b. Saunders and Mansour [29] and Cogotti [35] showed how this arrangement can be used to provide a reasonable replication of the turbulence properties at a buffeting distance of one vehicle length, although there were some discrepancies in the results due to the fluctuations in the natural wind during on-road testing that were not replicated in the wind tunnel.

In summary, passive devices appear to work well in adding turbulence to smooth flow, however the conditions that they can simulate are very limited. It is clear that an alternative method is required in order to simulate the complete on-road wind energy spectra.

Active devices have been shown to generate much larger length scales and capable of simulating the low frequency, high energy content of on-road wind. Examples of active drag based devices are the oscillating grids used by Kobayashi and Hatanaka [36] and upstream deployable blades as shown in Figure 1.16, at the Pininfarina wind tunnel facility [35, 37]. For the latter, Carlino et al. [38] showed that controlling the relative phasing of the opening and closing of the blades provides a dynamic yawing of the flow in the frequency range of $0 - 1$Hz, thus making it possible to investigate a meaningful range of the on-road energy spectra. As an addendum Carlino et al. [38] also demonstrated the ability of this TGS in generating the turbulent length scales found when following in the wake of an upstream vehicle and even programmed the

blades to simulate the flow behaviour during a real-time overtaking manoeuvre.

Active lift based devices such as a collection of vertical oscillating airfoils upstream of the test section, as shown in Figure 1.17, have been employed by Bearman and Mullarkey [39], Passmore et al. [40], Schröck et al. [41], Mankowski et al. [30] and Blumrich et al. [42]. These devices offer the greatest control over the turbulence behaviour with intensity determined by the amplitude of the aerofoil oscillation, and length scale by its frequency, although for the majority of devices, disturbances can only be introduced laterally. However, the design by Mankowski et al. [30] allows for three component disturbance with longitudinal and vertical velocity variations introduced through a set of shutters in the throat of the main collector and a horizontal aerofoil located at the top of the inlet respectively.
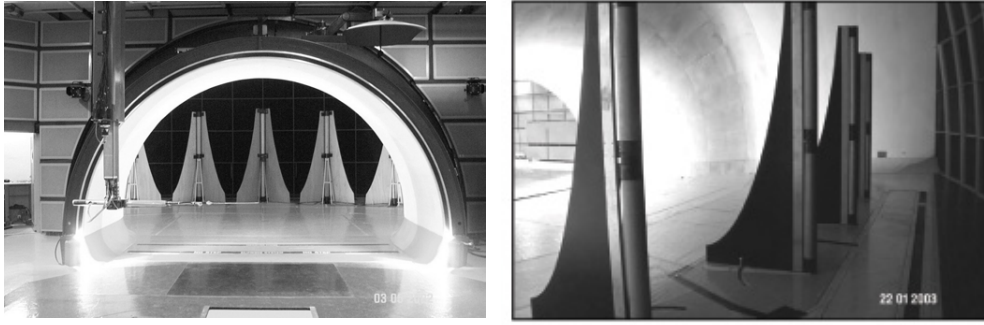
Figure 1.16: Active drag based turbulence generation system at Pininfarina [35, 37].
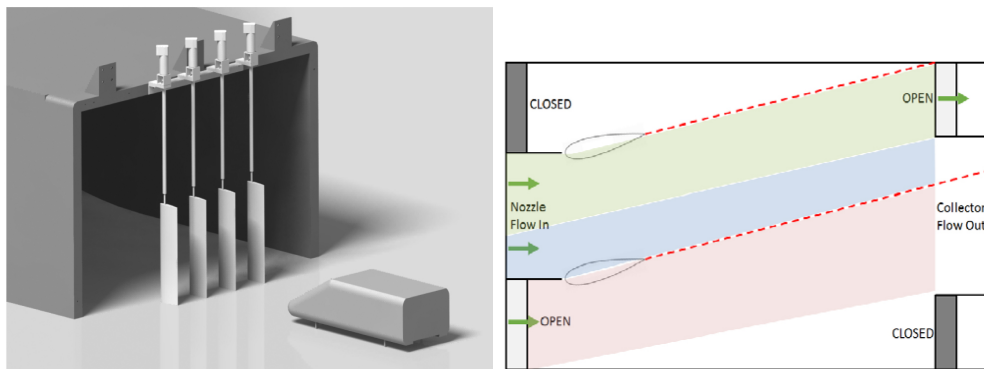
(a) Oscillating upstream aerofoils used by Schröck et al. [41].

(b) Upstream vanes used by Mankowski et al. [30].

Figure 1.17: Active lift based turbulence generation systems.

It is clear that there are a range of wind tunnel devices capable of replicating typical on-road turbulence levels however as already discussed, in addition to turbulence, the flow seen by a vehicle contains shear and simulating this property in a wind tunnel facility has proven difficult. The velocity profile seen by a vehicle is determined by upstream terrain over a distance much larger than the upstream length of wind tunnel facilities and thus to correctly simulate shear effects, this profile has to be imposed on the flow. A device which is capable of generating a realistic velocity profile, whilst including the unsteady turbulent behaviour has yet to be designed.

1.3.2 Computational Simulation

In more recent years, simulations using computational fluid dynamics (CFD) have become more feasible. This type of simulation removes many of the restrictions imposed by physical testing with turbulence and shear parameters such as intensity, length scale and velocity profile simply given as inlet boundary conditions, as shown in Figure 1.18.

(a) 0 degrees yaw

(b) 6 degrees yaw
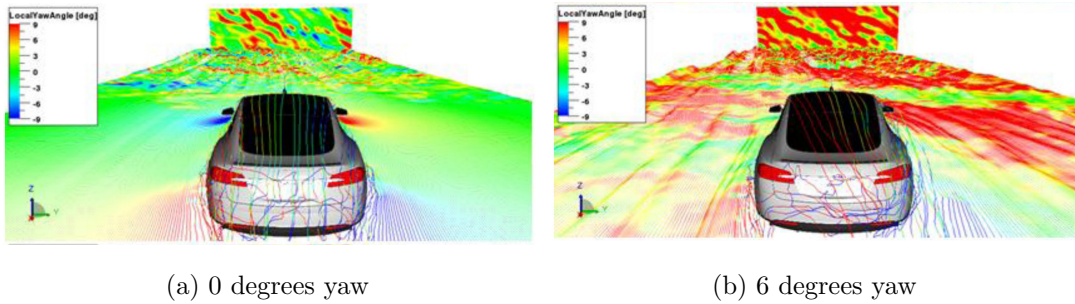
Figure 1.18: Example of inlet turbulence (7%) by D'Hooge et al. [43].

Many studies have reproduced realistic on road turbulence levels using CFD through defined, time-varying velocity functions at the inlet, such as Gaylard et al. [44, 45] and D'Hooge et al. [43, 46] with the emphasis on understanding the effect of realistic turbulence levels on the flow around a vehicle when compared to the smooth flow found in wind tunnels. Both studies show how increased turbulence intensity, up to 7%, increases overall drag and this is in agreement with the experiments of Howell et al. [33] and Newnham [34]. Plots of drag coefficient distribution, Figure 1.19, show how the wheels, backlight and bootdeck regions have the largest contribution to this drag

increase. Both studies agree that upstream turbulence increases the turbulent mixing within the separated flow structures, consequently reducing their size and pressure. This is most noticeable in the wakes of the front and rear wheels, as shown in Figure 1.20, which also shows how this effect is maintained at a typical on-road flow yaw angle of 6 degrees.
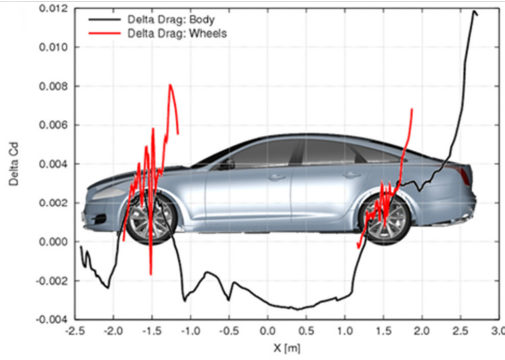
(a) Gaylard et al. [45]
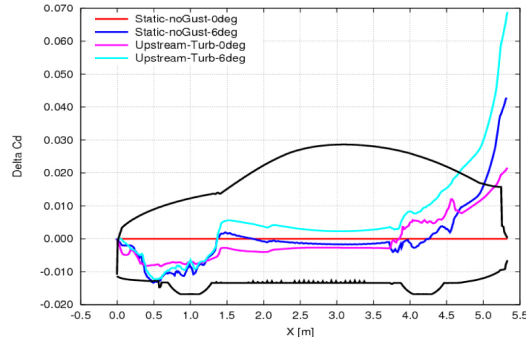
(b) D'Hooge et al. [46]

Figure 1.19: Drag coefficient delta distribution, upstream turbulence (7%) minus no turbulence.
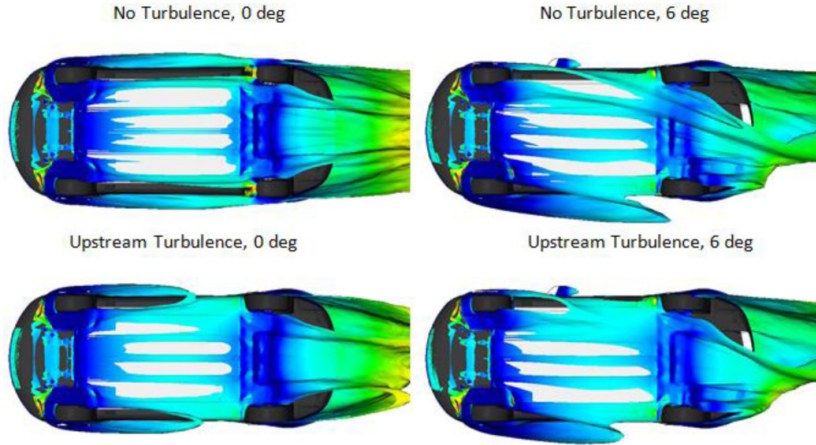
Figure 1.20: Isosurfaces of total pressure for yaw and upstream turbulence from D'Hooge et al. [46].

In addition to the impact on drag, high turbulence intensities are associated with cabin noise. Oettle et al. [47, 48, 49], Lawson et al. [21, 50] and Lindener et al. [51] have

published comprehensive results quantifying the effects of on-road turbulent flow on window surface pressures and cabin noise, with measurements taken from on road and wind tunnel tests. Most recently, Kounenis et al. [52] built on this work and showed how the introduction of turbulence representative of a moderate traffic environment produced a sound pressure level (SPL) modulation of up to 5dB at various locations on the driver side glass and 1-2dB at the driver's position in the cabin. Currently the effect of on-road conditions on aeroacoustics is a deep concern for aerodynamicists, as the noise heard in the cabin is often perceived as an indication of the vehicle's quality.

It is clear that there are a range of methods in simulating typical on-road conditions. Experimentally, only the most advanced facilities, with active turbulence generation systems are able to simulate conditions which cover the range of spectral energy encountered on the road, whilst the majority of passive systems can only generate the highest frequencies and lowest energy content. In addition, including realistic shear effects within a wind tunnel appear to be problematic. Computational simulations offer a way around this through dynamic boundary conditions. Using both approaches, it has been shown that typical on-road conditions can lead to increases in vehicle drag and cabin noise. These effects fall under 'quality and refinement' and contribute to the perceived quality of the vehicle and customer satisfaction, hence for automotive OEMs, accurately simulating a typical on-road environment is an important stage in a vehicle's aerodynamic optimisation.

1.4   Simulating Extreme On-Road Conditions

So far this review has only considered simulating typical on-road turbulence levels; conditions which impact on a vehicle's perceived quality. During the development of a vehicle, it is also important to consider extreme wind conditions such as the 3-second gust speeds shown in Figure 1.4. Such conditions can influence the vehicle's handling and stability, thus requiring a response from the driver. In mild cases, the vehicle response may be small enough to be classed as a quality and refinement issue, but more extreme conditions could present a safety risk. Simulating these conditions rather than testing on-road is highly desired, as it allows control over the test environment and

removes some of the risks placed on test drivers.

It is generally assumed that a driver will be able to provide an adequate response to prevent a significant deviation as any lateral or yaw accelerations are sensed, however this is not always the case. Along with the driver's ability, the frequency of the gust plays a large part in actual response of the vehicle. As shown by Wagner and Wiedemann [53], within a frequency range of $0.5\,\mathrm{Hz}$ to $2\,\mathrm{Hz}$, the driver's response can amplify the vehicle's response. This occurs as the vehicle reactions due to the crosswind and due to the driver's steering input approach an in-phase state at around a frequency of $1.4\,\mathrm{Hz}$. For frequencies $<0.5\,\mathrm{Hz}$ the driver has a positive influence on the vehicle's response, whereas at higher frequencies $>2\,\mathrm{Hz}$, the driver has little to no influence as the gust has passed before it is felt.

1.4.1 Experimental Simulation

In order to assess the vehicle's response to such an event, a desired flow disturbance has to be generated, either naturally or artificially. On road vehicle testing in extreme gusts is uncommon, due the rarity and risks of such events and hence the controlled environment of crosswind generators beside test tracks such as Figure 1.21 are a more appealing alternative.

(a) Crosswind generator at Applus IDIADA, Barcelona [54]
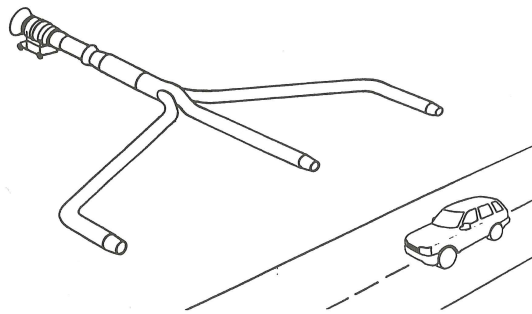
(b) MIRA crosswind generator [55]

Figure 1.21: Examples of crosswind generators.

One of the earliest examples of this type of testing was performed by Klein and Hogue [56], using the full-scale facility designed by Klein and Jex [57]. A crosswind velocity

of $15.7\,\text{m/s}$ (35 mph) and vehicle speed of $22.4\,\text{m/s}$ (50 mph) generating a flow yaw angle of 35° was applied to a collection of five vehicles, with and without a driver's input. Similarly, Howell [55] exposed a small Sports Utility Vehicle (SUV) to a severe at a slightly lower yaw angle. A trifurcated tail pipe attached to the exhaust of a jet engine generated a wind speed of $14.5\,\text{m/s}$, which when combined with a vehicle speed of $27.8\,\text{m/s}$ (100 km/h), produced a flow yaw angle of approximately 28°. The length of the gust was measured at ten car lengths, which when combined with the vehicle speed, corresponds to a disturbance frequency of $0.7\,\text{Hz}$. Although this value falls within the frequency range where Wagner and Wiedemann [53] showed that a driver can exaggerate the vehicle response, the tests by Howell [55] were open-loop, with no driver response. For a two second period after entering the crosswind, the steering wheel was held fixed. Gyroscopic rate transducers and accelerometers were fitted to measure the chassis moment rates and lateral acceleration respectively, while course deviation was measured with a dye trail. After two seconds, the lateral deviation from a collection of runs fell within a range of $2\,\text{m}$ to $3\,\text{m}$.

In an attempt to standardise such facilities and testing procedures, an International Standard ISO 12021:2010 [58] was derived. This standard prescribes a crosswind velocity of $20\,\text{m/s}$ and vehicle speed of $27.8\,\text{m/s}$ (100 km/h), thus a flow yaw angle of approximately 36° is generated. The minimum length of the gust is required to be at least $15\,\text{m}$ and preferably more than $25\,\text{m}$, whilst the ambient wind speed cannot exceed $3\,\text{m/s}$. Following on from the test procedure of Howell [55], the test is open loop with a fixed steering wheel position. This testing procedure eliminates any variability in the driver's response and determines the response as a function of the vehicle's properties. Required measurements are wind speed over the length and height of the wind zone and also lateral deviation, yaw velocity and lateral acceleration of the vehicle. The downside to this testing procedure is the limited flow field measurements that can be obtained, which makes it difficult to identify the aerodynamic structures responsible for the vehicle's dynamic behaviour. In addition, such tests cannot be performed until the late stages of prototype development, at which point, significant financial investment has been placed into the design and any changes are costly.

For these reasons, full scale and model scale wind tunnel tests earlier in the design

phase are an appealing alternative. In assessing a vehicle's crosswind sensitivity using such facilities, it is common practice to simplify the event and obtain the quasi-steady aerodynamic force and moment values at a range of static flow yaw angles. From the resulting database, stationary gradients of aerodynamic coefficients can be extracted. In general, a vehicle is deemed less sensitive to crosswinds, if the yawing moment gradient is small. This method was used by Stoll et al. [59] to assess the crosswind sensitivity of estateback and notchback geometries, in which the latter was more sensitive to gusts. Whilst this may at first appear counterintuitive, it can be traced back to a reduction in side area, reducing the rear side force and increasing the yawing moment. The advantage of this method is the convenience of testing, as the majority of wind tunnels can accommodate yawed models, however as the tests are quasi-steady, any unsteady effects of the gust passing over the vehicle are ignored and hence an alternative method is highly desired.

A real world crosswind introduces a time dependent yaw angle profile to the vehicle. Wind tunnel turntables are also capable of subjecting a vehicle to a time dependent yaw angle change, however the rotational speed of most turntables is slow in comparison to the rate of yaw angle change in a real world environment. Even if a turntable was able to rotate at the desired speed, Watkins et al. [60] showed how the additional angular velocity of the vehicle as it rotates, results in an inaccurate streamline curvature along the vehicle's length. During a simulation of a vehicle leaving a open region of crosswind, the resultant flow vectors would imply that the rear of the vehicle leaves the gust first. Hence, simulation using this turntable technique is not correct for gust penetration and exiting.

One of the earliest methods of correctly capturing this behaviour involved traversing a vehicle across the width of the working section on a purpose built track, originally designed by Beauvais [61] and used later by Macklin et al. [20]. This approach, shown in Figure 1.22, generally requires small scale, simple shaped models to avoid Reynolds number effects and requires a range of model scales to change the gust length. For these reasons, this method has received little attention.

Ryan and Dominy [62] introduced an alternative approach in which the model is kept
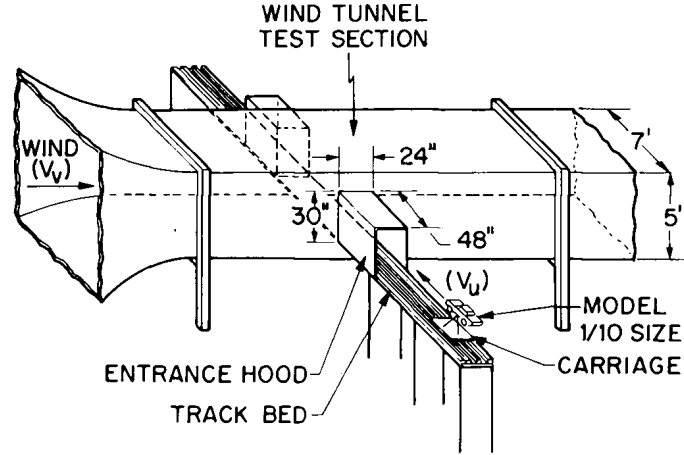
Figure 1.22: Wind tunnel track traversing system used by Beauvais [61].

stationary in a conventional wind tunnel, whilst a crosswind jet scans along the model, as shown in Figure 1.23. This is achieved with a secondary tunnel placed at a 30° angle to the axis of the main working section. The model is gradually exposed to the secondary flow through a moving belt with variable aperture or in an updated configuration, an actuated shutter mechanism [63, 64]. More recently, Volpe et al. [65, 66] used this experimental approach coupled with particle image velocimetry (PIV) apparatus to identify the flow structures present during a crosswind event. Although this method removes the gust length restrictions imposed by the track method, it is accompanied by unwanted undershoots and overshoots in the generated flow yaw angle due to mixing effects between the main and auxiliary flows on opening and closing of the shutters.

(a) Dominy and Ryan shutter mechanism [63, 64]

(b) Volpe et al. shutter mechanism [66]
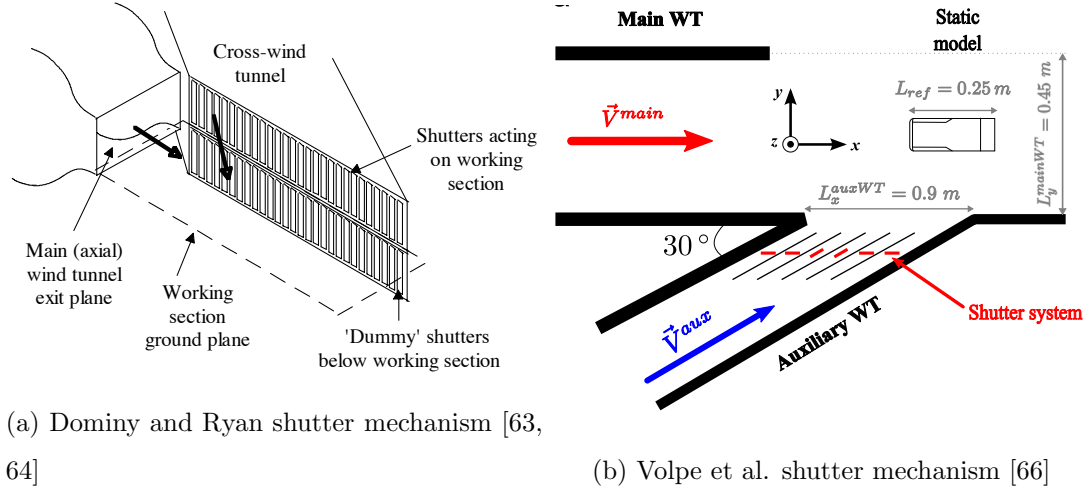
Figure 1.23: Wind tunnel facilities with additional crosswind jet.

Simulating the impact of gusts on a vehicle's response is a straightforward process when using track testing and crosswind generators as it places the real vehicle in the presence of the gust and allows it to respond. However, in a wind tunnel environment, behaviours of the vehicle such as lateral deviation and yaw angle change are not simulated as the vehicle is fixed in the working section. Therefore, when using these facilities, the effect of the vehicle's response on the aerodynamic is ignored. In order to obtain a prediction of the vehicle's dynamic response, the aerodynamic loadings are given to a vehicle handling model after the tests have taken place, in a one-way coupled manner. This input can be obtained from a set of quasi-steady simulations of a vehicle at a range of yaw angles interpolated over the crosswind profile, or from a transient history of aerodynamic loads from a single test, however there is still an underlining flaw in this one way coupled approach. The positional change of the vehicle during the event is not accounted for in the aerodynamics. For example, it can be predicted that in the presence of a crosswind a vehicle will yaw, with the front of the vehicle moving with the direction of the gust. As shown by Figure 1.7, for a gust which initially acts perpendicularly to the path, the additional yaw angle of the vehicle will reduce the resultant flow yaw angle. For large vehicle yaw angles, the reductions in the resultant flow yaw angle may be large enough to significantly alter the flow structures around the vehicle and impact the aerodynamic loads and consequently, the vehicle's response. This fully coupled system describes the real world interaction that takes place on the

road.

The methods of assessing vehicle response resulting from aerodynamic inputs are summarised as follows, where static refers to the one-way coupled methods and dynamic the fully coupled:

- Quasi-Steady Static Coupling - A database of steady state simulations at a range of yaw angles, with interpolated aerodynamic forces and moments over the gust length used as handling model inputs.

- Unsteady Static Coupling - A transient history of aerodynamic forces and moments over a static model used as handling model inputs.

- Unsteady Dynamic Coupling - A system where aerodynamic forces/moments and positional data are being exchanged simultaneously.

1.4.2 Computational Simulation

An alternative to physical testing is CFD simulation. As already discussed, this simulation method removes many of the restrictions imposed by physical testing, through dynamic boundary conditions capable of replicating the unsteady environment. In a similar fashion to experimental tests, it is possible to assess the vehicle's response to an extreme gust using the one-way coupled methods previously mentioned, but importantly, it is possible to simulate the fully coupled approach due dynamic meshing methods that allow for large motions of geometries during a simulation. Over the last ten years, research in this area has been lead by Tsubokura, Nakashima et al. [67, 68, 69, 70, 71, 72] with emphasis on heavy duty trucks, which due to their large lateral area and extreme weight variations make them highly susceptible to crosswinds.

In one of their first studies, Tsubokura et al. [67] assessed the computational methods that are capable of implementing the three coupled approaches using simplified two dimensional simulations. Quasi-steady static coupling to a simplified two-equation, two degree of freedom handling model was performed using a step input, formed from the aerodynamic side force and yaw moment at a steady-state flow yaw angle. The vehicle

response was then compared to that obtained using the unsteady dynamic method. This fully-coupled method included the motion of the vehicle in the CFD simulation via the overset grid or Chimera method [73], a dynamic grid method which uses a sub-grid around the vehicle and moves through the main grid and crosswind region, as shown in Figure 1.24. Hence by running the aerodynamic and handling simulations simultaneously, the vehicle's position could be updated continuously, giving the most accurate replication of the on-road event. The results of the quasi-steady approach showed a large time delay in lateral displacement and vehicle yaw angle responses when compared to the fully-coupled approach, suggesting that the gust penetration behaviour is not accurately captured using this approach. Later, this was confirmed by Nakashima et al. [68] who showed that the quasi-steady aerodynamic response was unable to capture an unsteady overshoot and undershoot of the aerodynamic yawing moment, formed as a the vehicle is gradually exposed to the gust along its length, when entering and exiting (>30° flow yaw angle).
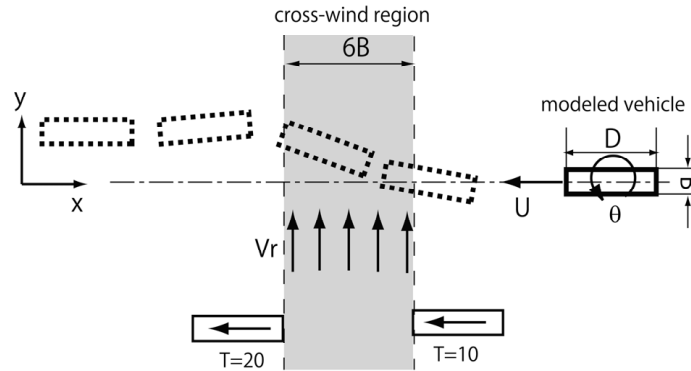
Figure 1.24: Overset model used for unsteady-dynamic coupling by Tsubokura et al. [67].

However, there are certain conditions, as shown by Hucho and Emmelmann [74] and Nakashima et al. [68], where long, shallow gust gradients in relation to the vehicle length and small flow yaw angles ≤10°, may bring about a quasi-steady behaviour of the yaw moment, hence justifying the use of this coupling method.

The overset grid method employed in the fully coupled, unsteady dynamic approach used by Tsubokura et al. [67] has the disadvantage of requiring a long fluid domain, equal to the simulated distance of the vehicle motion, and thus is computationally

34

expensive. Tsubokura et al. [67] suggested two alternative methods: a turntable model and convective crosswind model as shown in Figure 1.25. In the turntable model, a yawing motion of the vehicle is used to reproduce the transient flow yaw angle. However, as already shown by Watkins et al. [60], this method fails to capture the correct penetration and exiting behaviour and thus is not correct for this application. On the other hand, in the convective crosswind model, a band of crossflow is convected downstream with the main flow and passes over a fixed vehicle and this is the most common method of computationally simulating a crosswind event. Favre [75] used this method to investigate the effect of substantial crosswind (20° flow yaw angle) over simple geometries while Hemida and Krajnovic [76] investigated the effect of a realistic gust profile on a double-deck bus using the approach. This method includes the effects of the vehicle entering and exiting the crosswind, however since the vehicle is fixed in the domain it falls under a one-way coupled approach. A comparison of the turntable and convective crosswind model responses is shown in Figure 1.26, where the target response is obtained with the fully-coupled, overset method. As anticipated, the convective crosswind responses follow the target response more accurately, most likely due to the improvements in flow prediction when the vehicle is at the edges of the gust.

(a) Turntable model   (b) Convective crosswind model
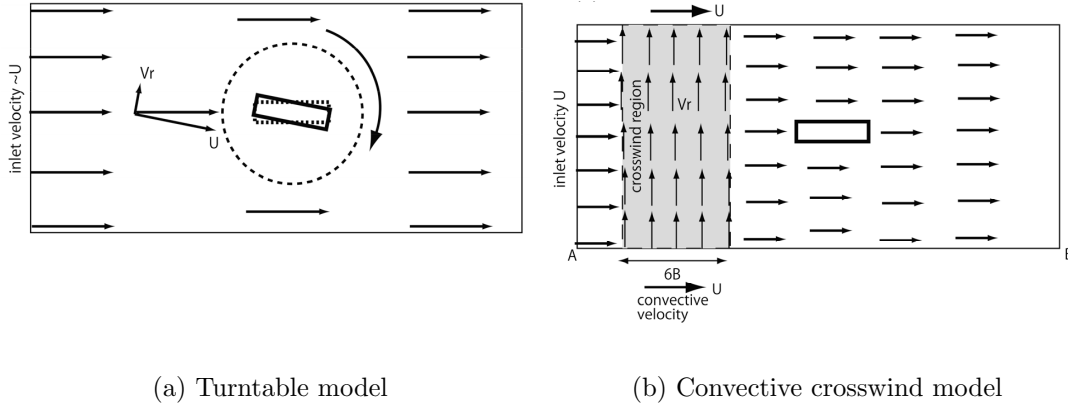
Figure 1.25: Crosswind models of Tsubokura et al. [67].

(a) Lateral displacement   (b) Yaw angle
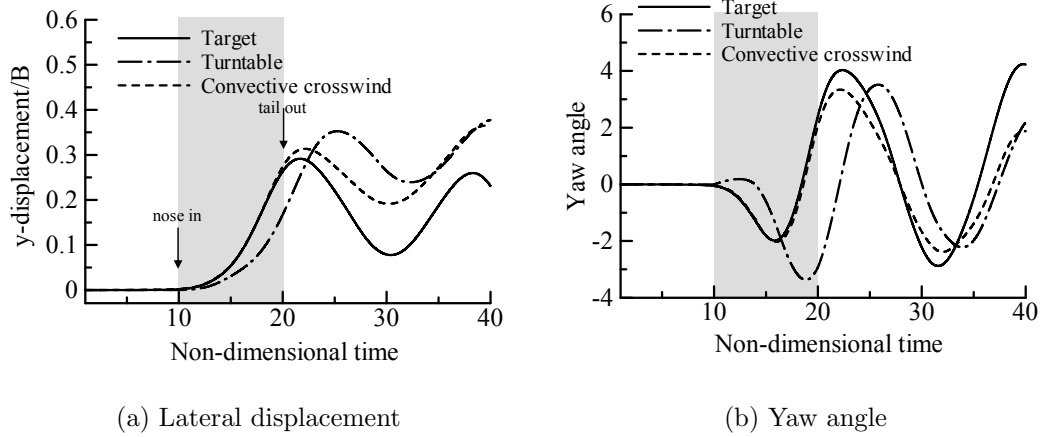
Figure 1.26: Comparison of the predicted response of simplified crosswind models [67].

A fully-coupled, unsteady dynamic approach that does not use the computationally heavy overset method was applied a few years later by Tsubokura and Nakashima [69] and Nakashima et al. [72]. The method uses grid-deformation based on the Arbitrary Lagrangian-Eulerian (ALE) formulation combined with a moving reference frame approach to include yaw rotation and lateral translation respectively. Thus these simulations are classed as having only two degrees of freedom. The effect of an extreme crosswind (45° flow yaw angle) on a heavy-duty truck is shown in Figure 1.27 and Figure 1.28 shows the magnitudes of the response and how they compare to those obtained with the quasi-steady static approach. Consistent with their previous two dimensional simulations, the quasi-steady static approach is unable to capture the response of the unsteady dynamic approach, most noticeably in the vehicle yaw angle. Figure 1.28 also gives an indication of a driver's steering input, as they attempt to recover from the course deviation. The quasi-steady approach clearly over predicts the peak steer angle values and this is responsible for a large over prediction in vehicle yaw angle after the gust has passed.

Despite their substantial work in this area, Tsubokura, Nakashima et al. fail to make comparisons between all three coupling methods, hence the necessity of the more computationally expensive unsteady dynamic coupling method cannot be verified. An unsteady static coupling may be sufficient to capture the response to a crosswind event, as this method includes the unsteady aerodynamic effects that the vehicle experiences
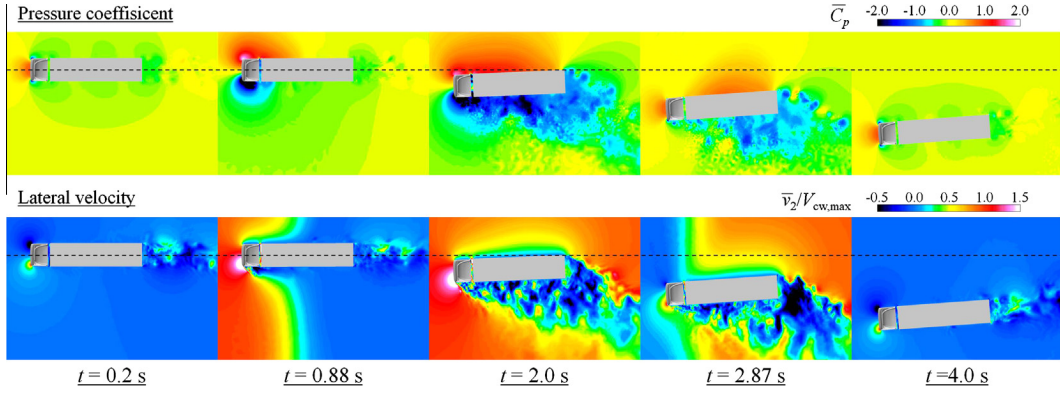
Figure 1.27: Snapshots of pressure coefficient and lateral velocity using the unsteady-dynamic approach [72].

(a) Lateral displacement

(b) Yaw rate

(c) Yaw angle

(d) Steering wheel angle
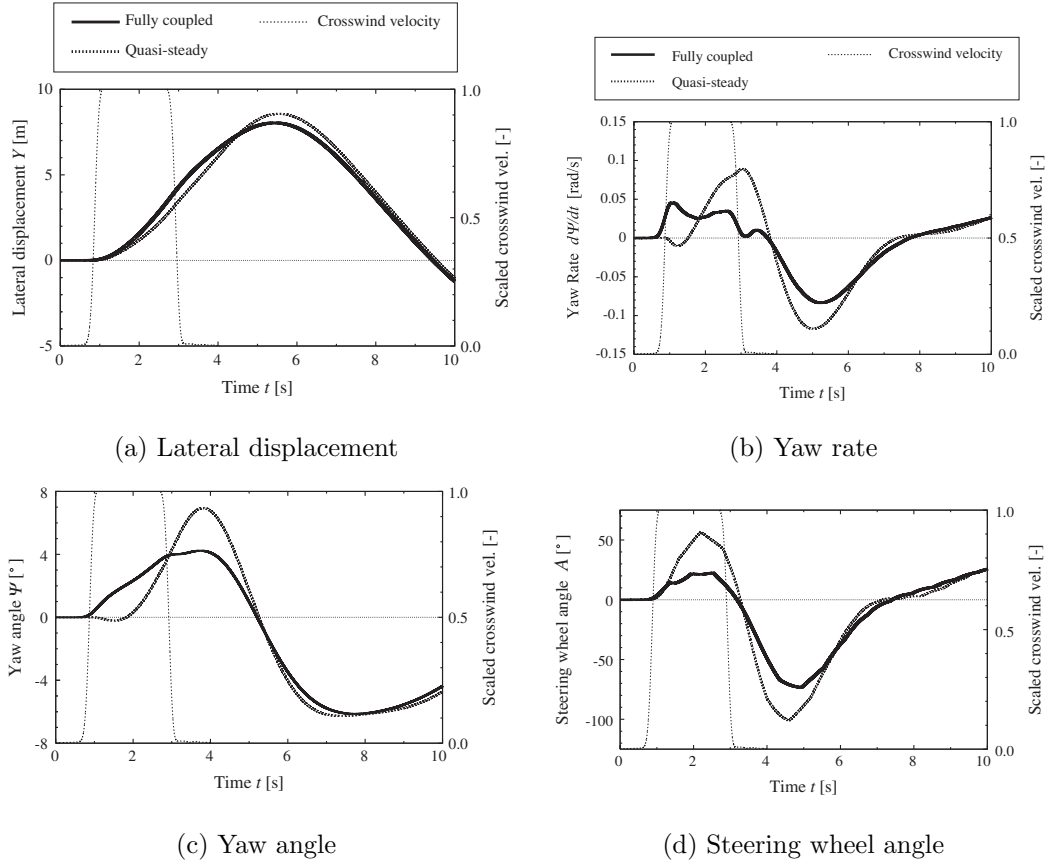
Figure 1.28: The predicted response of a heavy-duty truck to an extreme crosswind using the fully coupled 2DOF approach [72].

at the edges of the gust. In addition there is evidence in the force and moment histories of Nakashima et al. [70] to suggest that the aerodynamic rolling moment and lift force have a sizeable impact on the vehicle's response. Thus a fully coupled 6DOF simulation that includes rotation and translation about all three axes may yield a different outcome.

1.5 Summary

It has been shown that the environment through which a vehicle travels is unsteady. Shear and turbulence in the natural wind result in a time and position dependent velocity distribution over the vehicle, the effects of which cannot always be investigated using a wind tunnel. Disturbances to the smooth flow generated by such a facility can be introduced, but only the most sophisticated can reproduce the full range of energy spectra values typically experienced on the road. For this reason, the effect of turbulence on road vehicle aerodynamics has received much more attention than the effect of shear and the influence of the two combined appears to be unknown.

In addition to typical wind conditions, the understanding of a vehicle's behaviour during extreme crosswind events is important from a safety perspective and testing of such events is limited to test-track crosswind generators and prototype vehicles. Simulating the correct behaviour in a wind tunnel is fundamentally flawed as the vehicle remains fixed in position and is unable to dynamically respond to the gust. This implies that the vehicle remains on a constant trajectory through the gust and does not deviate. Changes to a vehicle's position and orientation whilst immersed in the highly yawed flow will produce variations to the aerodynamic loads, which in turn can influence the dynamics in a closed loop cycle. However, it is common for this effect to be ignored, and a vehicle's response is predicted in a one-way coupled manner using quasi-steady loads or unsteady loads produced by scanning a lateral velocity along the vehicle using a secondary tunnel.

Computational simulation removes many of the restrictions imposed by physical experiment, with time dependent inlet boundary conditions and dynamic grid methods

that allow geometries to move within a fluid domain. Such simulations, referred to as fully-coupled, unsteady dynamic, have been performed previously, but considering motion in only two degrees of freedom (lateral translation and yaw rotation) whilst there are several dynamic grid approaches that can be applied to model this motion. With the continual improvement in computational performance, the impact of such methods on accuracy and run times is constantly evolving. Finally, the need for such complex simulations is yet to be determined. Previous work suggests that a one-way coupled approach tends to over predict the values of deviation, but this research has focused heavily on large trucks, rather than typical family sized passenger vehicles. Due to the substantial reduction in lateral area, the variation in vehicle response may be minimal and thus a one-way coupled approach may be sufficient.

1.6 Objectives

The aim of this work is to design, implement and evaluate a fully-coupled, six degree of freedom system, of a vehicle's aerodynamics and dynamics. In particular, this system will be applied to the simulation of a severe crosswind.

In order to achieve this, there are several objectives that need to be fulfilled.

- Determine a suitable numerical methodology and turbulence model for accurate prediction of the flow around a road vehicle geometry. This is crucial as the aerodynamics and resulting loadings on the vehicle can have a large impact on handling properties.

- Evaluate and determine the most suitable methods of including moving geometry within a CFD simulation. This will allow any dynamic vehicle motions such as ride height, roll angle and global position changes to be included in the aerodynamics simulation.

- Design the coupling mechanism, in particular the method of communication between the CFD code and the handling model.

- Investigate the importance of shear and turbulence in the natural wind on a vehicle's aerodynamics. This will help to determine if such conditions will have significant impact on vehicle handling and need to be included in the fully-coupled simulations.

- Implement the fully coupled system using a severe crosswind test case and evaluate the fully-coupled response against the simplified one-way coupled approach.

The Flow around a Generic Road Vehicle

Contents

2.1 Introduction

In order to determine a best practices for simulation of the flow field around an automotive body, specifically a sports utility vehicle (SUV) geometry, a selection of methodologies will be assessed for their suitability in reproducing experimental results. Analysis will focus on wake structure and base pressure predictions which will have a large impact on the accuracy of the predicted drag value.

2.2 The Generic SUV Geometry

The Generic SUV model used for these tests was designed by Dr. Daniel Wood, within the Aeronautical and Automotive Engineering department of Loughborough University [77]. The design was the result of a thorough analysis of 39 SUVs, from 12 manufacturers with model years spanning 1970 to 2011. With 27 characteristic length measurements taken and collated: the vehicle side profiles, normalised by vehicle height, were overlaid as shown in Figure 2.1a. Geometrical trends over the years were extracted, such as increasing wheelbase and decreasing sill height and based on extrapolation of these trends, a 2017 Generic SUV geometry was predicted, as shown in Figure 2.1b.

| (a) Overlaid side profile of 39 SUVs | (b) Projected 2017 SUV Geometry |
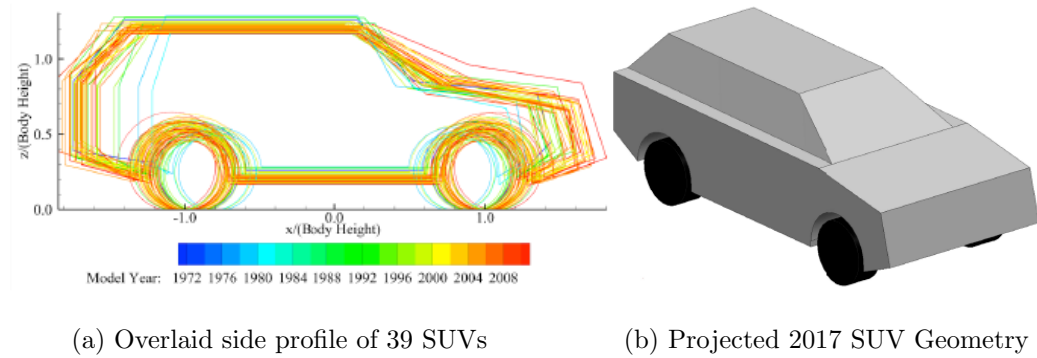
Figure 2.1: Design stages of the Generic SUV geometry.

The wind tunnel model is an evolution of this geometry, with modifications to make it suitable for experimental testing. The final model is shown in Figure 2.2 and features a steep diffuser of 30° and substantial taper angle of the body's front overhang along with radiused edges to promote attached flow. The model was dimensioned in such a way as to limit solid blockage in the Loughborough University model scale (LUMS) wind tunnel to approximately 5% which results in an overall model scale size of 25%. An overview of some of the key geometry dimensions is provided in Table 2.1. The model was designed to facilitate a number of different configurations, with changes in ride height, underfloor roughness and with and without wheels. Details of these configurations have been published by Wood et al. [77], and for this study, the standard configuration with nominal ride height (65 mm), wheels and no underfloor roughness as shown in Figure 2.2 is used.
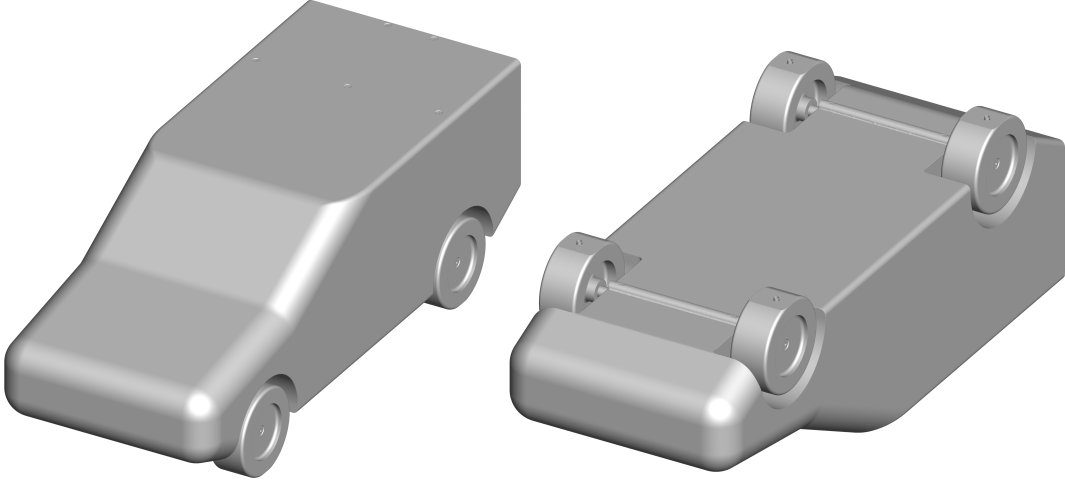
Figure 2.2: Generic SUV wind tunnel model.

Table 2.1: Generic SUV dimensions.

Length ($\mathbf{L}$)	1040mm
Width	410mm
Height	376mm
Wheelbase	650mm
Frontal Area ($\mathbf{A}$)	0.139m^2
Re ($\mathbf{L}$, 40m/s)	2.85×10^6

2.3   Experimental Data

The experimental Generic SUV data, used for the purposes of validation, was obtained by Wood et al. [77] in the LUMS wind tunnel. This wind tunnel is an indraft, low-turbulence facility, designed to accommodate automotive shapes of up to 1/4 scale at 5% blockage. The novel 'horseshoe' design and important dimensions are shown in Figure 2.3.

The geometry features a bell-mouth intake, settling chamber, contraction of ratio 7.3 : 1 and working section measuring $1.92\,\mathrm{m} \times 1.32\,\mathrm{m}$ in width and height. Flow is guided
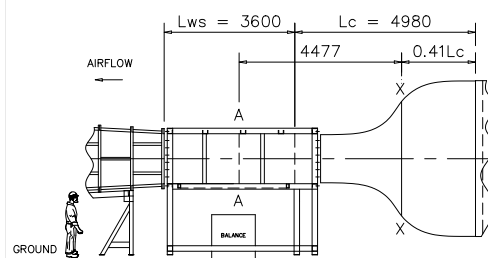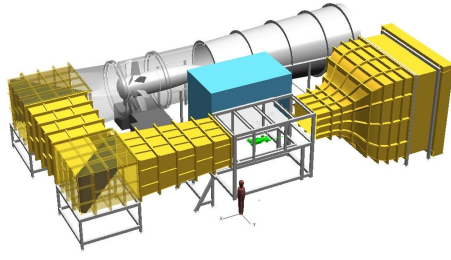
(a) 3D Solid Model of the LUMS wind tunnel   (b) Dimensions of the LUMS wind tunnel

Figure 2.3: The LUMS indraft, low-turbulence wind tunnel [78].

around the 90° corners of the tunnel by vertically mounted turning vanes. A 140kW fan located downstream of the second corner is capable of driving flow through the working section at a maximum speed of $45\,\mathrm{m/s}$. The contraction section and flow conditioning screens located in the settling chamber, limits freestream turbulence intensity to 0.15% in the centre of the working section, as measured by Johl et al. [79, 78]. Corner fillets originating at the start of the contraction aim to reduce secondary flows while diverging walls of the working section aim to eliminate any horizontal buoyancy in the flow. With a model installed, aerodynamic forces and moments can be measured using a six-component balance, located underneath the working section. Four pins of $8\,\mathrm{mm}$ diameter pass through the working section floor, with a $2\,\mathrm{mm}$ clearance ring, to support the model under each wheel and connect to the balance. This arrangement isolates the model from the ground but results in a wheel standoff. Transparent side walls in the working section allow flow field measurements using Particle Image Velocimetry (PIV) whilst more flow intrusive methods such as hotwire and cobra probe measurements are common.

In the Generic SUV tests, PIV was used by Wood et al. [77] to obtain two-dimensional, planar velocity fields along six planes, (three horizontal and two horizontal) in the vehicle's wake. These planes stretched downstream with a length of approximately 0.4**L** and their width, height and position relative to the vehicle is shown in Figure 2.4. Base and diffuser surface pressure values were recorded using an array of 75 pressure tappings, 63 on the base and 12 on the diffuser, but due to the scale of the model and size of the instrumentation located inside the model, tappings were limited to one half of these surfaces. As a result, experimental surface data is subject to

interpolation errors and assumes a symmetric base and diffuser pressure distribution. Finally, the six-component, underfloor, virtual centre balance measured aerodynamic force and moment data.

Surface pressures and forces were corrected for blockage effects using the MIRA correction based on continuity, Equations 2.1 and 2.2 where $\mathbf{A}'$ is the ratio of model frontal area to working cross sectional area ($\mathbf{A}'$=0.056 for the Generic SUV).

$$C_{P_{cor}} = 1 - \frac{1 - C_p}{(1 - \mathbf{A}')^{-2}} \tag{2.1}$$

$$C_{D_{cor}} = \frac{C_D}{(1 - \mathbf{A}')^{-2}} \tag{2.2}$$
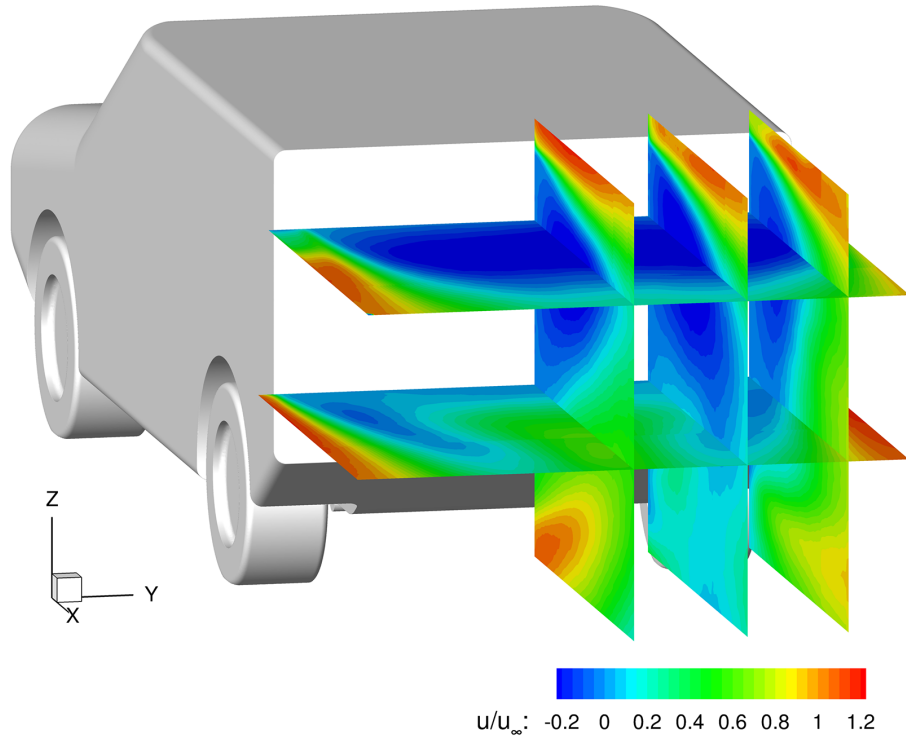
Figure 2.4: Experimental normalised **u** velocity on PIV planes.

A fixed ground plane in the tunnel required non-rotating wheels and led to the development of a floor boundary layer. No boundary layer reduction devices were employed and previous measurements in an empty tunnel at model centre have recorded thicknesses

(δ^{99}) of around 60mm. Coincidently, this height approximately corresponds to the ride height of the SUV, hence the flow in the underbody region will be strongly influenced by this tunnel boundary layer. Wheels were not in contact with the ground, which ensures balance measurements were not influenced by any grounding of the model. All wheels feature a flat on the tyre surface to simulate a typical contact patch and rested on pins, leaving a 4 mm clearance between the wheel and the ground, as shown in Figure 2.5.
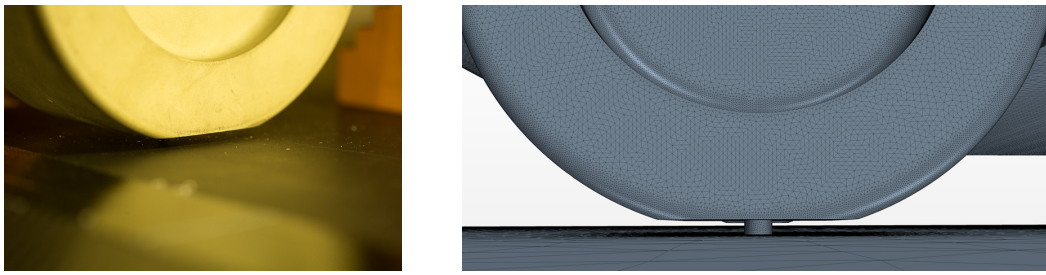
Figure 2.5: 4mm clearance between wheel and floor of the LUMS wind tunnel.

2.4 Computational Domain and Grid Generation

A simplification of the LUMS geometry is used to define the outer boundary of the computational domain. The complete indraft loop is not modelled, but is extended downstream from the end of the first diffuser with uniform cross-section, as shown in Figure 2.6. It is assumed that this simplification does not affect the flow within the working section and also avoids the 3D modelling of the corner turning vanes. The bell-mouth at the inlet of the tunnel has also been removed and the inlet of the computational domain is taken from the location of the final flow conditioning screen within the settling chamber, 0.20 m upstream of the contraction. The SUV body is located at the centre of working section replicating the experimental setup.

On the SUV's surface, triangles are limited to a size of 1 mm ($0.001\mathbf{L}$) to help maintain curvature and prevent any unphysical flow separation. Figure 2.7 shows the surface elements around one of the front wheels where due to the high curvature of the geometry and high flow velocity this may be an issue. The pins on which the model rests are 8 mm
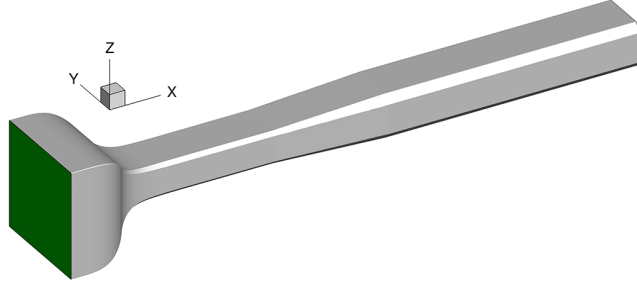
Figure 2.6: LUMS domain.

in diameter and thus their surface elements are limited to a smaller size of $0.25\,\text{mm}$ $(2.5 \times 10^{-4}\mathbf{L})$. The complete domain contains 4.4×10^6 surface elements, with 3.3×10^6 of those found on the SUV.
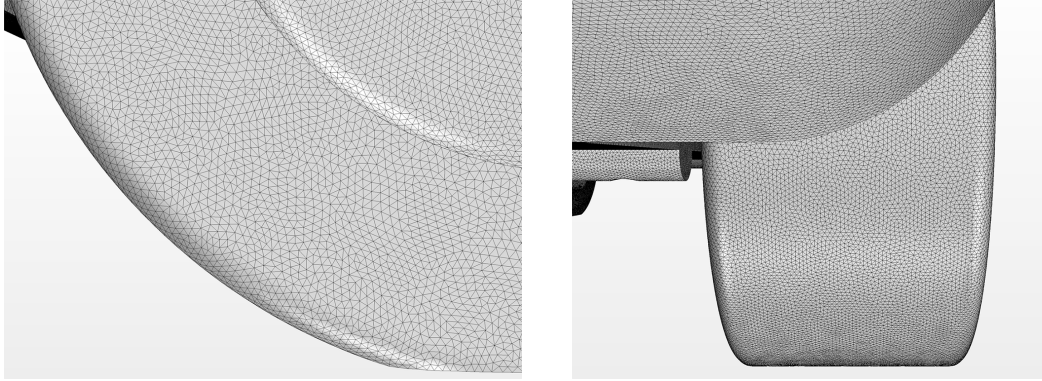
Figure 2.7: SUV surface grid.

In the simulations, the SUV boundary layers are resolved and not modelled using wall functions. Thus the thickness of the near wall layer for the SUV surfaces is set to ensure a non-dimensional near wall spacing $y^+ < 1$. Eleven additional layers of increasing thickness ensure even blending into the adjacent, $1\,\text{mm}$ isotropic, hexahedral, core grid elements, shown in Figure 2.8b. It is not practical to resolve the boundary layers along the tunnel walls due to the large surface area and significant amount of cells that would result, thus a near wall grid of $y^+ > 30$ is used and the velocity gradient at the walls is modelled using wall functions.

The hexahedral volume elements in the core grid are set using a dimension of $16\,\text{mm}$. Five refinement regions are added around the SUV where cells halve in size between

each refinement region from $16\,\text{mm}$ to $1\,\text{mm}$ ($0.015\mathbf{L}$ to $0.001\mathbf{L}$) elements. Downstream and within the first diffuser, elements are allowed to grow up to a size of $64\,\text{mm}$. The total number of volume elements for the complete domain is approximately 74×10^6.

(a) Vertical, axial cut through volume

(b) Prism layers on SUV surface

(c) Vertical, transverse cut through volume

(d) Refinement around SUV
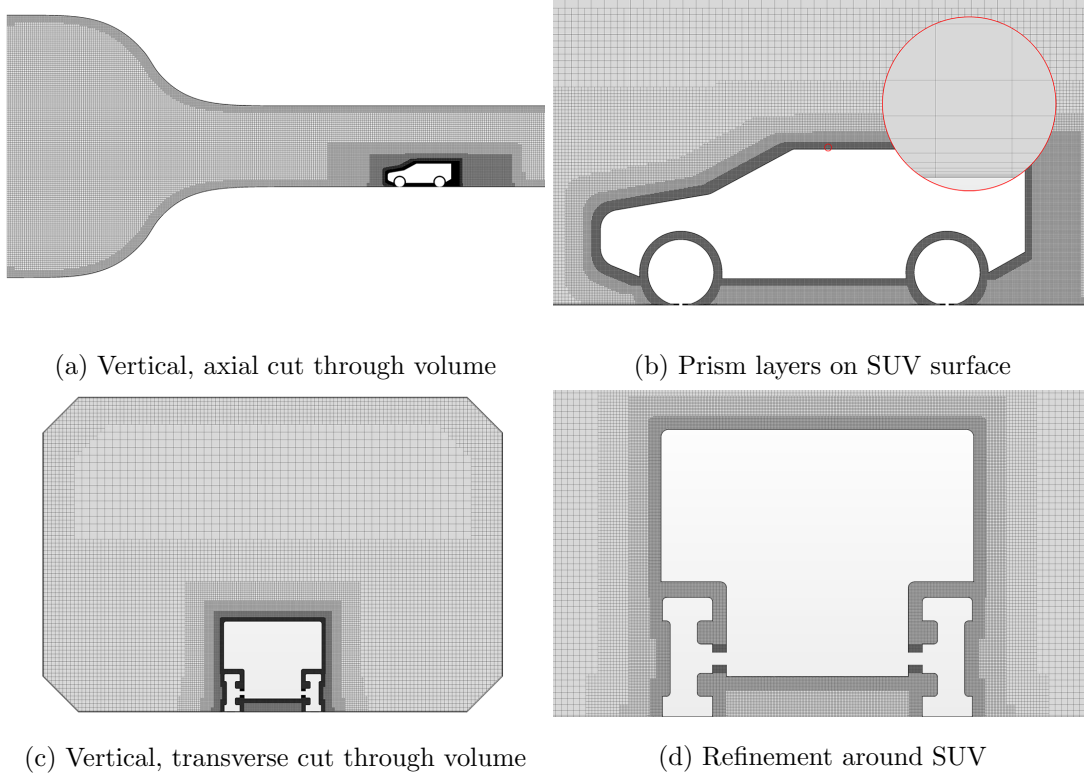
Figure 2.8: SUV volume grid.

2.5 Numerical Approach

Three methodologies are assessed for their suitability in predicting the experimental flow field. A single steady-state Reynolds-Averaged Navier-Stokes (RANS) method and two unsteady methods: unsteady RANS (URANS) and Detached-Eddy simulation (DES). For all methods, a segregated incompressible finite volume solver is used with a second order upwind scheme for convection and diffusion terms of the momentum and turbulence equations.

For the RANS method, turbulence is modelled using the $k-\omega$ SST model. This model was developed by Menter [80] with the aim of reducing a high sensitivity to values of

ω in the freestream (a behaviour of the standard $k - \omega$ model) by switching to a $k - \epsilon$ model outside of the boundary layer. As a result, this model performs wells in strong pressure gradients and large separated regions, both of which are features of the SUV flow.

The validity of this model in the flow prediction around automotive bodies has been shown by Ashton and Revell [81] and Ashton et al. [82]. In their studies, several RANS turbulence models have been compared for their accuracy in capturing the flow field around an Ahmed body [83]. This bluff bodied geometry features a large, smooth vertical base surface as well as a top roof slant which could vary in angle between 25° and 35°. Thus, inverted, this rear-end is geometrically similar to the Generic SUV and should exhibit comparable flow separation characteristics. From the wide selection of RANS turbulence models assessed in their study, the $k - \omega$ SST turbulence model provided the most accurate flow prediction of the flow velocity and turbulent kinetic energy over the top-slant and within the base wake. However the downstream length of the wake was still significantly over predicted. As the angle of the SUV diffuser is comparable, it will be interesting to see whether a RANS methodology will perform to a similar level.

For the URANS method, the $k - \omega$ SST turbulence model is maintained and time dependency is introduced with a second order temporal scheme and time-step $\Delta t = 2.5 \times 10^{-4}$ seconds (or non-dimensional $\Delta t U/L = 1 \times 10^{-2}$). This limits the CFL number to < 10 throughout the domain. In comparison, the DES simulation is performed using the Spalart-Allmaras IDDES formulation and to ensure a desired CFL < 1, the non-dimensional time-step is reduced by an order of magnitude, $\Delta t = 2.5 \times 10^{-5}$ seconds (or non-dimensional $\Delta t U/L = 1 \times 10^{-3}$). For both unsteady methods, the simulations are initialised using the converged RANS predictions to speed up the settling period. The initial transient is defined as the point at which the backward average of the drag and lift coefficients stabilises and settles. The flow fields are time averaged from this point for a period of 1 second or 40 convective flow units ($40 \times L/U$). All simulations are run using CD-Adpaco's Star-CCM+ v10.04.009 on 320 2.0GHz Intel E5-2650 processors of the HPC-Midlands facility,.

2.6 Boundary and Inlet Conditions

A velocity inlet and flow outlet are used at the entrance and exit of the domain respectively and no-slip boundary conditions are applied to the tunnel walls. A working section velocity of $40\,\mathrm{m/s}$ is desired to mirror the experimental tests. This velocity is measured by a pitot-static tube located at the end of contraction/start of working section, $0.2\,\mathrm{m}$ below the roof and $0.5\,\mathrm{m}$ right of centre. Thus, in order to set appropriate inlet values, a preliminary calibration study is required. A theoretical law derived by Batchelor [84] states that the $\mathbf{u}$ velocity component through a contraction increases with the inverse of the contraction ratio. Using this relationship, the flow should enter the contraction at a velocity of $5.46\,\mathrm{m/s}$, in order to achieve the desired working section speed. Due to the inclusion of settling chamber upstream of the contraction, it was found that the actual value defined at the inlet needed to be slightly lower, at a value of $5.39\,\mathrm{m/s}$. An inlet turbulence intensity value of 3% is required to achieve a value of 0.15% at the centre of the empty working section in accordance with the measurements of Johl [79, 78] and as no turbulence length scale measurements have been taken, an inlet value based on the aperture of the last flow conditioning screen $1.29\,\mathrm{mm}$, is used. The set of inlet conditions is given in Table 2.2.

Table 2.2: LUMS inlet conditions.

	Velocity ($\mathrm{m/s}$)	Turb. Intensity(%)	Turb. Length Scale (mm)
LUMS Domain	5.39	3	1.29

Using the above inlet conditions, a simulation of an empty working section was performed. For this simulation, the Generic SUV geometry was removed from the domain along with the five grid refinement regions but the non-dimensional near wall grid spacing $y^+ > 30$ on the tunnel walls was maintained. Figure 2.9a shows the predicted boundary layer profile on the floor at the centre of an empty working section. Also shown is the experimental profile measured by Johl [78] at the same location. The results suggest that the simulation provides a good replication of the boundary layer, most noticeably in the upper half of the profile. Below $30\,\mathrm{mm}$, a small velocity overshoot is present, which shows up greatest in the lowest levels of the boundary layer,

although this is emphasized due to the coarse resolution of the measured values (a factor of the physical apparatus size).
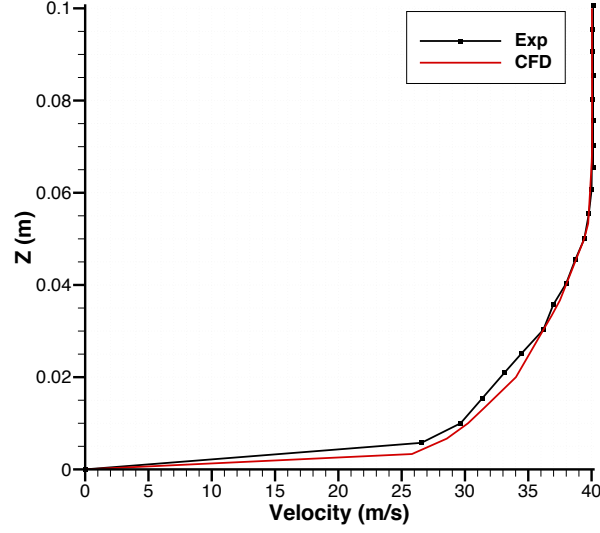
(a) Boundary layer comparison at the centre of the working section (station A)
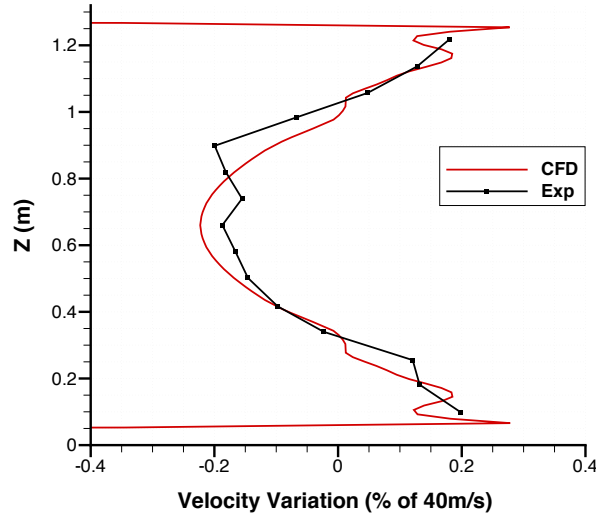
(b) Velocity variation at station A (variation expressed as a percentage of $40\,\mathrm{m/s}$)

Figure 2.9: Validation of the simulated flow in an empty working section by experiment values.

Above the boundary layer and in the freestream, the velocity variation with height at the centre of the working section is shown in Figure 2.9b, where all values are expressed as a percentage of the pitot velocity. Again, a good correlation with experiment values is clear, with the simulation capturing the velocity profile reasonably well. A slight difference in the values around the core of the working section exists, but this is due to the limited number of experimental measurements which make up the average velocity profile. Due to the duration of physically obtaining these measurements, the experiment profile represents an average of only three tests and thus, is heavily weighted by variations between each test.

Accurate simulation of the wind tunnel flow is crucial for future simulations which use the LUMS wind tunnel, and the results from this preliminary study give confidence in the simplified domain, generated grid and chosen boundary and initial conditions.

2.7   Results

Before any flow field comparisons are made between the methodologies, an important result from the steady state RANS simulation is discussed. The behaviours of the drag coefficient and momentum and turbulence residuals for the RANS simulation are shown in Figure 2.10. It can be seen that there is good convergence during the first 750 iterations, however after this point, the solution is unable to settle at a steady state.

The source of these numerical fluctuations can be found by analysing the standard deviations or root mean squares (RMS) of the pressure and **u** velocity variables on and around the SUV, Figure 2.11. Using this method provides a quantitative measure of the numerical fluctuations in these variables over the last 2000 iterations. It is clear that the inability to converge to a steady state solution is a result of large fluctuations in the underbody flow, particularly in the wakes of each wheel, Figure 2.11a. Furthermore, by analysing the RMS of pressure in Figure 2.11b, the fluctuations in the drag coefficient can be identified on the shoulders of each wheel, within their housings and on the diffuser surface. With such large fluctuations, the most sensible method is to average the flow field over the last 2000 iterations. This data is presented henceforth in Figures

2.12 and 2.13 for comparison with time-averaged URANS and DES predictions in the form of coloured contours of **u** velocity, normalised by the freestream velocity of 40 m/s and constrained to the PIV planes.
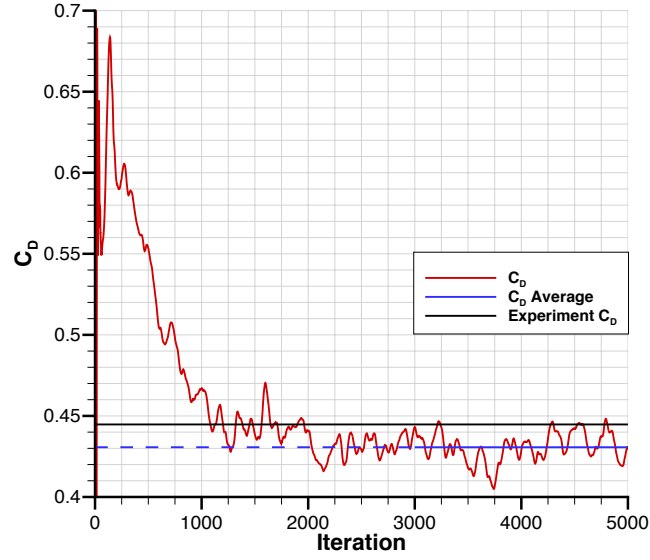
(a) Drag coefficient evolution (average taken over final 2000 iterations)
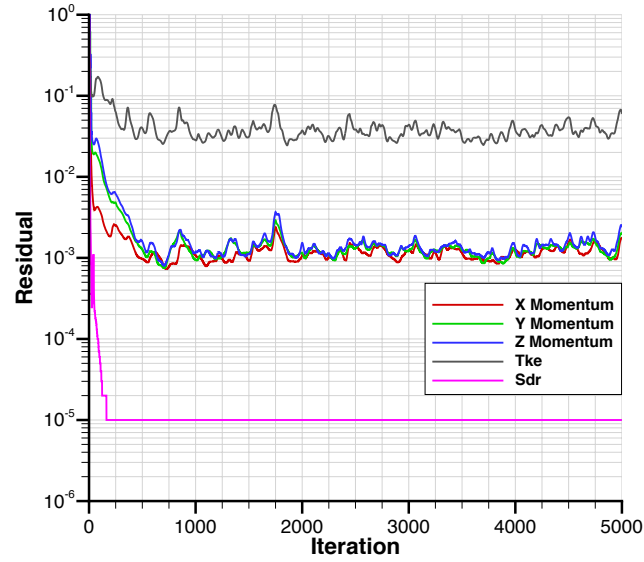
(b) Residuals

Figure 2.10: Behaviour of the RANS drag coefficient and residuals.
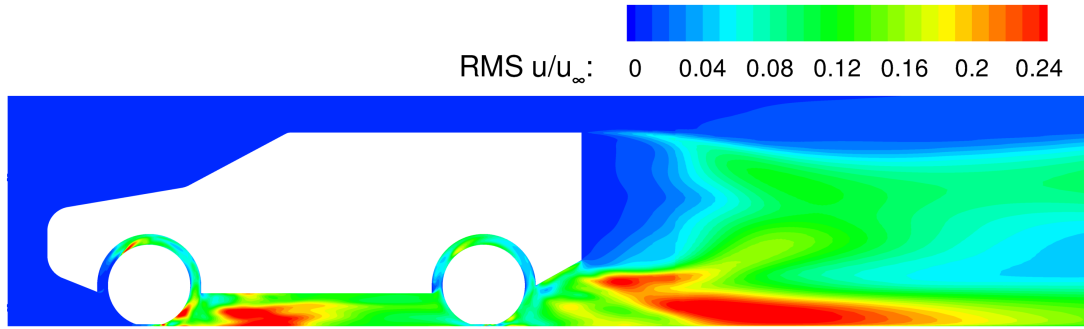
(a) RMS of normalised **u** velocity, PIV Plane Y=0.17
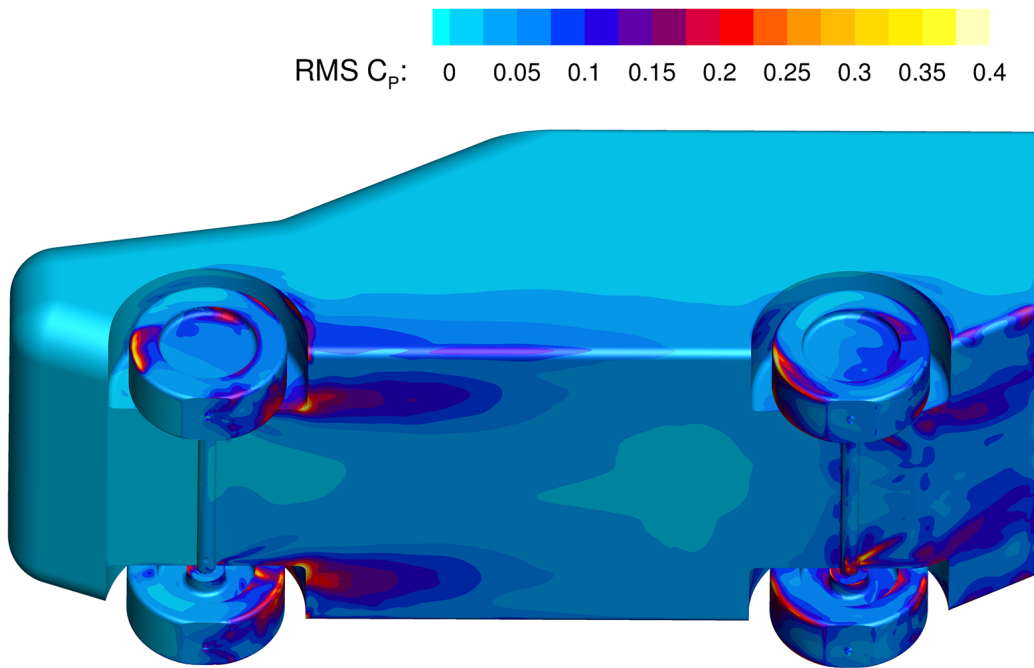
(b) RMS of pressure coefficient on SUV surface

Figure 2.11: Standard deviations of velocity and pressure on and around the SUV over the last 2000 iterations.
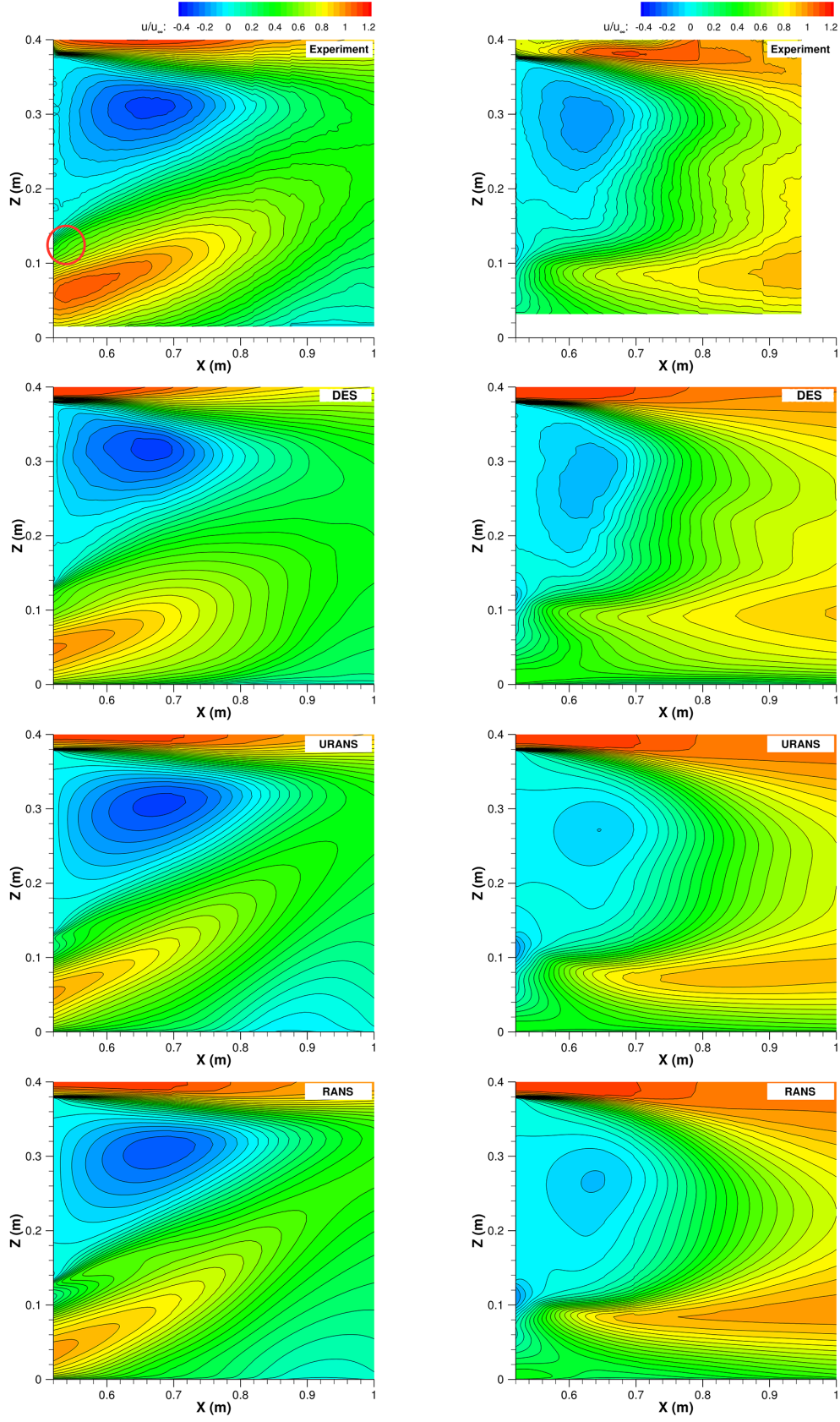
Figure 2.12: Experimental and computational normalised **u** velocity comparison on vertical PIV planes. Centreline: Y = 0 (Left) and behind wheels: Y = 0.17 (Right) [77].
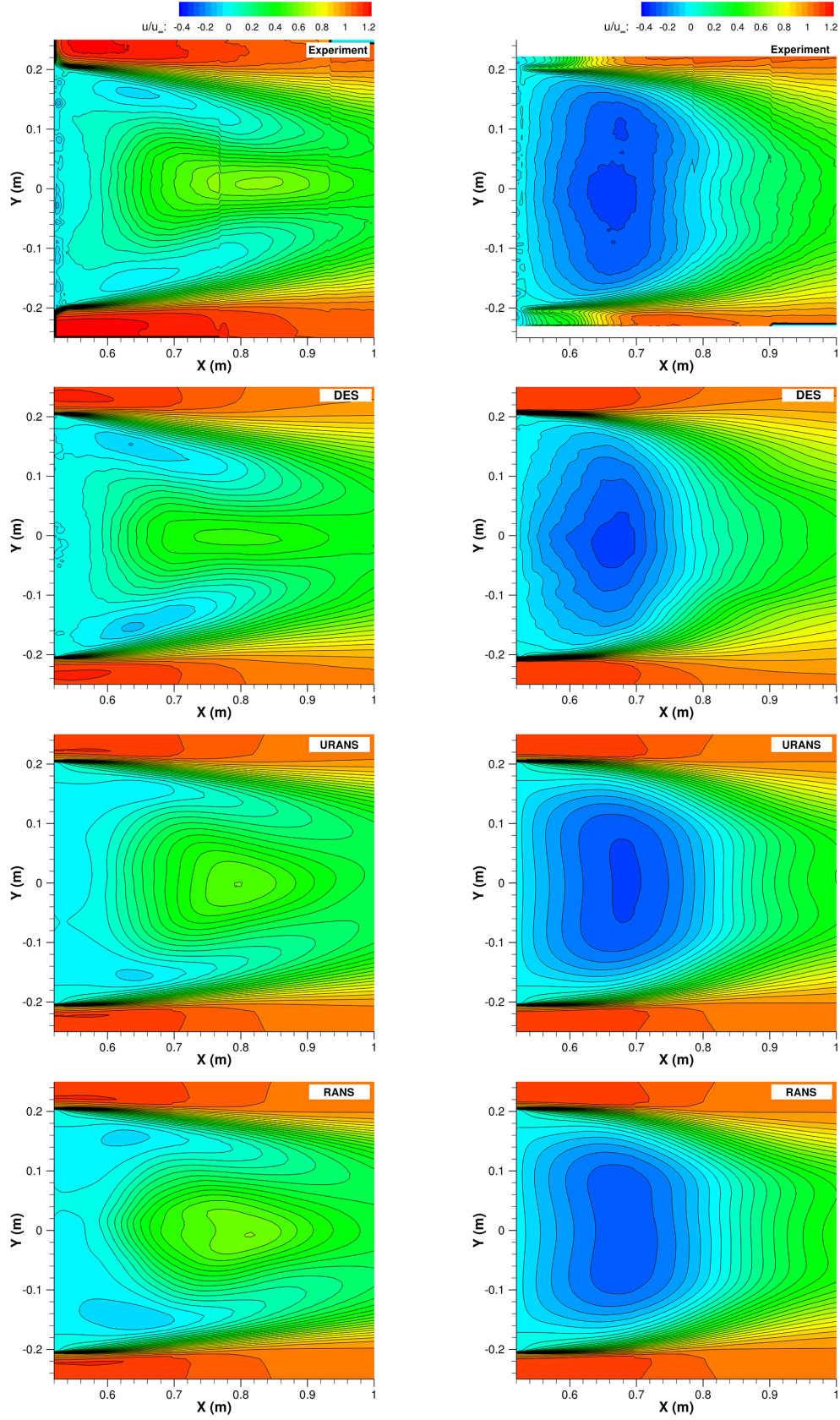
Figure 2.13: Experimental and computational normalised **u** velocity comparison on horizontal PIV planes. Lower: Z = 0.187 (Left) and upper: Z = 0.318 (Right) [77].

On first inspection, all methodologies appear to predict the wake structure reasonably well, with arguably, no obvious, large-scale differences in the flow. In order to extract some of the finer differences, Figure 2.14 shows a selection of overlaid contour levels from these planes.

(a) Y = 0

(b) Y = 0.17

(c) Z = 0.187

(d) Z = 0.318
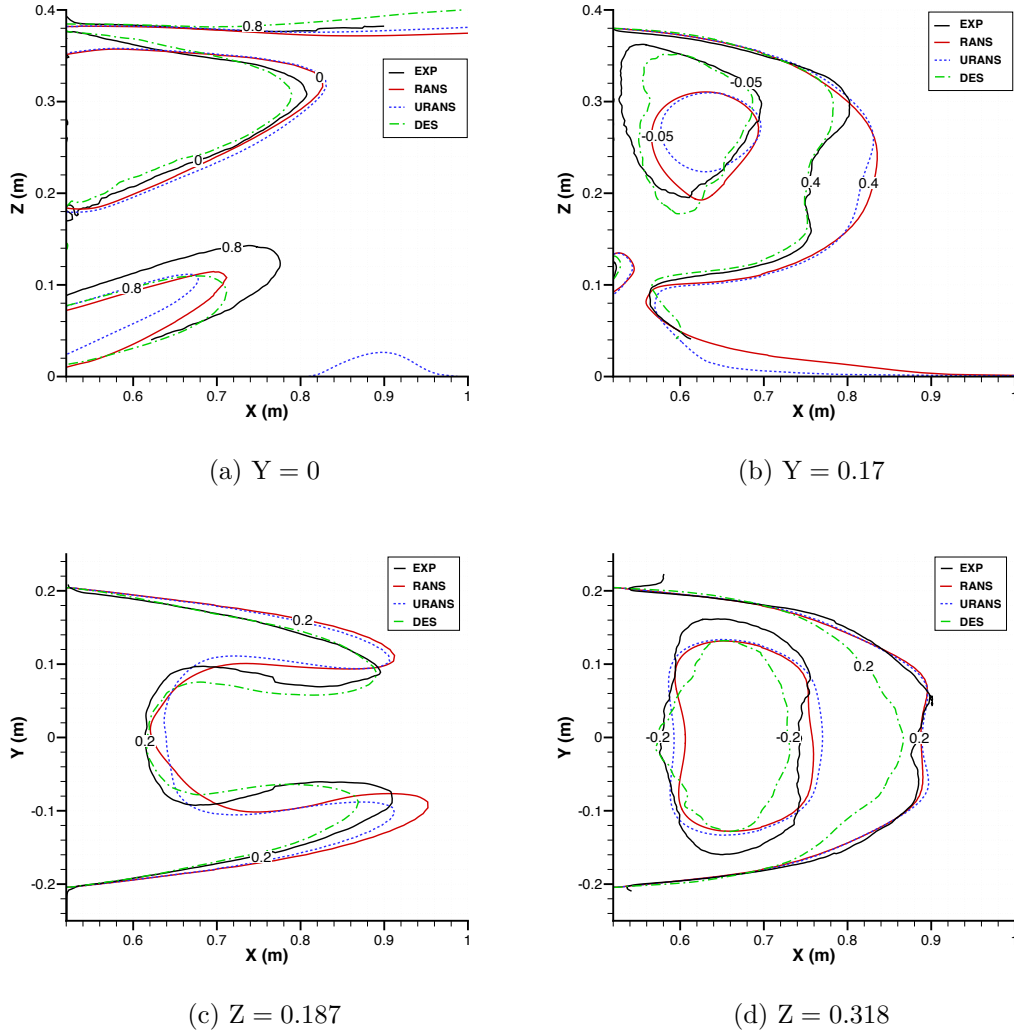
Figure 2.14: Overlaid normalised **u** velocity contour levels [77].

All methodologies provide a reasonable prediction of the large recirculating base wake structure in the centreline plane Y = 0. The overall length of this structure varies between the methodologies: URANS and RANS over predicting and DES under-predicting the length, but despite this, the contouring of velocity levels within this region are fairly consistent with the experiment. Towards the ground, the strength

of the high velocity flow which exits the underbody and is accelerated by the diffuser also varies slightly between the methodologies, and are on average, an under prediction of the experiment. There is a much larger variation in the path of this flow and in fact one may argue that the URANS and RANS methods provide a more accurate prediction of the direction present in the experiment. On closer inspection through the flow streamlines of Figure 2.15, it appears that this is coincidental as the RANS and URANS methodologies both predict a separation bubble over the diffuser surface which leads to a stronger upwash into the base wake. On the other hand, the DES prediction shows attached flow in this region and although no experimental measurements in this region have been taken, evidence of attached diffuser flow can be seen in the contouring of the experiment results highlighted in Figure 2.12.

As expected, these results are comparable to the Ahmed body simulations of Ashton et al. [81, 82], who showed that switching from a RANS to a DES methodology provided a more accurate velocity prediction in the wake. More specifically, DES was shown to increase the magnitude of turbulent kinetic energy (TKE) in the top-slant shear layer which led to more turbulent mixing and a shorter recirculation region. The Generic SUV is similar to the Ahmed body in the rear end geometry, with a vertical base surface and 30° diffuser comparable to the top-slant. Although no turbulent kinetic energy values were recorded in the SUV experiments, Figure 2.16 shows the differences in TKE between URANS and DES predictions over the diffuser surface. The DES methodology clearly predicts much higher levels of turbulent kinetic energy which is ultimately responsible for keeping the flow attached over this surface as already shown in Figure 2.15. These larger energy levels are transported into the base wake which promotes more turbulent mixing and a shorter base wake, which is consistent with Ashton et al. [81, 82]. However, in this particular case, the increase in turbulent kinetic energy is a result of differences in the flow prediction over the rear axle, a geometric feature not present in the Ahmed body simulations of Ashton et al. [81, 82]. It is unconfirmed whether without the rear axle, the angle of slant alone would effect the TKE prediction, due to rounding of the diffuser's bottom edge which is designed to promote flow attachment.
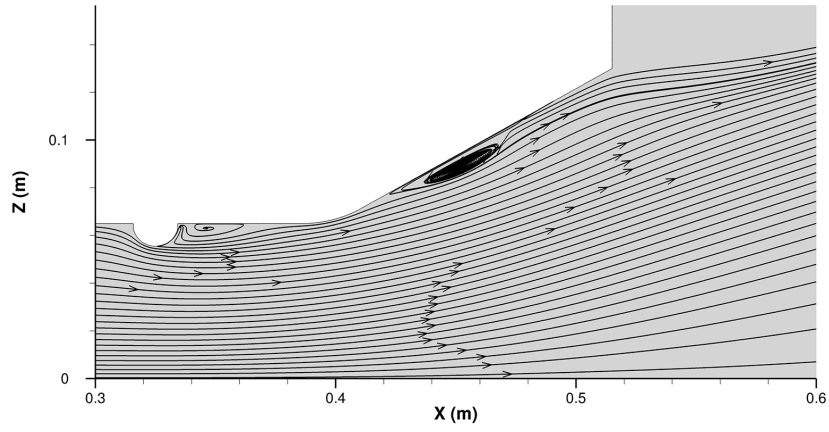
(a) URANS
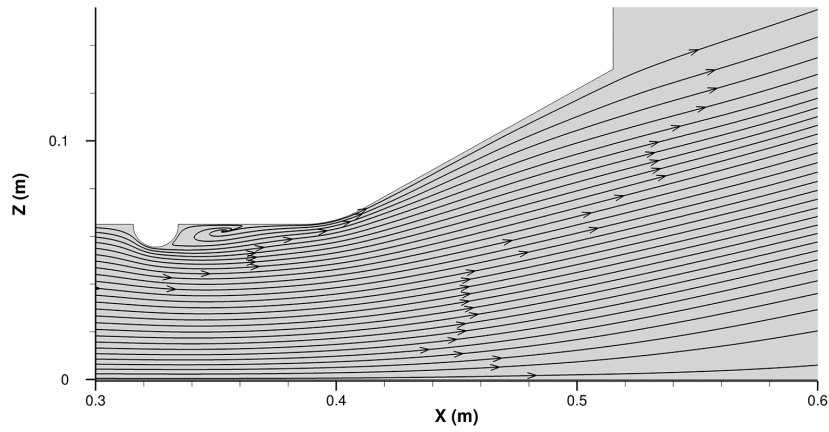
(b) DES

Figure 2.15: Streamlines over the rear diffuser in the centreline Y = 0 plane.
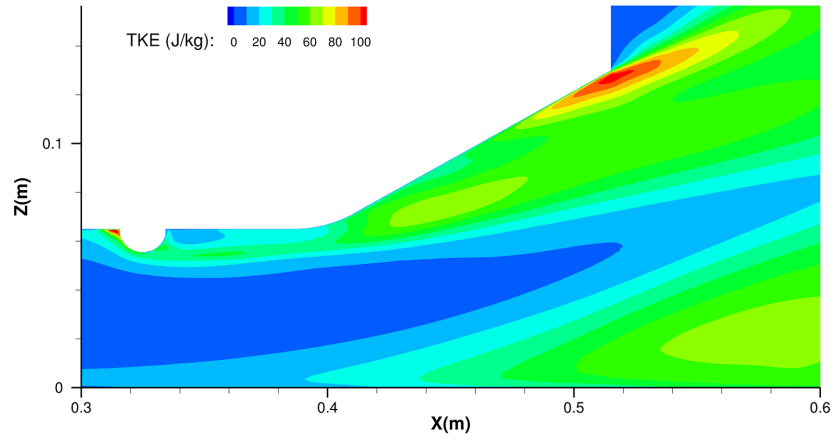
(a) URANS
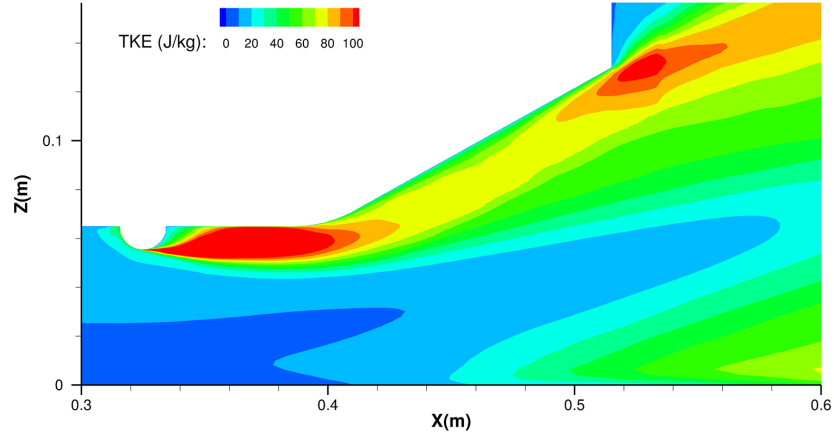
(b) DES

Figure 2.16: Turbulent kinetic energy over the rear diffuser in the centreline Y = 0 plane.

Moving outboard to the plane inline with the wheels Y = 0.17, the quality of the RANS and URANS predictions deteriorates in comparison to the DES. A more clearly defined over prediction in the downstream length of the base wake structure and a weakening of the strongest recirculation value are features of both the RANS and URANS predictions and strong indicators to a reduction in turbulent mixing and inability to correctly resolve the highly unsteady wakes of the rear wheels.

In the lower horizontal plane, the low velocity horseshoe structure is formed due to the entrainment of the wheel wakes into the base wake. Again, due to the highly unsteady nature of the flow in this region, the DES methodology outperforms the RANS based methods in predicting the shape and volume of this structure. A slight asymmetry in the results suggests that a longer averaging period (> 40 convective flow units) is required, however, this structure still displays a level of asymmetry in the experimental results which were averaged over a much longer period (5480 convective flow units). Thus, due to the length of simulated time required, increasing the averaging period in an attempt to obtain symmetric results is computationally impractical at present.

On the upper horizontal plane, wake asymmetry is even more clear in the DES prediction, suggesting a large-scale, low frequency bi-stability in the wake. The levels of recirculation are coherent with the experiment, however the overall shape of the wake varies towards the tail, with a more rounded shape predicted. Interestingly for the same averaging period, the URANS prediction does not display the same level of asymmetry and as a result, the shape of the wake in this plane is more consistent with the experiment.

In terms of wake structure alone, these comparisons show that a RANS or URANS methodology is unable to accurately capture the entire experimental wake structure, generating unwanted flow separation over the diffuser and over predictions in the length of the base wake. A DES methodology is the preferred choice. By keeping the flow over the diffuser attached and resolving the highly unsteady flow in the wake of the rear wheels, the velocity distribution in the base wake more accurately matches the experimental flow field.

As well as flow velocity within the wake, comparisons of base pressure are performed

in Figure 2.17, where the pressure coefficient values have been corrected for blockage using Equation 2.1. It is clear that the move from a RANS to a URANS methodology does not offer any improvements with both methods over predicting the pressure in the centre of the base. In comparison, the distribution obtained with DES matches the experiment much more closely, with pressure values evenly growing up the base surface. On the diffuser, limited pressure tappings restrict a thorough comparison to the experiment over the entire surface, however differences between the computational predictions can be assessed. Behind the wheels, pressure distributions are similar between all predictions, but towards the centreline, the RANS and URANS separation bubble is clearly identified by a region of low pressure.

The accuracy of the base pressure prediction has a strong influence on the body's drag coefficient. As shown in Table 2.3, the base drag contributes to approximately 46% of the total drag coefficient. It is important to mention that the experimental base C_D has been calculated using an area weighted integration from the coarsely distributed pressure tappings on one half of the base. Thus in order to make a true comparison, the simulation averages have been calculated in the same fashion, with base pressures extracted from the same locations rather than using the finer resolution of the surface grid. In contrast, the total C_D and C_L values were measured using the underfloor balance, thus the simulation values represent the sum of both the pressure and shear force components over all surface elements.

The high qualitative accuracy of the DES base pressure prediction is reflected in the base drag coefficient value, differing by only 6 counts (1 drag count = 0.001) to the experiment. For the URANS and RANS predictions, these errors are much larger, 27 and 23 counts respectively. In terms of total C_D error, these values are reduced to 4, 16 and 14 counts respectively, implying an over prediction in drag elsewhere on the SUV. However without experimental drag evolution data over the body, the source(s) cannot be identified.

The errors in lift coefficient are consistently large across the methodologies: -104, -107 and -99 counts for DES, URANS and RANS respectively, with all simulations predicting a negative lift in contrast to the experiment. The same is true for both front

(a) Experiment

(b) DES

(c) URANS

(d) RANS
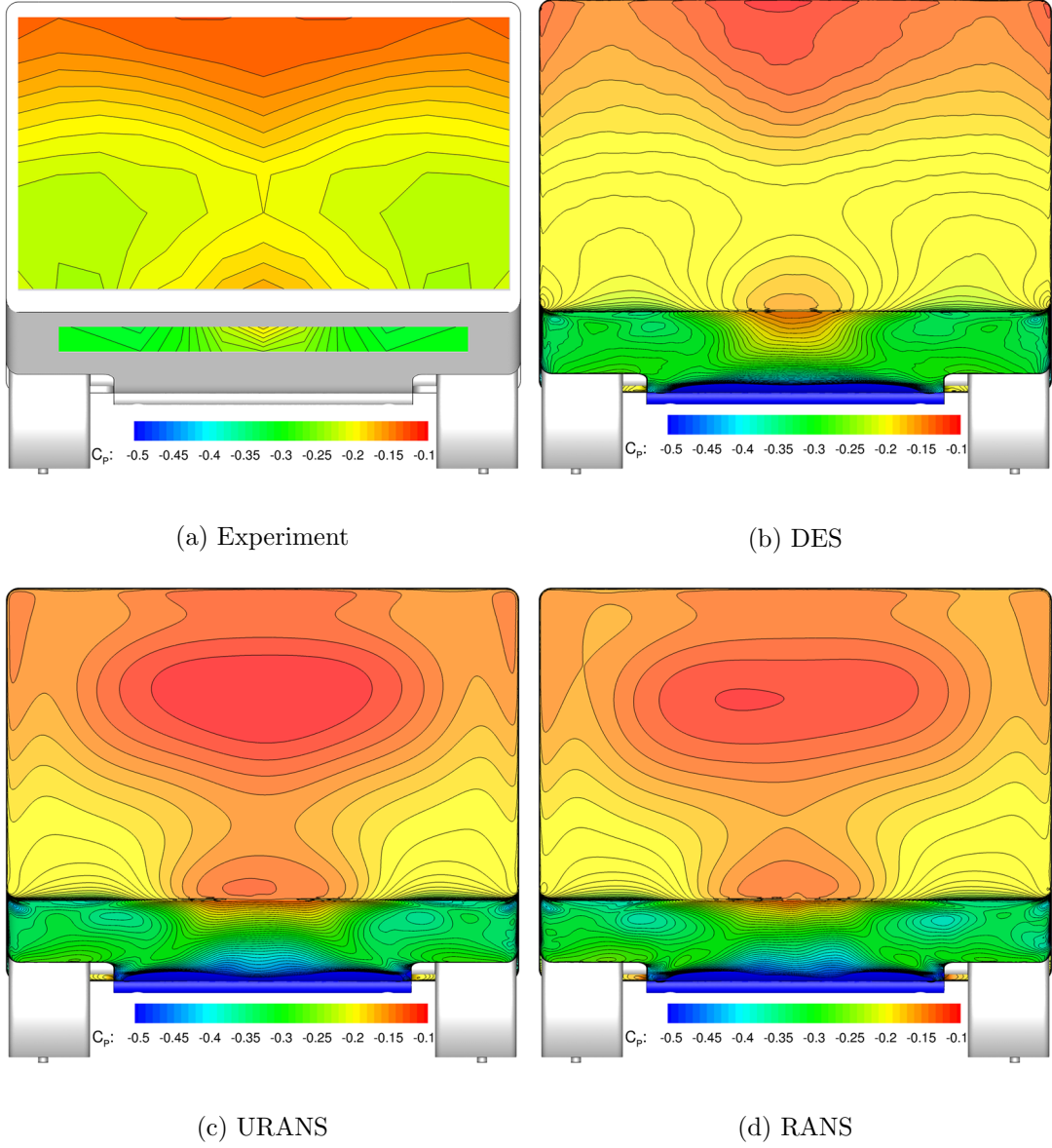
Figure 2.17: Base and diffuser pressure coefficient distribution [77].

and rear lift values, with simulations predicting a weaker lift or stronger downforce for all methodologies. This consistency suggests that there is something in the experiment setup that is not being correctly simulated. One explanation may involve the standoff between the wheel and floor of the tunnel and in particular the clearance around the pins on which the model rests. The pins have diameter of 8 mm, whereas the holes in the floor have a diameter of 12 mm, leaving a 2 mm clearance around the pin. With the tunnel running, the pressure difference inside and outside the working section will draw

flow through the gaps and into the working section. This will lead to an increase in pressure on the flat of each wheel and an overall increase in lift force. Again, without experimental pressure data on these surfaces this cannot be confirmed. It would be possible to investigate this effect computationally by creating additional inlets around the pins, however as this is an undesirable effect of the experimental facility and not representative of the on-road interaction between a wheel and the ground, no resources have been invested in exploring this.

Table 2.3: Averaged force coefficients.

	Exp	DES	URANS	RANS
Base C_D	0.203	0.197	0.176	0.180
C_D	0.445	0.441	0.429	0.431
C_L	0.041	-0.063	-0.066	-0.058
C_{L_F}	0.194	0.133	0.120	0.115
C_{L_R}	-0.153	-0.196	-0.186	-0.173

A comparison of the computational resources required for the three simulations used in this study is shown in Table 2.4. The high cost of running a DES simulation in comparison to RANS or even URANS is clear. In order to obtain a converged and equally averaged solution, the time taken to run a DES simulation in comparison to RANS and URANS is increased by a factor of approximately 35 and 9 times respectively. Therefore it is reasonable to suggest that if computational resources are limited, a URANS methodology can be used to provide an initial, economical flow field prediction. However as shown by the flow field comparisons, a DES methodology should always be used where possible to provide the most accurate representation of the experimental flow.

Table 2.4: Computational costs and run times.

	RANS	URANS	DES
Computational time step Δt (s)	-	2.5×10^{-4}	2.5×10^{-5}
Wall clock time per iteration or Δt (s)	3.00	12.03	10.49
Simulated time averaging window (s)	-	1	1
Number of iterations or Δt in averaging window	2,000	4,000	40,000
Wall clock time for averaging window (s)	6,008	48,095	419,600
Total number of iterations or Δt	5,000	5,000	50,000
Total wall clock time (s)	15,021	60,150	524,500
Speed up factor from DES	34.92	8.72	**1**

2.8   Summary

This study has shown that a RANS methodology is unsuitable for the simulation of wind tunnel flow around a Generic SUV geometry. Large numerical fluctuations due to the wheel wakes and their interactions with the body prevent a converged steady-state solution. As a result, an unphysical average over solver iterations was generated in an attempt to remove the fluctuations from the final solution. Despite this averaging, there were large differences to the experiment flow, with separation over the diffuser, reductions in turbulent mixing, and an overall longer base wake. A URANS methodology introduced a meaningful time dependency into the solver but offered no improvement in accuracy to the final time-averaged flow field. A DES methodology is the preferred choice as this approach was capable of matching the attached experiment diffuser flow and resolving the highly unsteady flow in the wake of the rear wheels.

The respective accuracies of the flow field predictions were reflected in the base pressure distributions and force coefficient values. The base drag coefficient differed by only 6 counts to the experiment compared to 16 and 14 counts for the two RANS based methods. All lift coefficient values were under predicted, regardless of the methodology. This suggested that the experiment setup was not correctly simulated and a theory concerning the clearance around the balance pins and standoff between the wheels and ground was proposed.

In terms of computational expense, the DES methodology added significant cost to the simulation. The RANS prediction was obtained in approximately $1/35^{\text{th}}$ of the time and URANS $1/9^{\text{th}}$. It was suggested that a URANS methodology could be used to provide an economical flow field prediction should computational resources be limited, however where possible, a DES methodology should always be used.

THE FLOW AROUND AN OSCILLATING DAVIS BODY

Contents

3.1 Introduction

In determining a suitable technique of including geometry motion within a computational fluid domain, simulation of an oscillating Davis model is performed. In particular, the simulation will recreate the experimental tests performed by Baden-Fuller [85]. The advantages of this particular test case are the simplicity of the model and an existing strong understanding of the specific flow topology [86, 87]. As a result, any differences that may exist in the choice of motion technique should be clearly identifiable and not, as may be the case with a more detailed and realistic geometry, lost in the complexity of the flow.

3.2 A Review of Motion Techniques

Including motion of geometry within an automotive CFD simulation is becoming a more common occurrence, driven primarily by concerns regarding correct wheel simulation. The difference in flow physics between static and rotating wheels and the contribution to overall vehicle drag has been shown comprehensively over the years [88, 89, 90, 91]. As a result, this has been recognised by the 'United Nations Economic Commission for Europe' (UNECE) in their 'Worldwide Harmonised Light Vehicles Test Procedure' (WLTP), which states that for determination of vehicle road load for use in emissions calculations, the aerodynamic drag obtained using wind tunnel facilities shall incorporate rotating wheels and a moving ground. For this reason, the inclusion of wheel rotation in experiment will become standard practice for automotive OEMs, and the importance of being able to move geometry within computational simulation will be magnified.

The most straightforward method of including wheel rotation in CFD simulation is via traditional boundary conditions, where rotating surfaces are described by imposing a rotational velocity as a wall boundary condition. For a surface of revolution such as a solid, cylindrical wheel this boundary condition is exact as shown in Figure 3.1, but for realistic wheel designs, it does not accurately reproduce the effect of rotation. In particular, the transient changes in pressure distribution and mass flow through the wheel caused by the rotation of the wheel are neglected [92]. Thus the rotating wall boundary condition cannot be used with confidence to investigate key aspects of wheel design [93]. In spite of this, studies that do use the rotating wall boundary condition show reasonable validation results for overall vehicle force values and because of this, the method is commonly used despite the inaccuracies in flow physics, [94, 95, 96, 97].

An alternative and more commonly used method is the Moving Reference Frame (MRF) approach [91, 98, 99, 100, 101]. This approach requires the definition of an 'MRF region' around the rotating component, in which an artificial momentum is added to the flow without physically moving the solid or mesh elements . At the interface, flow properties are directly translated from the rotating to the stationary regions however,
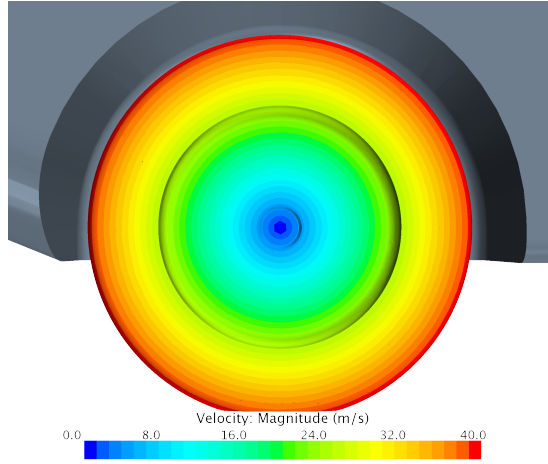
Figure 3.1: An example of the rotating wall boundary condition on a simplified wheel.

as flow within the MRF region is quasi-steady, any transient effects of the rotation are not translated across the interface. The size of the MRF region for which momentum is applied should ideally only include those fluid elements which are swept through by the rotating geometry. If the region is too large, an excessive amount of angular momentum will be added to the flow, creating unphysical results in the flow field [100]. For this reason, a popular method of employment is to model the rotation of the wheel hub using the MRF approach and to use a rotating wall boundary condition on the tyre surface. An example of this technique is shown in Figure 3.2a and has been performed by Waschle [91] and Landstrom et al. [98, 102] amongst others.

The MRF approach is generally considered to provide a good approximation of wheel rotation however, one should bear in mind that as the wheel is not physically rotating in the MRF, the positioning of the spokes can have a critical impact of the resulting flow field [103]. A way of resolving this issue is the addition of mixing planes at the interfaces to average the properties of the flow circumferentially, however this adds to the cost of the simulation and still does not account for any transient wake effects resulting from the rotation.

In order to include these transient effects, a sliding mesh approach can be employed within an unsteady simulation. When using this approach, a sliding mesh region is defined in a similar fashion to the MRF region as shown in Figure 3.2b, however unlike

(a) A moving reference frame (MRF) volume (b) A sliding mesh region defined around the defined around the wheel hub [98]   wheel hub [92]
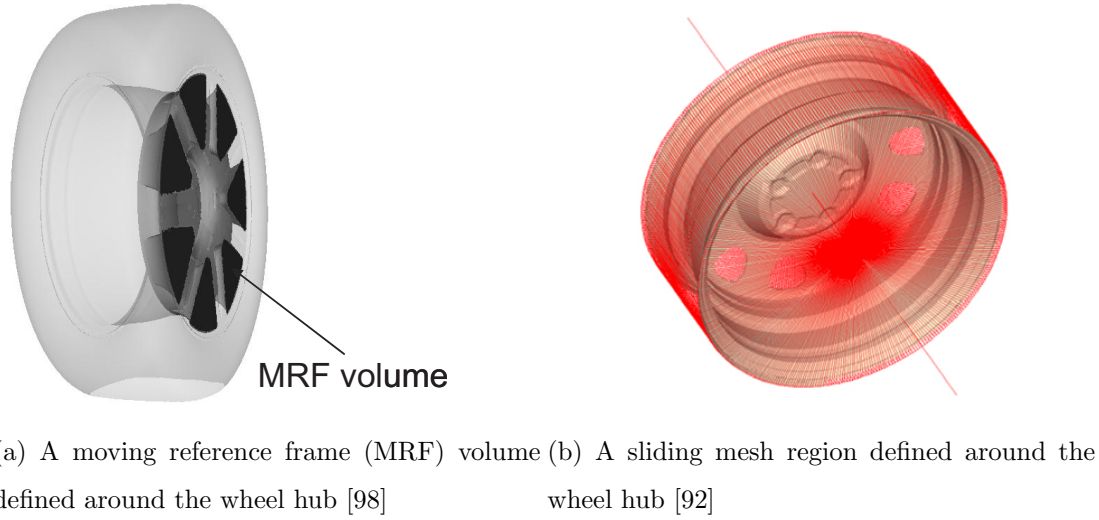
Figure 3.2: Methods of simulating wheel hub rotation.

the MRF, all geometry and mesh elements within the region physically rotate. Thus, for every time-step, the location of the wheel's spokes are changing and flow is allowed to move through the sliding mesh while subject to the highly transient effects of the rotating geometry. An advantage of this approach is the versatility in its application, as rotation of non-axisymmetric geometry can be simulated. Conversely the approach comes with the added cost of running an unsteady simulation.

A number of comparison studies have shown an improvement in flow field accuracy when using the sliding mesh approach rather than the MRF and rotating wall methods, [92, 97, 103, 104]. Kandasamy et al. [97] showed a greater accuracy in predicting aerodynamic force coefficients for a collection of vehicle rear end variants ranging from estateback to fastback and a selection of these results are shown in Figure 3.3. Across the majority of designs, errors in the drag coefficient appear higher for both rotating wall and MRF with a maximum error of 5% in both cases, compared to a value of 2% for the sliding mesh. The errors in lift coefficient are even more conclusive with consistently smaller deltas using the sliding mesh approach across all rear end designs.

The application of these approaches in automotive aerodynamics simulations is not restricted to wheel rotation; other dynamic motions of road vehicles can be simulated using these methods. One example where the sliding mesh approach is directly applicable is for simulation of vehicle yawing motions. This has been shown by Tsubokura et

al. [105], Theissen [23] and Wojciak [22] in reproduction of dynamic yawing motion of a vehicle on a wind tunnel turntable. With a sliding mesh region enclosing the complete vehicle geometry as shown in Figure 3.4, rotation about the yaw axis can easily be achieved.
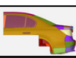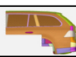
Rear Ends A, B, C, D and variants		Experimental Results (AWK)		PowerFLOW (Sliding Mesh)		PowerFLOW (Rotating Wall)		PowerFLOW (MRF)	
		Front Ends FE-1 Base	(*-*) - (*-1) Rear End Deltas	Front Ends FE-1 Base	(FE-1) - (Exp) Absolute Error	Front Ends FE-1 Base	(FE-1) - (Exp) Absolute Error	Front Ends FE-1 Base	(FE-1) - (Exp) Absolute Error
A-1 Base	CD*	1.000	0.000	0.996	-0.004	1.000	0.000	1.011	0.011
	CLF*	0.004	0.000	0.000	-0.004	-0.023	-0.027	-0.011	-0.015
	CLR*	0.013	0.000	0.011	-0.002	-0.005	-0.018	0.001	-0.012
B-1 Base	CD*	1.151	0.000	1.129	-0.022	1.118	-0.033		
	CLF*	-0.052	0.000	-0.048	0.004	-0.071	-0.019		
	CLR*	-0.046	0.000	-0.048	-0.002	-0.049	-0.003		
C-1 Base	CD*	1.008	0.000	1.004	-0.004	1.008	0.000	1.027	0.019
	CLF*	-0.026	0.000	-0.025	0.001	-0.047	-0.021	-0.032	-0.006
	CLR*	0.044	0.000	0.051	0.007	0.034	-0.010	0.043	-0.001
C-2 Trunk raised 30 mm	CD*	1.019	0.011	1.008	-0.011	1.011	-0.008		
	CLF*	-0.027	-0.001	-0.025	0.002	-0.045	-0.018		
	CLR*	0.012	-0.032	0.021	0.009	0.010	-0.002		
C-3 Trunk edge rounded	CD*	1.095	0.087	1.091	-0.004	1.129	0.034	1.144	0.049
	CLF*	-0.027	-0.001	-0.022	0.005	-0.045	-0.018	-0.031	-0.004
	CLR*	0.159	0.115	0.145	-0.014	0.134	-0.025	0.146	-0.013
C-4 Roof edge extended 100 mm	CD*	1.038	0.030	1.034	-0.004	1.057	0.019		
	CLF*	-0.031	-0.005	-0.030	0.001	-0.049	-0.018		
	CLR*	0.073	0.029	0.070	-0.003	0.061	-0.012		
D-1 Base	CD*	1.042	0.000	1.038	-0.004	1.091	0.049	1.084	0.042
	CLF*	-0.004	0.000	0.002	0.006	-0.020	-0.016	-0.011	-0.007
	CLR*	0.122	0.000	0.126	0.004	0.108	-0.014	0.111	-0.011

Figure 3.3: Effect of motion technique for rotating wheel simulation [97].
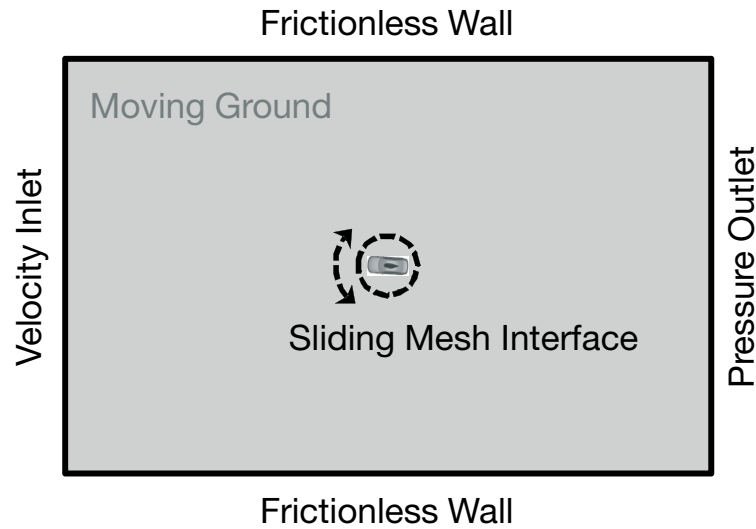
Figure 3.4: Sliding mesh boundary conditions of Wojciak [22]

Motion relative to other objects, such as overtaking manoeuvres can also be performed using the sliding mesh approach [106, 107, 108]. However, in order to fix the domain dimensions whilst keeping the desired level of grid refinement around the moving vehicle, grid deformation is commonly used in addition to the sliding mesh. Figure 3.5 shows how when using this approach, the domain is initially split longitudinally into two sections: a static region on one side of the domain containing the overtaken vehicle, and a sliding mesh region on the other side containing the overtaking vehicle. The sliding mesh is then split into three sections. A region of constant size fixes the grid refinement around the vehicle, which is bookended by two regions in which the grid elements are allowed to deform, stretching and shrinking accordingly to account for the motion of the vehicle along the domain. This type of motion would not be possible with the sliding mesh technique alone, as the inlet and outlet boundaries on either side of the sliding interface would no longer coincide.
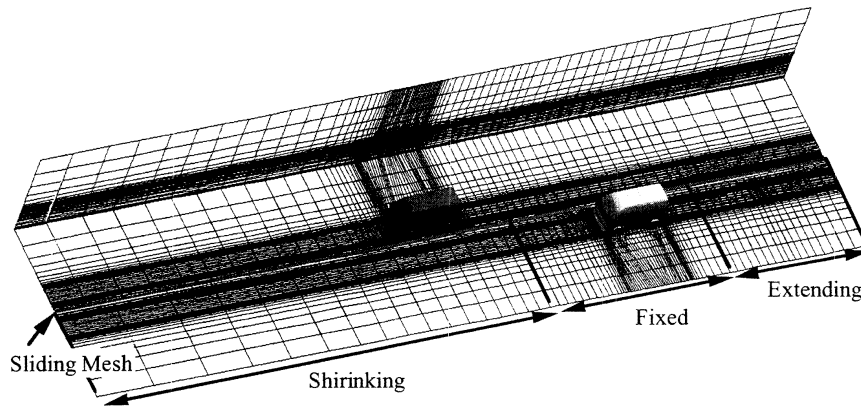
Figure 3.5: Dynamic grid technique to simulation overtaking [106].

All the motions discussed so far have only one degree of freedom: rotation about a single axis or translation along a fixed path. For more complex motions, the use of the techniques discussed so far is limited. One example is a superposed steering action on top of wheel rotation. For the simulation of wheel rotation, it has been shown that a cylindrical MRF or sliding mesh region can be defined around the wheel hub as this shape is symmetrical about the rotation axis. With the addition of steering motion, this shape is no longer appropriate as a symmetrical region about both the rotation and steering axes is required (a sphere). In addition this region can no longer only surround the central hub and has to expand to also enclose the tyre surface as both the hub and

tyre undergo the steering motion. However, due to the contact with the ground and the close proximity of the chassis, a shape with these symmetrical properties is not possible and thus the use of the MRF and sliding mesh approaches is limited.

A second motion with more that one degree of freedom is body movement on a suspension system, with potential motions including pitch, roll and heave. Again the limitations of the MRF and sliding mesh approaches are exposed due to the close proximity of the wheels and ground. In other industries such as aerospace and marine, this is not an issue as the bodies are surrounded by fluid and are located far from external wall surfaces. Dean et al. [109] and Morton et al. [110] demonstrated this in the simulation of high speed aircraft manoeuvres containing up to six degrees of freedom.

In order to simulate these complex motions, alternative techniques are required. One example is grid deformation which is usually coupled with the arbitrary Lagrangian-Eulerian (ALE) method to handle the motion of the grid vertices. Grid deformation has already been touched upon in this review for the simulation of overtaking, and was shown to help remove many of the limitations of the MRF and sliding mesh approaches. In this approach, volumetric grid elements are able to deform to allow motion of solid geometry, thus no additional regions need to be defined and the close proximity of wall boundaries are not an issue. Cheng et al. [111] and Tsubokura et al. [105, 112] showed how this technique was capable of simulating flow around a vehicle subjected to a dynamic pitching oscillation. More recently Kawamura and Ogawa [113] combined pitch and heave, motion in two degrees of freedom, to investigate the effect of unsteady aerodynamic lift force on vehicle dynamics and Kawakami et al. [114] combined lateral and yaw motions to investigate the effect on aerodynamic side force and rolling moment.

These studies clearly demonstrate the suitability of the grid deformation technique for simulation of chassis motions in multiple degrees of freedom, however care has to taken when employing this method for large scale motions. Excessive grid distortion, highly skewed elements and negative volume cells are all potential consequences of the method and can deteriorate the quality of the flow prediction. For this reason, the grid deformation technique is only suitable for small scale motions unless coupled with additional methods such as the sliding mesh as shown in simulation of overtaking.

3.3 Overset Grid Method

The overset grid method was developed by Steger et al. [73] in collaboration with the NASA Ames Research Center as a means of generating a high quality, structured grid around complex geometries. By dividing the geometry into several parts, a collection of individual grids can be patched together, or overlaid to form one single computational domain with data exchanged between the grids via inter-grid communication methods. Fittingly, the method is also known as the Chimera approach, named after the legendary Greek creature that was compounded of incompatible parts.

Over the years, research into the method has been funded due to prominent mission-critical projects of the NASA Johnson Space Center's Space Shuttle Program and a useful review of the internal technology development has been performed by Chan [115]. The earliest application of the structured overset grid method to a real engineering problem [115], is taken from Buning et al. [116] who adopted the method to perform ascent analysis of the integrated space shuttle vehicle, in the wake of the 1986 Challenger accident. As shown in Figure 3.6, individual, high quality grids were generated around the external tank (ET), solid rocket booster (SRB) and orbiter (ORB) components. For each grid intersection, a background and overset region was identified and a hole was cut in the background mesh to accommodate the overset grid. The specific details of this hole cutting procedure are described in detail shortly and Figure 3.7 shows the result of the hole cutting procedure on each grid.
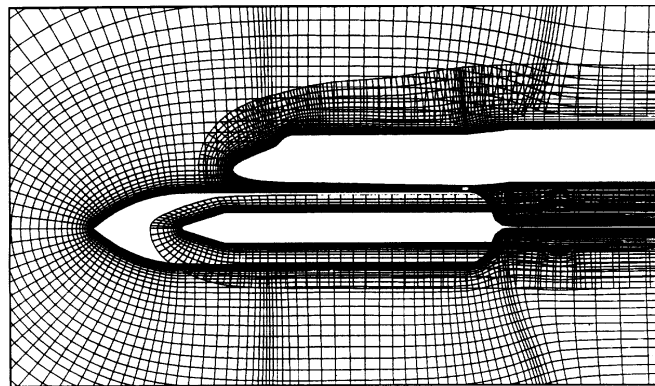
Figure 3.6: Overset grids around an integrated space shuttle vehicle [117].

It was realised that the overset grid method could also be applied to relative body-motion simulations, with individual geometry parts moving through the domain. Thus the hole cutting procedure would take place at every simulation time-step. This realisation initiated studies into separation characteristics of the solid rocket boosters from the external tank [118] and debris analysis after the Shuttle Columbia accident in 2003 [119]. The success of these simulations has led to higher fidelity simulations with significantly finer grids and the overall development of six-degree of freedom (6DOF) multi-body motion capabilities [115].

(a) ET Grid

(b) ORB Grid

(c) SRB Grid
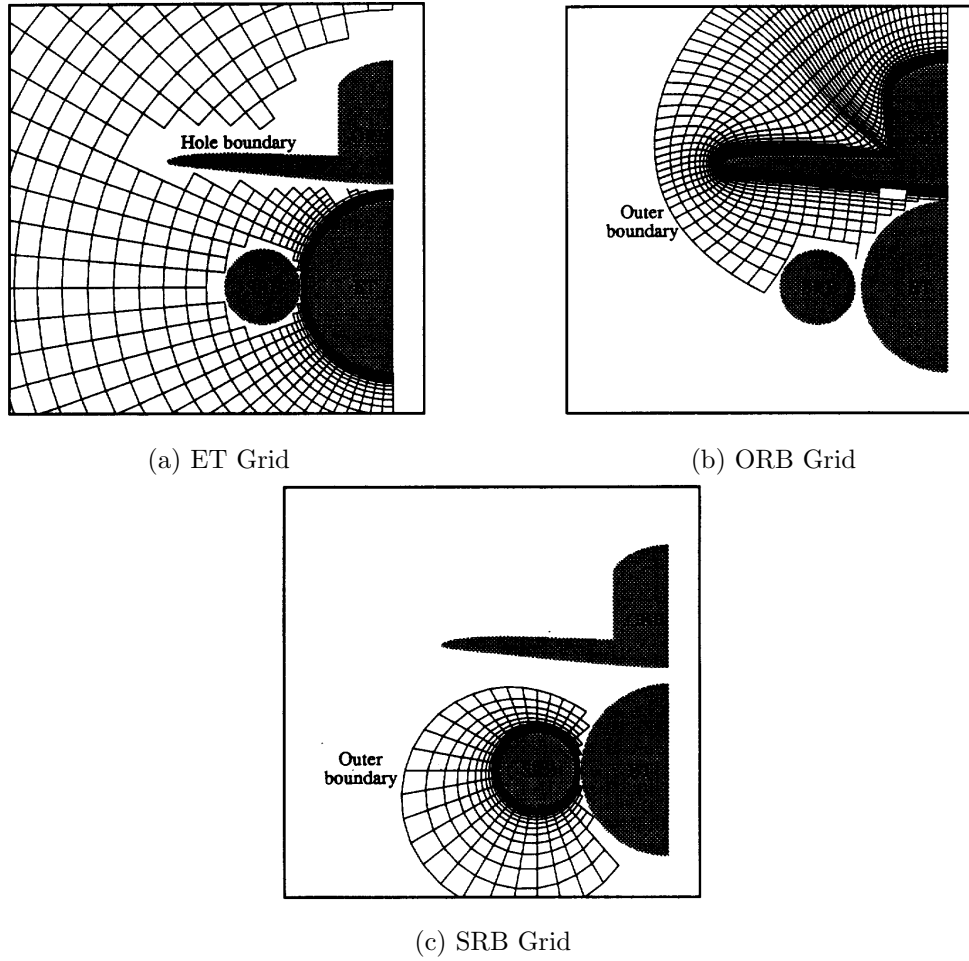
Figure 3.7: Holes cut in the grids around the space shuttle [117].

In order to describe the steps in implementing the overset grid method, a simple, two-dimensional example has been created in which a structured overset grid around a square body sits within a larger background grid. These two grids are shown separately and overlaid in Figure 3.8. With an overset mesh boundary condition applied to the outer boundary of the overset region, the hole cutting procedure takes place. There are variations across codes in the algorithms employed in this step, but generally speaking, all algorithms determine, for each cell in the background region, wether the cell centroid lies underneath the overset region. If this is the case, the cell is classed as inactive and temporarily removed from the background mesh, thus creating a hole, as shown in Figure 3.9. However to ensure successful inter-grid communication, there is a slight overlap in the background and overset active cells so that no unwanted holes are left in the assembled grid. The inactive cells are not permanently deleted from the background region because should the overset grid move, inactive cells may need to become active at a later time.

(a) Background Grid   (b) Overset Grid

(c) Background and Overset Grids Overlaid
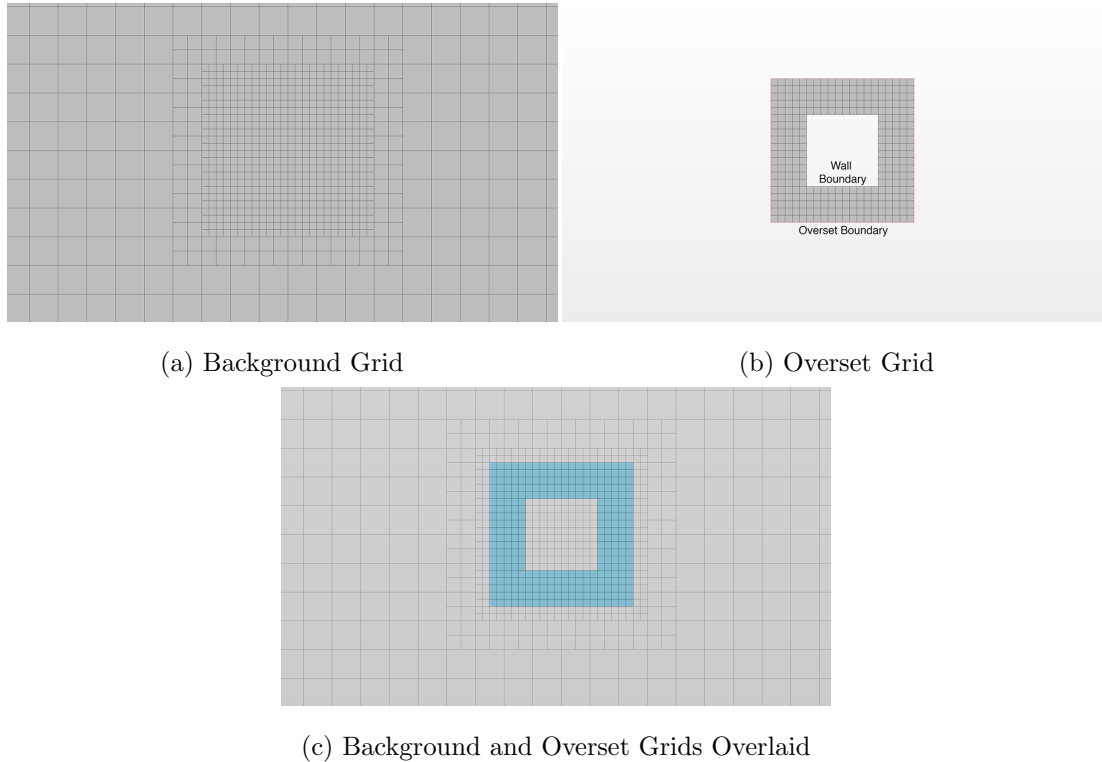
Figure 3.8: A 2D example of background and overset grids.

(a) Hole cut in Background Grid

(b) Initialised Grid

(c) Background Grid
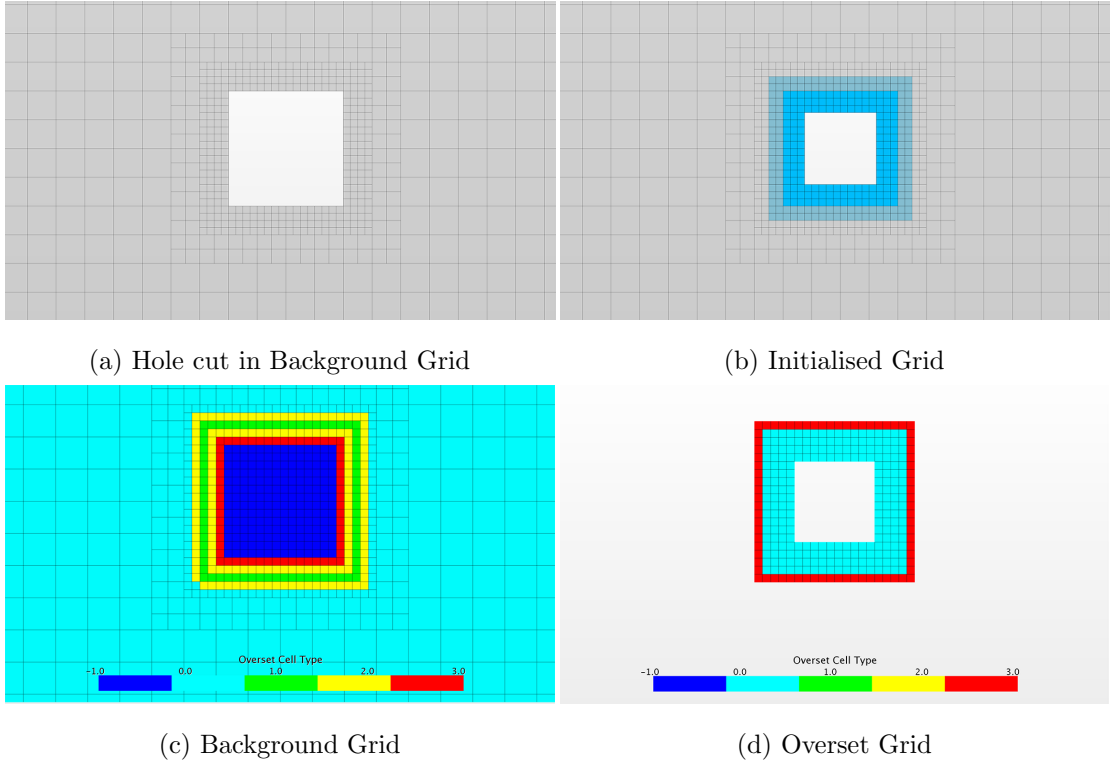
(d) Overset Grid

Figure 3.9: A 2D example of hole cutting and initialised overset grid.

With a hole cut in the background region, the next step of the overset grid procedure is acceptor and donor cell search. Acceptor cells (also referred to as ghost cells) are defined as the first layer of inactive cells adjacent to active cells. Thus, these cells form a seal around the inactive region of the background grid and active cells of the overset grid, as shown coloured in red in Figure 3.9. Donor cells, shown in green, are active cells of the background grid which are overlaid by the overset's acceptor cells. Between these two cell types, data transfer takes place. The accuracy of the transfer is determined by the order of the interpolation scheme used and also the difference in grid element size between the two regions at this point. For this reason it is recommended that the background region has additional refinement at the point of intersection with the overset region. This can have an impact on computational cost especially for moving geometry, as the background grid refinement will have to be put in place pre-emptively over the anticipated path of the overset region.

In the automotive industry, examples of the overset grid method are few and far between. This is surprising as there are several potential applications where this technique

could be useful. For example, design optimisation studies which require evaluation of component geometry variations such as the profile or inclination of vehicle's rear spoiler. With an overset grid around the spoiler, variations to this geometry can be performed without the time consuming and expensive task of re-meshing the complete domain for every design. However, an application of this type could not be found in literature.

Peters et al. [120] applied the structured grid technique to assemble a high quality grid consisting of 176 individual grids, around the complex shape of the DrivAer fastback model, shown in Figure 3.10. Surface pressure values obtained using the assembled grid, agreed reasonably well with results obtained using traditional gridding techniques. However, a significant drawback and a possible reason for the scarce application of the method in the automotive industry is the substantial labor time and expertise required to generate the overset grids, approximately 90 man hours in their study.

(a) Overlapping surface grids

(b) Intersection of volume grids between Hood and Windshield
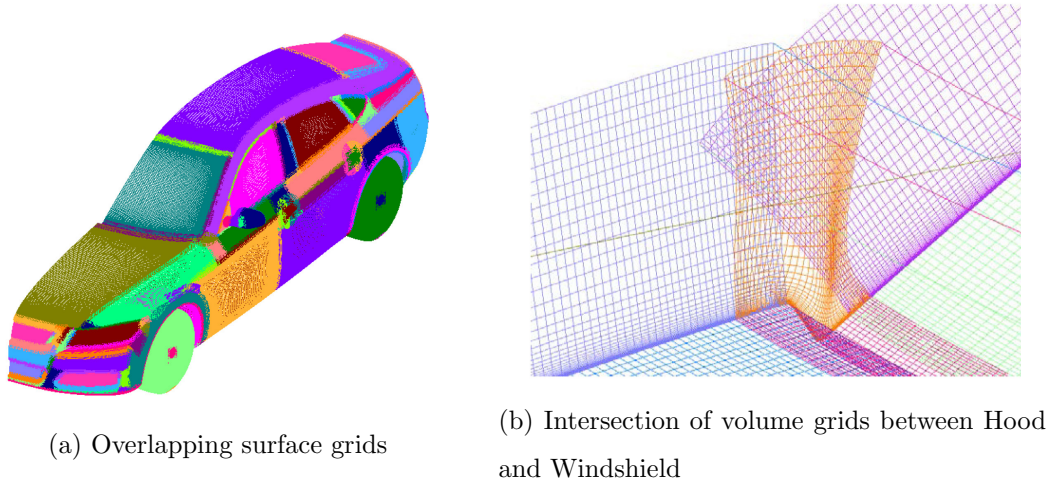
Figure 3.10: Structured overset grids used by Peters et al. [120].

For road vehicle body motion simulations, Tsubokura et al. [67] and Carbonne et al. [121] applied the method to investigate the effect of unsteady aerodynamic forces due to a crosswind on a vehicle's path. Although useful, this simple, two-dimensional test case does not take full advantage of the method's 6DOF capabilities. Similarly, Winkler et al. [122] used the overset grid method to study the effect of crosswinds on a road vehicle, shown in Figure 3.11. The simplified bus geometry used in their study represents a more realistic on-road problem as the large side area results in a vehicle more susceptible to this type of event. However, in a similar fashion to Tsubokura et

al. [67], motion was restricted to the dominant motions, yaw angle rotation and side translation, thus only two degrees of freedom. Again, the full 6DOF capabilities of the method were not exploited.
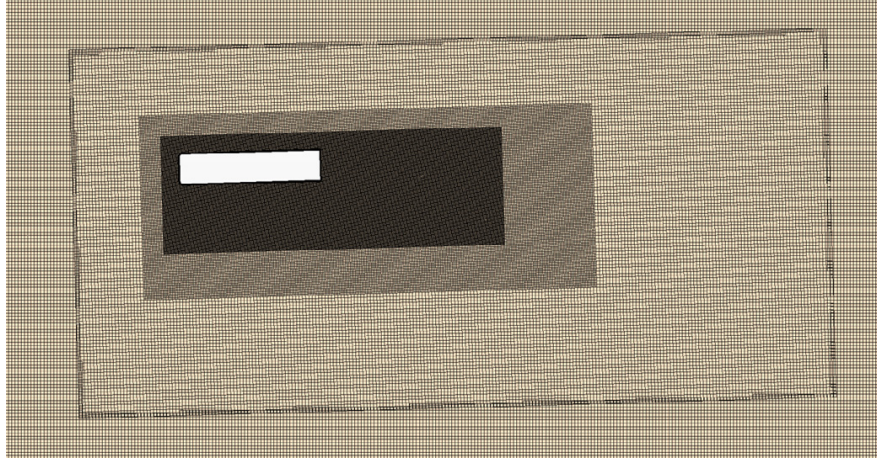
Figure 3.11: Overset grid used by Winkler et al. for evaluation of vehicle behaviour in a crosswind [122].

3.4 Experimental Data

The Davis model used in these tests was taken from the original development by Davis [86]. The geometry features a long front slant, short roof and a sloped 20° backlight. This fastback shape is more representative of a production vehicle than the more commonly used Ahmed body [83], whilst the simple geometric features allows the assessment of more fundamental flow field characteristics. The wind tunnel model was built to $1/6^{\text{th}}$ scale with a characteristic length $\mathbf{L}$=0.625 m, frontal area of 0.036 m^2 and a blockage factor of approximately 1.4% based on the model frontal area and cross-sectional area of the LUMS wind tunnel working section. Other important dimensions such as width ($\mathbf{W}$) and height ($\mathbf{H}$) are provided in Figure 3.13. Baden-Fuller investigated the effect of rounded and square rear pillars but for this study, only the rounded pillars are used. As a result, all edges were rounded to a radius of 20 mm. The ground clearance between the model and the floor was set to 40 mm.
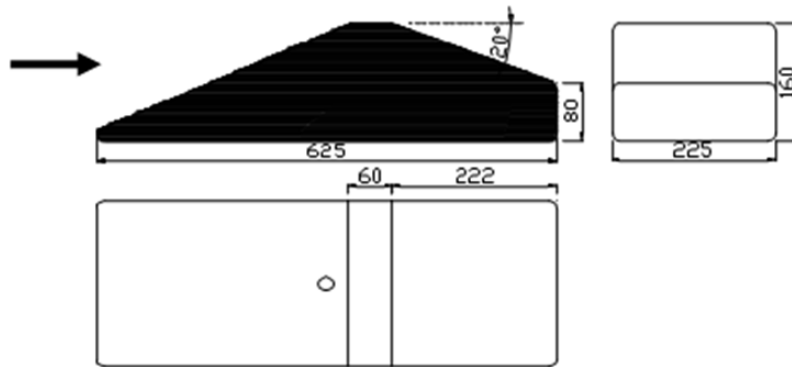
Figure 3.12: Davis model drawing [85].

The experimental tests were performed in the LUMS wind tunnel and were divided into two sets: static tests of the model at several fixed yaw angles and dynamic tests where the model was driven in a sinusoidal yaw angle oscillation. For the static tests, the model was connected to the underfloor balance and turntable of the working section however, for the dynamic tests, the desired oscillating frequency of 1Hz and amplitude of ±10° was too high for the balance yaw drive, so an oscillating model rig was used. This rig was an adaptation of the one designed by Mansor [123] in which free oscillation

of the model, driven by the aerodynamic yaw moment, was performed. The springs in Mansor's rig were replaced by an electric motor and crank arm and the model was connected to the rig using a 20 mm diametre support shaft and low-friction bearings, as shown in Figure 3.13.
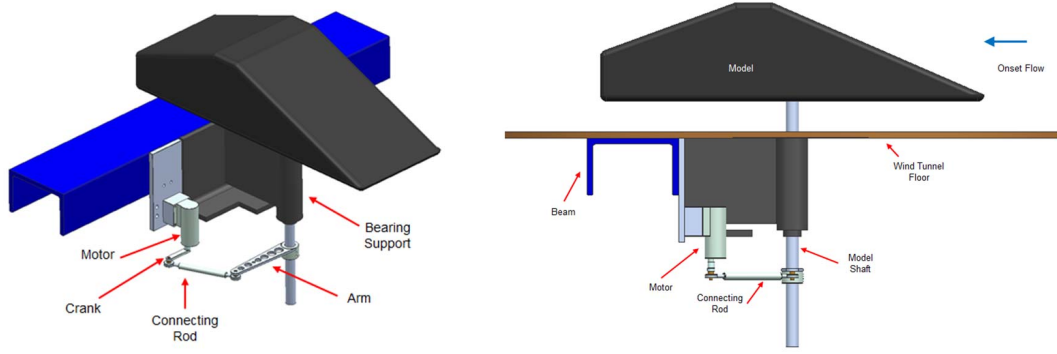
Figure 3.13: Driven oscillation model rig used by Baden-Fuller [85].

The amplitude of the driven oscillation was designed at $\pm 10°$, however due to flexing in the motor caused by the inertia of the model, a consistent overshoot in yaw angle produced an actual amplitude of $\pm 11°$. The oscillation frequency of 1Hz and wind speed of 40 m/s corresponds to a reduced frequency of $K = 0.098$ using the definition of Sims-Williams [124] shown in Equation 3.1. A 10 second sample of the motion is shown in Figure 3.14.
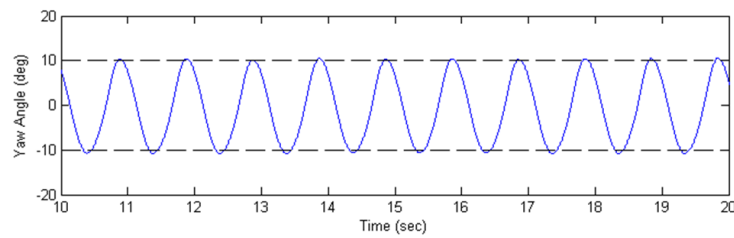
Figure 3.14: A sample of the oscillating model motion [85].

$$K = \frac{2\pi f \mathbf{L}}{u} \tag{3.1}$$

For both sets of tests, two-dimensional, planar velocity fields were recorded using particle image velocimetry (PIV) on two vertical cross planes parallel to the base of the

model. These planes were located 0.25**L** and 0.5**L** downstream from the base surface. In addition, surface pressure values were recorded using an array of 241 pressure tappings located symmetrically on both sides of the model and on the backlight and base surfaces. The exact locations of these tappings are shown in Figure 3.15. As a result, experimental surface pressure distributions are subject to interpolation errors. Extracted values of pressure were corrected for the 1.4% blockage using equation 3.2 where **A**′ is the ratio of model frontal area to working section cross sectional area (**A**′=0.0148 for the Davis body at 0° yaw angle).

$$C_{p_{cor}} = \frac{C_p + 2\mathbf{A}'}{1 + 2\mathbf{A}'} \tag{3.2}$$
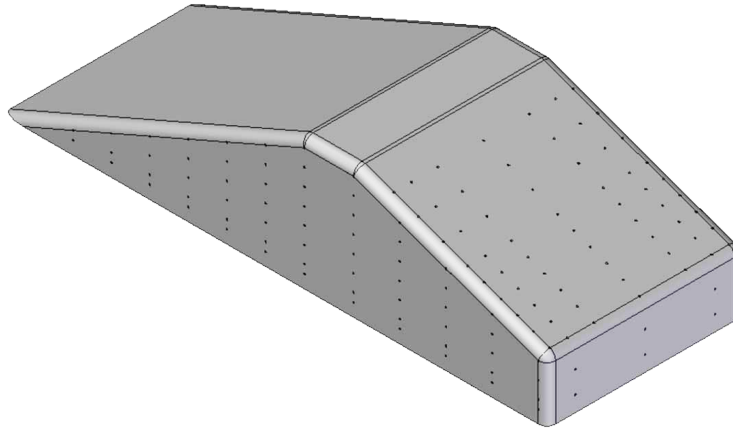
Figure 3.15: Davis model pressure tapping locations [85].

The tests differed in their measurements of aerodynamic forces and moments. For the static tests, the six-component, underfloor, virtual centre balance was used. Whereas for the dynamic tests, the model was not connected to the balance, thus forces and moments were calculated through an area weighted integration of the surface pressures.

3.5 Computational Domain and Grid Generation

To determine a suitable grid for prediction of the Davis model flow field with reasonable accuracy, two static tests at yaw angles of 0° and −10° are simulated initially. This is

then followed by the dynamic tests, using two motion techniques: the sliding mesh and overset grid methods. For this reason, a total of four computational grids have been generated.

As the experimental tests took place in the LUMS wind tunnel, the outer domain generated in the previous SUV case study can be transferred. This simplified geometric model features the contraction and first diffuser sections and was shown to provide an excellent replication of the empty working section flow.

For the two static grids, the Davis model is placed at the centre of the turntable at the appropriate yaw angle. On the surfaces of the model and support shaft, triangular surface elements are limited to a size of $1\,\text{mm}$ $(0.0017\textbf{L})$ in order to maintain the curvature of the model's radiused edges, Figure 3.16. As a result, approximately 7×10^5 elements define the model's surface and contribute to a total of 1.8×10^6 for the complete domain.

(a) Leading Edge   (b) Base Surface
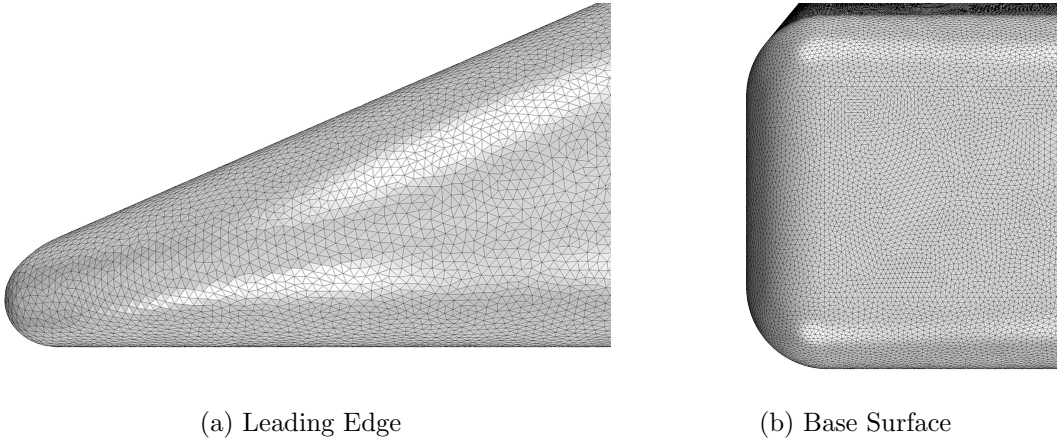
Figure 3.16: Davis model surface grid.

Growing outwards from the surface, prism layers are defined to capture the developing boundary layer. A non-dimensional wall spacing value $y^+ < 1$ and 8 prism layers to a total thickness $1\,\text{mm}$ $(0.0017\textbf{L})$ are used to resolve the near wall velocity gradient. Unlike the SUV case study, wall functions are used on the walls of the tunnel, thus the near wall spacing value is increased to $y^+ > 30$.

A polyhedral mesher is selected to discretise the fluid volume. A slow expansion rate of 1.2 is chosen to slow the growth of volume element size from the edge of the model prism

layers, thus keeping a moderate level of refinement around the entire model. Elements grow up to a maximum volume of approximately $0.001 \, \mathrm{m}^3$ in the bulk of the domain. Over the rear half of the model, a volumetric control region of fixed $2 \, \mathrm{mm}$ ($0.0034\mathbf{L}$) diametre elements is added to capture the wake of model with reasonable accuracy. As shown in Figure 3.17d for the $-10°$ yaw angle grid, the location of the refinement region is also yawed, thus its location with respect to the vehicle is consistent. Finally, the grids are subjected to 8 optimization cycles to ensure the highest quality. The total number of volume elements is approximately 15.7×10^6 for both grids.

(a) Vertical, axial cut through volume

(b) Wake Refinement

(c) Horizontal cut through volume, 0° yaw

(d) Horizontal cut through volume, $-10°$ yaw
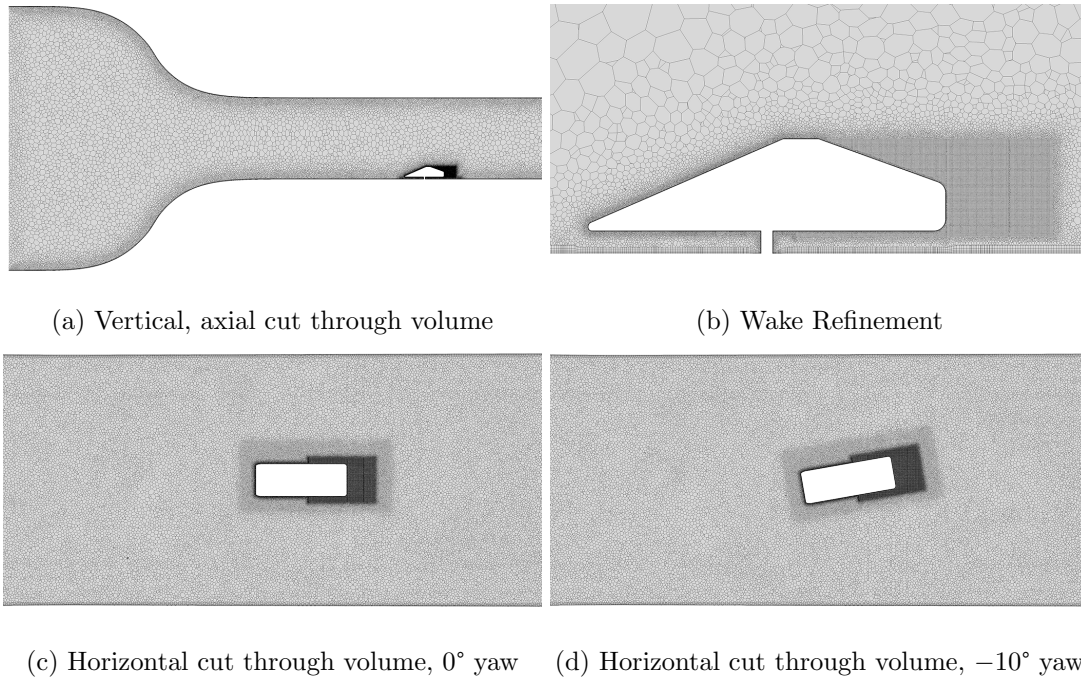
Figure 3.17: Static Davis model volume grid.

For the first dynamic grid using the sliding mesh approach, the domain is split into two separate regions. A cylinder is defined around the Davis model with the same diameter of the wind tunnel turntable $1.6 \, \mathrm{m}$ and a chosen height of $0.4 \, \mathrm{m}$ ($2.5\mathbf{H}$). This cylindrical region is then subtracted from the LUMS domain to generate a new 'background' domain. At the intersection of the background and sliding mesh regions, an in-place internal interface is created to allow data transfer between the to regions. To maintain accuracy of this transfer, a similar element size on the interface is set in both the sliding and background mesh regions. The resulting total number of volumetric elements is approximately 16×10^6 with 10×10^6 in the sliding mesh region and 6×10^6

84

in the background. The two regions are shown in Figure 3.18.

(a) Vertical, axial cut through sliding mesh region

(b) Vertical, axial cut through background region

(c) Horizontal cut through sliding mesh region (d) Horizontal cut through background region
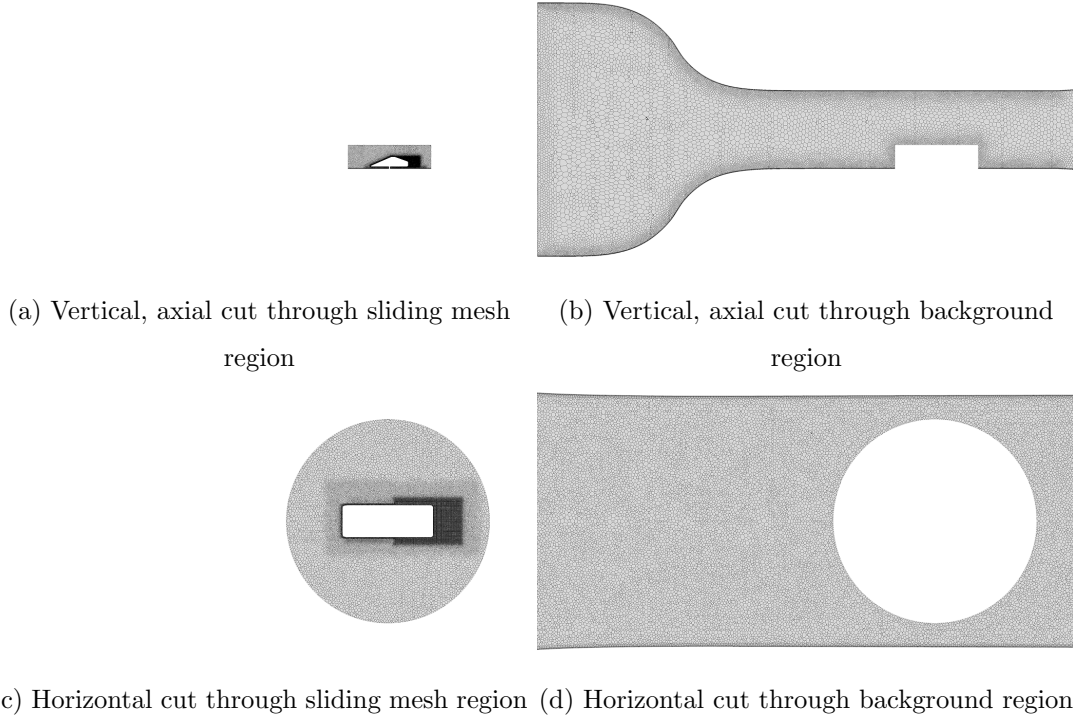
Figure 3.18: Sliding mesh volume grid.

For the overset approach, the same cylindrical region can be used as the overset grid however, the background grid is different. No subtraction takes place, and the background grid simply takes the form of the empty LUMS domain. As shown in Figures 3.19 and 3.20, additional refinement is required in the background region in the volume where the overset grid lays, in order to maintain accuracy of the inter-grid communication. As a result, the number of elements in the background grid increases to 6.4×10^6 and the total number to 16.4×10^6.

(a) Uninitialised overset grids

(b) Initialized overset grids

(c) Hole cut in background grid

(d) Initialized overset grid region
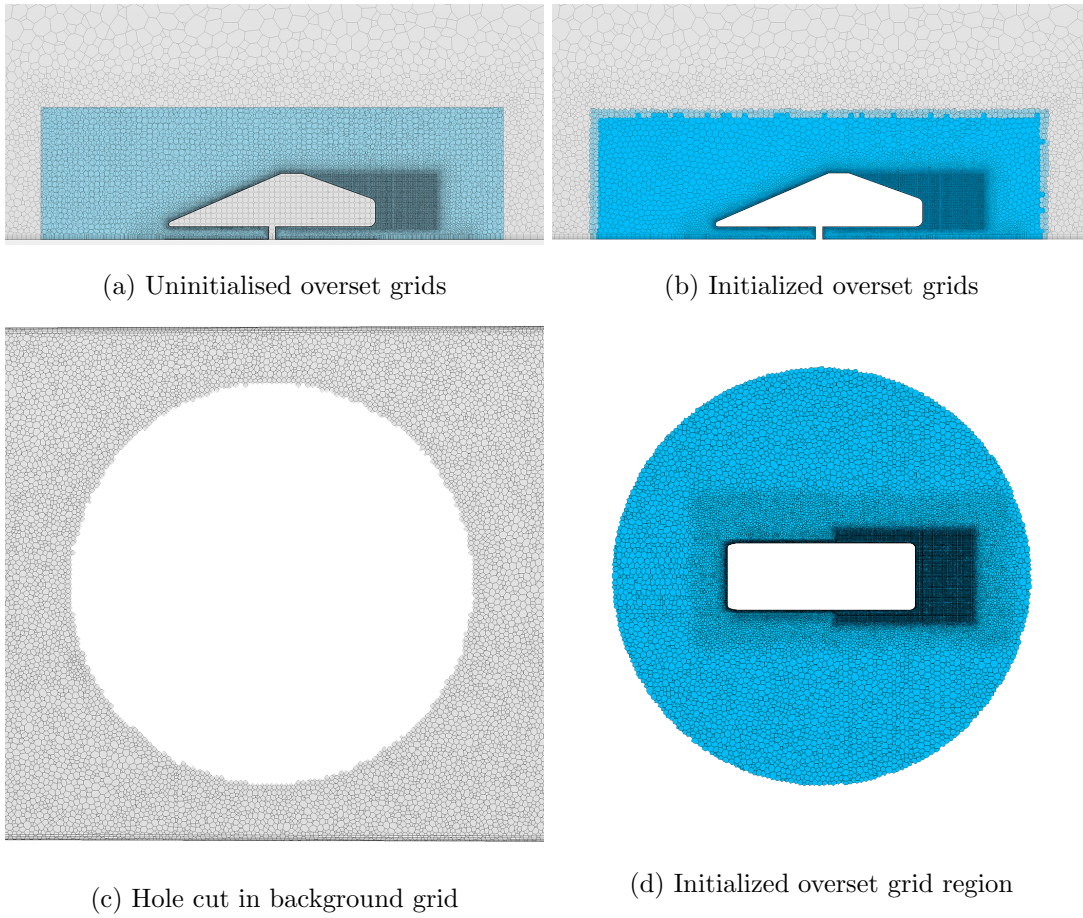
Figure 3.19: Overset volume grid.

(a) Background

(b) Overset

(c) Background
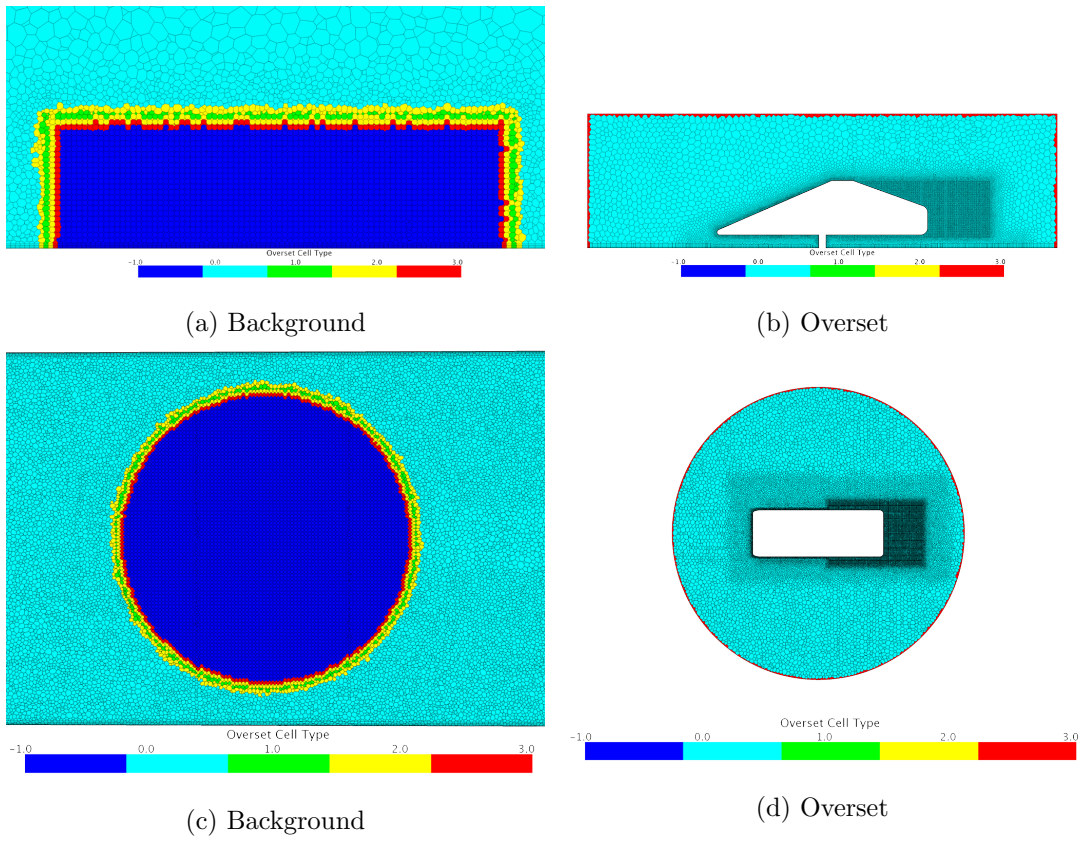
(d) Overset

Figure 3.20: Overset grids: -1: inactive, 0: active, 1: donor, 2: active (intermediate cell layer used by the hole cutting process), 3: acceptor.

3.6 Numerical Approach and Boundary Conditions

As intended, the numerical approach and boundary conditions follow on from the results of the first SUV case study. The IDDES formulation of the Spalart-Allmaras Detached Eddy turbulence model is selected, alongside a second order temporal scheme with a time-step of $\Delta t = 2.5 \times 10^{-5}$ seconds (non-dimensional $\Delta t U/L = 1.6 \times 10^{-3}$). This limits the CFL number to < 1 in the smallest wake elements.

A DES method is usually applied to much finer grids with a total number of elements closer to 100×10^6, however a grid containing this level of refinement is impractical due to current computational resources and the simulated time required to capture several periods of the model's oscillation. In a thorough evaluation of computational methods for the simulation of flow around an Ahmed body, Ashton and Revell [81] obtained reasonable results using a DES methodology on a grid of similar size. The main shortcoming of their approach was a slight under prediction of the turbulent kinetic energy in the initial separated shear layer of the 25° rear slant. This led to a reduction of turbulent mixing in the wake and ultimately an over prediction of the downstream wake length. This may be a similar issue for the Davis model which features a comparable 20° rear slant.

For the static cases, simulations were initialized using a steady state RANS solver before switching to DES for 10 convective flow units ($10 \times L/U$) to allow the flow to settle. This was followed by an averaging period of 40 convective flow units (0.625 seconds). Similarly, the dynamic simulations were initialized at a fixed 0° yaw angle using the same procedure. After this, the model was allowed to oscillate at the same rate as the experiment for a total of two time periods (2 seconds).

An inlet velocity of 5.39 m/s and turbulence intensity of 3% provides values of 40 m/s and 0.15% respectively in the working section. As shown in Case Study 1, at the model's location in the tunnel, these boundary conditions also provide an accurate replication of the boundary layers formed over the tunnel walls and the velocity variation over the total height of the working section. Baden-Fuller [85] found that the model was insensitive to Reynolds number effects above a critical value of 1.3×10^6 based on model

length **L**. Hence these tests were performed at a Reynolds number of 1.7×10^6.

3.7 Results - Static Tests

The results of the two static tests at 0° and −10° yaw are presented first. A comparison of the wake flow field at 0° yaw angle in the two PIV planes located at 0.25**L** and 0.5**L** downstream of the model are presented in Figure 3.21. The colouring of the contours indicates values of the in-plane velocity magnitude (v and w velocity components) and are expressed as a percentage of of the onset velocity (40 m/s). In addition, in-plane velocity vectors are overlaid on top of the contours to show the direction of the flow as well as its strength.

For the 0° yaw angle at 0.25**L**, the computational results are in good agreement with the experiment, with an accurate prediction of the location and strength of the two counter-rotating vortices which dominate the wake flow. This accuracy is maintained downstream as indicated by the high similarity between results in the 0.5**L** plane. One noticeable difference between the results is the slight asymmetry in the experimental flow field. This is especially interesting given the difference in averaging windows: the computational results represent an average of 0.625 seconds or 40 convective flow units whereas the experimental PIV measurements represent a much longer average of almost 300 seconds or 19,200 convective flow units. This suggests that the experimental asymmetry is a consequence of yawed onset flow conditions or imperfections in the model which have not been included in the simulation. This is consistent with the Generic SUV experimental results shown in Case Study 1 which also displayed an asymmetric, yawed flow field at 0° yaw angle for a similarly long averaging window and the results of Pavia et al. [125] and Perry et al. [126] who showed, that a simplified square-back vehicle exhibited a long-period bi-stability in the flow using the same facility,.

This experimental asymmetry is maintained in the surface pressure values as shown in Figure 3.22. A higher pressure at the front lower edge of the body's right hand side and asymmetric distribution over the backlight and base surfaces suggest that the onset flow is slightly yawed with respect to the body. Although the time averaging window

(a) Simulation 0.25**L**

(b) Simulation 0.5**L**

(c) Experiment 0.25**L** [85]

(d) Experiment 0.5**L** [85]

Figure 3.21: Davis model 0° yaw angle PIV planes showing in-plane velocity magnitude as a percentage of onset velocity (40 ᵐ/ₛ).

is shorter in comparison to the PIV data, (2048 convective flow units compared to 19,200), the simulated surface distribution is much more symmetric for a considerably shorter window (only 40 convective flow units).

The coarseness of the experimental pressure tappings and resulting data interpolation makes comparison to the more detailed distribution and peak regions such as the suctions at the roof edges slightly misleading. For this region a second distribution has been generated using interpolation of the simulation pressure values extracted only at the locations of the experimental tappings. Using this to compare to the experiment it

(a) Simulation

(b) Simulation Coarsened

(c) Experiment [85]
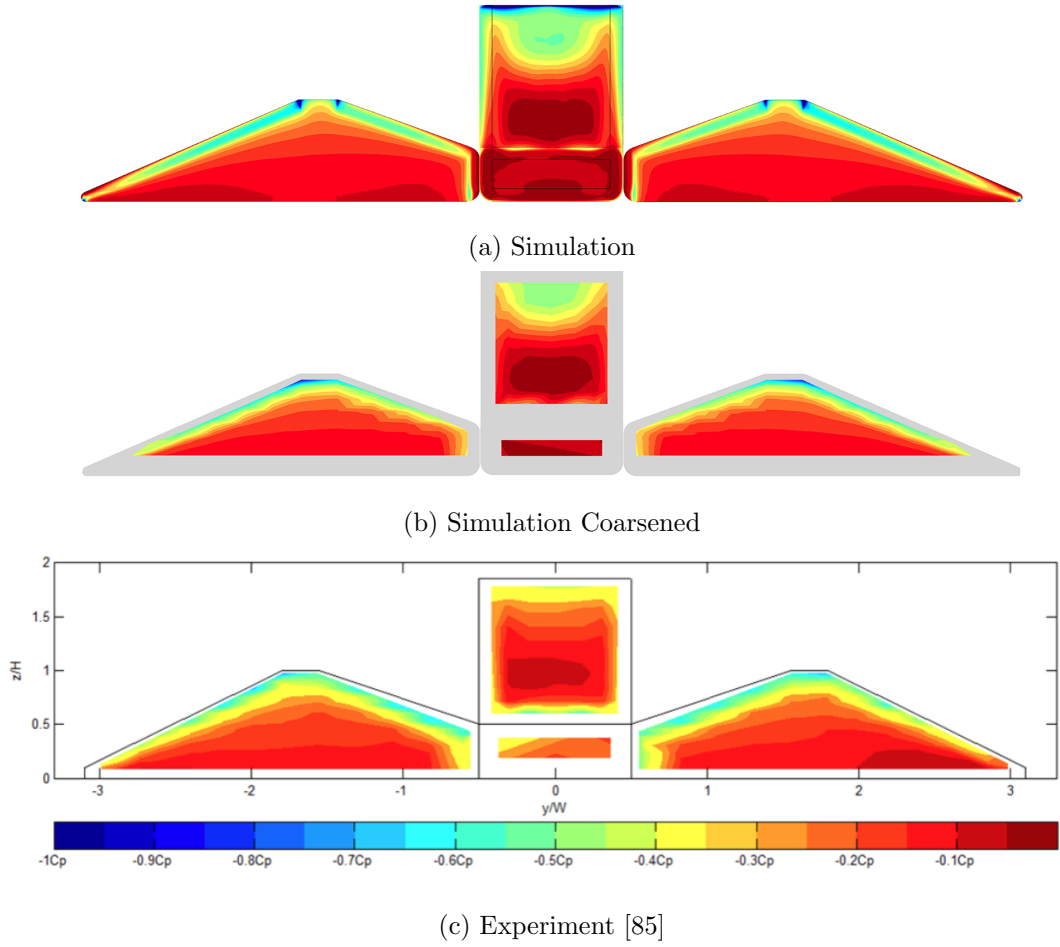
Figure 3.22: Davis model 0° yaw angle surface pressure coefficient.

is clear that the pressure distribution on the sides of the body is predicted well, with the exception of the slight asymmetry. This has a direct influence on the high accuracy of the C pillar vortices identified in the PIV planes which are sourced by this flow along these surfaces. Contrastingly, on the backlight, there are differences in the distribution most clearly towards the roofline. A U shaped region of lower pressure is predicted in the simulation which is not present in the experiment. This lower pressure indicates a much stronger flow separation from the roof's trailing edge and is clear evidence of an under prediction of the turbulent kinetic energy in the initial separated backlight shear layer in agreement with the Ahmed body simulations of Ashton and Revell [81]. The reduction in turbulent mixing keeps the flow separated over the upper portion of the slant but is contained by the strong C pillar vortices. As a result, the pressure recovery over the lower half of the backlight is slightly over predicted in strength. The

anticipated over prediction in wake size as a consequence of the turbulent mixing deficit as shown by Ashton and Revell [81] is not relevant in this case. As shown in the PIV planes, the wake is dominated by the C pillar vortices, which due to the longer backlight, are much stronger in comparison to those present in the Ahmed body flow and hence control the size and structure of the wake.

The large differences in backlight surface pressure distribution are not reflected in the force coefficients. Table 3.1 presents the force coefficients calculated from an area weighted integration of the surface pressures at the pressure tapping locations. The simulation backlight lift and drag contributions differ to experiment by 7 and 16 counts respectively. This is a useful example of how reliance on force coefficient comparisons can be misleading. The large differences, specifically the stronger suction towards the top of the backlight and the over prediction in pressure recovery towards the lower edge appear to balance out in the area weighted average.

On the base surface, the pressure distributions appear significantly different with much lower pressures found in the experiment. The effect of using coarsely distributed pressure tappings (only six tappings on the base surface) is evident by comparing the two simulation distributions. The reasonable level of symmetry seen in the full simulation data is lost in the coarse interpolation procedure, implying an unphysical asymmetric nature of the flow and this may also be the case with the experiment results. There appears to be an disproportionate difference in the drag coefficient values, however, it is believed that the experimental value reported by Baden-Fuller is incorrect by an order of magnitude based on an interpreted average pressure value on the base surface.

Table 3.1: Force coefficients at 0° yaw angle, calculated from integration of surface pressures at tapping locations.

	Experiment [85]	Simulation
Backlight Lift	0.254	0.247
Backlight Drag	0.092	0.108
Base Drag	0.009	0.110

At $-10°$ yaw angle, an A pillar leeward vortex is formed in addition to the two C pillar trailing vortices. These three vortices are identifiable in the velocity fields shown in Figure 3.23. The locations and strengths of the two trailing vortices are matched well by the simulation, however this is not the case for the A pillar vortex. The rotational strength of this structure appears to be over predicted and is located higher up the body, aligned with the roof.

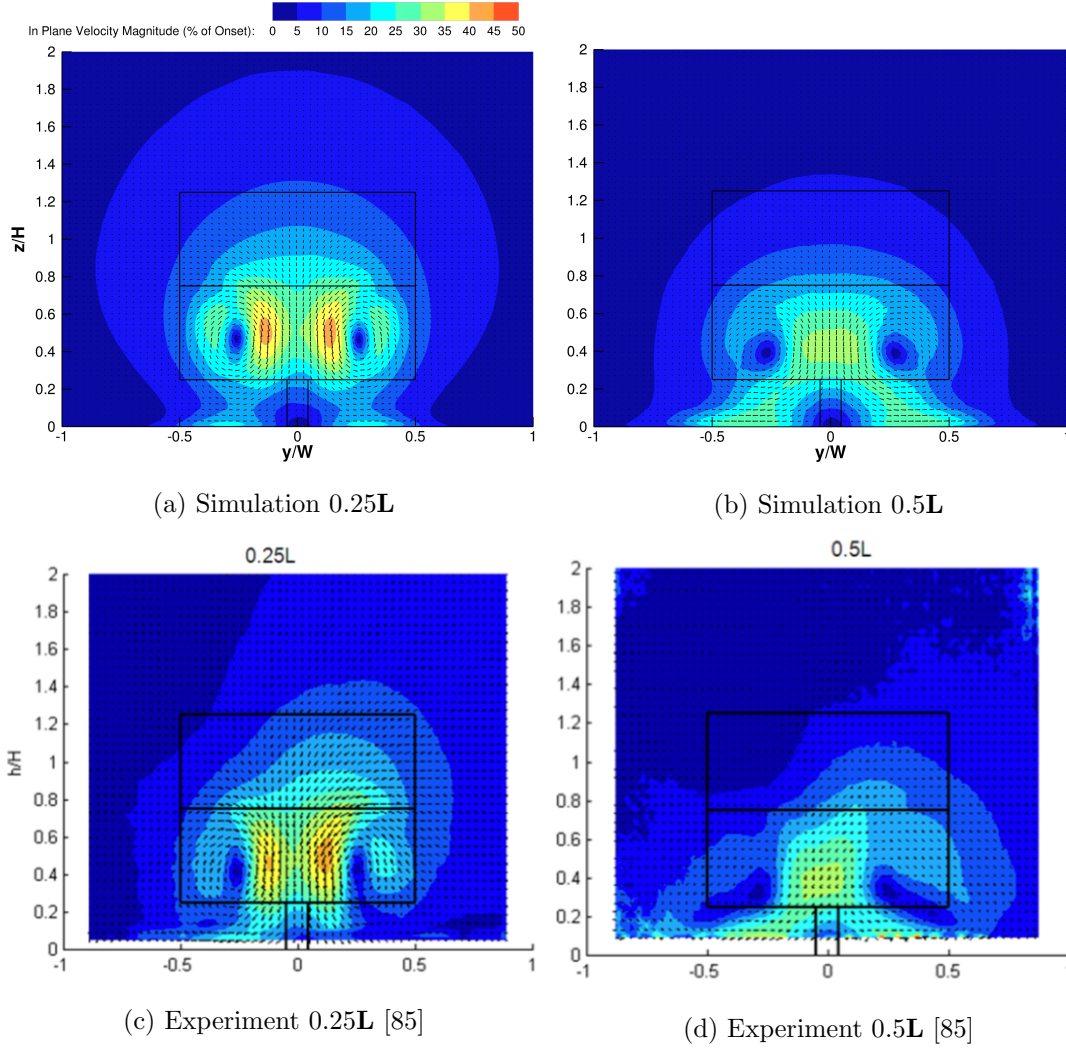(a) Simulation 0.25**L**　　　　　　　(b) Experiment 0.25**L** [85]
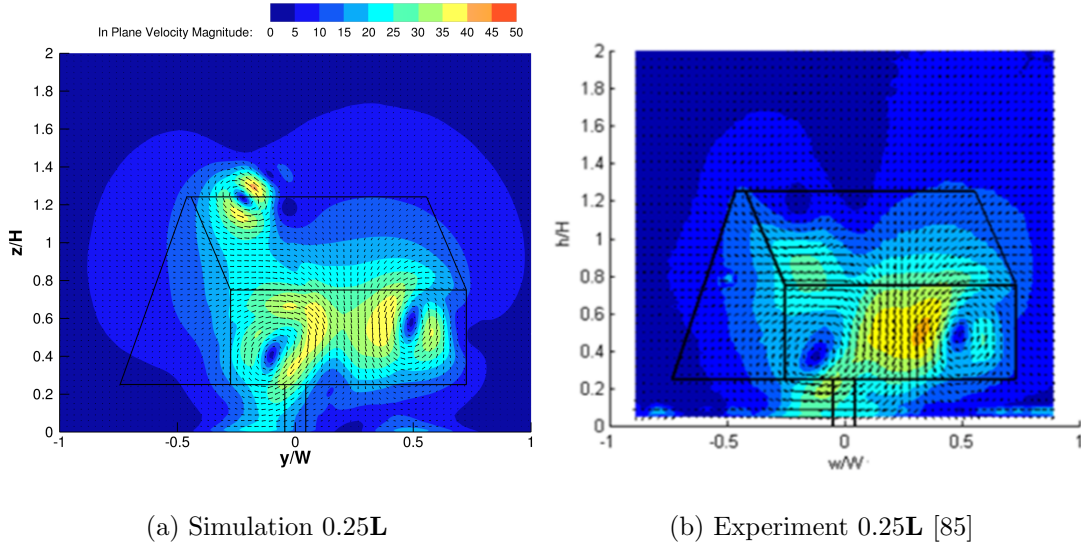
Figure 3.23: Davis model $-10°$ yaw angle PIV planes showing in-plane velocity magnitude as a percentage of onset velocity ($40\,\mathrm{m/s}$).

It is predicted that the inaccuracies in the A pillar vortex are a consequence of the short time averaging window in comparison to the experiment rather than an effect of the coarse grid and computational method. Baden-Fuller showed how this A pillar vortex is an unsteady flow feature, with a weak, periodic separation behaviour. In all instantaneous experimental vectors field, the A pillar vortex was present but its location varied vertically and laterally with significant but seemingly uncorrelated changes to its size and strength. An example of the instantaneous, experimental flow field is shown in Figure 3.24a which shows the position of the vortex at $(y/\mathbf{W} = -0.25, z/\mathbf{H} = 1.3)$, a location which more closely agrees with the simulation. Using cross-correlation based conditional averaging on the experimental data, repeated modes were extracted and it was found that the vortex could separate at the roof trailing edge or remain attached all the way down the backlight. Figure 3.24b shows the result of experimental vortex

core tracking on the leeward side confirming the unsteady nature of this flow structure. Given this behaviour, lengthening the simulation's averaging window in an attempt to achieve a similar mean vortex location is computationally impractical at this stage.

(a) Experimental instantaneous vector field at 0.25**L**

(b) Experimental leeward side vortex core tracking at 0.25**L**
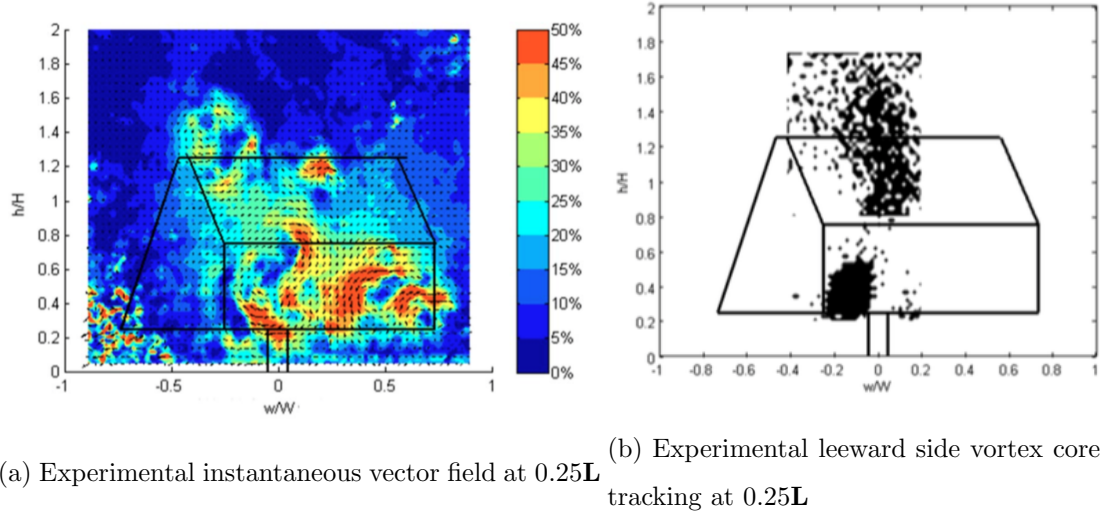
Figure 3.24: Davis model −10° yaw angle unsteadiness in the A pillar vortex [85].

A comparison of the surface pressure distribution at −10° yaw angle is presented in Figure 3.25. The predicted distribution on the windward side of the body is in excellent agreement with the experiment, whereas on the leeward side, the effects of the A pillar vortex unsteadiness and the shorter time averaging window are evident in the low pressure region underneath this flow structure. This is made even clearer by Figure 3.26, which shows the difference in pressure $|\Delta C_p|$, between the windward and leeward sides of the body. Despite this, the overall effect on the balance measured side force and yaw moment coefficients shown in Table 3.2 is small, with values differing by only 9 and 5 counts respectively, to the experiment. On the backlight, a similar behaviour to that seen in the 0° yaw angle simulation exists. An over prediction in the roof separation is indicated by the larger region of low pressure towards the top of the backlight and an over prediction in the pressure recovery on the lower portion can be seen. Again, on the base surface, there is a significant change in the pressure distribution, but due to the coarseness of the pressure tappings, conclusions on the simulation accuracy for this surface cannot be made with confidence.

(a) Simulation

(b) Simulation Coarsened

(c) Experiment [85]
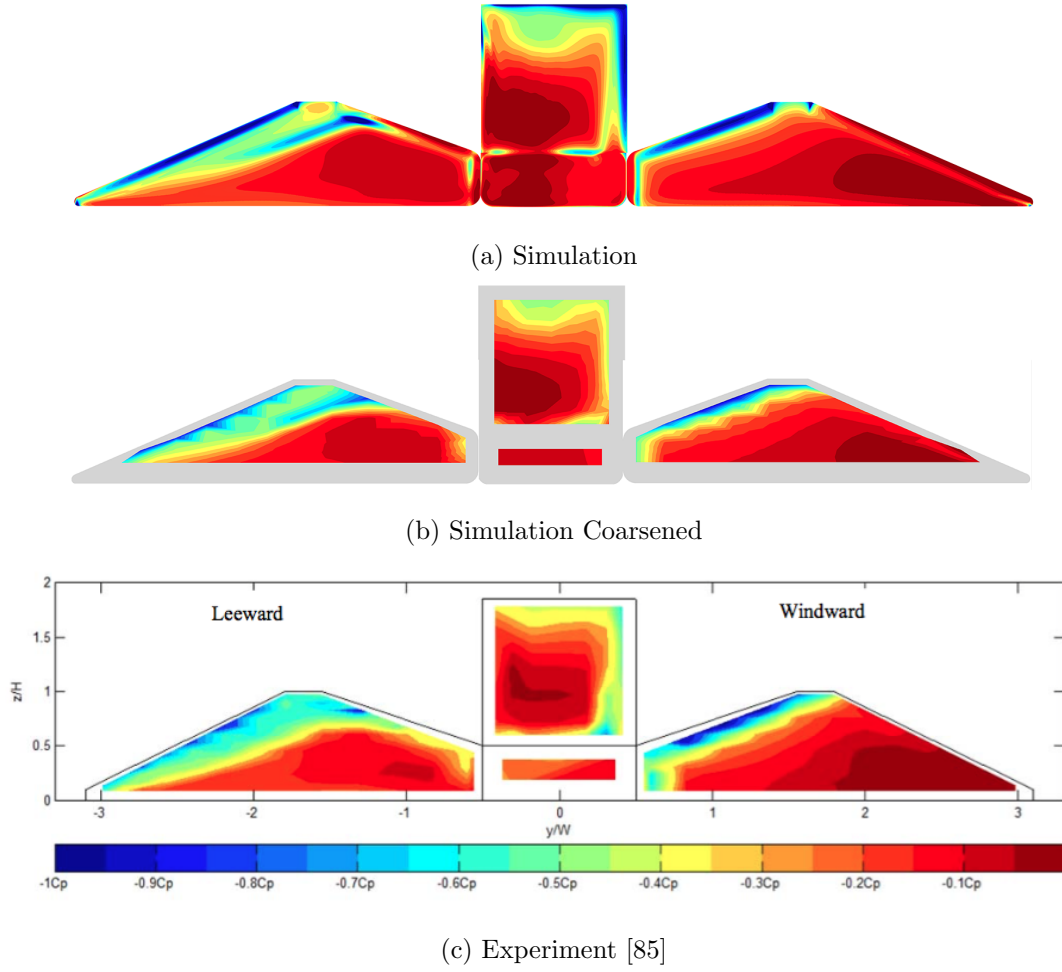
Figure 3.25: Davis model $-10°$ yaw angle surface pressure coefficient.

There is good evidence to suggest that the current grid and computational methodology can be used to provide an accurate prediction of the flow field at static yaw angles up to the designed maximum yawed angle of the oscillating rig. The largest effect of the coarse grid appears to be an over prediction in the separation off the roof trailing edge over the entire yaw angle range. The wake dominating trailing vortices are predicted well, as is the unsteady A pillar vortex which is formed as the yaw angle increases. In conclusion, this grid and methodology can be adopted for use in the dynamic simulations.

95

(a) Simulation
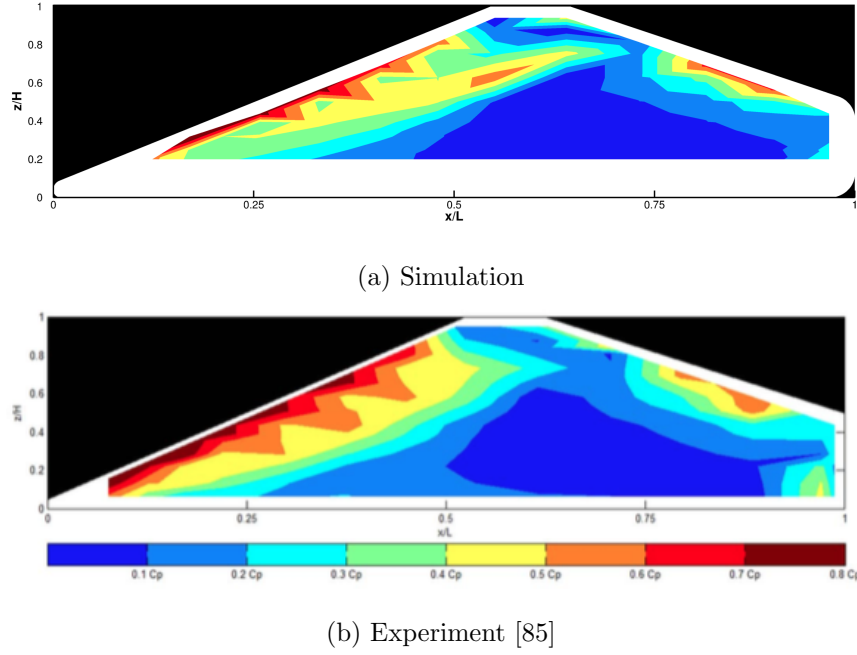
(b) Experiment [85]

Figure 3.26: Davis model $-10°$ yaw angle, $|\Delta C_p| = |C_{p\ windward} - C_{p\ leeward}|$.

Table 3.2: Force coefficients at $-10°$ yaw angle, (measured by balance in experiment).

	Experiment [85]	Simulation
Side Force	-0.217	-0.208
Yaw Moment	-0.062	-0.057
Front/Rear Side Force	-0.171/-0.047	-0.161/-0.047

3.8   Results - Dynamic Tests

The results for the driven 1Hz sinusoidal oscillation are now presented. Initially the sliding mesh method is used and later comparisons will be made to the overset technique. Figure 3.27 shows the behaviour of the side force coefficients for one oscillation period. For both experimental and computational results, front and rear side force values have been calculated using the total side force and yawing moment, as shown in Equation 3.3. This data has been smoothed using a low pass filter to remove some of the small scale unsteadiness in the side force. Also shown are the experimental coefficients which have been periodically averaged over 1056 oscillation periods to remove

cycle-to-cycle variations in frequency and magnitude due to the supply voltage and the effect of the forces on the motor. Finally, the quasi-steady experiment values at static yaw angles have been included.

$$C_{Y_F} = \frac{C_Y}{2} + C_{MZ}, \qquad C_{Y_R} = \frac{C_Y}{2} - C_{MZ} \tag{3.3}$$
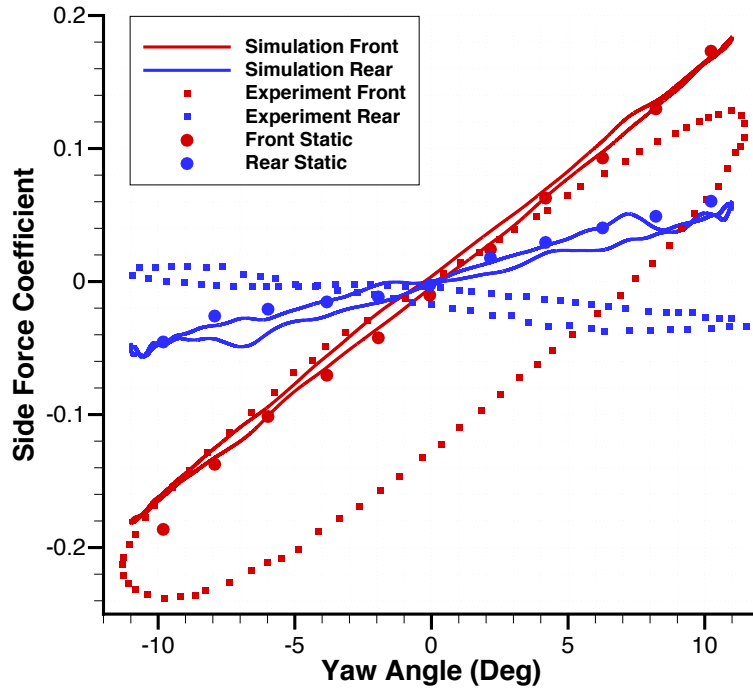
Figure 3.27: 1Hz oscillation: Side force coefficient.

It is clear that the simulation does not predict the large hysteresis that is present in the experiment, with the front and rear side force following the static values. It is also clear that the hysteresis present in the experiment only exists around the front half of the body. Baden-Fuller showed that this hysteresis was a consequence of a time lag in the evolution of the leeward A pillar vortex. Isosurfaces of Q criterion=$200\,000\,\text{s}^{-2}$ are useful in identifying this vortex in the simulation results and Figure 3.28 shows the high similarity and lack of any lag in this structure at the two $-10°$ yaw angle states. In this instance, increasing and decreasing yaw angle is independent of sign and thus refers to growth in the absolute value of the yaw angle.

(a) −10° Increasing   (b) −10° Decreasing
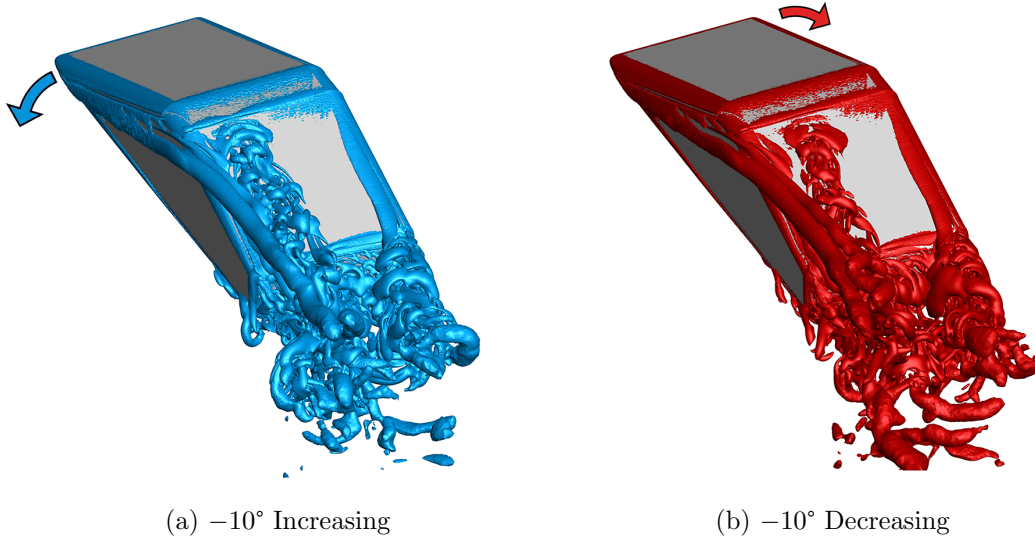
Figure 3.28: 1Hz oscillation: Isosurfaces of Q criterion=$200\,000\,\text{s}^{-2}$.

Figure 3.29 shows the surface pressure on the sides of the body, instantaneous pressure for the simulation and averaged at the same position over multiple oscillation periods for the experiment. The high similarity in simulation pressure distributions between −10° increasing and −10° decreasing yaw angle could be expected from the lack of hysteresis observed in the force coefficients, whereas variations in the experimental distributions can be identified as expected. At −10° and increasing in yaw, the experimental pressure distribution bears a much closer resemblance to the 0° static distribution of Figure 3.22 than the −10° static distribution of Figure 3.25. However, on the windward side, there is evidence of yawed flow with high suction over the C pillar. The beginning of a shift in pressure along the windward A pillar indicates a delay in the dissipation of the A pillar vortex that was formed on this side of the body when it was at positive yaw. The experimental hysteresis in this region is confirmed by Figure 3.30 which shows the behaviour of pressure at a single tapping location under the A pillar.

(a) Simulation −10° Increasing

(b) Simulation −10° Decreasing

(c) Experiment −10° Increasing [85]

C_p: -1 -0.9 -0.8 -0.7 -0.6 -0.5 -0.4 -0.3 -0.2 -0.1 0

(d) Experiment −10° Decreasing [85]
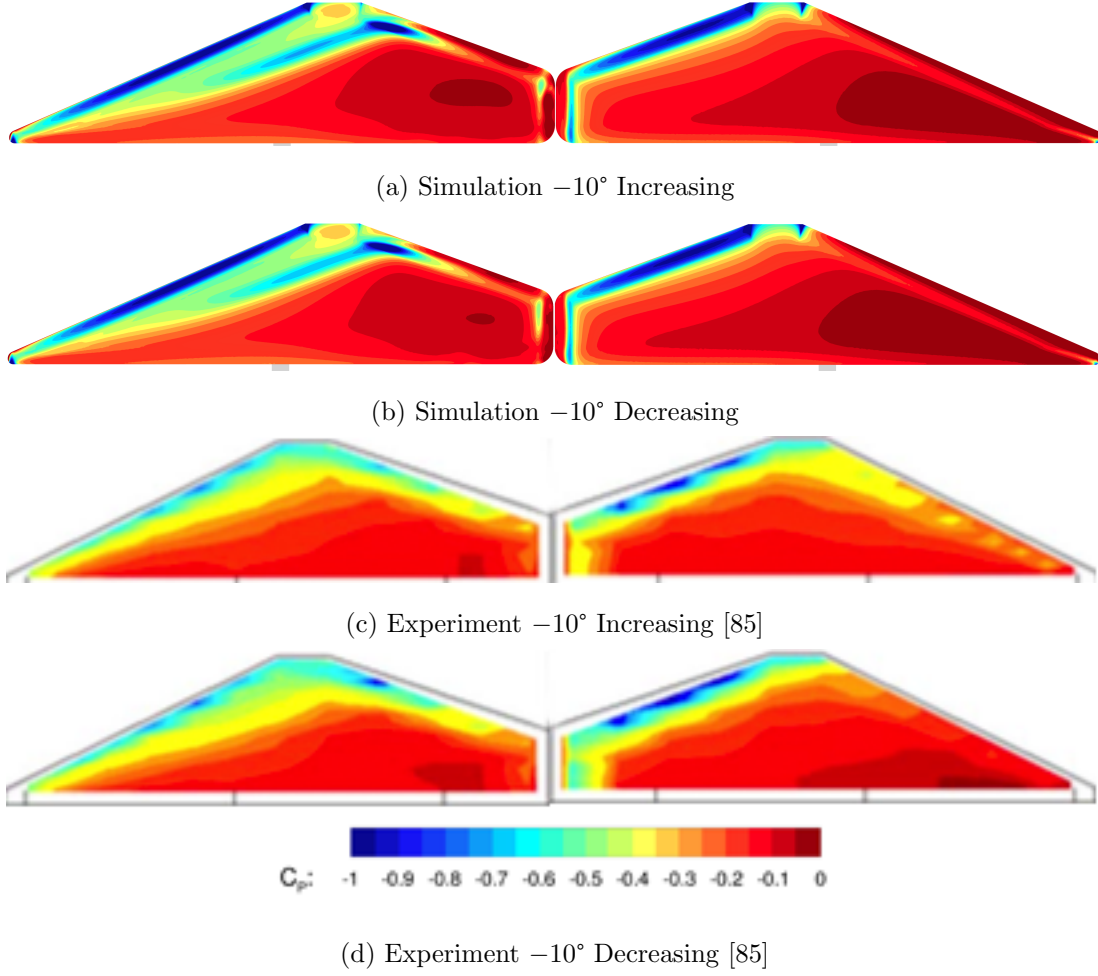
Figure 3.29: 1Hz oscillation: Surface pressure on sides of the oscillating Davis body (windward RHS and leeward LHS).

At −10° and decreasing in yaw angle, the pressure distribution is much closer to that when static at −10°, albeit with a stronger suction over the leeward C pillar indicating the location and strength of the leeward A pillar vortex. It is clear that the behaviour of the A pillar vortex over the front half of the body is the main source of the hysteresis that exists in the experiment.

The existence of hysteresis at this reduced frequency ($K = 0.098$) is surprising. Sims-Williams [124] described how at frequencies as low as this, the flow can be expected to behave in a quasi-steady manner. This is consistent with the simulation results which displayed minimal hysteresis and suggests that an external source such as yawed onset flow or imperfections in the wind tunnel model are responsible for the experimental
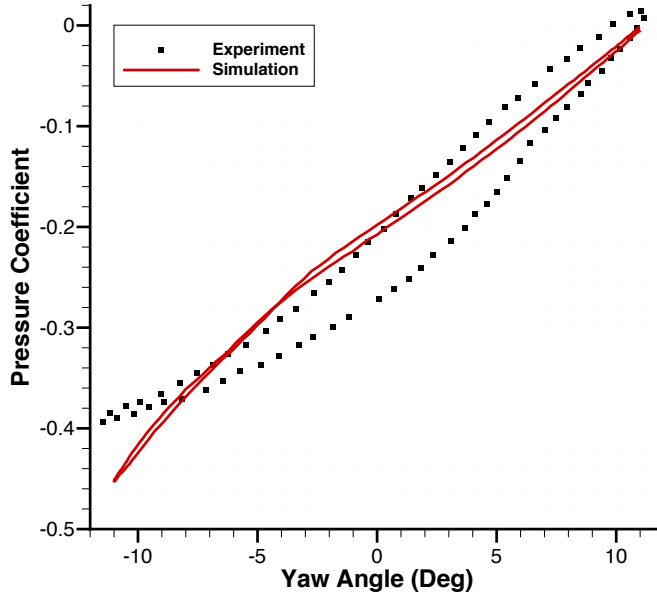
Figure 3.30: 1Hz oscillation: Pressure at A pillar tapping location.

time lag. Asymmetric A pillar radii or leading edge imperfections could introduce variations in the formation of the A pillar vortex and evidence of this is shown by the shift in the origin of the front side force hysteresis which is not centred about zero. On close inspection of the physical wind tunnel model, such features are found. Due to the nature in which the model is assembled, from a base plate and upper section, an offset in the leading edge geometry is present. This is more clearly shown in Figure 3.31 and it is unknown whether any attempts were made to reduce this offset during the tests. If present in the wind tunnel tests, it is reasonable to assume an early separation from the leading edge and possible reattachment will exist. Evidence of this is shown in the experiment pressure distributions around the leading edge.

Figure 3.31: Leading edge of the wind tunnel model.

In an attempt to generate flow hysteresis, the simulation has been repeated at the higher frequency of 10Hz, which corresponds to a reduced frequency of $K = 0.98$. This frequency falls around the value where the flow will no longer be quasi-steady, as stated by Sims-Williams [124] and hence hysteresis can be expected. The same oscillation amplitude has been used for the higher frequency simulations.

The side force behaviour at this higher frequency is shown in Figure 3.32. As expected hysteresis has been generated, but unlike the experiment results at 1Hz, the amount of hysteresis has increased at a similar rate in both the front and rear side force contributions. It is clear from Figure 3.33 that the A pillar vortex has not fully developed along the length of the body as it increases in yaw angle. However when returning, sufficient time has passed for the vortex to grow in strength and downstream length, hence the two different values of side force at $-10°$ yaw angle. In a similar fashion, the time taken for this vortex to convect downstream and pass the body is longer than the time taken for the body to return to $0°$ yaw, hence the asymmetric flow topology at this angle. The two topologies that are generated are dependent on the direction of rotation and interestingly are mirror images of each other. Hence, the overall hysteresis, unlike the experiment, is centred about $(0, 0)$.
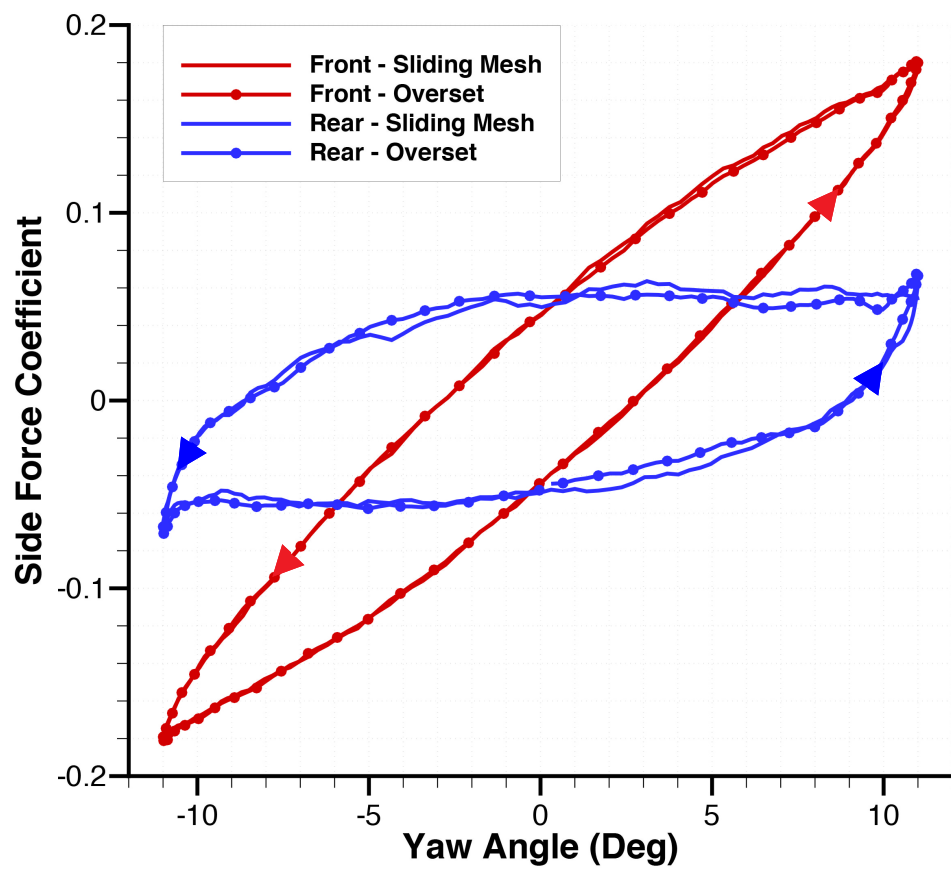
Figure 3.32: 10Hz oscillation: Side force coefficient.

(a) −10° Increasing

(b) −10° Decreasing

(c) 0°: Negative rotation

(d) 0°: Positive rotation
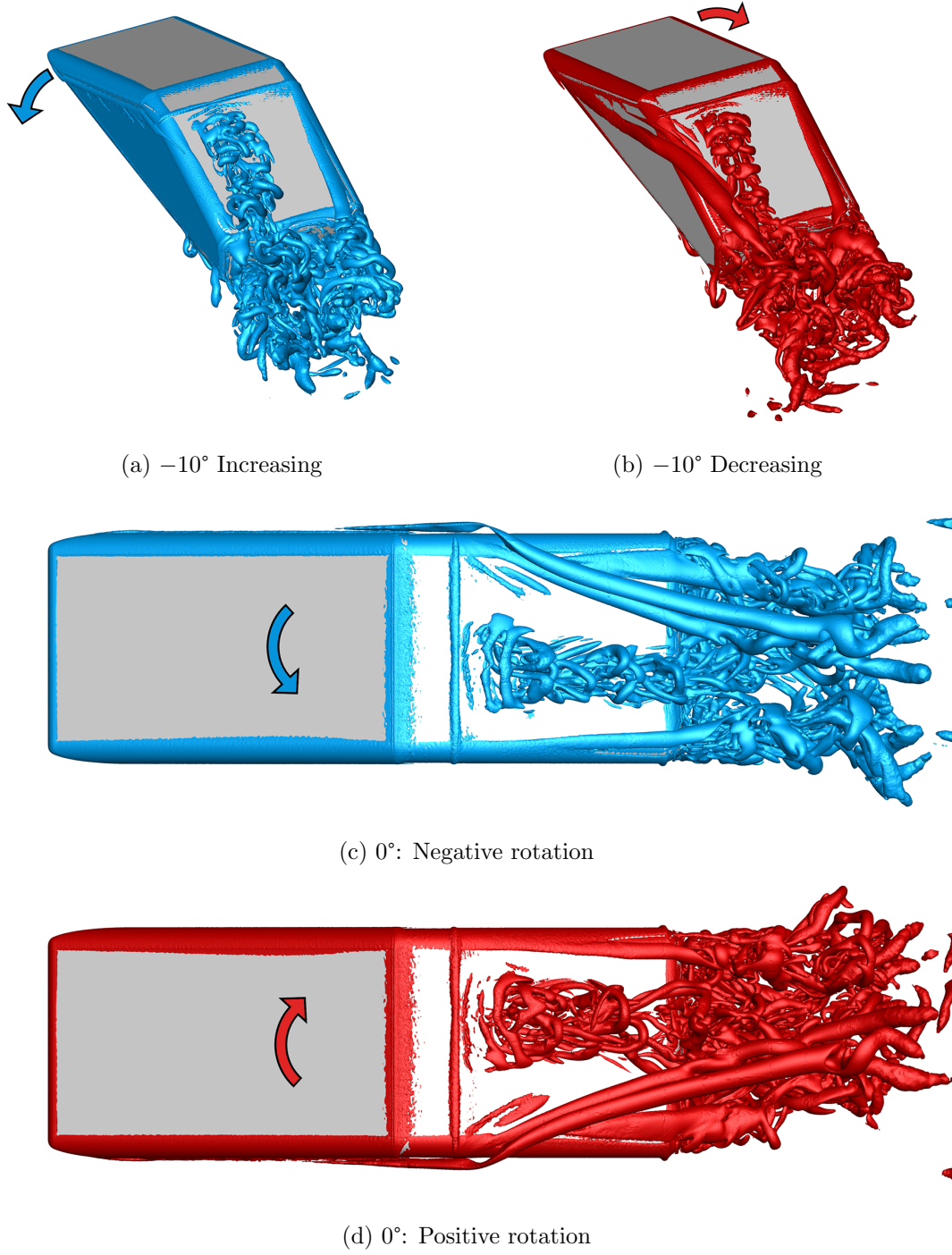
Figure 3.33: 10Hz oscillation: Isosurfaces of Q criterion=$200\,000\,\mathrm{s}^{-2}$.

3.9 Results - Motion Evaluation

The overset grid approach was only applied to the higher frequency 10Hz oscillatory motion and not the lower 1Hz motion. In terms of computational resources this was considerably more efficient since the oscillation period and thus time to obtain a comparison of one complete rotation is much shorter. The choice of motion technique, sliding or overset grid, has a minimal effect on the flow prediction for this particular simulation. This was shown in Figure 3.32 in which the force coefficient curves of the two approaches lie on top of each other. The largest difference between the two approaches was computational expense. Table 3.3 shows the cost per time step and for one complete oscillation period for each method. Also included in this table, is the cost for a static simulation, which is used to show the effect on cost of including motion in general. For this particular simulation, the sliding grid approach is clearly a much faster option, offering a speed up of approximately 84% over the overset grid, although whether this level of speed up is maintained for more complex motions or finer grids is undetermined.

Table 3.3: Computational costs of motion techniques.

	Static	Sliding Grid	Overset Grid
Wall clock time per Δt (s)	5.78	7.28	13.36
Wall clock time per oscillation period (s)	-	29,188	53,432
Speed up from overset grid approach	2.31	1.84	**1**

3.10 Summary

In the simulation of the Davis body wind tunnel tests by Baden-Fuller, a coarse computational grid with a DES turbulence model has been used to provide results with a good level of accuracy. At static yaw angles, the dominant flow structures such as trailing vortices were predicted well and the location of the leeward A pillar vortex present at large yaw angle is consistent with the unsteady behaviour of this structure that was

found in the experiments. A slight over prediction in the amount of separation off the roof trailing edge is an indication of a lack of turbulent kinetic energy in the backlight shear layer and this is consistent with existing literature.

For the dynamic tests in which the body undergoes a driven, periodic sinusoidal rotation in yaw angle, the flow hysteresis found in the experiment could not be matched at the same frequency. The simulated flow displayed a quasi-steady behaviour obtained from static yaw angle tests and this is consistent with existing literature for the given reduced frequency value. The source of the experiment hysteresis was located in side pressure distributions underneath the front A pillar. It was suggested that this was due to an external source such as yawed onset flow or asymmetric A pillar radii that would cause variations in the flow around this edge and formation of the A pillar vortex. Imperfections in the wind tunnel model's leading edge added further evidence to this claim. Increasing the oscillation frequency by an order of magnitude was found to generate a large flow hysteresis, visualised in both the front and rear side force coefficients. Iso surfaces of Q criterion were used to identify the largest source of this hysteresis: the delay in the formation and dissipation of the A pillar vortex.

The choice of motion technique, sliding or overset grid, had a minimal effect on the flow prediction for this particular simulation. The largest difference was found in computational expense where the time taken to run using the overset grid approach was a factor of approximately 1.84 times slower than when using the sliding mesh.

THE FULLY-COUPLED SYSTEM

Contents

4.1 Introduction

The aim of this study is to design and implement a coupled system between CFD software and a vehicle dynamics model. In this particular system, aerodynamic loadings will be used as an input into a dynamics model to cause or influence body motion. This motion will be returned to the CFD simulation where the position of the body is updated. Thus the two simulations run simultaneously, with continuous data exchange.

A suitable test case for a system of this type is the experiments of Mansor [123], in which the Davis model rotates in yaw due to variations in the aerodynamic yaw moment. The motion is restricted by a pair of springs which limit the angular displacement and rate, thus producing an oscillatory motion. A simplified sketch of the test rig is shown in Figure 4.1. This arrangement is the basis for the tests performed by Baden-Fuller [85] which were simulated in Chapter 3, however, the motion is no longer controlled by an electric motor but by the properties of the springs, the inertia of the model and the aerodynamic yaw moment. A single degree of freedom, second order equation serves

as a simple dynamics model and this is shown in Equation 4.1 where I_{zz} is the body's moment of inertia, C_r is the mechanical damping term, K_r is the mechanical stiffness term and M_Z is the aerodynamic yaw moment input.
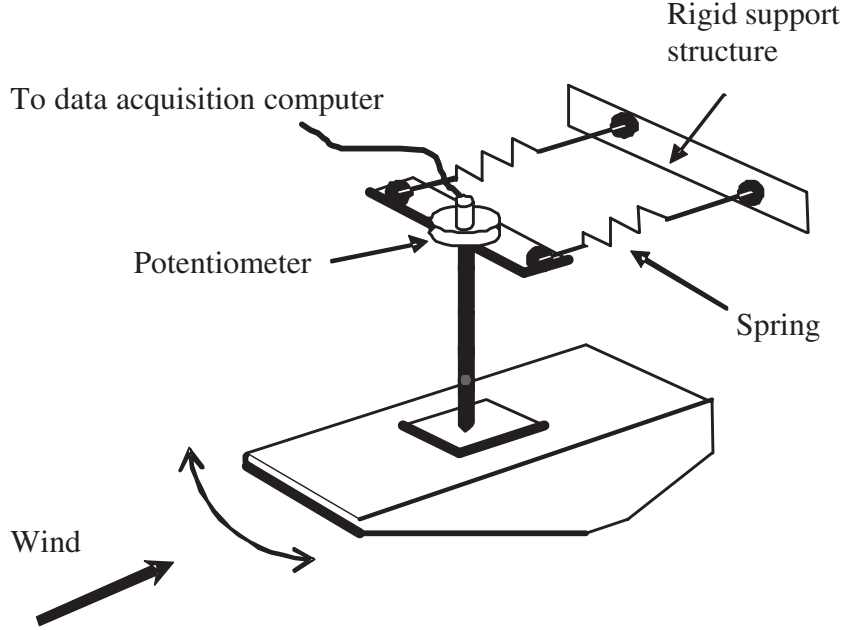
Figure 4.1: The Mansor oscillating test rig [123].

$$I_{zz}\ddot{\beta} + C_r\dot{\beta} + K_r\beta = M_Z. \tag{4.1}$$

The test rig was designed so the effect of both reduced frequency and Reynolds number could be investigated by varying the properties of the springs or the wind speed. A total of ten springs with increasing levels of stiffness were used in the experiments, with a reduced frequency range of (0.1–1.6), using the definition of Sims-Williams [124]. Similarly, the range of Reynolds number tested was (4.3×10^5– 1.7×10^6). For this computational study, only one spring type is used. The K5 spring used by Mansor [123] has a linear stiffness K_s, of 806 N/m which when installed as a pair on the rig (separated by a distance of $2b$) provides a torsional stiffness K_r, of 16.12 Nm/rad, Equation 4.2. Mansor estimated the model's moment of inertia, $I_{zz} = 0.095$ kgm^2 and calculated the natural frequency of the rig with these springs installed, $\omega_n = 13.01$ rad/s using Equation 4.3. A value for the mechanical damping C_r was determined using a

wind-off oscillation test in which the model was released from an initial yaw angle with no wind input and the yaw angle response recorded. It was found that for an oscillation frequency in the range of 1–2Hz, a damping ratio value ζ of approximately 0.005 (0.5% of critical damping $\zeta = 1$) is appropriate and correlates to a C_r value of approximately 0.0124 $\mathrm{Nms/rad}$ using Equation 4.4.

$$K_r = 2K_s b^2 \tag{4.2}$$

$$\omega_n = \sqrt{\frac{K_r}{I_{zz}}} \tag{4.3}$$

$$C_r = 2\zeta\omega_n I_{zz} \tag{4.4}$$

Using these values and the graphical programming environment Simulink, the second order spring equation 4.1 can be visualised by the dynamics model shown in Figure 4.2.
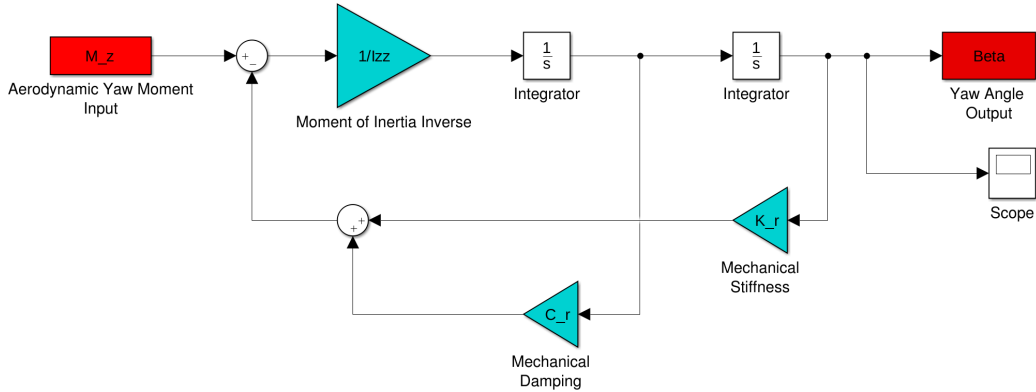
Figure 4.2: Simulink model of spring equation.

This model has been validated using the same wind-off test method: a value of $M_Z = 0$ is set as the aerodynamic input and an initial yaw angle $\beta_0 = 17°$ is set at the second integrator. The model's yaw angle response is shown in Figure 4.3 alongside the outer bounds of the equivalent experimental response.
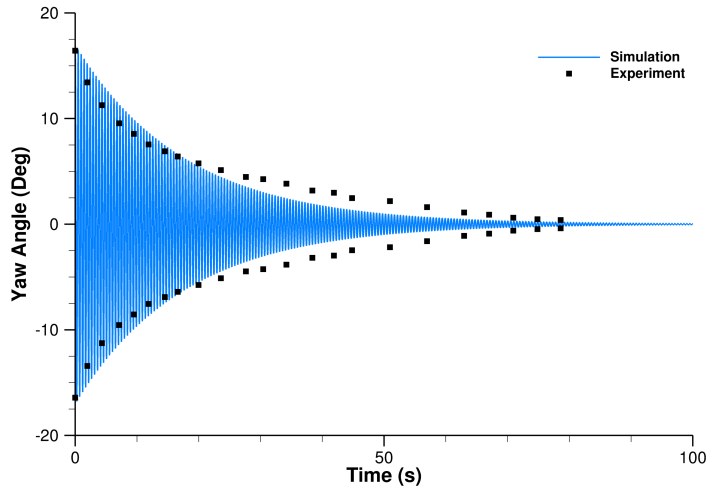
Figure 4.3: Wind-off yaw angle response.

4.2 The Coupled System

For the coupled system, a feedback loop is added to return the angular yaw rate to the CFD simulation as shown in Figure 4.4.

The data exchange between the CFD code and the dynamics model is handled via a Level-2 MATLAB S-Function and Javascript coding. This S-Function controls the opening of a port over which data is sent back and forth. The actual transfer is performed by a collection of Java macros as both Simulink and Star-CCM+ can be controlled using Java APIs. The procedure of connecting the two simulations and the data exchange is described below.

1. Initialise CFD simulation
2. Initialise and run Simulink model
3. Port opened with specified hostname and number
4. Run connector macro in Star-CCM+ and connect to open port
5. Yaw rate and solution time values sent from Simulink
6. CFD solution advanced one time-step
7. Aerodynamic yaw moment value sent from Star-CCM+
8. Data received by Simulink and simulation advanced one time-step
9. Step 5–8 repeated automatically
10. Finish time reached and port closed
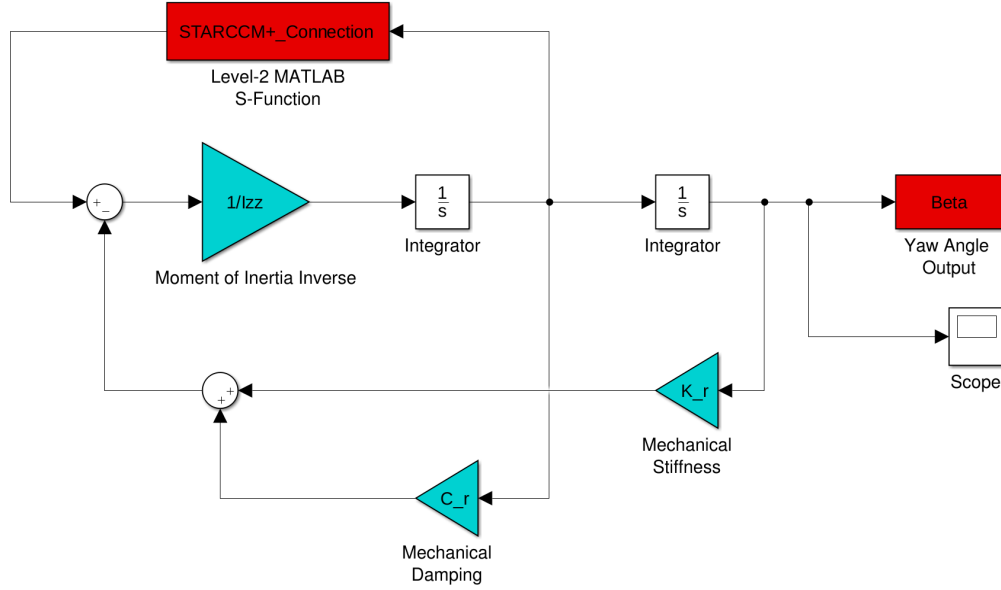
Figure 4.4: Coupled model of spring equation.

This coupled model has been used for the wind-on simulations, which were conducted at wind speeds of 10, 20 and 40 m/s or reduced frequencies of 0.79, 0.39 and 0.20 based on the wind off natural frequency of the rig.

4.3 Computational Grid and Numerical Approach

The only difference between the experimental setups of Mansor [123] and Baden-Fuller [85] were the radii of the Davis body edges, 10mm for Mansor and 20mm for Baden-Fuller. However, the Baden-Fuller model has been used for these simulations so that the computational grid and boundary conditions can be taken directly from the previous case study. This will be taken into account when comparing to the experimental response. It was shown in the previous case study, that the choice of motion technique had a minimal effect on the resulting flow prediction, and the only difference was found in computational cost. For this reason the sliding grid approach containing approximately 16×10^6 polyhedral elements has been selected.

In order to determine the effect of the aerodynamic yaw moment on the body's motion,

a minimum simulated time of 10 seconds has been chosen based on preliminary analysis of the experimental results. It was found that this time window corresponds to approximately 20 oscillation periods when using the K5 spring, and should provide an adequate sample to determine the effect of any aerodynamic stiffness and damping on the body's yaw response. However, due to the now substantial length of the simulation, changes to the numerical methodology are required to obtain results in a practical time frame. A URANS methodology with $k - \omega$ SST turbulence modelling has been chosen for which the time step is increased by an order of magnitude to 2.5×10^{-4} seconds ($\Delta t U / L = 1.6 \times 10^{-2}$). The Simulink dynamics model was initialised with the same time step value and thus when running, the data exchange between the two simulations took place at every time step.

A URANS methodology was shown to provide an economical prediction of the flow around the Generic SUV geometry with the largest inaccuracies found in the prediction of the wheel wakes. As the Davis body is a more geometrically simplified vehicle design, this methodology should provide reasonable results. This assumption has been tested by repeating the 10Hz driven oscillation simulation of the previous case study using the URANS approach. Figure 4.5 shows a similar level of hysteresis in the front side force coefficient when compared to the DES methodology however, the rear contribution is clearly over predicted. Figure 4.6 shows that a larger leeward A pillar vortex and lower shedding frequency, keeps the vortex in place over the rear half of the body for longer, and is the source of the larger rear contribution. This may not be a significant issue for the free oscillation simulations as the maximum reduced frequency to be tested (0.79) is lower than the value at this driven frequency (0.98). In this instance, the benefits of reduction in computational cost outweigh the potential improvements in flow field accuracy due to the length of simulated time needed.

The initial yaw angle of the body was set to $\beta_0 = 17°$ in reproduction of the experiment and the flow was initialised using a steady-state RANS methodology followed by 10 convective flows units using URANS. Thus the flow is fully developed at this static yaw angle. It is unclear whether this is the correct approach, as the experimental yaw response data suggests that the body was displaced by an external force from 0° yaw angle up to 17° with the wind on. The rate of this displacement is not known, and may

in fact vary between tests, thus the flow field at the start of the oscillation ($\beta_0 = 17°$ yaw angle) may not be fully developed. This may contribute to or even cause, hysteresis of the flow.
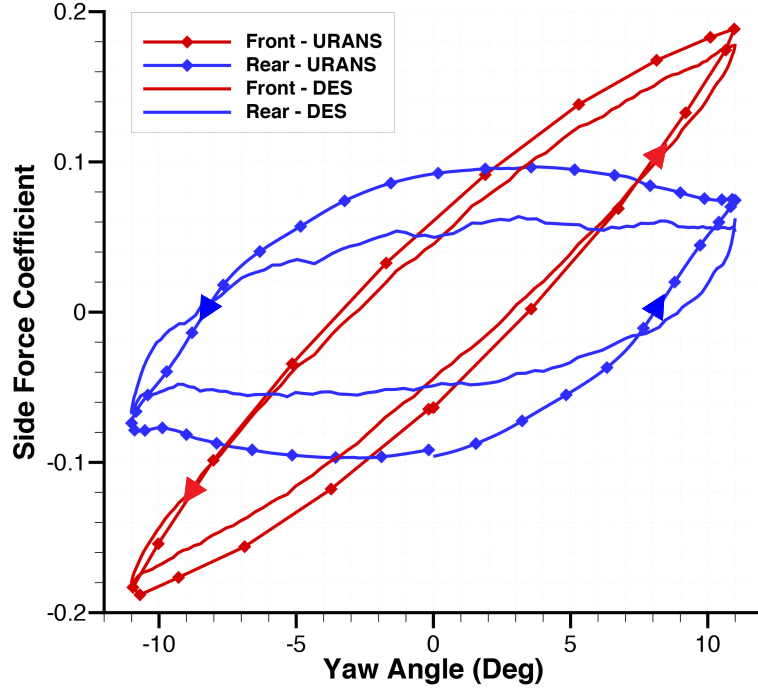
Figure 4.5: Side force coefficient URANS vs DES, 10Hz driven oscillation.

(a) URANS: Negative rotation.

(b) URANS: Positive rotation.

(c) DES: Negative rotation.

(d) DES: Positive rotation.
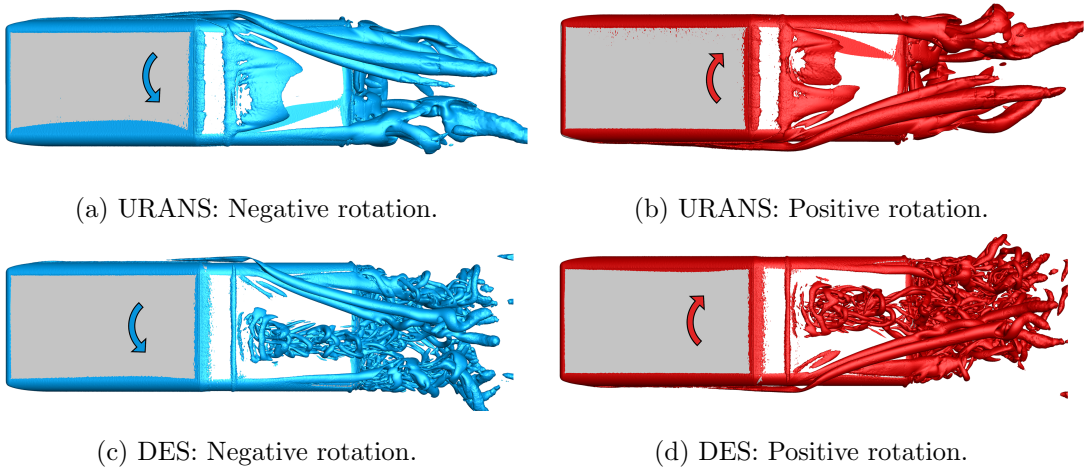
Figure 4.6: URANS vs DES at 0° yaw angle, 10Hz driven oscillation: Isosurfaces of Q criterion$=200\,000\,\mathrm{s}^{-2}$.

4.4 Results

The effect of aerodynamic stiffness and damping on the body's yaw angle response is clearly shown in Figure 4.7: by increasing the wind speed, the oscillation of the body is more heavily damped and the frequency of the oscillation is reduced.
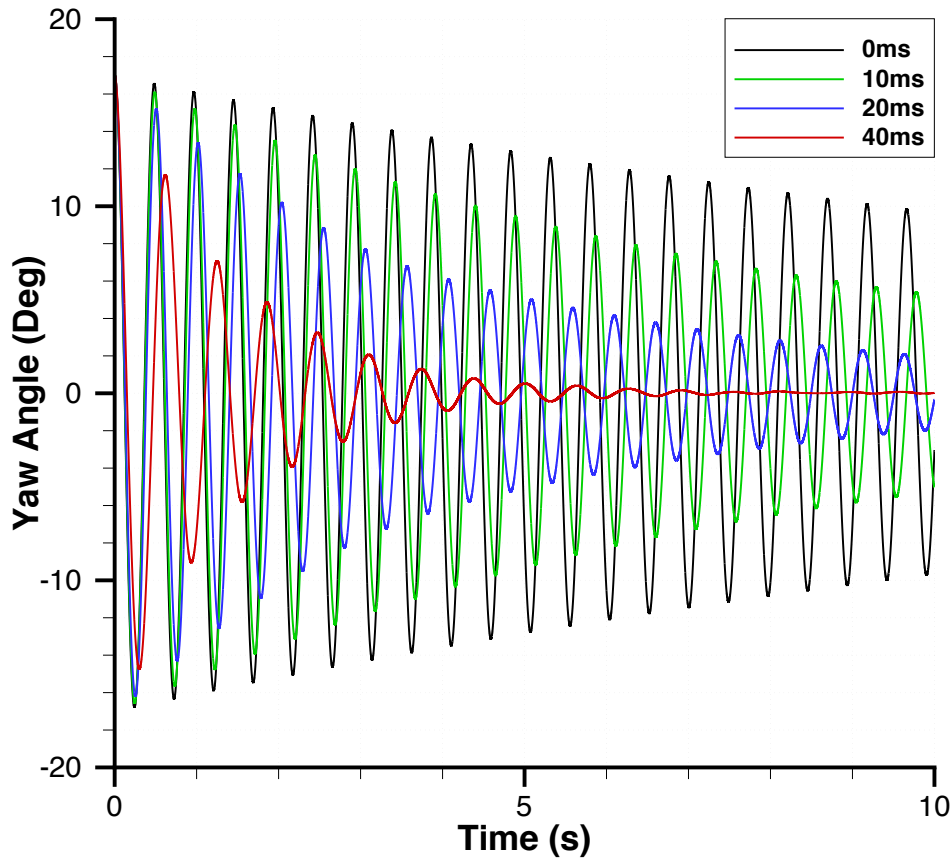
Figure 4.7: Simulated yaw angle response at different wind speeds.

The dominant frequency values for each response have been obtained using a Fast Fourier Transform (FFT) and presented as a damped frequency ratio $f_{d_{\mathrm{on}}}/f_{d_{\mathrm{off}}}$ (between wind on and wind off conditions) in Figure 4.8. The values have been plotted against reduced frequency, calculated using the definition of Sims-Williams [124]. The three simulation data points fit the experiment data curve exceptionally well. This curve was formed through testing of all ten springs at a full range of wind speeds, thus producing

a large span in reduced frequency values. The data trend implies that as reduced frequency is increased, the effect of aerodynamic stiffness on the body's rotation is reduced.
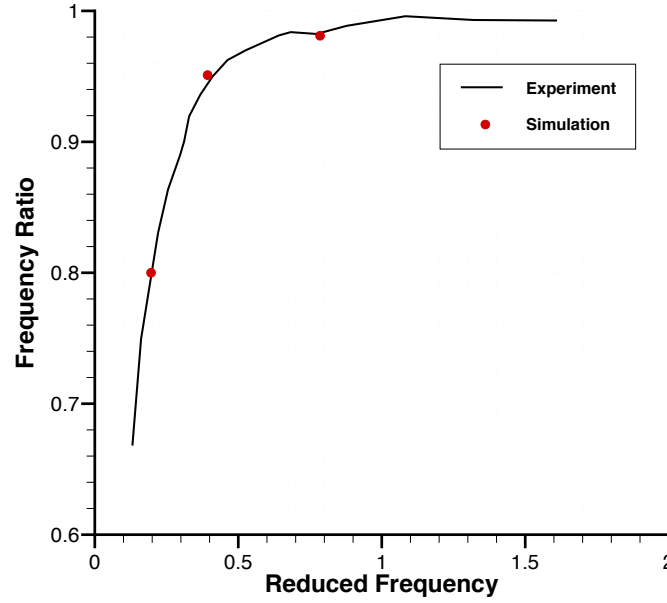
Figure 4.8: The effect of reduced frequency on the damped frequency ratio $f_{d_{\text{on}}}/f_{d_{\text{off}}}$.

Stiffness can be defined as a force which acts to oppose a displacement, whereas damping is a force which acts to oppose a motion. Thus the aerodynamic force can be decomposed into a stiffness and damping component. These components will have an opposite sign to the mechanical components, for example, when the model is at a given yaw angle, the mechanical spring stiffness will act in a direction to return the model to its initial orientation, whereas the aerodynamic stiffness will act to increase the yaw displacement.

The reduction in aerodynamic stiffness and reduced frequency increases suggests a shift, or hysteresis in the aerodynamic yaw moment. Figure 4.9 shows the yaw angle displacement along with the aerodynamic yaw moment for 10 and 40 m/s wind speeds. Although due to the scaling, Figure 4.9 does not clearly show any delay between the responses at either speed, cross correlation of the signals reveal a phase angle shift between the aerodynamics and displacement of approximately 12° for a wind speed of

$10\,\mathrm{m/s}$ and $0°$ for $40\,\mathrm{m/s}$. Thus, the result follows the principle of aerodynamic stiffness. The result is also consistent with the data collected by Sims-Williams [124], as the values of reduced frequency fall within the range where the aerodynamics move from a quasi-steady to an unsteady behaviour.

It has already been shown that at high reduced frequencies, there is a hysteresis in the aerodynamic yaw moment. As the velocity and displacement responses are already $90°$ out of phase, this hysteresis increases the phase angle between the yaw moment and velocity response further and moves closer towards the anti-phase state, as shown in Figure 4.10. Therefore, it can be expected that at high reduced frequencies, a reduction in aerodynamic damping will exist. This is the case as already shown in Figure 4.7, where for the same spring properties, a decrease in wind speed and thus increase in reduced frequency, lowers the total damping of the system.

In contrast to the experimental results shown in Figure 4.11, self-sustained oscillation of the body is not found at the higher wind speed. A self-sustained oscillation implies that there is no damping acting on the system or in other words, the aerodynamic damping is equal in magnitude to, and thus cancels out, the mechanical damping. The reason this does not occur in the simulations is unknown, however, some possible explanations are made. The smaller model edge radii of 10mm in comparison to the simulation's 20mm, may introduce a stronger sensitivity to Reynolds number. This may effect the formation of the pillar vortices which have been shown to have a dominant influence on the aerodynamic yaw moment and any hysteresis in this load. Alternatively, the increase in wind speed and resulting increase in drag force may introduce additional mechanical damping into the system. More specifically, the increase in load on the supporting shaft may increase the friction on the bearings. The value of mechanical damping used in the simulations was obtained from the wind-off response, thus any change to this value caused by the increase in wind speed is not accounted for. One final explanation may concern the accuracy of the turbulence model. The self-sustained oscillation was found to exist even with no initial body displacement. This suggests that the oscillation is driven by an unsteady vortex shedding from either side of the body which the current $k - \omega$ SST turbulence model and larger time step value may be unable to resolve.

116
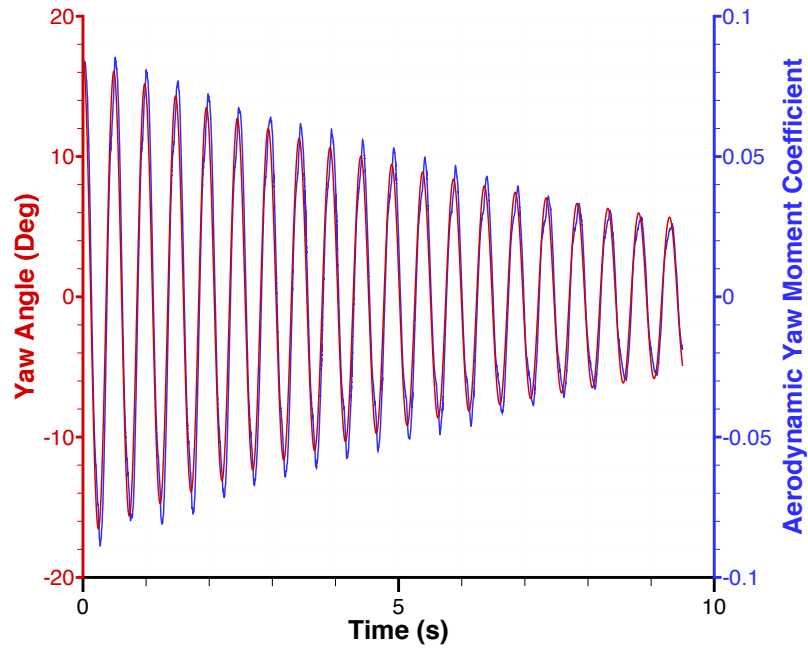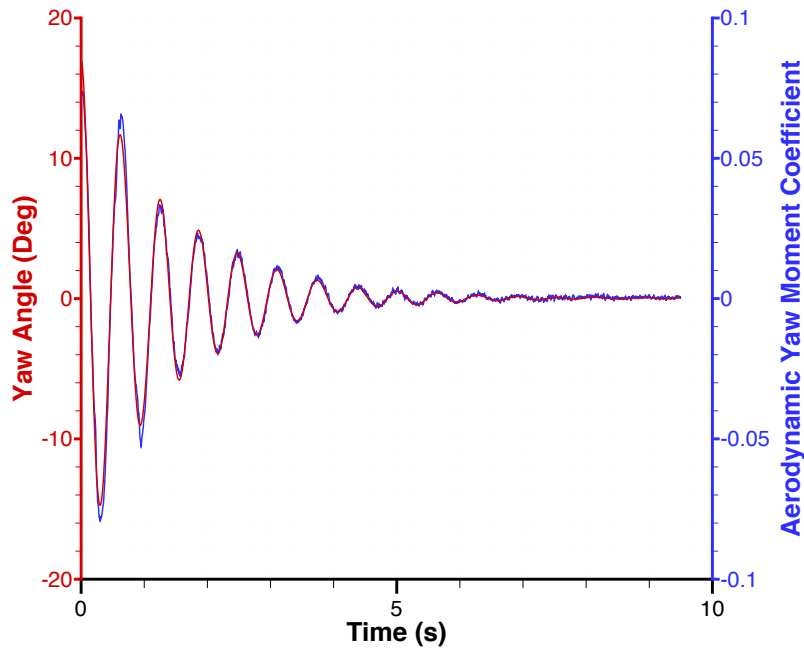
(a) $10 \, \mathrm{m/s}$

(b) $40 \, \mathrm{m/s}$

Figure 4.9: Hysteresis of the aerodynamic yaw moment with respect to angular displacement for different wind speeds.
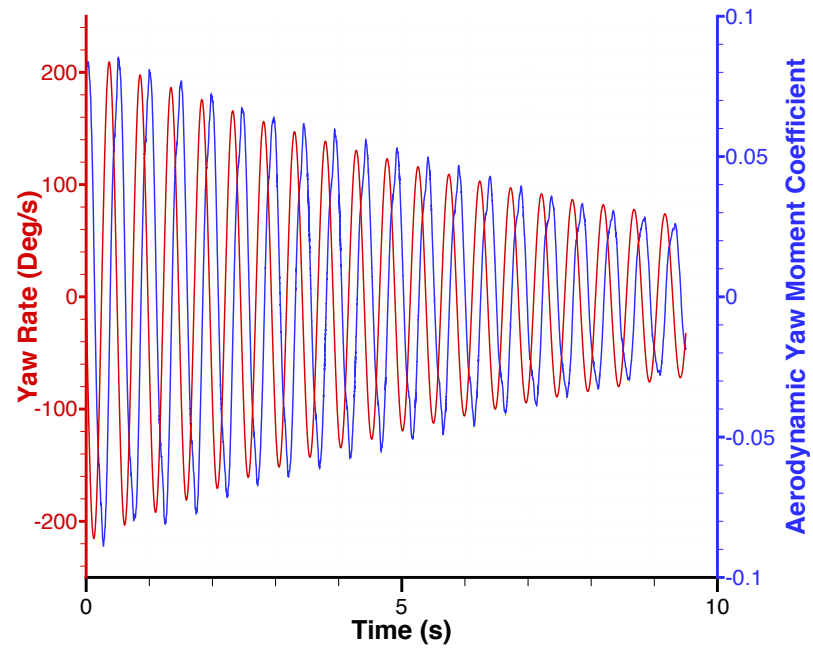
(a) $10 \, \text{m/s}$
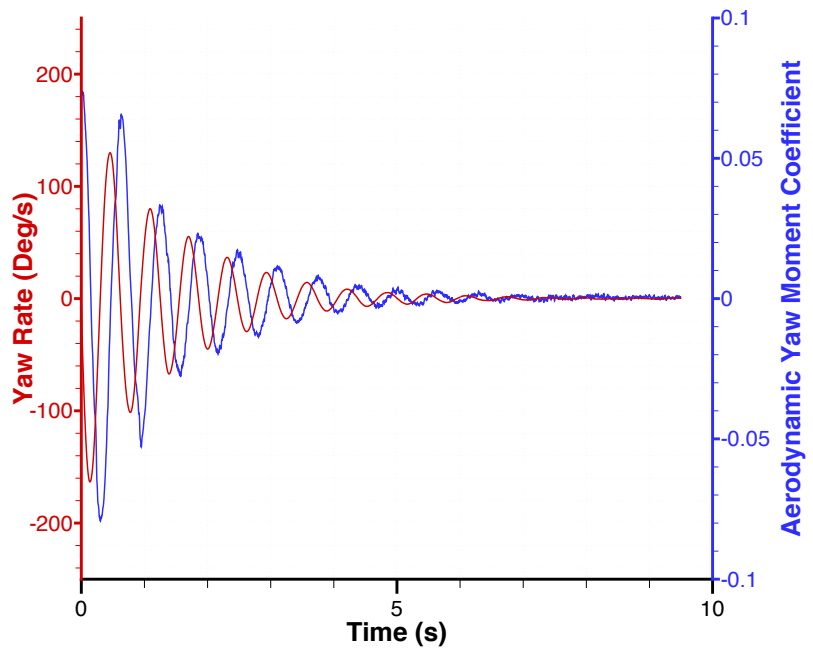
(b) $40 \, \text{m/s}$

Figure 4.10: Hysteresis of the aerodynamic yaw moment with respect to angular velocity for different wind speeds.

118
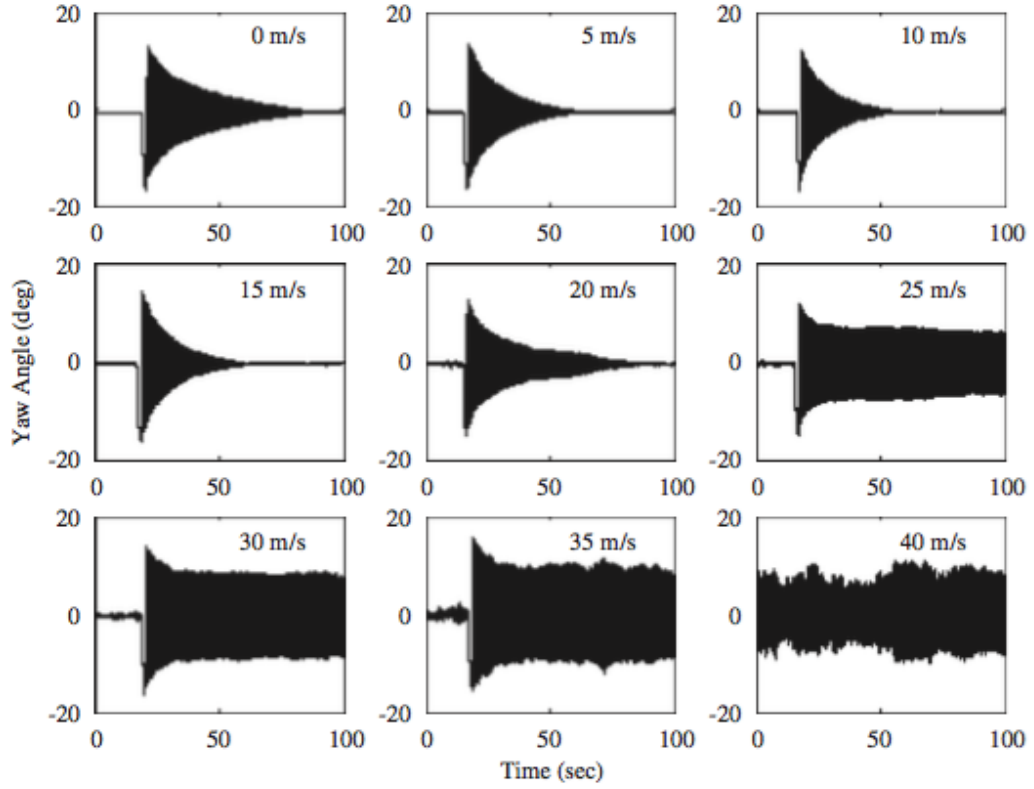
Figure 4.11: Experiment yaw angle response at different wind speeds [123].

4.5 Summary

Despite the lack of self-sustained oscillation, these results clearly demonstrate the effectiveness of the proposed fully coupled system for simulating aerodynamically driven motions. As originally intended, aerodynamic data is given to a dynamics model which returns positional data in a continuous closed-loop cycle. For the current simulations, the rate at which data can be transferred appears to have a negligible effect on the total expense when compared to a single, moving geometry, CFD simulation. As a result, this underlying coupling mechanism can be applied to more complex motions containing multiple degrees of freedom and influence by more aerodynamic loading components.

A REALISTIC ROAD VEHICLE IN A REAL WORLD ENVIRONMENT

Contents

5.1 Introduction

The natural wind contains both shear and turbulent effects as shown in Chapter 1, conditions which are rarely included when assessing a vehicle's aerodynamic performance. The main reason for this is this difficulty in generating such conditions during physical testing. On road tests rely on the desired conditions occurring naturally, and when they do, limited apparatus prevents detailed measurements of both the natural wind's behaviour and the effect on the flow around the vehicle. On the other hand, wind tunnel tests offer a degree of control and repeatability over the upstream conditions whilst also allowing detailed capture of the flow and accurate force measurements. Despite these benefits, tests are often limited in the magnitude of flow unsteadiness that can be generated and are unable to produce the levels of shear in the natural wind. For this reason, such facilities cannot be used for all conditions experienced on the road.

It was shown in Chapter 1 that computational simulation removes many of these physical restrictions imposed when studying the effect of a real world environment on a vehicle's aerodynamics. Time dependent boundary functions can be used to generate an infinite number of potential flow conditions and thus are a much more appealing method of assessing the effects of a real world environment on a road vehicle.

The effects of realistic turbulence levels on a vehicle's aerodynamics have been discussed previously, where it was shown that added turbulence leads to more mixing in the wheel and base wakes. This increase in mixing lowers the pressure within these structures and ultimately increases the drag. On the other hand the effect of shear is relatively unknown. This is surprising given the ease in which a velocity profile can be implemented at the boundaries of a CFD domain. Furthermore, the effect of both shear and turbulence together, thus providing the closest representation of the natural wind, has yet to be determined. For these reasons, a computational investigation to determine the effects of shear and turbulence in the natural wind on a vehicle's aerodynamics is undertaken here.

5.2 Simulation Approach

The vehicle geometry used for these simulations is the full-scale DrivAer model as first presented by Heft et al. [127]. This geometry can take three vehicle forms through interchangeable rear ends. Due to the benefits this can provide in the grid generation process, both the estate and fastback variants have been selected for use in this study. Testing two different vehicle types has a more purposeful benefit, as it helps to identify any effects and conclusions that may be specific to that class of vehicle. It is understood that this could be improved further by widening the range of geometries, as even with different rear end geometries, the DrivAer model maintains the same characteristic dimensions such as length, width and height, the latter of which may be most important for wind shear. The model is a closed design with no internal cooling flow, features a smooth underbody, side mirrors, with non-rotating wheels and treadless tyres. All tyres have been sliced at a height of 10 mm to produce an approximate contact patch and these flat surfaces rest on the fixed ground of the domain. The geometry, in both forms,

(a) Estate

(b) Fastback
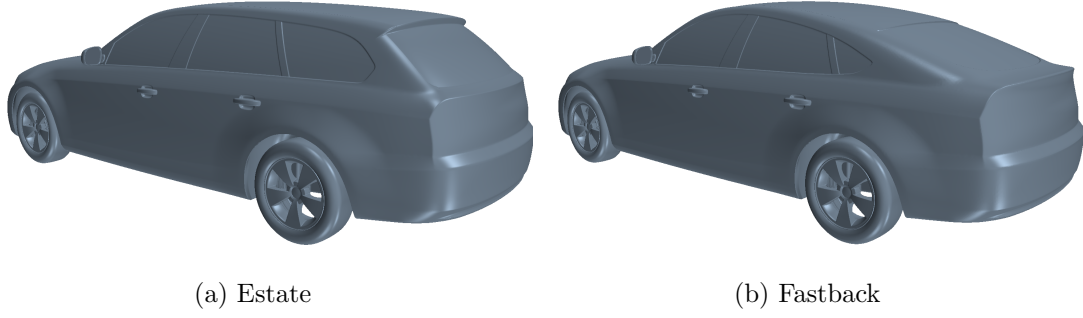
Figure 5.1: The DrivAer model.

Table 5.1: DrivAer model dimensions.

Length (**L**)	$4.613\,\mathrm{m}$
Width	$1.753\,\mathrm{m}$
Height	$1.418\,\mathrm{m}$
Wheelbase	$2.786\,\mathrm{m}$
Frontal Area (**A**)	$2.168\,\mathrm{m}^2$
Re (**L**, $27.8\,\mathrm{m/s}$)	8.9×10^6

is shown in Figure 5.1 with Table 5.1 providing some of the key dimensions. Initially, the effect of shear alone without any turbulence is investigated, thus two gust profiles are required: with and without shear. Without shear, a wind speed of $4.9\,\mathrm{m/s}$, constant with height, is applied perpendicular to the vehicle's path. When combined with a vehicle speed of $27.8\,\mathrm{m/s}$ ($100\,\mathrm{km/h}$) a resultant flow yaw angle of $10°$ with a magnitude of $28.2\,\mathrm{m/s}$ is generated. As shown previously in Figure 1.9, this yaw angle falls towards the upper limit that a vehicle will typically experience on the road. For the shear profile, an adaptation of the power law, Equation 5.1, is used with the gradient velocity v_g taking the value of $4.9\,\mathrm{m/s}$ and the roughness exponent, $\alpha = 0.16$ describing open, smooth terrain. For a fair comparison, the same mass flow should act over the side area of the vehicle. Thus, the height at which the gradient wind acts is calculated by equating the flow rate equation, as shown in Equation 5.1. It follows that the gradient wind velocity of $4.9\,\mathrm{m/s}$ should act at a height of $z = 0.561\,\mathrm{m}$ or 39.5% of the height of the car.

$$\overbrace{Q = av = 4.61 \times 1.418 \times 4.9}^{\text{Without Shear}} = \overbrace{4.61 v_g \left(\frac{z}{z_g} \right)^{\alpha}}^{\text{With Shear}} = av = Q$$

$$32.031 = 22.589 \int_0^{1.418} \left(\frac{z}{z_g} \right)^{0.16} \mathrm{d}z$$

$$= 19.473 \left[\frac{z^{1.16}}{z_g^{0.16}} \right]_0^{1.418}$$

$$= \frac{29.2}{z_g^{0.16}}$$

$$z_g = 0.561 \, \mathrm{m} \tag{5.1}$$

The two v velocity profiles are shown in Figure 5.2 where it can be seen that without shear, the velocity at the roof of the car is approximately 0.862 times the value with shear. When combined with the vehicle's velocity vector, the resultant three dimensional flow velocity is shown in Figure 5.3. As already stated, without shear, the wind generates a constant resultant flow velocity vector, however, with shear, the angle and magnitude of this vector increases with height.
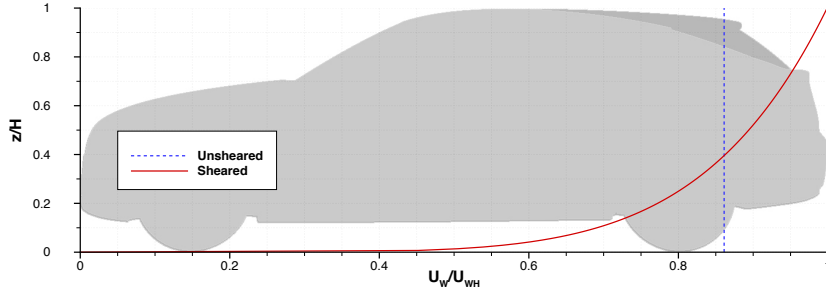
Figure 5.2: Sheared and unsheared lateral velocity profiles.

In the next stage of this study, the effect of turbulence on top of shear is investigated. Turbulence is introduced into the flow using the synthetic eddy method (SEM) as proposed by Jarrin et al. [128]. The desired intensity and length scale values of these turbulent structures are taken from literature and represent typical on road conditions as shown in Figure 1.12, an intensity and length scale seen by the vehicle of 8% and 2 m respectively. The intensity at the inlet is assumed to be homogeneous across all three components of velocity, this disagrees with literature, but without measured values of
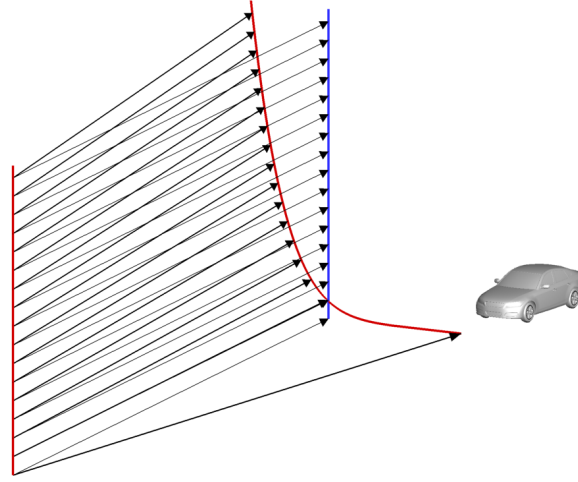
Figure 5.3: Sheared and unsheared resultant velocity profiles.

the Reynolds stress tensor obtained from experiment this uniformity is unavoidable in the selected code. An instantaneous snapshot of the flow with this turbulence is shown in Figure 5.4 and the variation in the three components of velocity one car length upstream of the vehicle and at roof height are shown in Figure 5.5. From this velocity distribution, the actual turbulence intensity experienced by the vehicle can be calculated, $I_u = 8.0\%$, $I_v = 6.5\%$ and $I_w = 5.1\%$. Clearly the turbulence is no longer homogenous as defined at the inlet due to dissipation of the velocity through the coarse grid upstream of the vehicle and the presence of the ground. As shown in Equation 5.2, the ratio between the components matches the theoretically determined ratio more favourably than the experimentally measured values.

$$\sigma_u = \sigma_v = \sigma_w = \overbrace{1 : 0.8 : 0.5}^{\text{Theoretical [1.11]}}$$
$$= \overbrace{1 : 1.01 : 0.61}^{\text{Experimental [1.20]}}$$
$$= \overbrace{1 : 0.81 : 0.64}^{\text{Simulated}} . \tag{5.2}$$
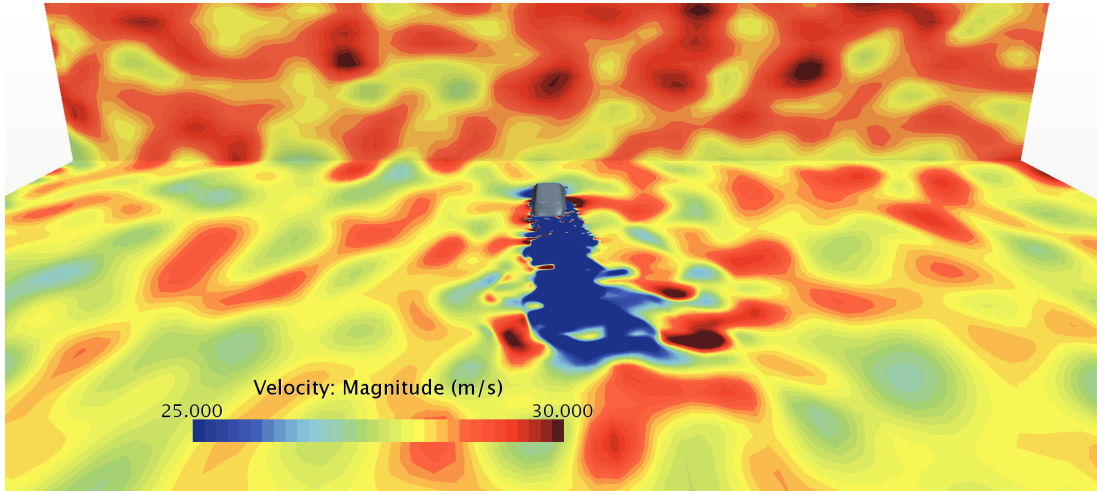
Figure 5.4: Simulated turbulent and sheared flow field.
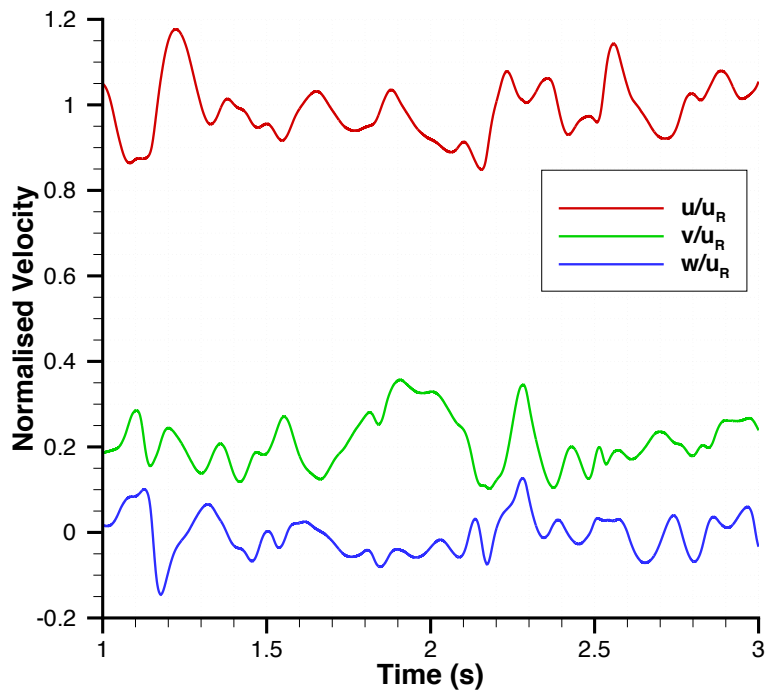
Figure 5.5: Turbulent velocity field measured one car length upstream at roof height.

126

5.3   Computational Grid and Boundary Conditions

For each vehicle type, the full-scale geometry is positioned in a computational domain of size x=18**L**, y=13**L**, z=3**L** at a distance of 5**L** and 6**L** from the primary and secondary inlets respectively, as shown in Figure 5.6.
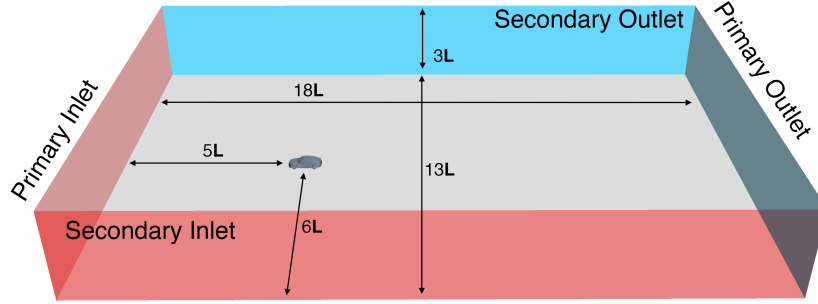
Figure 5.6: DrivAer model computational domain.

On the majority of the vehicle's surface, grid elements of size 0.001**L** are used, a value taken from the SUV simulations of Chapter 2. However, due to the more realistic, and thus more geometrically complex model, smaller elements of size 0.0001**L** are required in certain locations in order to maintain a reasonable quality of highly curved, critical features such as the A and C pillars. Figure 5.7 shows a section of the surface grid around these features. To within a small range, the total number of surface elements for the estate and fastback geometries are consistent, approximately 3.6×10^6.

(a) Front left wheel   (b) A pillar and side mirror
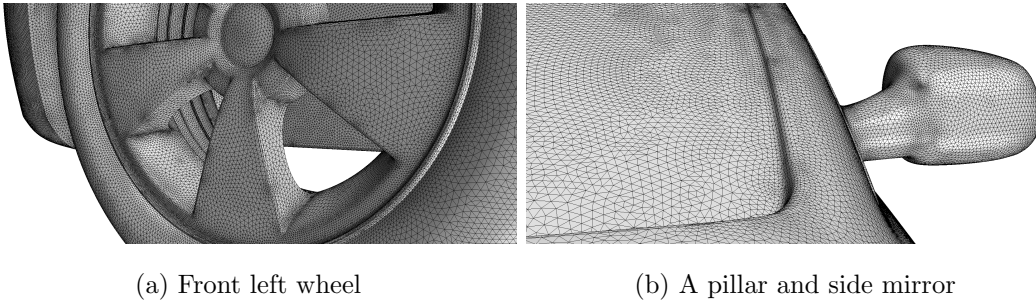
Figure 5.7: Surface grid of the DrivAer model.

Extruded from the surface, 8 prism layers to a total thickness of 5 mm (0.001**L**) with a ratio of 1.2 between the layers are used to capture the boundary layer. A non-dimensional near wall spacing value $y^+ < 1$ over the entire surface ensures that the

boundary layer is resolved and not modelled using wall functions. Two hexahedral volume grids are generated using identical parameters: elements grow uniformly in size from the outer prism layer into a region of fixed 10 mm (0.002**L**) sized elements. This region has been shaped in order to capture the yawed wake caused by the crosswind and stretches 0.5**L** downstream and 0.3**L** to the leeward size of the vehicle. This first refinement region is enclosed by a second of fixed sized 80 mm (0.017**L**) elements. This region stretches much further downstream to a length of 2.7**L** and out to leeward side by a distance of 1**L**. Away from this second refinement, grid elements grow uniformly up to a maximum size of 640 mm (0.14**L**). These refinement regions are shown in Figure 5.8. As a result, the total number of volume elements is approximately 69×10^6 for both grids.

(a) Estate centreline

(b) Fastback centreline

(c) Horizontal cut at axle height

(d) Transverse cut through wheelbase centre
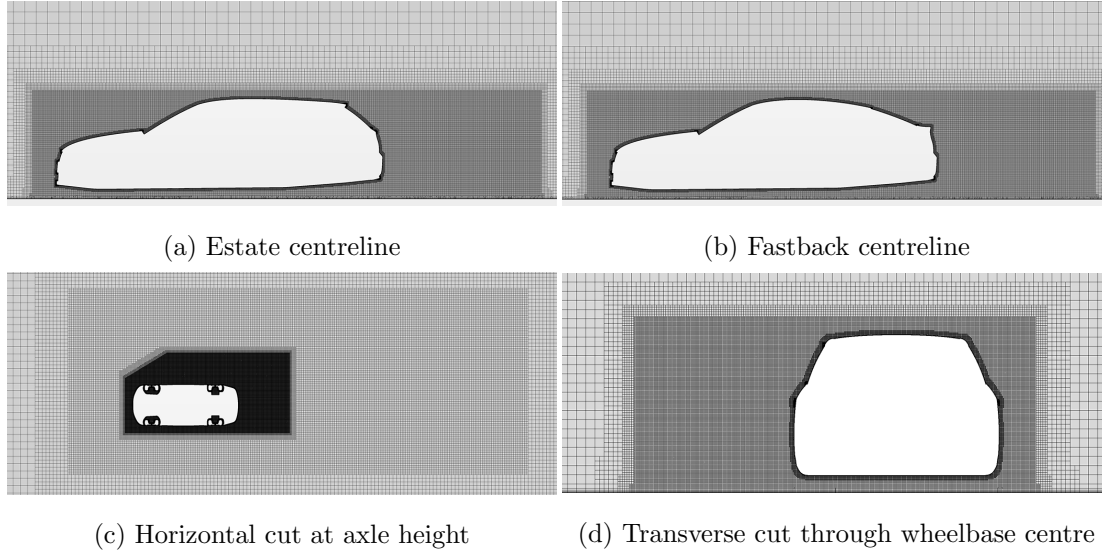
Figure 5.8: Volume grids around the DrivAer estate and fastback geometries.

5.4 Numerical Approach

The numerical method used for these simulations is taken from the practices used in the previous SUV and Davis model simulations. A segregated, incompressible, finite volume, semi-implicit, pressure based solver is chosen for all simulations with a hybrid 2nd order upwind/bounded central-differencing convection scheme. Turbulence is modelled with the IDDES variant of the Spalart-Allmaras Detached-Eddy model. Figure

5.9 shows the locations where the solver switches from RANS to LES: RANS in the boundary layer and LES away from the vehicle. Consequently, an LES solver is used in the coarse grid upstream of the vehicle, which will limit the scales of turbulence that can be resolved when artificial turbulence is introduced at the inlet. A second-order temporal scheme limits the numerical dissipation of the sheared and unsheared velocity profiles and time-step of 1×10^{-4} seconds (non-dimensional $\Delta t U_R / L = 6 \times 10^{-4}$ ensures a Courant number below one within the wake of the vehicle. Five inner iterations per time-step ensure consistent convergence of the residuals. All CFD simulations are carried out using Star-CCM+ v10.04.009 from CD-Adapco.
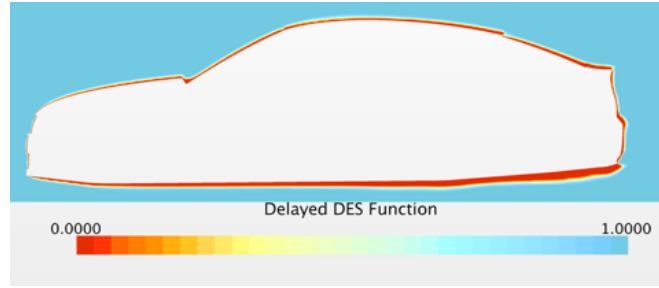
Figure 5.9: Delayed DES Function f_d ($f_d = 0$ RANS treatment, $f_d = 1$ LES treatment).

This numerical method is in close agreement with that used by Ashton and Revell [129] and Ashton et al. [82] in their determination of an appropriate numerical method to simulate the flow around the estate and fastback variants of the DrivAer model. They showed that a DES method offered considerable improvements over RANS based methods in terms of force coefficients wake flow field prediction. The main differences from their simulation setup are the smaller time-step value and larger face count on the DrivAer surface.

All simulations were initialised using a steady state RANS solver, before switching to DES for a settling period of 1 second or 6 convective flow units; ($6 \times L/U_R$). The simulations were then allowed to run for 2 seconds (12 convective flow units) during which the flow field was averaged. Ideally, this averaging interval would be longer but due the number of simulations in this study, computational resources were limited. One 3 second simulation, with or without shear, took approximately 58 hours to run in parallel on 320 cores of the HPC-Midlands Facility, UK. When turbulence was added

using the SEM method, this wall clock time increased to approximately 108 hours due to an increase in the time per iteration. This highlights the significant impact on computational cost when including synthetic turbulence using this method.

5.5 Results

5.5.1 Sheared Wind Profile

The effects of a sheared wind profile are shown through force and moment coefficients in Tables 5.2 and 5.3. The values are presented alongside those at 0° yaw angle, without a wind input, to show the effect of wind in general. In addition, these values can be compared to a number of experiments that have been conducted at zero yaw and a measure of simulation accuracy can be determined. The reference velocity used in the coefficient calculations is taken as the resultant of the vehicle and wind velocities, U_R, as shown in Equation 1.18, however, it is unclear whether this is the appropriate quantity to use. The forces and moments act in the body coordinate system, (aerodynamic drag opposing the vehicle's forward direction) and hence there is an argument that the reference velocity should be the velocity of the vehicle U_{veh} alone. The coefficient values using this alternative reference velocity are also presented in Tables 5.2 and 5.3, and show increases of up to 13 counts in some cases. Although this does not affect the overall conclusions as all values are calculated using the same reference velocity, in other applications such as emissions calculations, the value and hence definition of drag coefficient is especially important. In addition, at larger yaw angles where the difference between U_R and U_{veh} is much greater, the variation between these values will be even larger.

Table 5.2: Estate force and moment coefficients (reference velocity = U_R and [U_veh]).

Estate	0° Yaw	10° Yaw		
		Unsheared	Sheared	Sheared and Turbulent
C_D	0.309 [0.309]	0.358 [0.368]	0.357 [0.368]	0.372 [0.384]
C_L	-0.166 [-0.166]	-0.015 [-0.016]	0.012 [0.012]	-0.0002 [-0.0002]
C_{LF}/C_{LR}	-0.111/0.055 [-0.111/0.055]	-0.082/0.067 [-0.084/0.068]	-0.078/0.090 [-0.081/0.093]	-0.090/0.090 [-0.092/0.092]
C_Y	0 [0]	0.411 [0.423]	0.409 [0.422]	0.393 [0.406]
C_{MX}	0 [0]	0.056 [0.058]	0.056 [0.058]	0.053 [0.055]
C_{MZ}	0 [0]	0.077 [0.079]	0.077 [0.079]	0.074 [0.076]

Table 5.3: Fastback force and moment coefficients (reference velocity = U_R and [U_veh]).

Fastback	0° Yaw	10° Yaw		
		Unsheared	Sheared	Sheared and Turbulent
C_D	0.257 [0.257]	0.333 [0.343]	0.335 [0.345]	0.338 [0.348]
C_L	-0.020 [-0.020]	0.056 [0.058]	0.071 [0.073]	0.032 [0.033]
C_{LF}/C_{LR}	-0.081/0.061 [-0.081/0.061]	-0.051/0.107 [-0.052/0.110]	-0.042/0.114 [-0.044/0.117]	-0.060/0.092 [-0.062/0.095]
C_Y	0 [0]	0.351 [0.362]	0.354 [0.365]	0.337 [0.348]
C_{MX}	0 [0]	0.048 [0.050]	0.049 [0.050]	0.045 [0.046]
C_{MZ}	0 [0]	0.096 [0.098]	0.093 [0.096]	0.092 [0.095]

For both vehicle types, a sheared wind profile has a minimal effect on the vehicle's force and moment coefficients, when compared to a constant velocity profile with the same

mass flow acting over the height of the vehicle. For the fastback, a sheared profile raises the drag by 2 counts, whereas for the estate, the drag reduces by a single count. The distributions of drag over the height of the vehicle are presented in Figures 5.10a and 5.10b, where the solid lines represent the front contribution to drag, and the dotted, the rear. The front distributions for the two vehicles are very similar, as could be expected for the identical front end geometry, and the sheared profile only appears to effect the drag generated over the lower portion of the front bumper. In addition, the distributions for the two yawed cases are the same as the zero yaw case, suggesting that the rise in drag which accompanies an increase in yaw angle is purely due to an increase is base drag, this is consistent with the claims of Kawamata et al [130].
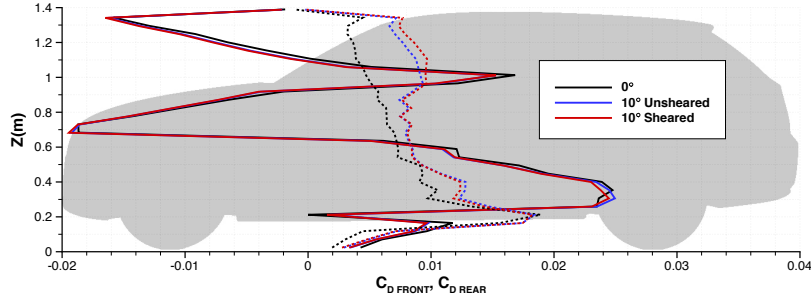
(a) Estate
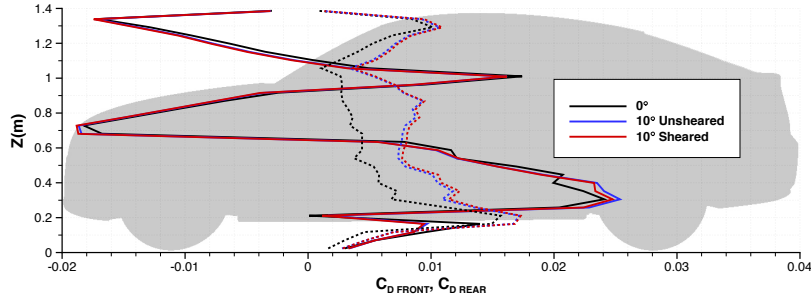
(b) Fastback

Figure 5.10: The effect of shear on drag coefficient distribution (Front - solid, Rear - dashed).

It is clear that the small differences in overall drag coefficient is caused by small variations in the rear distribution. For the fastback, the drag with sheared profile is consistently higher over the height of the vehicle, thus reflecting the overall increase of total drag. In contrast, the rear distribution over the estate is much more balanced,

undershooting the unsheared distribution at low heights and overshooting towards the roof. This behaviour is consistent with the magnitude of the wind velocity which is a function of height and a result of the estate's larger lateral area over which this wind acts.

In addition to drag, side force and yaw moment are important quantities, especially in crosswind flows, as they have a direct impact on the handling qualities of a vehicle. A vehicle's sensitivity to crosswinds is usually determined using the stationary gradients of side force coefficient $dC_Y/d\beta$ and yaw moment coefficient $dC_{MZ}/d\beta$, with the latter deemed most important as stated by Stoll et al. [59]. These values have been calculated assuming a linear relationship between the coefficients and yaw angle over the range $0°$ to $10°$. A larger side force coefficient gradient of the estate, $0.041/°$ compared to $0.035/°$ of the fastback, is a result of a larger rear lateral area and thus greater rear side force contribution. Figures 5.11a and 5.11b show the distribution of side force coefficient along the length of the vehicle and confirm this. The larger rear side force also has the effect of restoring the yaw moment and thus the yaw moment coefficient gradient of the estate is smaller than the fastback, $0.008/°$ compared to $0.010/°$. As a vehicle is defined to be less sensitive to crosswinds if the yaw response is small, these results suggest that the fastback will be judged more sensitive to crosswinds than the estate [59]

Stoll et al. [59] obtained very similar experimental values of the stationary side force and yaw moment coefficient gradients for the DrivAer estate geometry, $dC_Y/d\beta = 0.039/°$ and $dC_{MZ}/d\beta = 0.007/°$. These values were obtained from a wind tunnel yaw sweep, where the change in flow yaw angle was achieved by oscillating upstream airfoils rather than a secondary crosswind inlet or rotation of the model on a turntable. The high similarity of these values to those simulated places confidence in the computational values but also the linear assumption of the force coefficients over the yaw angle range. In addition to these results, Stoll et al. [59] also obtained values for the third DrivAer geometry variant, the notchback, $dC_Y/d\beta = 0.036/°$ and $dC_{MZ}/d\beta = 0.008/°$. These values imply that this vehicle type will be more sensitive to crosswinds than the estate, but not as susceptible as the fastback.
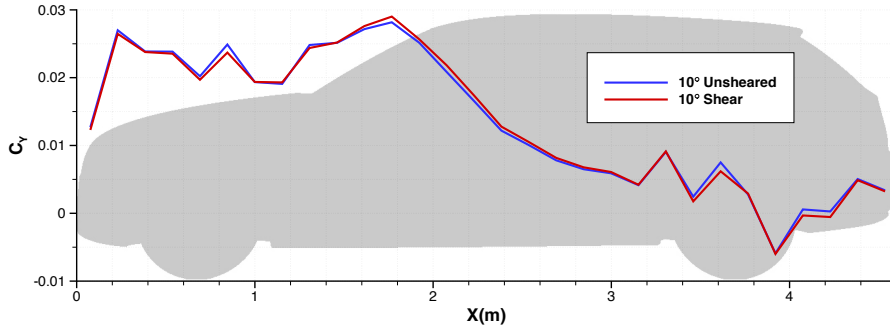
(a) Estate
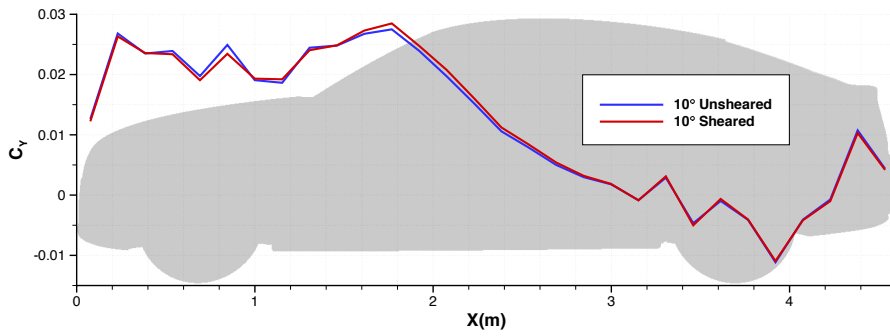
(b) Fastback

Figure 5.11: The effect of shear on side force coefficient distribution.

Figures 5.11a and 5.11b show that the majority of the contribution to the total side force contribution comes from the front half of the vehicle. This is due to the large pressure difference between the windward and leeward sides over this half of the vehicle. The maximum value for both vehicles occur over the A pillar, where a strong flow separation and low pressure on the leeward side is produced due to the high velocity yawed flow which accelerates over and across the windscreen.

Much like the drag coefficient, the effect of shear on the side force coefficient is small. For the estate, a sheared wind profile reduces the side force coefficient by just 2 counts, whereas for the fastback, shear increases the coefficient by 3 counts. Analysing the side force distributions, Figures 5.11a and 5.11b, the high similarity can be visualised. As expected, due the identical front end geometries, the front side force distributions of the estate and fastback are very similar. In the region of largest side force contribution, from the front of both vehicles up to the midpoint of the windscreen, a sheared profile

has very little effect on the side force. There is a slight difference in the distributions within the range of the front wheels due to the smaller velocity of the sheared profile which acts in the lower regions and to which the bottom halves of the wheels are exposed. This reduces the pressure acting on the wheels and hence lowers the side force in comparison to the unsheared case.

Over the passenger compartment and main section of the vehicle, the effect of shear is still minimal despite the higher velocity which acts over the upper 60% of the vehicle's height. Figures 5.12a and 5.12b show the lateral velocity distribution constrained to a transverse plane located at $x = 2\,\mathrm{m}$, close to the top of the windscreen. It can be seen that despite the large velocity variation of the sheared profile, the local velocity field around the vehicles are almost identical. As a result, the surface pressure distribution at this point, especially the pressures on the windward and leeward sides, shown in Figure 5.13, are very similar between the sheared and unsheared cases.

The minimal differences in front and rear side force distribution are reflected in the yaw moment coefficient values. For the estate, the slightly larger contributions without shear over the front wheels and over the rear balance out, resulting in a negligible impact on the final yaw moment coefficient value. However for the fastback, the same behaviour over the front, but identical distributions over the rear cause a slight increase in yaw moment coefficient, 3 counts, without shear.

So far, the magnitudes of the force coefficient variations have been small, a maximum of 3 counts, however these magnitudes increase for the lift coefficient. Tables 5.2 and 5.3 show how the lift coefficient with a sheared wind profile is much larger for both vehicle types, 27 counts for the estate and 15 counts for the fastback. In addition to side force, this force can have a large effect on the handling of the vehicle. As shown by Howell and Le Good [131], similar magnitudes in lift coefficient can influence the subjective performance of a vehicle during a high speed lane change manoeuvre. For the estate, the majority of the increase is sourced in the rear contribution (approximately 85% of the increase) whereas for the fastback the increase is much more even over both the front and rear. These increases can be more clearly identified in the lift distribution along the length of the vehicle, shown in Figures 5.14a and 5.14b.
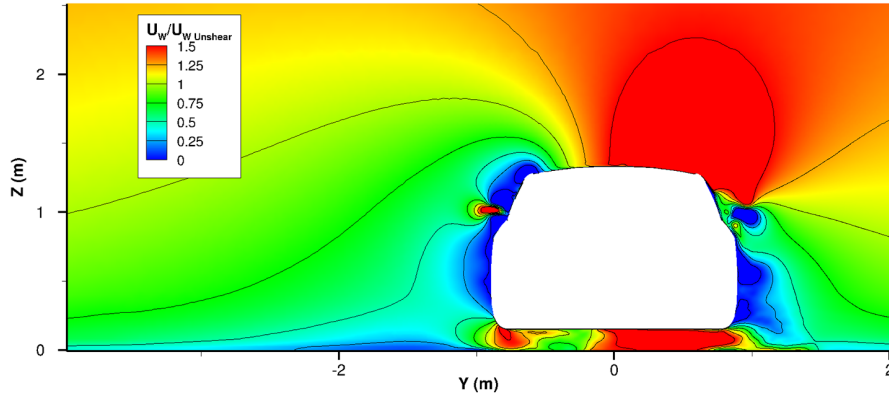
(a) Sheared
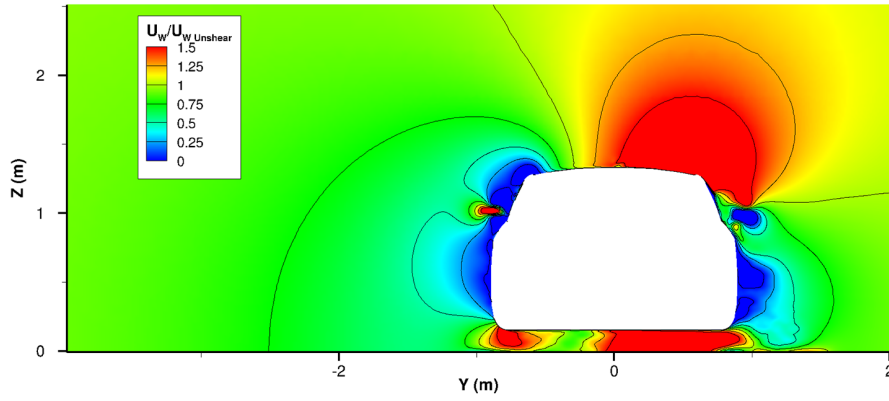
(b) Unsheared

Figure 5.12: Mean transverse velocity at $x = 2\,\mathrm{m}$ (Top of windscreen).

The increase in lift is a result of the lower velocity underneath the vehicle and thus higher pressure on the underbody, similarly a higher velocity over the roof results in a lower pressure on this surface. Evidence of this has been seen in Figure 5.13, which shows a slight variation in the suction strength over the roof and leeward A pillar. This trend continues downstream from the windscreen as indicated by the distributions shown in Figures 5.14a and 5.14b and results in a much more substantial impact on the total lift coefficient.
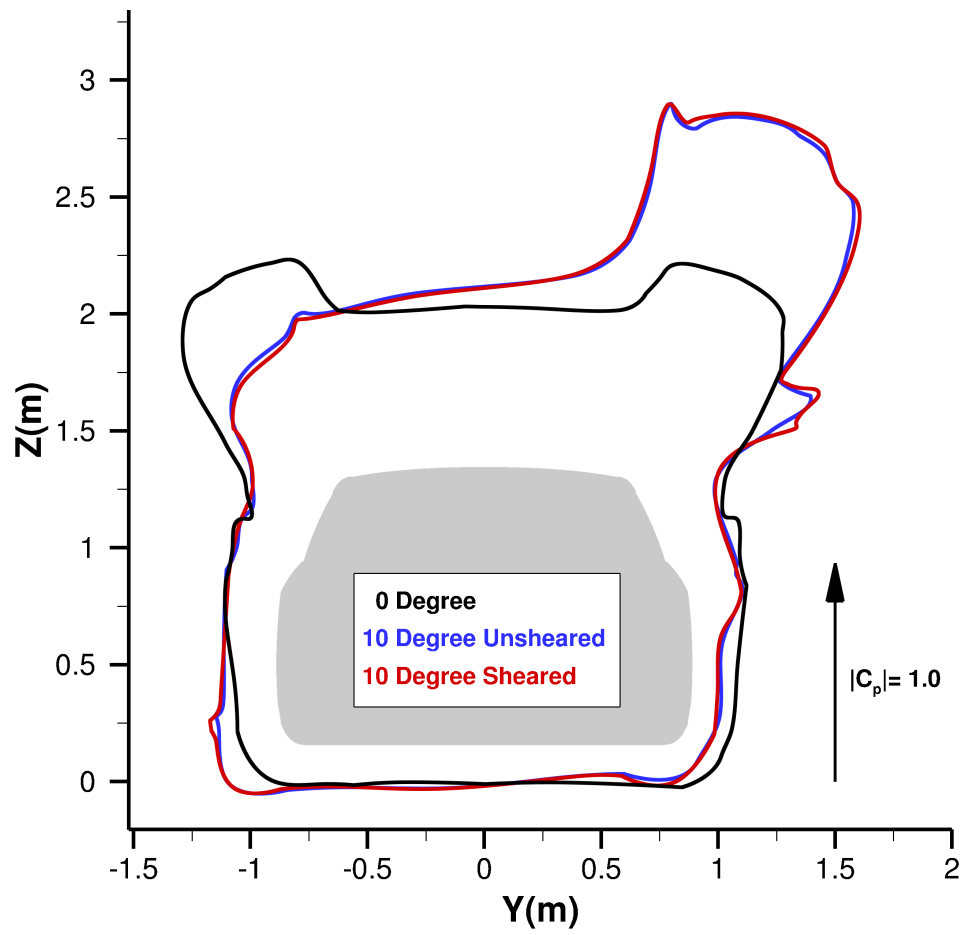
Figure 5.13: Fastback surface pressure distribution at $x = 2\,\mathrm{m}$.
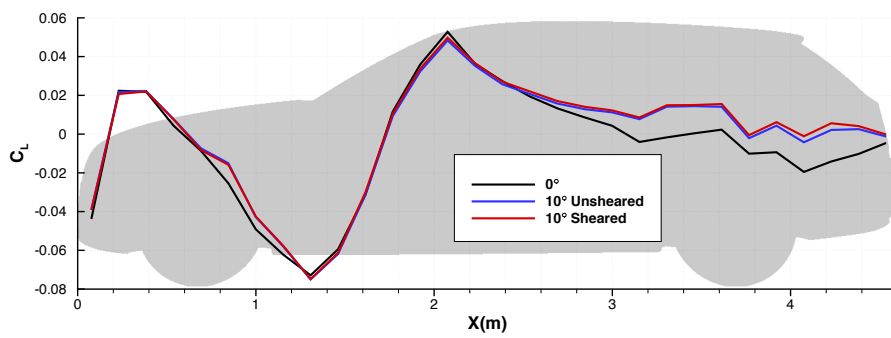
(a) Estate
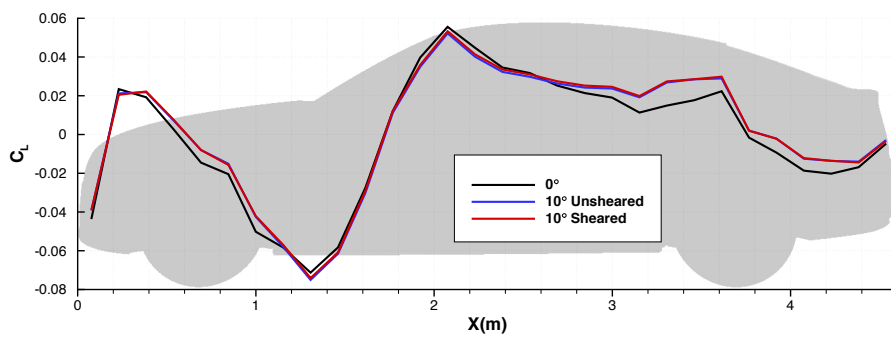
(b) Fastback

Figure 5.14: The effect of shear of lift force coefficient distribution.

5.5.2 Sheared Wind Profile with Turbulence

The effect of a sheared velocity wind profile with added turbulent structures, the sizes and strengths of which are typical of on road conditions, can be seen in Tables 5.2 and 5.3. For both vehicle types, these flow conditions cause the vehicle's side force coefficient to decrease, by 14 counts for the fastback and 18 counts for the estate. Figures 5.15a and 5.15b show the evolution of side force along the length of the two vehicles and Figures 5.16a and 5.16b show the delta of side force coefficient ΔC_Y between the turbulence and baseline cases. The majority of the decrease can be sourced over the front halves of the vehicles and as this portion of the geometry is identical between the two vehicle types, the profile of the delta curve in this region is maintained.

(a) Estate

(b) Fastback
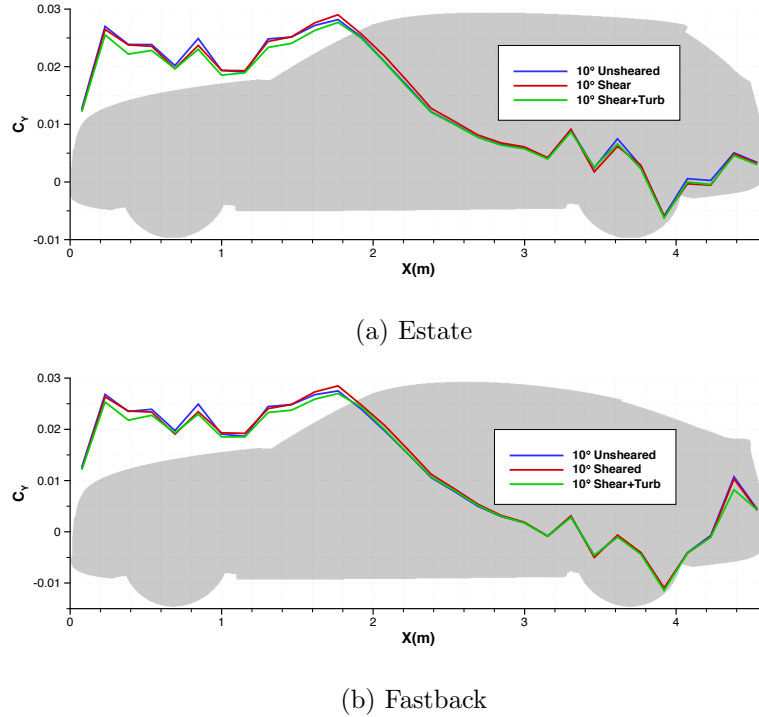
Figure 5.15: The effect of shear and turbulence on side coefficient distribution.

Isosurfaces of total pressure coefficient, $C_{p_{total}} \leq 0$, rendered by values of pressure coefficient C_p, provide a useful visualisation of the wake structures around the vehicle, Figures 5.17 and 5.18 and suggest that with added turbulence, the sizes of these structures are reduced. This is consistent with the work of Gaylard et al. [44, 45] and

(a) Estate

(b) Fastback
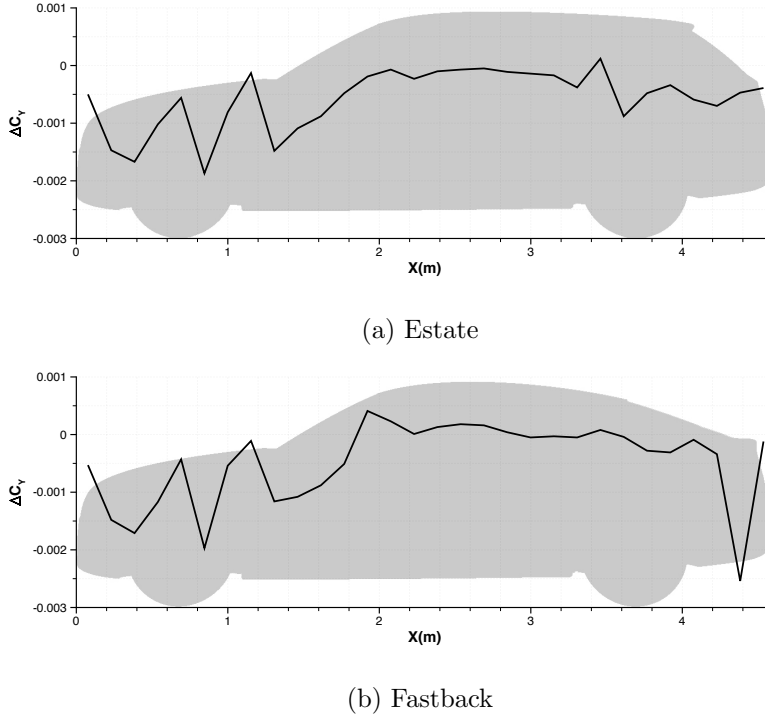
Figure 5.16: Delta of side coefficient $\Delta C_Y = C_{Y_{Shear+Turb}} - C_{Y_{Unsheared}}$.

D'Hooge et al. [46], who showed that turbulence intensity levels of up to 7% delays flow separation and thus reduces wake sizes. On first inspection, the large reduction in the size and length of the front wheel wakes, particularly that of the wheel on the windward side and the leeward A pillar vortex, appear to be responsible for the decrease in side force coefficient. However, analysing the flow around the front bumper at the height of the wheel axles $z = 0.32\,\mathrm{m}$, there is a suggestion that the flow yaw angle has reduced, Figure 5.19. An increase in the velocity around the windward corner and decrease around the leeward side can be identified in the contouring of lateral velocity, whilst the direction of the upstream streamlines indicate a reduction in yaw angle. Further evidence of this can be seen in the direction of the wheel wakes, Figures 5.17 and 5.18, which also appear to be more inline with the vehicle. This is a consequence of the short time averaging period which is unable to completely smooth out the turbulent structures and reproduce the exact sheared velocity profile over the entire domain. Therefore, without calculating and subjecting the vehicle to this lower yaw flow angle, or running the simulations for longer, it is unclear whether the reduction in side force coefficient is a result of the change in upstream conditions or a consequence of delayed

separation due to higher turbulence intensity levels.

Due to the reduction in side force coefficient and the location of this reduction towards the front of the vehicle, the yaw moment coefficient is also reduced. As already discussed, the vehicle's yaw response is the critical parameter when crosswind sensitivity is concerned, thus these results suggest that subjecting the vehicle to steady onset flow (a uniform or sheared velocity profile) will provide a worst case condition.

Unsheared

Sheared

Sheared and Turbulent
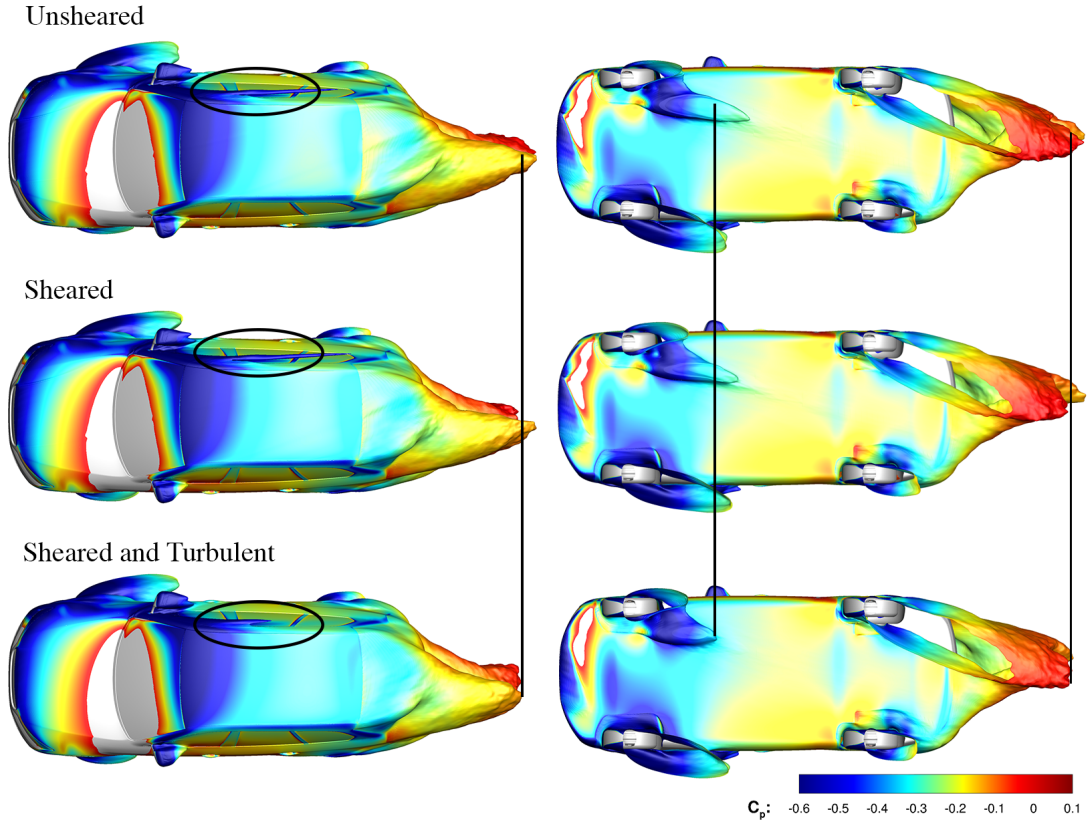
Figure 5.17: Estate: Isosurfaces of $C_{p_{total}} \leq 0$, rendered by values of pressure coefficient C_p.

Unsheared

Sheared

Sheared and Turbulent

C_p: -0.6 -0.5 -0.4 -0.3 -0.2 -0.1 0 0.1
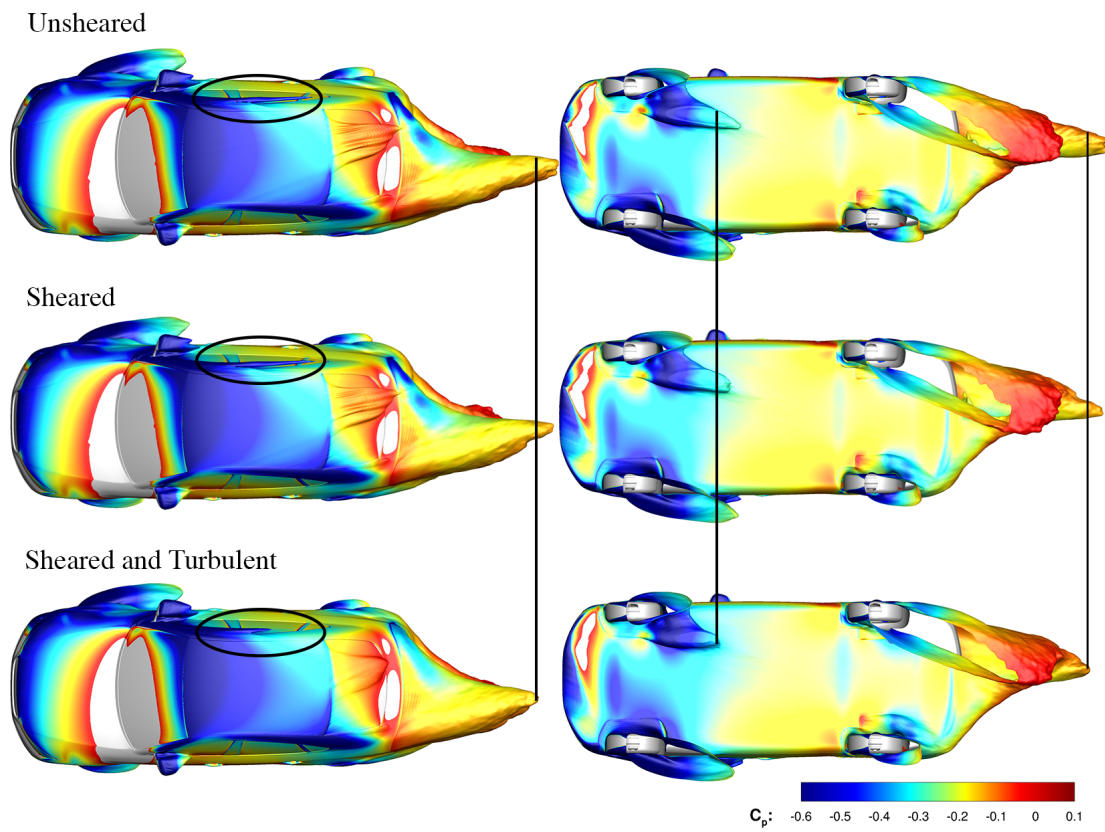
Figure 5.18: Fastback: Isosurfaces of $C_{p_{total}} \leq 0$, rendered by values of pressure coefficient C_p.

(a) Unsheared

(b) Sheared

(c) Sheared and Turbulent
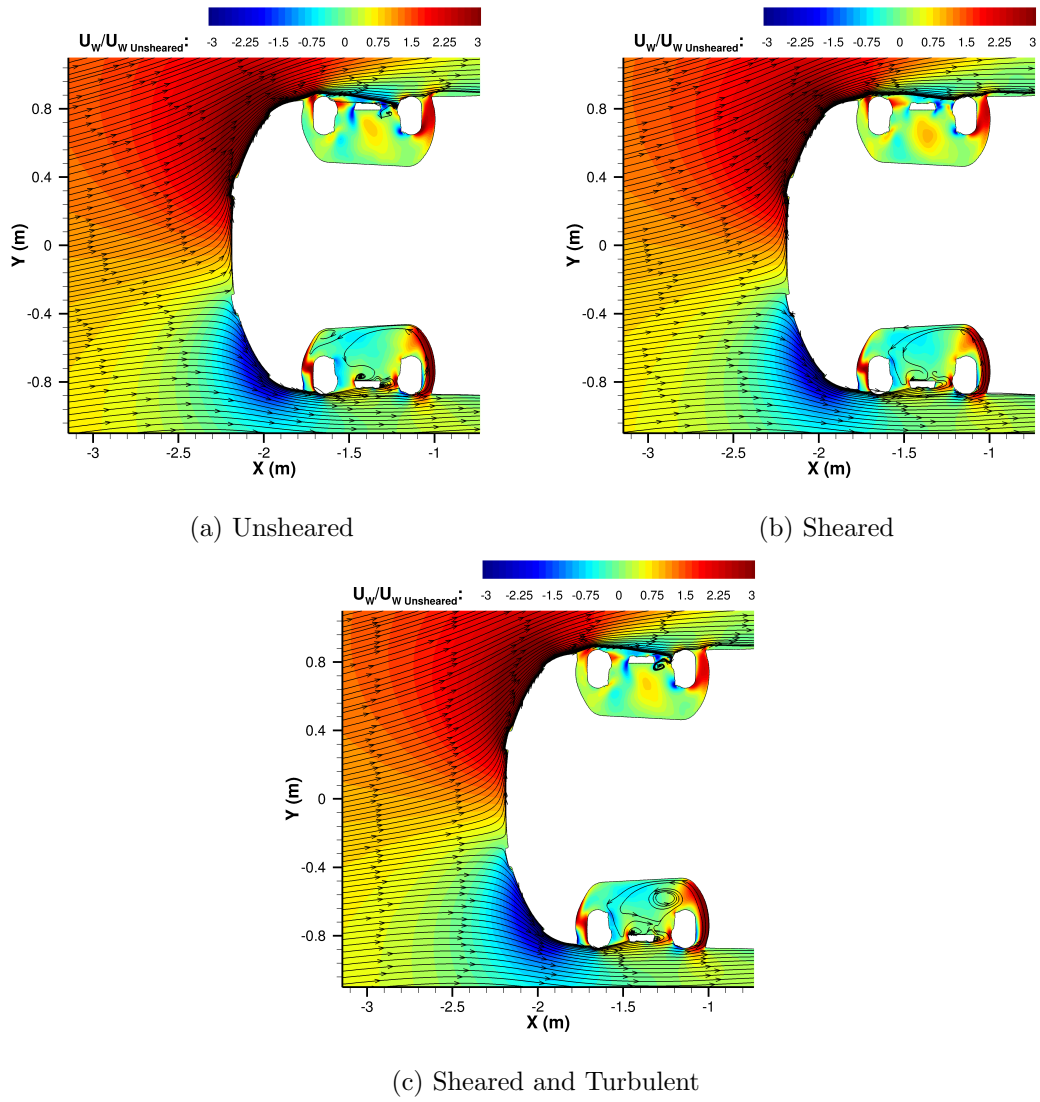
Figure 5.19: Flow around the front windward corner, plane at axle height $z = 0.32\,\mathrm{m}$.

In agreement with the work of Gaylard et al. [44, 45], D'Hooge et al. [43, 46], Howell et al. [33] and Newnham [34], the addition of freestream turbulence causes an increase in drag coefficient. For these geometries, the magnitude of this increase is much larger for the estate geometry than the fastback, 14 and 5 counts respectively, when compared to coefficients obtained using the baseline, unsheared flow conditions. As the only difference between the vehicles lies in the rear end geometry, it is reasonable to expect that the variation in drag will be sourced in this region and this is confirmed by the ΔC_D shown in Figures 5.20a and 5.20b.

(a) Estate
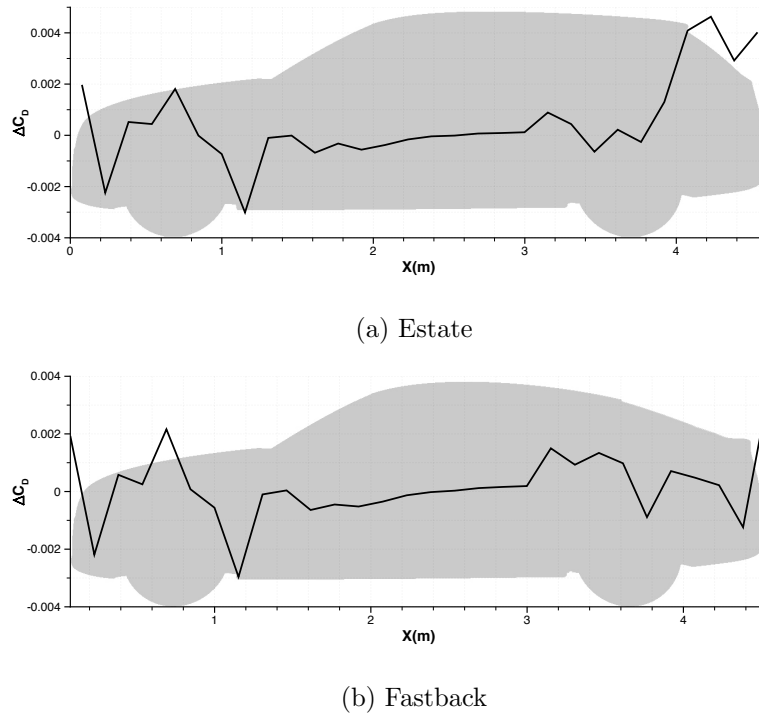
(b) Fastback

Figure 5.20: Delta of drag coefficient $\Delta C_D = C_{D_{Shear+Turb}} - C_{D_{Unsheared}}$.

The fastback geometry used by Gaylard et al. [45] displayed a much larger increase in drag coefficient, up to 24 counts, for similar turbulent conditions albeit at an averaged zero degree yaw angle. It their case, it was found that increases in turbulent mixing as a result of the higher intensity levels in the onset flow, delayed flow separation around the highly curved rear corners and generated more inboard flow. This in turn increased the suction at the outer edges of the base surface, generating a larger drag coefficient. However, this is not the case for the DrivAer geometry, as the sharp edges of the base surface as shown in Figure 5.1, promote a fixed separation point and hence the ΔC_D

144

in this region is small in comparison.

For the estate geometry, the much larger increase in drag coefficient can be sourced using Figures 5.21 and 5.22, which show the time averaged base pressure distribution and flow structures in the wake. As flow separates from the roof trailing edge, the increase in turbulent mixing strengthens and tightens the wake's upper vortex to the rear of the vehicle, leading to a reduction in pressure on the rear screen. In comparison, the flow over the fastback remains attached along the majority of the backlight surface, as shown in Figure 5.23, and hence a comparable increase in drag does not exist.

(a) Unsheared

(b) Sheared

(c) Sheared and Turbulent
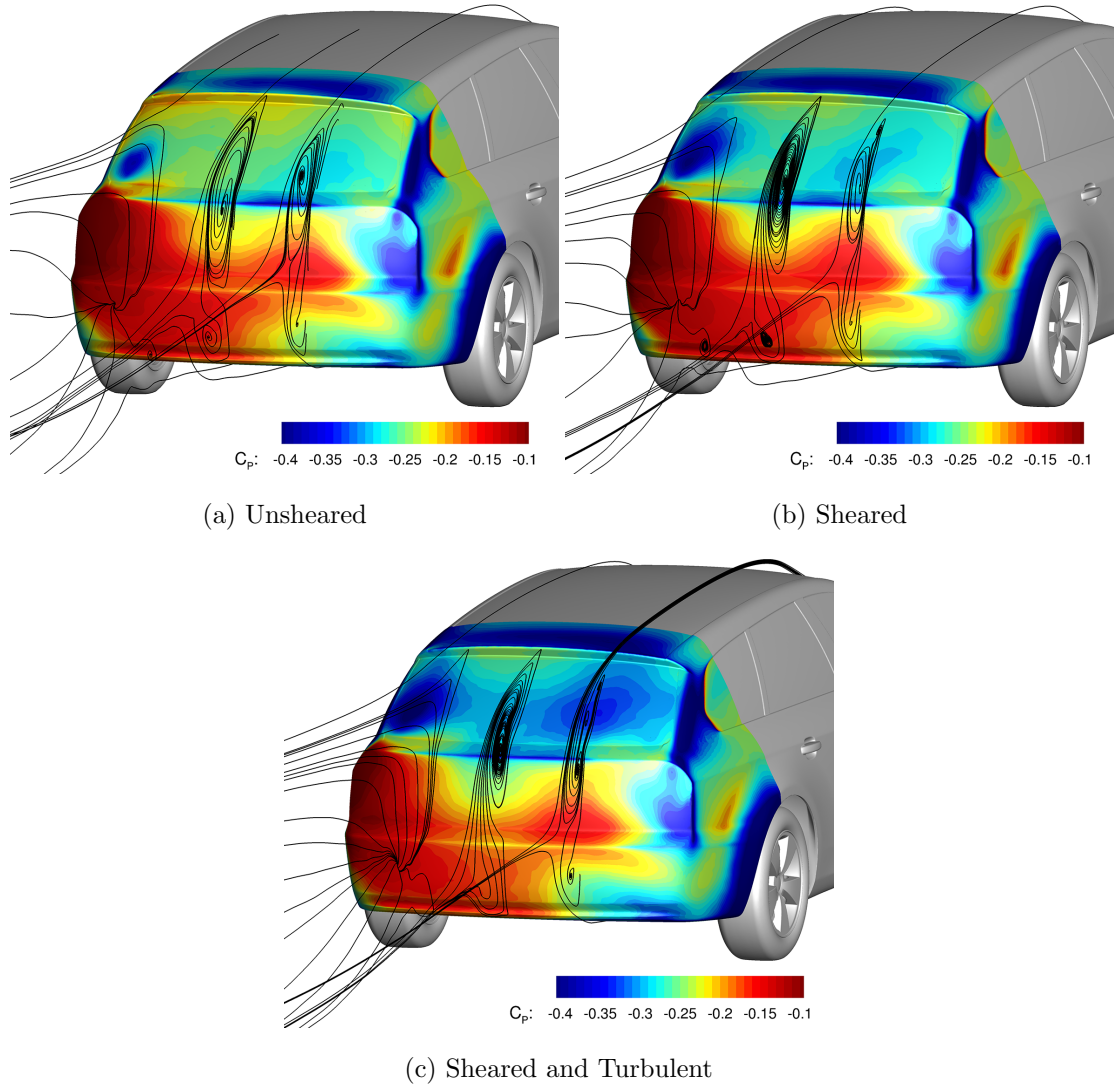
Figure 5.21: Estate: Time averaged base surface pressure coefficient and flow streamlines in planes $Y = -0.318, 0, 0.318$m.

(a) Unsheared

(b) Sheared

(c) Sheared and Turbulent
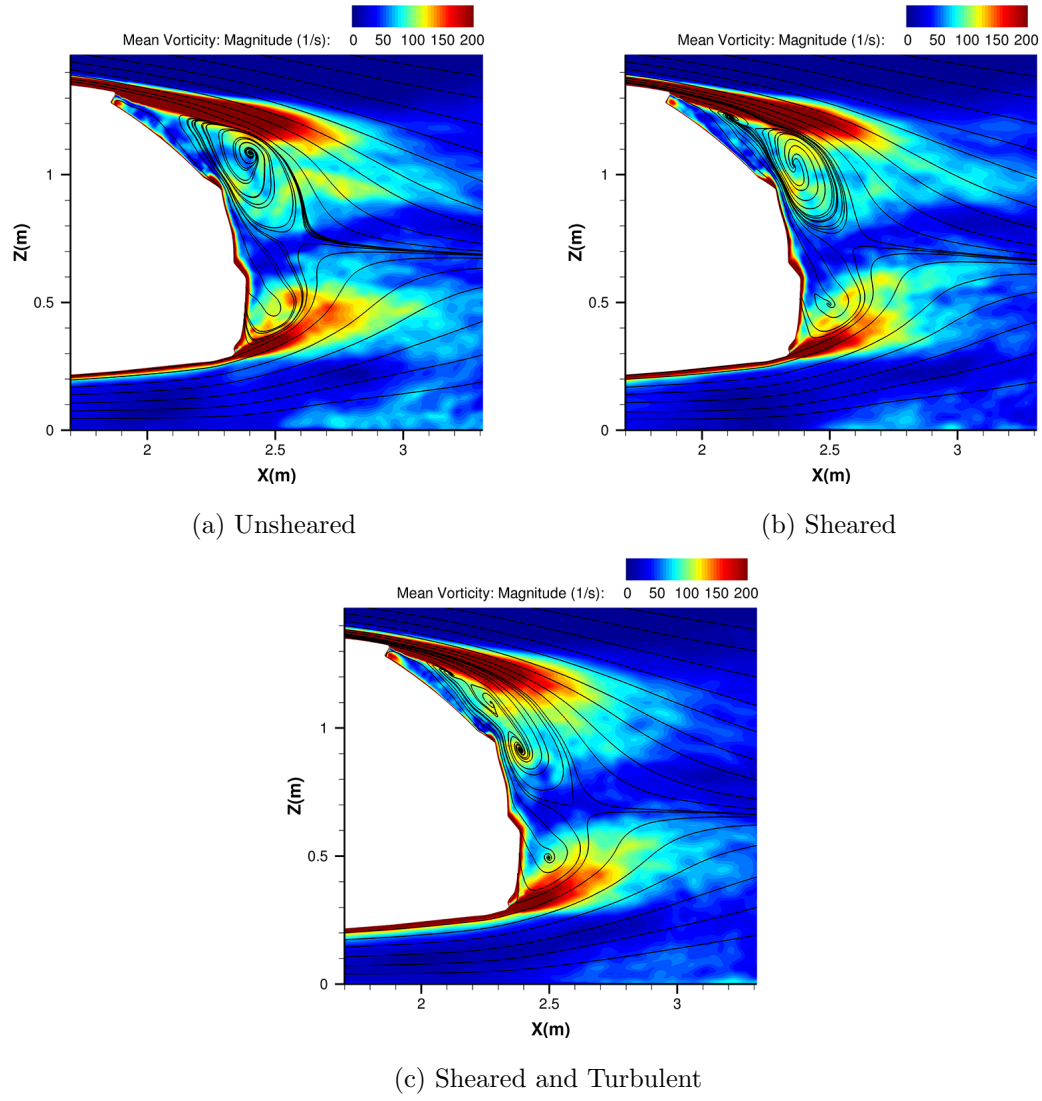
Figure 5.22: Estate: Time averaged vorticity magnitude in plane $Y = 0.318$m.

(a) Unsheared

(b) Sheared

(c) Sheared and Turbulent
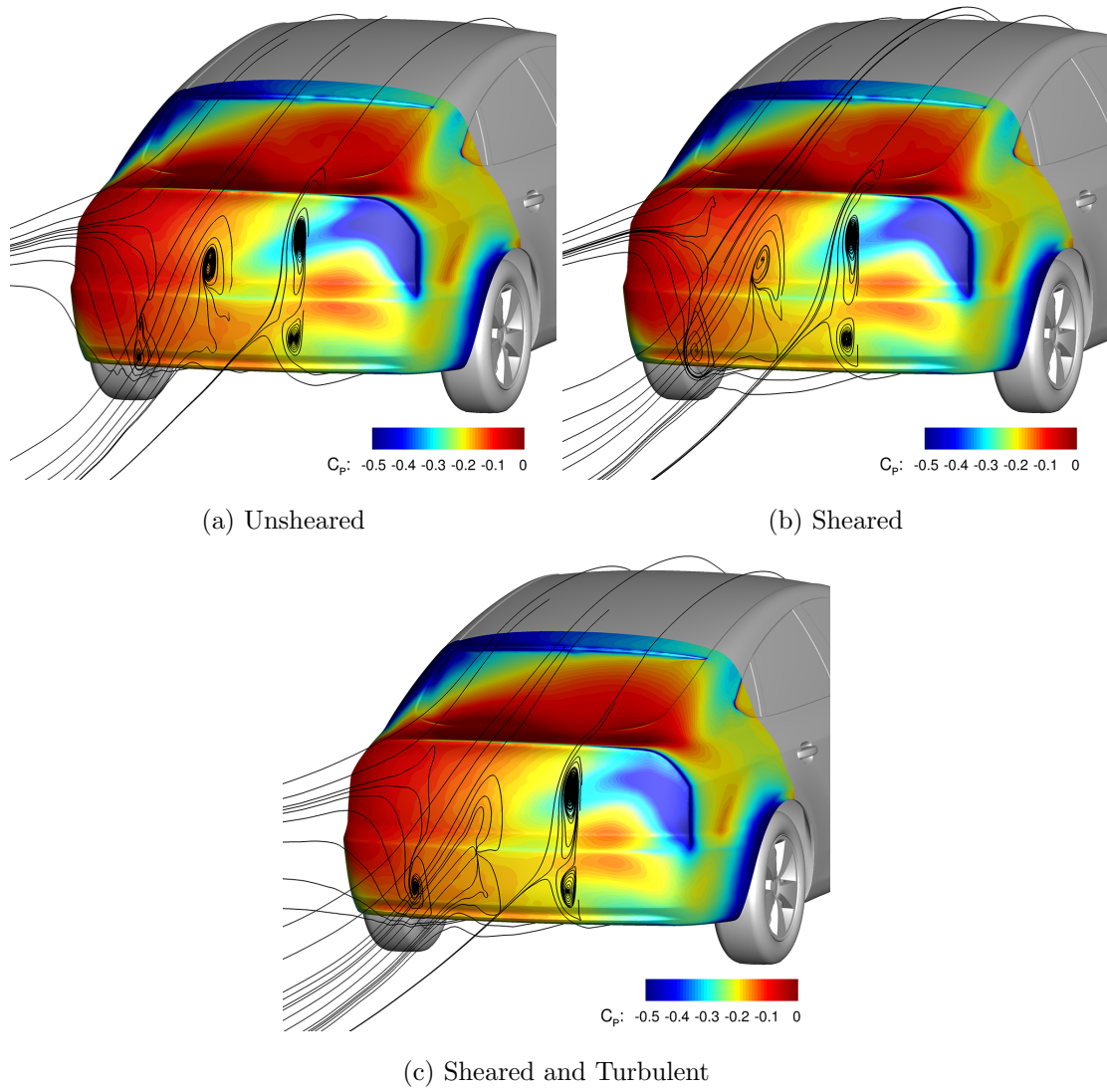
Figure 5.23: Fastback: Time averaged base surface pressure coefficient and flow streamlines in planes $Y = -0.318, 0, 0.318$m.

5.6 Summary

It has been shown that a sheared crosswind velocity profile, representative of the conditions experienced when travelling through smooth open terrain, has a minimal effect on a vehicle's aerodynamic loading when compared to those generated with a uniform velocity profile. However, caution must be taken with this conclusion as only two vehicle types have been evaluated, and are very similar in geometric dimensions and styling. It was suggested that of the two geometries, the fastback will be more sensitive to crosswinds, due to the larger stationary yaw moment gradient, and a sheared velocity profile did not appear to affect this result.

With the introduction of freestream turbulence, of 8% intensity seen by the moving vehicle, on top of a sheared velocity profile, much larger variations to the aerodynamic loads were found. An increase in drag coefficient, consistent with existing literature, arose most noticeably for the estate geometry, due to a strengthening of the wake's upper vortex. In contrast, the side force and yaw moment coefficients were found to decrease with the realistic flow conditions. It was unclear, whether this reduction was a result of a reduction in wake size, especially those of the front wheels, or a lowering of the onset flow angle due to the short time averaging window.

Overall the results suggest that the fastback geometry presents a larger safety concern in the presence of crosswinds, and the steady, uniform flow conditions, provide the maximum aerodynamic loads relevant to vehicle stability in this type of event. Hence, these conditions will serve as a useful application of the six degree of freedom, fully coupled system.

A FULLY COUPLED, SIX DEGREE OF FREEDOM RESPONSE TO A CROSSWIND EVENT

Contents

6.1 Introduction

The fully coupled system is now applied to the simulation of crosswinds. An event of this type can introduce large disturbances to a vehicle's aerodynamic loads, which in turn can have a large impact on its handling and stability. Hence, this event is a relevant and meaningful application of the fully coupled technique.

As opposed to simulating a naturally occurring crosswind, the flow conditions and test

procedures will initially follow those set out in an international standard for experimentally assessing road vehicle sensitivity to lateral winds, ISO 12021:2010 [58]. This standard uses an artificial, 20 m/s gust, produced by a crosswind generator adjacent to a test track, as shown in Figure 6.1. A vehicle is driven through the gust at a speed of 27.8 m/s (100 km/h), on what is initially, a trajectory perpendicular to the gust. This generates a severe flow yaw angle of approximately 35° and a resultant flow velocity of 34 m/s. The standard is open-loop, meaning no driver response is permitted. The steering wheel is simply held fixed for a two second period after entering the gust and as a result, the vehicle deviates from the intended course. This deviation is a direct consequence of the aerodynamics and not the driver's ability which can vary across test drivers, hence the test procedure is highly repeatable and provides a good measure of the vehicle's sensitivity to crosswinds.
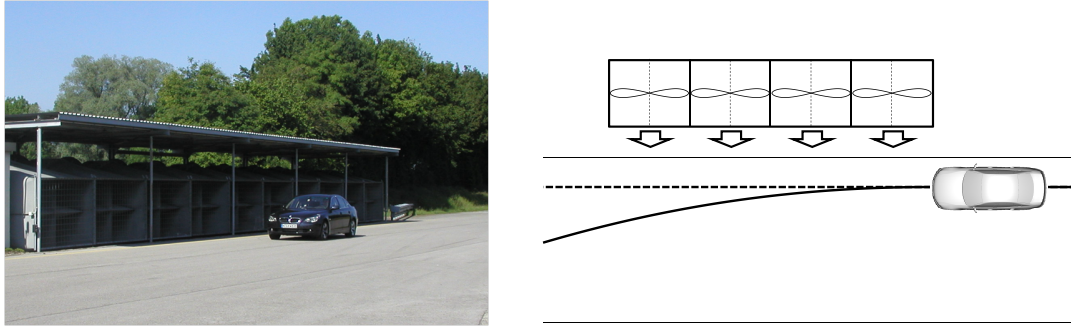
Figure 6.1: An example of a crosswind generator facility and vehicle response [23].

It has been shown in Chapter 5 that the inclusion of a realistic sheared wind profile with typical on-road turbulence levels has a minor effect on the vehicle's aerodynamics. Hence computationally simulating this experimental test rather than using measured, on-road gust data is sufficient for assessing a vehicle's response to an event of this type and will hopefully promote and ease any future experimental validation of the results obtained using this fully coupled simulation.

In addition to this open loop test procedure, the same flow conditions will be used for a closed loop simulation, with a modelled driver in the loop aiming to maintain the vehicle's initial trajectory. This is described in Figure 6.2. Using the results of both simulations, the influence of the driver on the vehicle's response can be obtained, and the effectiveness of their input can be determined.

(a) Open Loop
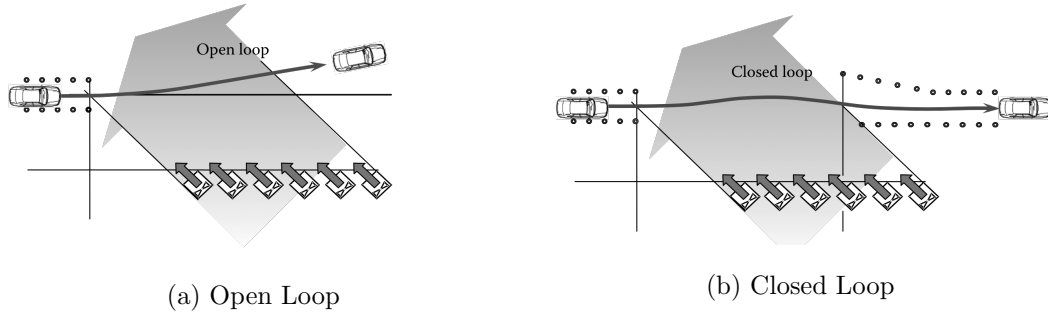
(b) Closed Loop

Figure 6.2: Example vehicle responses during open and closed loop tests [132].

The vehicle geometry chosen for these simulations is the fastback variant of the DrivAer model. It was shown previously that this geometry has the potential of being the most sensitive to crosswinds when compared to the estate and notchback variants, based on the calculation of stationary yaw moment coefficient gradient. As the main reason for performing this test is to expose any safety concerns, this geometry is the most appropriate. In addition, this geometry has the benefit that the numerical approach and grid refinement can be transferred from the previous study.

6.2 Crosswind Profile

Two gusts have been generated, with lengths corresponding to 4 and 12 car lengths respectively. Both lengths comply to the minimum length prescribed by the standard, and at a vehicle speed of $27.8 \, \text{m/s}$, correspond to a disturbance frequency of approximately 1.5Hz and 0.5Hz. It has been shown previously by Wagner and Wiedemann [53], that at frequencies between 0.5Hz and 2Hz, a driver can amplify the vehicle's response. Hence after the initial open-loop simulation, the closed-loop simulations can be used to investigate this result further.

Although a crosswind facility generates a step change in lateral velocity, this is not seen at the vehicle due to mixing layers at the edges of the gust. Such conditions occur on the road when passing gaps in roadside obstacles during gusty conditions, as illustrated by Favre [75] in Figure 6.3a. Hucho and Emmelmann [74], showed that the profile of a mixing layer seen by a moving vehicle approximately follows a cosine function, shown

in Figure 6.3b and described by Equation 6.1, where v_{max} is the maximum strength of the crosswind in the undisturbed region and X_{ML} is the width of the mixing layer. As shown in Figure 6.3a, the value of X_{ML} is dependent on the distance from the fans. For these simulations, the width of a mixing layer X_{ML} is chosen as one car length corresponding to a frequency of 6Hz or a reduced frequency value of 1.5, based on the forward speed of the vehicle. It has already been shown in the oscillating Davis model simulations, that such high values of reduced frequency results in flow hysteresis. This was also confirmed by Hucho and Emmelmann [74], who found that increasing the length of a gust's mixing layer, thus lowering the reduced frequency, reduced the transient behaviours of a vehicle's side force and yaw moment coefficients. Therefore it is reasonable to expect a transient behaviour in these forces for the generated gust profiles.

(a) Mixing layers in an on-road scenario [75]

(b) Cosine function for modelling mixing layers [74]
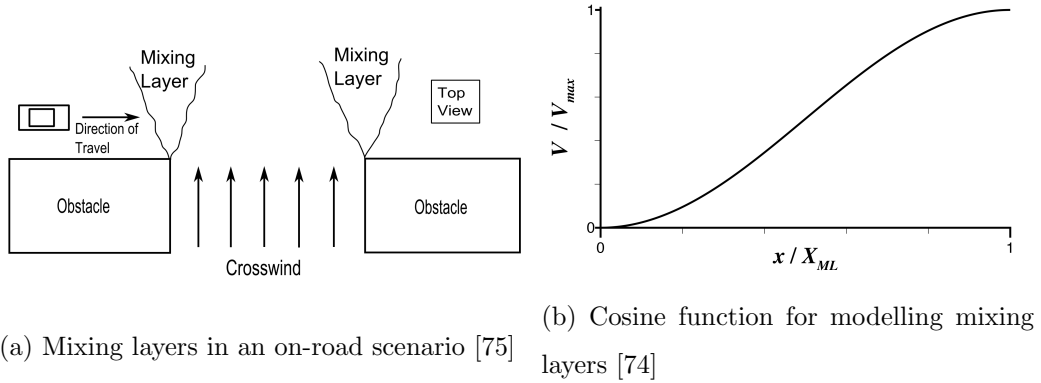
Figure 6.3: Crosswind mixing layers.

$$v(x) = \frac{v_{max}}{2}\left(1 - \cos\left(\frac{x}{X_{\mathrm{ML}}} \cdot \pi\right)\right). \tag{6.1}$$

Equation 6.1 provides a global description of the mixing layer profile, however from the moving vehicle's perspective the profile will vary with respect to time. Equation 6.2 describes this, where T_{ML} represents the time taken to pass through the mixing layer.

$$v(t) = \frac{v_{max}}{2}\left(1 - \cos\left(\frac{t}{T_{\mathrm{ML}}} \cdot \pi\right)\right), \qquad T_{\mathrm{ML}} = \frac{X_{\mathrm{ML}}}{U_{veh}}. \tag{6.2}$$

The resulting profiles of the gust seen at the vehicle follow a trapezoidal shape, shown in Figures 6.4 and 6.5, where $t = 0$ corresponds to the front of the vehicle hitting the crosswind region. Due to a time lag as the gust passes down the vehicle's length, it is only fully immersed in the maximum yawed flow for 1 and 9 car lengths respectively. These profiles are similar to the ones used by Favre [75], and represent a third of all on-road gusts, as found by Wojciak [22].
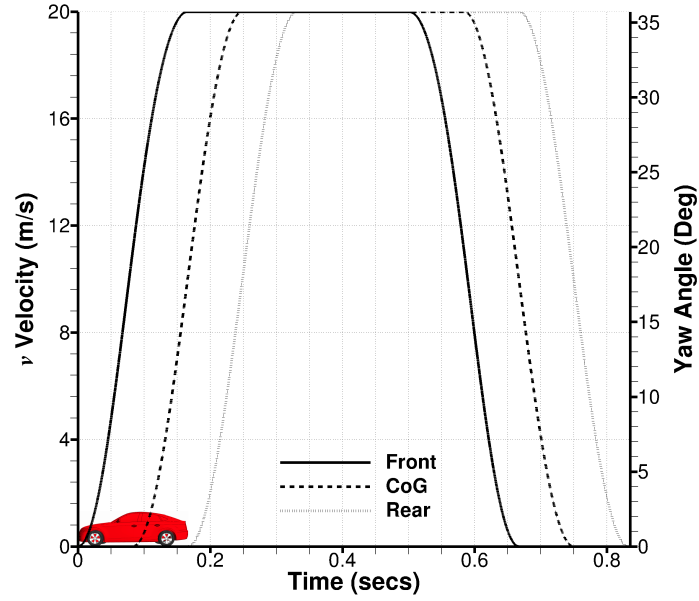
Figure 6.4: Crosswind profile for gust of length 4**L** (1.5Hz at $U_{\mathrm{veh}} = 27.8$m/s).
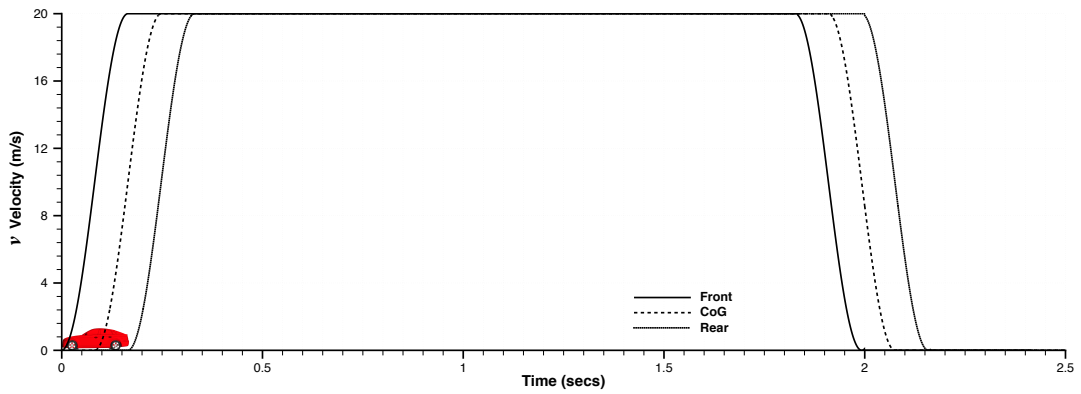
Figure 6.5: Crosswind profile for gust of length 12**L** (0.5Hz at $U_{\mathrm{veh}} = 27.8$m/s).

6.3 Simulation Approach and Boundary Conditions

Whilst the aim of this study is to apply the fully coupled system to the simulation of crosswind, in order to determine whether this level of complexity is need, it is important to make comparisons to existing, one way coupled methods. As found in the literature these methods are as follows:

- Quasi-Steady Static Coupling - A database of steady state aerodynamic force and moments at a range of yaw angles, interpolated over the gust profile and used as a vehicle dynamics model input.

- Unsteady Static Coupling - A transient history of aerodynamic forces and moments over a static model used as a vehicle dynamics model input.

The aerodynamic response for the quasi-steady case is formed from two quasi-steady solutions of constant flow yaw angle: 0° and 36°. These solution are obtained using an arrangement of traditional boundary conditions with an inlet, outlet and slip walls as shown in Figure 6.6a. For the 0° yaw angle case the u velocity component is set to 27.8 m/s at the inlet whereas for the 36° yaw angle case, the vehicle is yawed in the domain and the resultant velocity of 34 m/s is applied through the inlet u velocity component. The resulting quasi-steady aerodynamic force and moment values are then interpolated over the crosswind profile to form an input for the vehicle dynamics model.

The boundary conditions for the unsteady static simulation are more complex, as they need to be capable of exposing the vehicle to a time dependent velocity profile. There are several arrangements that can achieve this, the most popular of which is a pair of inlets and outlets in an arrangement shown in Figure 6.6b. Tsubokura, Nakashima et al. [72, 133, 67, 68, 70, 134] and Favre [75] showed how this approach requires a pair of functions at each inlet in order to convect the crosswind profile over the vehicle. At the main inlet, the u velocity function describes the vehicle's velocity and a time dependent v velocity function introduces the crosswind profile. At the secondary inlet, the u velocity function still describes the vehicle's velocity but the v velocity function describing the crosswind now depends on time and position.

154

(a) Quasi-steady Static

(b) Multiple Inlets and Outlets

(c) Periodic

(d) Unsteady Dynamic
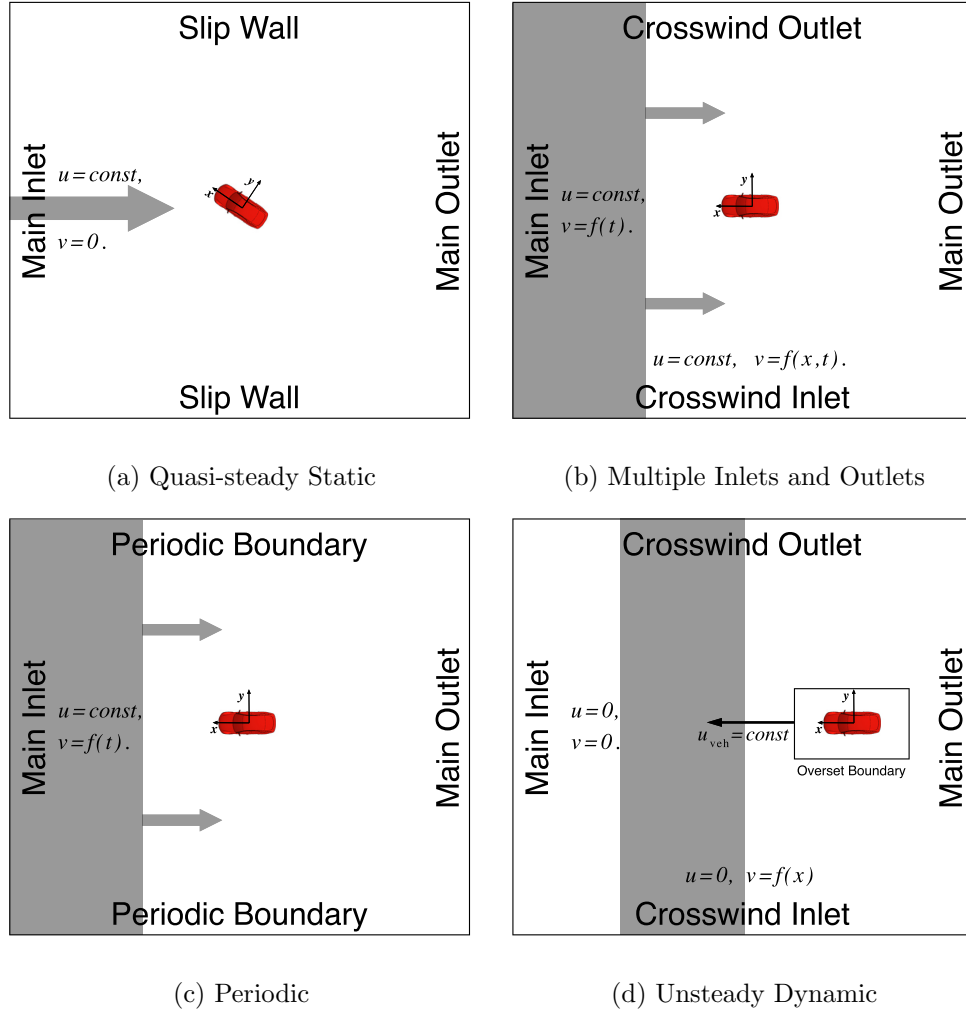
Figure 6.6: Boundary conditions for all simulation approaches.

An alternative to this replaces the secondary inlet and outlet with periodic boundaries, an arrangement more typically using in the simulations of turbo-machinery blading. By removing the additional inlet and outlet, only two velocity functions at the main inlet remain, as shown in Figure 6.6c. When using this method, it is important to ensure that the domain is wide enough to prevent any flow disturbances from re-entering the domain on the windward side and influencing the flow around the vehicle, however for typical vehicle speeds and domain sizes this interference is rare. The method has been used successfully in crosswind related applications by Demuth and Buck [135] and Theissen [23].

So far the arrangements discussed all feature static geometry over which the gust passes,

a frame of reference fixed on the vehicle and comparable to a wind tunnel arrangement such as that used by Dominy and Ryan [63, 64] and Volpe et al. [65, 66]. In contrast, the overset grid approach allows a switch to a global frame of reference, so that the crosswind's position is fixed in the domain and the vehicle passes through. Thus, this approach only requires a single, position dependent v velocity function at a secondary inlet and no u velocity function at either. However, additional grid refinement along the predicted path of the vehicle is required in order to reduce the interpolation error between the overlapping grids and thus the increases in computational cost makes this method a less attractive option.

From the three options discussed, the periodic boundary conditions have been chosen for the unsteady static simulations. This method is the most straightforward to implement as it only requires one set of velocity functions at the main inlet and no additional grid refinement due to moving overset grids. Therefore, the crosswind profile is introduced via a v velocity disturbance at the main inlet and convected downstream by the u component.

A one off simulation of the unsteady-static approach using overset boundary conditions was performed in order to highlight any unwanted artifacts of the overset method. Although results are not presented, there was a negligible impact on the forces and flow field between the overset and traditional, fixed vehicle methods. Thus fair comparisons between the methods can be made.

Including a six degree of freedom vehicle response in the CFD simulations for the fully coupled, unsteady dynamic approach adds a higher level of complexity to the boundary conditions. The vehicle motions that need to be included can be split into two categories. The 'global group' describes motions of the entire vehicle and includes longitudinal and lateral translations along with yaw rotation. The 'body group' contains motion of the vehicle's sprung mass on its suspension system, namely vertical translation (heave) as well as pitch and roll rotations. Nakashima et al. [72] suggest a combination of grid deformation and a non-inertial reference frame to include all six degrees of freedom. In their approach, grid deformation based on the arbitrary Lagrangian-Eulerian (ALE) method was used for the small-scale body motions as well

as the yaw rotation, while longitudinal and lateral translations were implicitly treated through additional terms in the Navier-Stokes equations. The multiple inlet and outlet boundary conditions were used to convect the crosswind over the vehicle, thus the flow's frame of reference was fixed on the vehicle. As the yaw rotation of the vehicle was physically modelled via grid deformation, the vehicle's frame of reference yaws, however after any motion of this type, the flow's u velocity component imposed at the main inlet will no longer represent the reciprocal of the vehicle's forward velocity as the two frames of reference no longer align, shown in Figure 6.7. Nakashima et al. accounted for this via additional longitudinal and lateral translational terms to ensure the flow's u velocity component coincided with the vehicle's forward direction throughout the simulation.

Whilst this method has proven effective at including motion within a CFD simulation, grid deformation can only be used for small scale displacements such as those experienced on a vehicle's suspension system and small yaw angle rotations. For large-scale motions, grid deformation can generate highly skewed grid elements and impair the accuracy of the flow prediction. The overset grid approach offers an alternative, capable of including both large and small scale motions. The proposed method of including motion in all six degrees of freedom for a fully coupled, unsteady dynamic simulation uses two nested overset regions: one around the complete vehicle and one around the vehicle's sprung mass. In this arrangement, the global and body motions can be treated separately without deteriorating the quality of the grid elements.

The global overset grid moves in only three degrees of freedom, whilst the body grid moves in six with the addition of heave, pitch and roll motions. As a result of using this method, the vehicle 'drives' through the domain and through the band of crosswind, as shown in Figure 6.6d. Due to the switch in frame of reference from a typical wind tunnel arrangement to an on road observer's perspective, this is a direct replication of the vehicle driving passed the crosswind generator and hence could be used to simulate more complex manoeuvres.
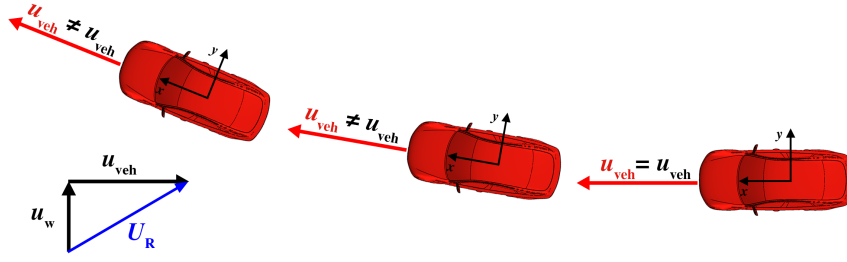
Figure 6.7: The effect of yaw rotation on simulation boundary conditions: vehicle forward velocity no longer aligned with u component of inlet velocity.

6.4 Computational Grids

For the three cases, two grids are generated: a static grid and a dynamic grid with domain sizes $(x = 20\mathbf{L}, y = 13\mathbf{L}, z = 3\mathbf{L})$ and $(x = 25\mathbf{L}, y = 10\mathbf{L}, z = 3\mathbf{L})$ respectively. As the overset grid moves through the domain in the dynamic simulation, the length of the domain is determined by the desired duration of the simulation. A value of 25 car lengths at a vehicle speed of $27.8 \, \mathrm{m/s}$ corresponds to just over 4 seconds, sufficient for a one second initialisation period during which the flow can develop and then a 2 and 2.5 second simulation time for the two gusts respectively. This is not the case for the static grid, as the vehicle remains stationary in the domain, and hence the domain can be shorter in length. The large width value of the static grid ensures that disturbances do not re-enter the domain on the windward side when using the periodic boundary conditions. This value is reduced for the dynamic grid as such boundary conditions are not used and hence, this narrowing can remove unnecessary grid elements.

As already discussed, two overset regions are required for motion in six degrees of freedom. One overset region, highlighted red in Figure 6.8, includes all four wheels while the second, highlighted in blue, contains only the vehicle's sprung mass and lies nested, within the first. This arrangement allows the global and body motions of the vehicle to be applied separately. Even though the geometry is fixed in the static simulations, the overset regions are maintained in the static grid for consistency in grid refinement, but also allows yawing of the vehicle for use in the quasi-static 36° yaw

angle simulation without additional re-meshing.
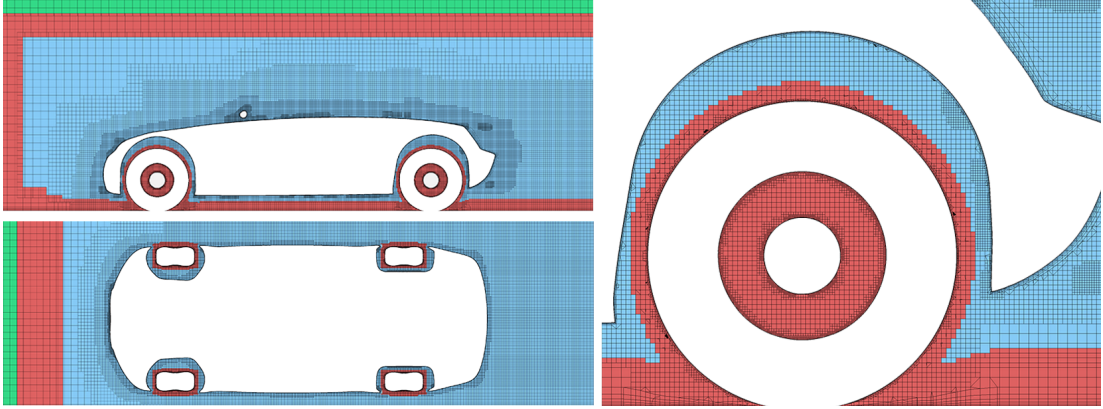
Figure 6.8: Nested overset grid arrangement used by static and dynamic grids.

The position of the refinement that is contained within the overset grids, shown in Figure 6.8, has been taken from the previous DrivAer model grid as the shape of this region is still able to capture the predicted flow yaw angle generated over the vehicle. The volume element size within this refinement is double the value used previously, with an isotropic dimension of 20 mm (0.004**L**). The coarsening of the grids when compared to the previous DrivAer model grid is required in order to speed up the hole cutting and interpolation stages of the overset grid procedure. This allows acquisition of results in practical times.

Unlike the local refinement, the global refinement and position of the vehicle within the domain varies between the two grids. For the static grid, the vehicle is positioned approximately 6**L** from the inlet, this allows a one second initialisation period before the crosswind reaches the vehicle. In the region upstream of the vehicle, refinement is added to reduce the numerical dissipation of the crosswind profile and as a result, the static grid contains a total of approximately 1.6×10^7 active, hexahedral elements. Figure 6.9 shows a horizontal slice through the front portion of the domain at axle height and gives an indication of the locations of the refinement and vehicle position. For the dynamic grid, the vehicle is initially positioned at the far end of the domain, close to the main outlet, thus a refinement region which spans the width of the domain is positioned at a distance corresponding to one second upstream of the vehicle to maintain the crosswind velocity profile. The length of this refinement varies due to

the differences in length of the two crosswind profiles, but this does not have a large effect on the total element count. An additional refinement region runs along the length of the domain, along a predicted path of the vehicle as shown in Figure 6.9. This is needed so that the size of the donor grid elements in the outer overset region matches those of the background; thus reducing interpolation errors during the inter-grid data exchange. Due to this additional refinement, the total number of elements increases to approximately 2×10^7.
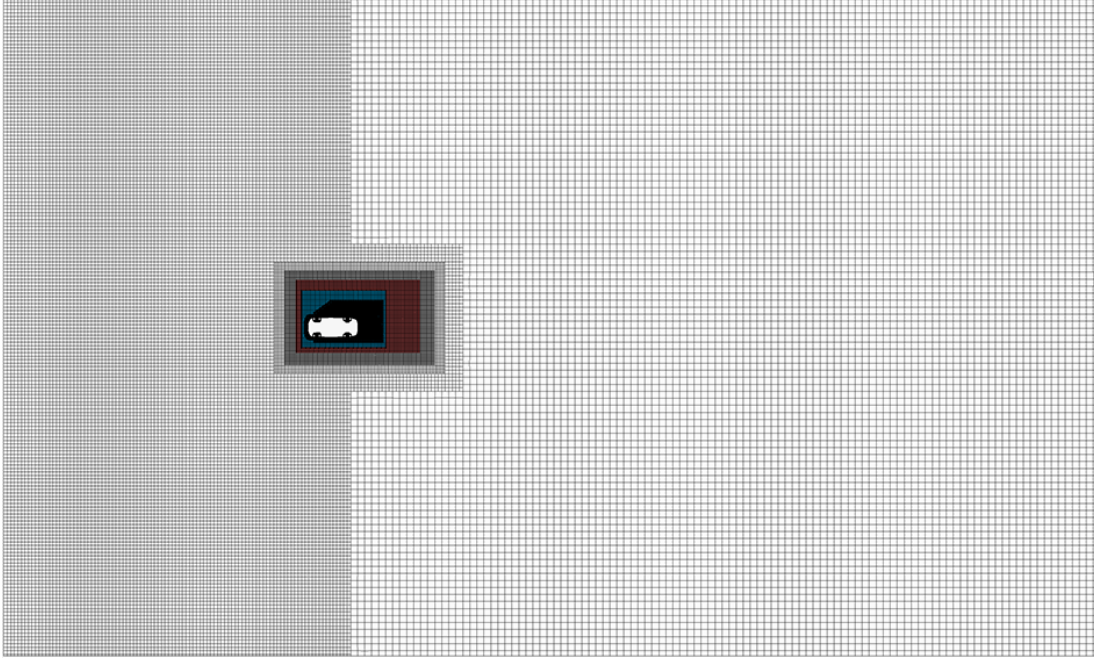
(a) Upstream Portion of Static Grid
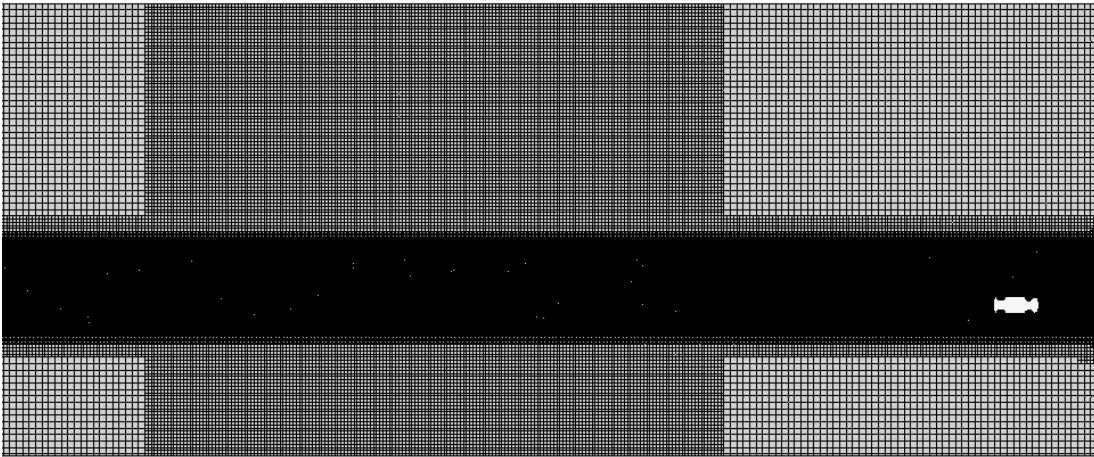
(b) Dynamic Grid

Figure 6.9: Position of vehicle and grid refinement within the domain.

6.5   Numerical Approach

Again the numerical method follows on from the previous DrivAer model simulations with a segregated, incompressible, finite volume, semi-implicit, pressure based solver chosen for all simulations and a hybrid 2nd order upwind/bounded central-differencing convection scheme. Turbulence is modelled with the IDDES variant of the Spalart-Allmaras Detached- Eddy model. A second-order temporal scheme limits the numerical dissipation of the crosswind profiles and a time-step of 1×10^{-4} seconds (non-dimensional $\Delta t U_R/L = 6 \times 10^{-4}$ ensures a Courant number below one within the LES region. Five inner iterations per time-step ensure consistent convergence of the residuals. All CFD simulations are carried out using Star-CCM+ v10.04.009 from CD-Adapco.

As already discussed in the oscillating Davis model study, a DES method is usually applied to much finer grids with a total number of elements closer to 100×10^6, however a grid containing this level of refinement is impractical due to current computational resources and the increase in physical time that accompanies the overset grid technique. Table 6.1 shows the values of drag and lift coefficient at zero yaw angle that are obtained when using this coarse grid alongside the fine grid and several experimental values. It is clear that this grid and numerical approach is capable of predicting the geometry's drag coefficient well. Furthermore the traditional boundary condition method, or the moving overset technique appears to have a minimal impact on the drag, with a variation in the coefficient value mimicking the variation between the two experiment values. The difference in lift coefficient is most likely a result of the variations in the mounting of the model between the simulation and experiment, the latter featuring a large vertical mounting strut and small clearance between wheels and ground.

The fully coupled system follows the same format as designed in Chapter 4, with the addition of a complex vehicle dynamics and driver model. The system is summarised in Figure 6.10. Due to the differing timescales between the fluid and the vehicle motion, a difference in timesteps between the aerodynamics and dynamics simulations was introduced. Thus the data exchange between the two simulations only takes place once

every 10 fluid timesteps.

Table 6.1: Drag and lift coefficient values using coarse overset grids.

	C_D	C_L
Unsteady Static	0.258	-0.038
Unsteady Dynamic	0.254	-0.022
Fine Grid (Chapter 5)	0.257	-0.020
Wieser et al. [136]	0.258	-0.096
Heft et a. [127]	0.254	-
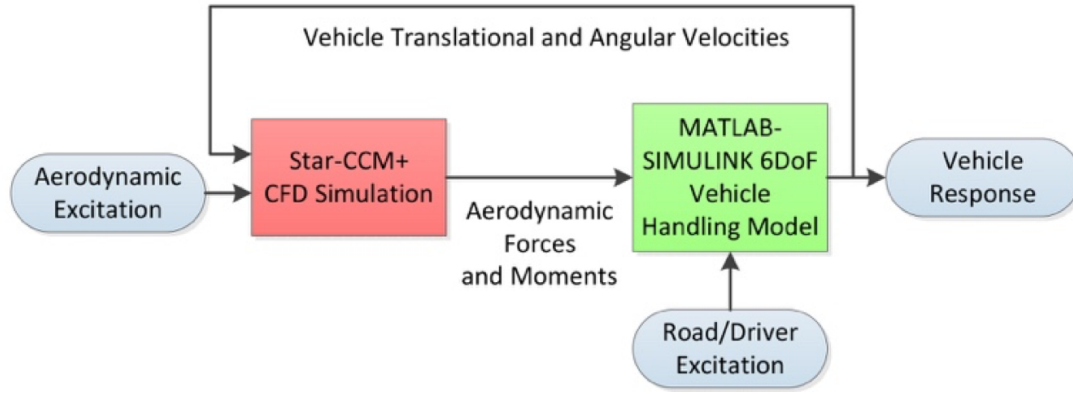
Figure 6.10: Fully coupled vehicle aerodynamics and dynamics system.

6.6 Vehicle Dynamics and Driver Model

The vehicle handling and dynamics model was designed by Dr. Matt Best in the Aeronautical and Automotive Engineering department of Loughborough University [137]. The same model is employed on the in-house, 6 degree of freedom Stewart-type platform driving simulator. The vehicle is modelled as a rigid body, free to move in six degrees of freedom under the influence of nominal drag and tyre forces found from a combined slip Pacejka formula. The vertical load used in these calculations is computed assuming a linear spring-damper suspension system compensated by suspension link forces that act at static roll centres. The model has been assembled in the model-based design environment Simulink, integrated within MATLAB, and initialised with

values representative of an average family saloon as shown in Table 6.2. The model includes the weight of the driver with no additional passengers or load.

Table 6.2: Vehicle initialisation parameters.

Kerb Weight + Driver (kg)	1345+75
Wheel Mass (kg)	[40, 40, 40, 40]
Roll Inertia (kg m^2)	532
Pitch Inertia (kg m^2)	2000
Yaw Inertia (kg m^2)	2150
Wheelbase (m)	2.786
Height of mass centre above ground (m)	0.53

The vehicle dynamics coordinate system follows the SAE standard J670 [138] and is shown in blue in Figure 6.11. The centre of this coordinate system is located at the vehicle's centre of gravity, split 47/53% along the length of the vehicle and 0.38$\mathbf{H}$ above the surface of the road (approximately coinciding with the top of the wheel hubs). This weight distribution is representative of a front wheel drive vehicle. In contrast, the vehicle's aerodynamics are referenced in a separate coordinate system, defined in SAE J1594 [139] and shown in black in Figure 6.11. In this coordinate system, the origin is located on the ground at a mid-track, mid-wheelbase location and the directions of the x and z axes are reversed. This switch in direction is a result of a desire for positive aerodynamic drag and lift values but in spite of this switch, the sign convention of all aerodynamic moments is consistent with the vehicle dynamics. For use in the vehicle dynamics model, all aerodynamic forces and moments are converted into the vehicle dynamics coordinate system and thus acts through the vehicle's centre of gravity.

The driver model was also developed by Best [137] and is a simple path following model for which the driver provides lateral control through a steering input. For these particular simulations, the driver provides no longitudinal control as the vehicle is in a cruise control condition. The parameters which define the model are preview time to a single point on the road ahead t_p, a proportional lateral gain K_lat, a driver reaction time t_lag, and a final parameter defining a basic approximation of the understeer gradient K_ug.
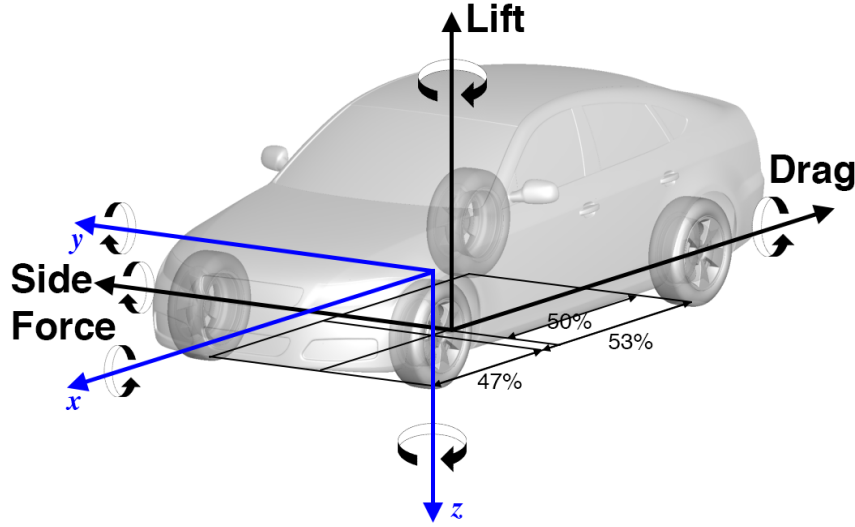
Figure 6.11: Vehicle aerodynamics (black) and dynamics (blue) coordinate systems.

Figure 6.12 shows the calculation of the preview point P after preview time t_p, and the lateral deviation from both linear and circular track types. Under a fixed steered wheel angle δ at time t and constant forward speed u, the forward path radius can be defined from the well known steady-state handling equation,

$$R = \frac{L_W + K_\mathrm{ug} u^2(t)/g}{\delta(t)}.$$ (6.3)

With a vehicle orientation ψ, units vectors are,

$$\hat{t}_G = \begin{pmatrix} \cos \psi \\ \sin \psi \end{pmatrix}, \hat{n}_G = \begin{pmatrix} -\sin \psi \\ \cos \psi \end{pmatrix}$$ (6.4)

and the angle traversed along the arc,

$$\theta = u(k)T_p/R.$$ (6.5)

The preview point P can then be calculated using the arc centre O,

$$P = G + \left(1 - \begin{pmatrix} \cos \theta & -\sin \theta \\ \sin \theta & \cos \theta \end{pmatrix} \right) R\hat{n}_G.$$ (6.6)

The deviation of this point from the line segment track type can be calculated,

$$d_L = (P - S_L) \cdot \hat{n}_L$$ (6.7)

and steering control is applied (with time delay t_{lag}) based on correction of the current value $\delta(t)$, and the predicted future point error d_L,

$$\delta(t + t_{\text{lag}}) = \delta(t) + K_{\text{lat}}d. \tag{6.8}$$
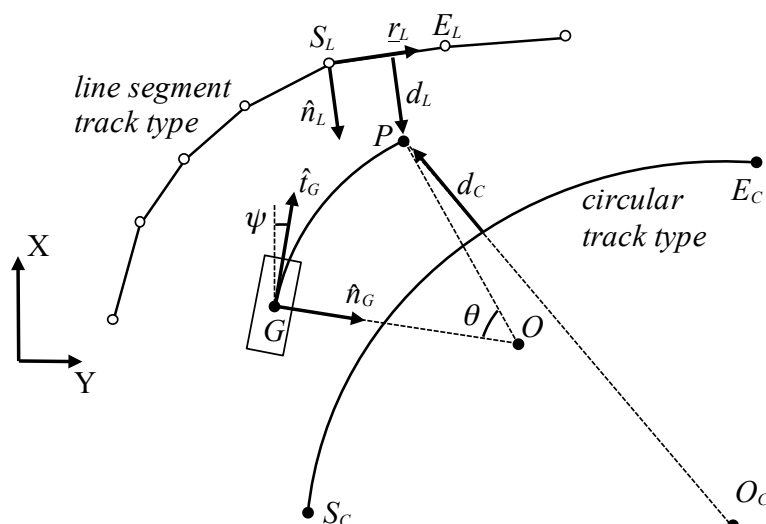
Figure 6.12: Preview point and lateral deviation from both circular and line track types [137].

This driver model has been tuned to real driver steering data recorded on the in-house vehicle simulator. Participants were advised to maintain their position within the lane of a two-laned dual carriageway whilst the vehicle was subjected to the long crosswind profile. The gust was applied to the vehicle through external aerodynamic loads obtained from the unsteady static open loop simulation. No warning or prior knowledge of the gust was given to the participants. There is an argument to suggest that this information should have been provided as a gust of this profile typically occurs when exiting a tunnel or passing over an open bridge for which the driver may be given a visual cue and be prepared to react. From a total of ten participants, five responses were excluded as they represented a poor driver's response, either failing to return to the lane or returning with a significant delay. Such responses could be utilised to investigate the effect of variation in driver ability, but for the current initial simulations it was felt that a competent driver's response was appropriate. For this reason, the remaining five responses were used to calculate an average steer angle response and

this is shown in Figure 6.13.
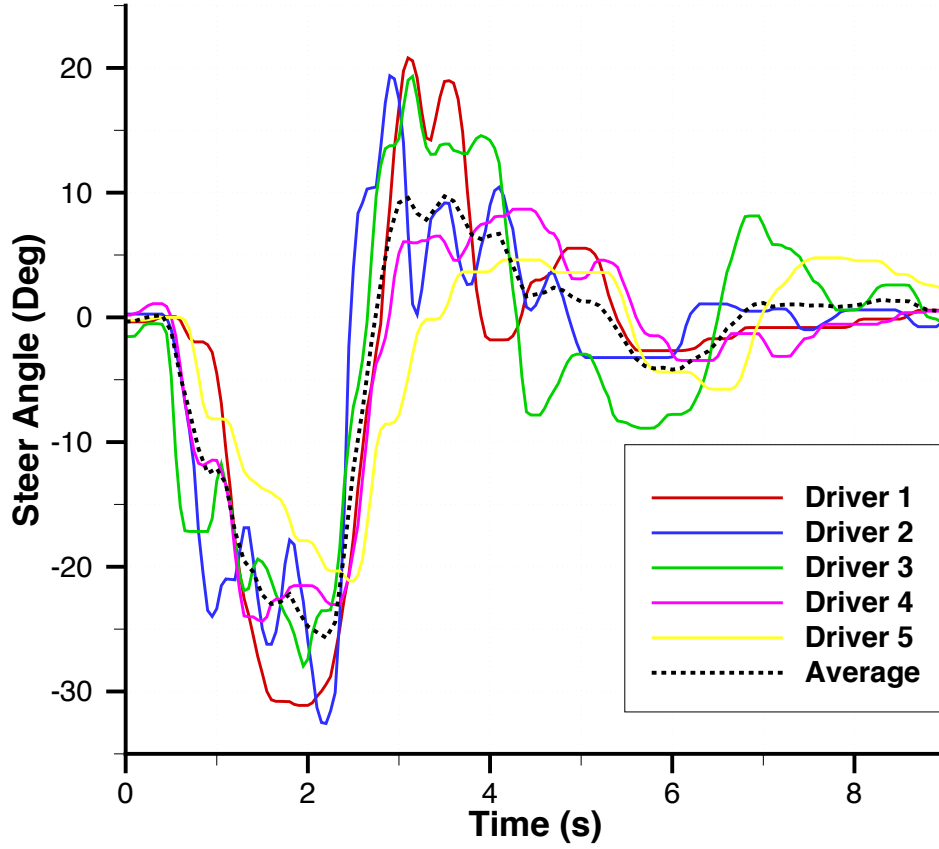
Figure 6.13: Recorded driver response and calculated average.

A low pass filter was applied to the average steer angle response to remove the unphysical small scale fluctuations resulting from the averaging process. The driver model was tuned to this smoothed average response using an unconstrained, multivariable minimisation function. More specifically, the optimal solution was found by minimising the covariance of the difference between the modelled and reference steer angles. The variables that were tuned were the preview time t_{p}, proportional lateral gain K_{lat}, driver reaction time t_{lag}, and approximation of the understeer gradient K_{ug}. The optimal values are presented in Table 6.3, with the modelled steer angle response shown in Figure 6.14. Although the value of driver reaction time appears small (from the reference data it is expected that this value is approximately 0.5 seconds) the current

value provides a suitable curve fit to the reference data over the initial steer input. This suggests that the t_{lag} parameter is ill-defined, and not a true representation of the driver's reaction time. It is most likely that this parameter represents a generic time lag that is dependent on the values of additional parameters such as the preview time.

Table 6.3: Tuned driver model parameters.

t_{p} (s)	K_{lat}	t_{lag} (s)	K_{ug}
1.132	0.003	0.041	0.188
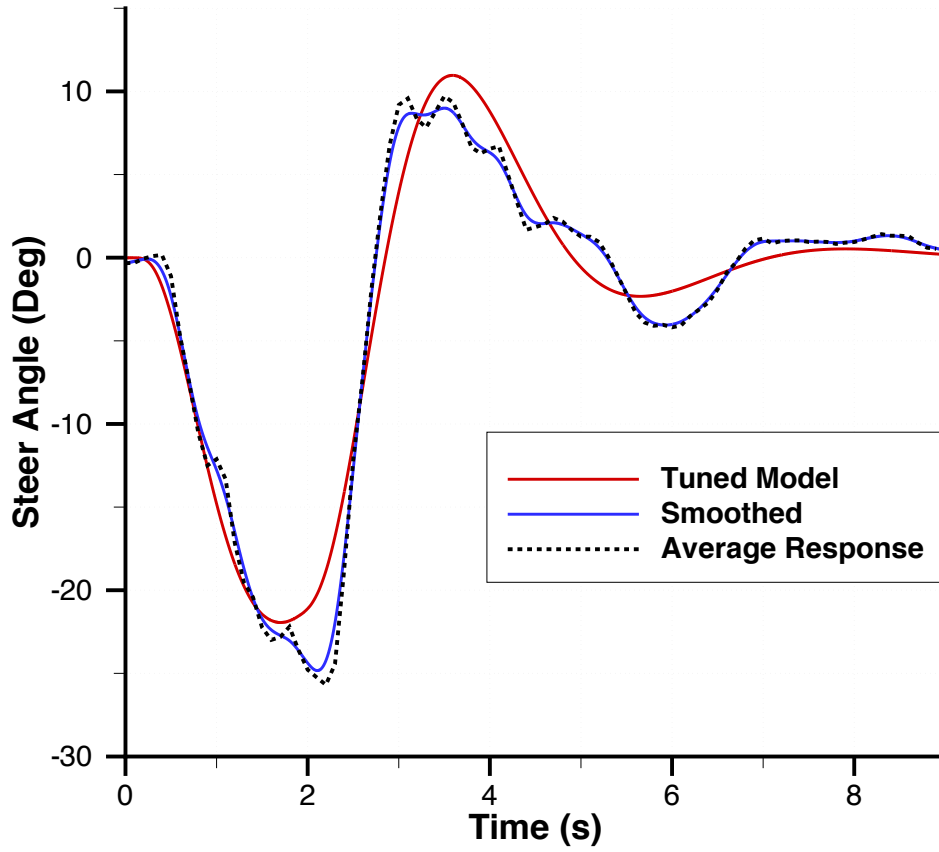
Figure 6.14: Tuned driver response.

6.7   Results - No Driver Response

The results of the open loop manoeuvre, without a driver's response, are analysed first, with Figures 6.15a and 6.15b showing the behaviour of the vehicle as it moves through the two bands of crosswind. The figures have been scaled consistently, and therefore show the differences in gust length with reasonable accuracy. The overlaid horizontal lines are set at a distance of 1.8 m apart to indicate half a typical motorway lane width.

In an initial analysis of the vehicle's response, the gust appears to alter the yaw angle of the vehicle and as there is no driver response, the vehicle deviates laterally from its initial path. Within the simulated time, this deviation is large enough to encroach upon the adjacent lane in both events and hence presents a severe safety concern. The underlying aerodynamics that are responsible for this response and the compete vehicle six degree of freedom behaviour is now discussed in more detail.

(a) Short Gust (4**L**)

(b) Long Gust (12**L**)
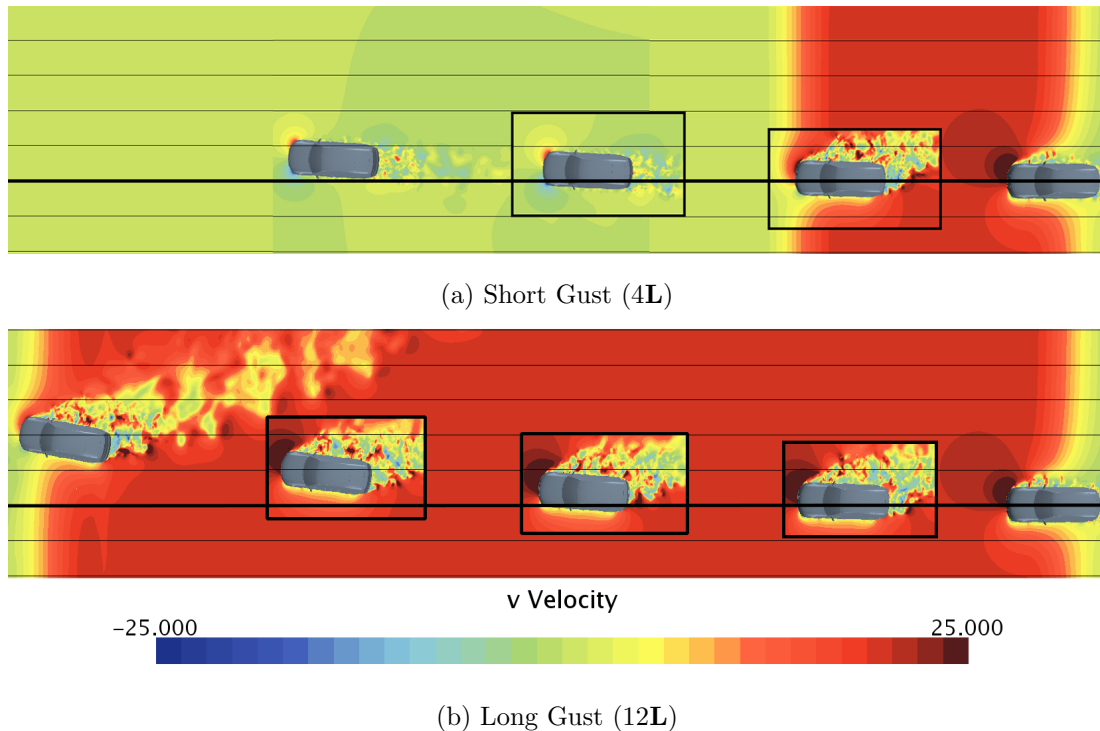
Figure 6.15: Motion of the vehicle in the fully coupled, open loop simulations.

6.7.1 Short Gust

The effect that the gust has on the aerodynamic side force and yawing moment, and the influence of the coupling method for the short event are presented in Figures 6.16 and 6.17. In these figures, all forces and moments are defined using the standard SAE aerodynamic coordinate system SAE J1594 [139], thus the moment centre is defined at mid-wheelbase, mid-track on the surface of the road. However as already discussed, for use in the dynamics model, these forces are converted into a vehicle dynamics coordinate system. All vehicle response figures use this dynamics coordinate system.

Over the duration of the gust, there appears to be very little difference in the predicted loads between the two unsteady approaches. The timings and gradients of the increase and decrease in side force and yaw moment display minimal variations between the two. In comparison, there is a clear delay in the loadings when using the steady static approach. This is caused by the time dependent effect of the gust travelling along the length of the vehicle, whereas the steady state approach assumes that there is a constant force acting over the entire vehicle. In this case, the aerodynamic response follows the timing of the aerodynamic centre's exposure to the gust.

The front of the vehicle enters the gust at $t = 0$ and the side force builds. As the length of the gust's mixing layer was set to one car length, by the time the maximum yawed flow hits the front of the vehicle, the rear is only starting to feel the presence of the gust. By point A, the entire front half of the vehicle is immersed in the maximum yawed flow, and due to the angle and strength of the resultant velocity vector, the flow's front stagnation is shifted from a central position, to the front windward corner, as shown in Figure 6.18a. In this state, the front contribution to the total side force dominates over the rear and the aerodynamic yaw moment over shoots the steady static value. This behaviour agrees well with the observations of Hucho and Emmelmann [74] and the experiments of Beauvais [61]. In addition, this behaviour is in keeping with the phenomenon of flow hysteresis identified earlier, conforming to the relationship of reduced frequency and unsteady aerodynamic loads.

At point B, the entire vehicle is immersed in the maximum yawed flow and thus an
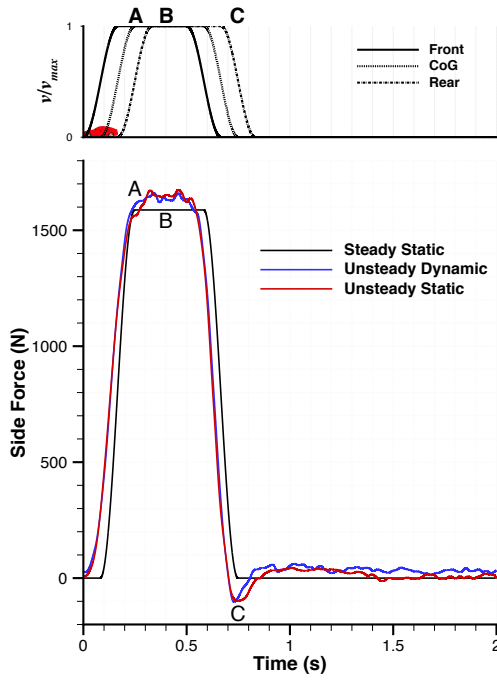
Figure 6.16: Short gust: Side force
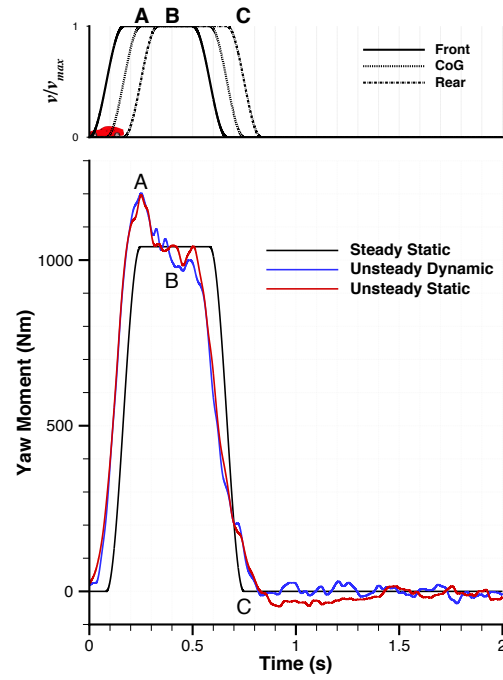
Figure 6.17: Short gust: Yaw moment

increase in rear side force restores the yaw moment to the steady static value. The front of the vehicle then starts to exit the gust, indicated by the early decrease in both loads, and by point C, the entire front half of the vehicle has left the crosswind region. This point correlates to a negative peak in side force, caused by the larger resultant velocity and thus low pressure acting over the rear windward side. A similar peak does not exist in the yaw moment as this load is most strongly influenced by the location of the high pressure stagnant flow on the vehicle's front bumper, which has returned to a central position as shown in Figure 6.18b.

The largest differences between the two unsteady methods occur during the latter half of the event. It is predicted that the early decrease in aerodynamic yaw moment seen in the unsteady dynamic response is a result of including the vehicle's dynamic response in the CFD simulation. Figure 6.19 shows that during the gust, the vehicle's yaw angle increases up to a value of 2.5°. Interestingly, with the arrangement of the crosswind and vehicle velocity, this positive increase in the vehicle's global yaw angle, decreases the resultant flow velocity acting on the vehicle, as shown previously in Figure 1.7 and Equations 1.18 and 1.19. Although the resultant yaw angle can be shown to increase,
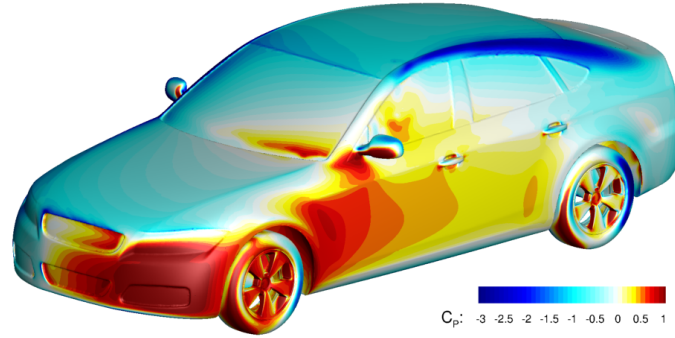
(a) Point A
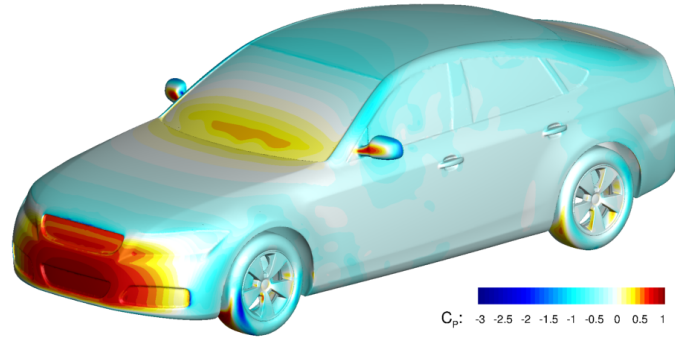
(b) Point C

Figure 6.18: Short Gust: Pressure coefficient at the entrance and exit of the gust.

it is thought that the reduction in dynamic pressure dominates over the yaw angle change and is responsible for the early drop off in the aerodynamic yaw moment, thus imparting an aerodynamic damping on the vehicle's motion. After leaving the gust, the vehicle's yaw angle continues to grow due to the build up in vehicle's yaw momentum. The data curves show that the yaw angle eventually settles at a value between 3.5° and 3.8°. Variations in this value are a result of the delay in the steady static aerodynamic response and the early decrease in aerodynamic yaw moment identified in the unsteady dynamic response. These results imply that a one-way coupled, unsteady static method provides an over estimated or *'worst case'* prediction of the vehicle's yaw response which would be a *'safe'* technique to use in a design process.
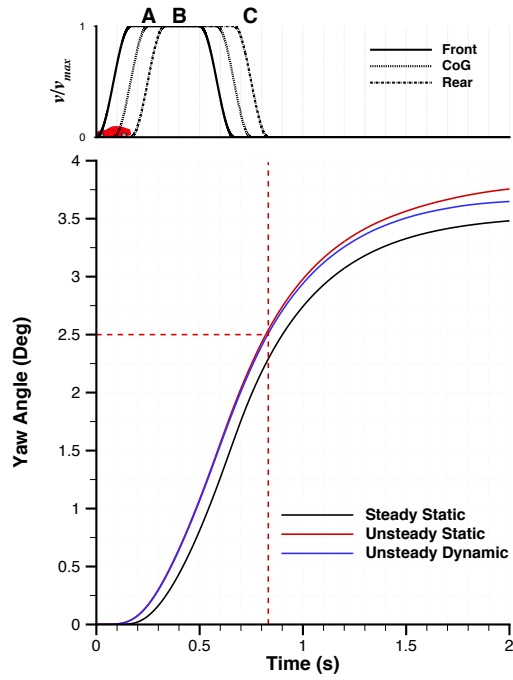
Figure 6.19: Short gust: Yaw angle
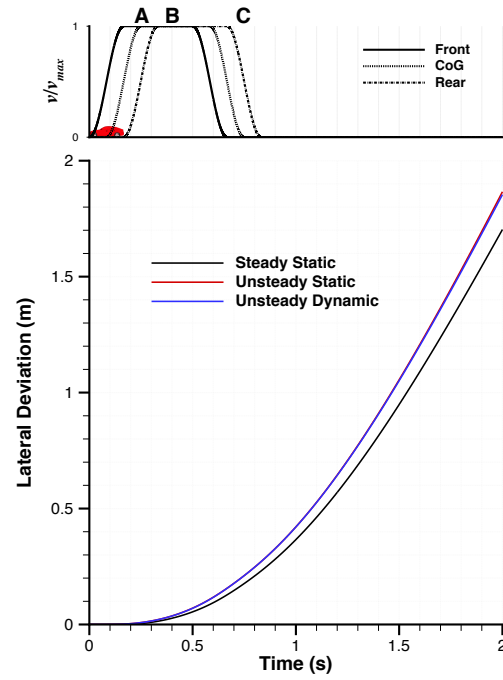
Figure 6.20: Short gust: Lateral deviation

The vehicle's lateral deviation is shown in Figure 6.20. This deviation is a result of the change in yaw angle only, as the friction acting on the tyres is large enough to prevent any lateral slip. Whilst immersed in the gust, the vehicle deviates by only 0.25 m and as no driver response can be applied, this deviation grows up to a total distance of approximately 1.85 m after 2 seconds, corresponding to half a typical motorway lane width. The variations between the unsteady method's yaw angle response do not appear to have a substantial effect on the total displacement, whereas the delay in aerodynamic response between the steady and unsteady methods results in an 8% reduction in the final value. These results are comparable to the recent two degree of freedom crosswind simulations by Carbonne et al. [121] and Winkler et al. [122], who showed a similar behaviour in vehicle response and aerodynamic loadings for various methods.

In addition to yaw rotation and lateral deviation, the current study considers motions in six degrees of freedom. Figures 6.21 and 6.22 show how the vehicle undergoes a negative roll angle displacement (into the gust) as a result of a large increase in aerodynamic roll moment. The use of two separate coordinate systems to describe aerodynamics and dynamics introduces some confusion when analysing this results, as a positive

aerodynamic roll moment appears to produce a negative vehicle roll angle. However when converted into the vehicle dynamics coordinate system, the positive aerodynamic roll moment becomes negative, due to the difference in origin height between the two sets of axes. As was the case with the yaw moment, a delay in the development of the roll moment is a feature of the steady static response, whereas the timing in the two unsteady methods is much more comparable. On top of this rolling motion, the body pitches, nose down, and the centre of gravity is raised by 6 to 8 mm. When combined, these three motions describe a overall downward motion of the windward front corner during the gust which is consistent with the movement of the flow's large front stagnation region. For all motions, the maximum angular displacement is small, most likely due to the realistic levels of suspension stiffness and body inertia. Therefore the seemingly large response differences between the coupling methods are exaggerated by the scales of the figures and ultimately have a minimal impact on the overall response of the vehicle.
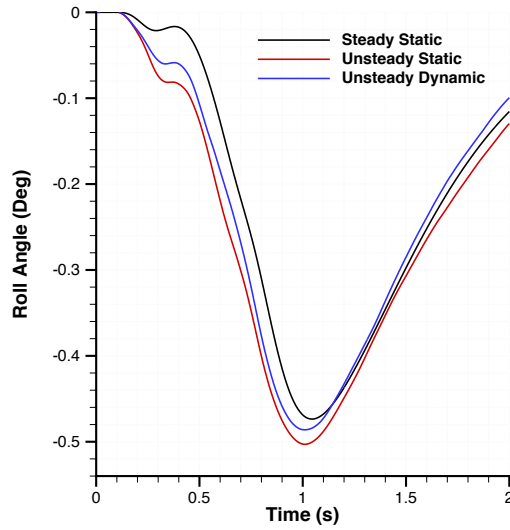
Figure 6.21: Short gust: Roll angle   Figure 6.22: Short gust: Roll moment
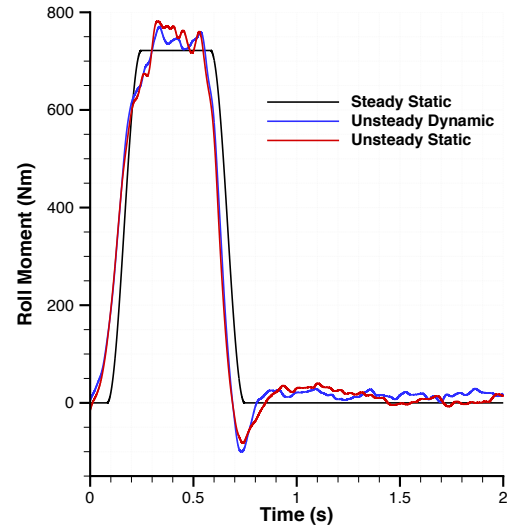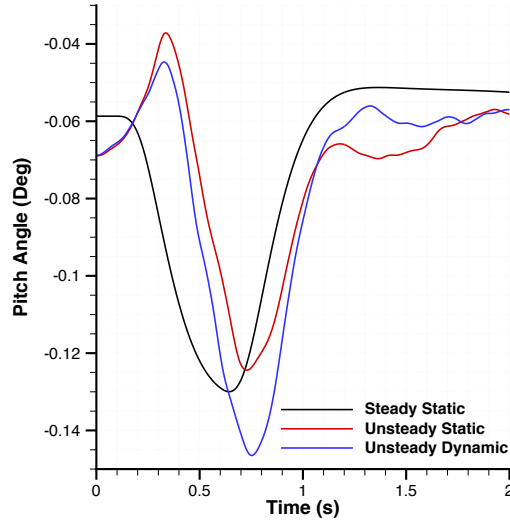
Figure 6.23: Short gust: Pitch angle
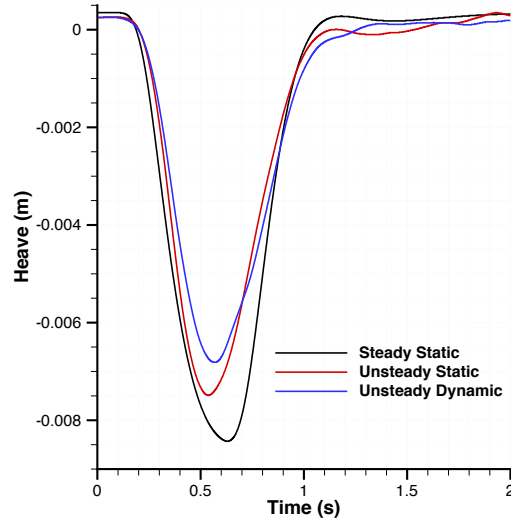
Figure 6.24: Short gust: Heave

6.7.2 Long Gust

For the long gust, the aerodynamic and vehicle responses show many of the same properties as identified in the short gust. Figures 6.25 and 6.26 show the same delay in the steady static side force and yaw moment, whilst the high similarity between the two unsteady methods as the vehicle enters the gust, specifically the percentage of the over shoot in yaw moment, is maintained. Over the latter half of the event and as the vehicle exits, the reduction in yaw moment previously identified is more substantial, due to a larger vehicle yaw angle whilst immersed in the gust, reaching a value of approximately 11.25°, as shown in Figure 6.27. A second consequence of the large yaw angle is that the vehicle is exposed to the gust for longer. The resulting curved trajectory through the gust is evident in the aerodynamic side force by a delay beyond the steady static, when exiting the gust. This effect was not as clear in the short gust as the change in yaw angle and hence path through the gust was much more direct.

As shown by Figure 6.27, at 2.5 seconds, after the vehicle has emerged from the gust, the yaw angle is clearly over predicted by both one-way coupled methods. This is due to the larger aerodynamic yaw moment generated over the latter half of the event when using these techniques. As with the short gust, the deviation is a result of the change in yaw angle during the event and at the end of the event, this deviation

174
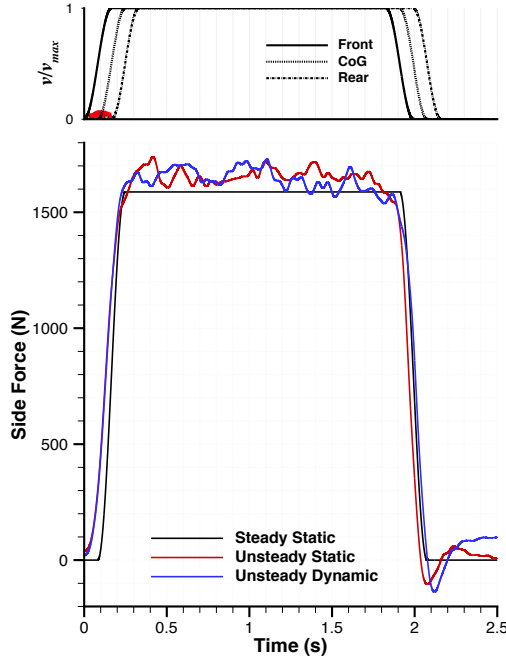
Figure 6.25: Long gust: Side force
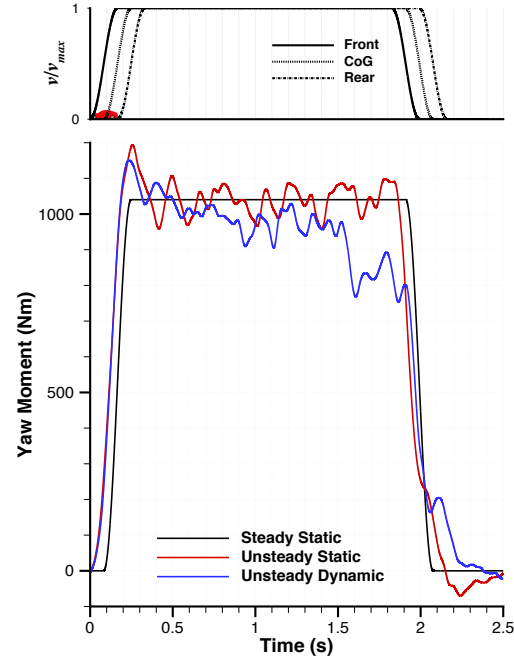
Figure 6.26: Long gust: Yaw moment

has grown to approximately 5.7 m. At this moment, the entire vehicle lies within the adjacent lane. Again due to the delay in the steady static yaw angle, the final deviation value when using this method is reduced, by approximately 7% from the unsteady static, a percentage comparable to the reduction value calculated for the short gust. Interestingly the predicted deviation for the unsteady dynamic method falls between the two one-way coupled methods, which suggests that for this gust length, the steady static delay has a stronger effect on the deviation, than the inclusion of vehicle motion within the simulation. The unsteady static method still provides a *'worst case'* estimate of the vehicle's yaw, but now also lateral response. Based on the current trend, it is reasonable to predict that for an even longer crosswind event, the one-way coupled methods will substantially over predict the lateral deviation, as the differences in vehicle yaw angle and hence aerodynamic yaw moment during the gust will be magnified even further.

The magnitude of the deviation for this long gust is comparable to full-scale experiments of Howell [55]. After repeatedly subjecting an SUV vehicle to an artificially generated crosswind with total length of ten car lengths and mixing layers of three car lengths, this vehicle deviated in the range of 2 m to 3 m after 2 seconds. Figure
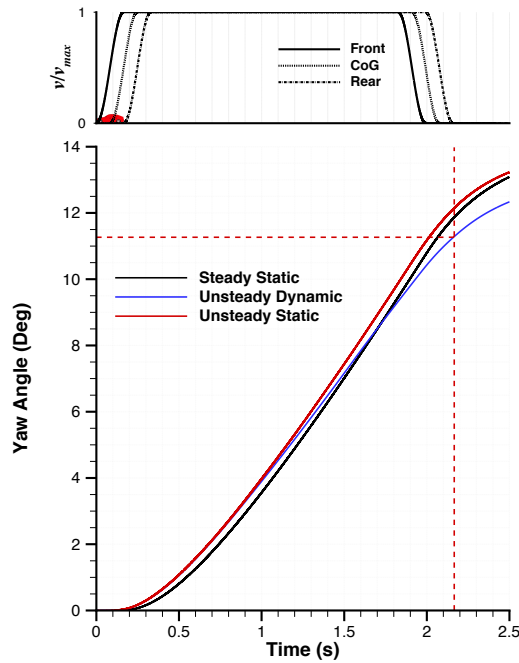
Figure 6.27: Long gust: Yaw angle   Figure 6.28: Long gust: Lateral deviation
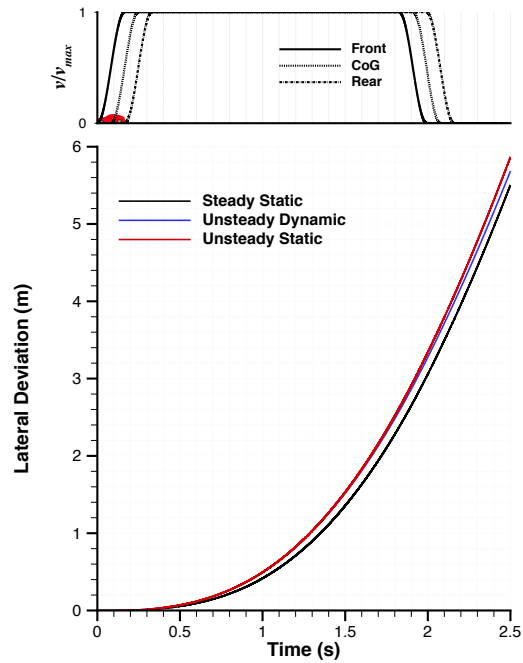
6.28 shows that after a similar amount of time, the predicted deviation of the fast-back is approximately 3.2 m. The difference between these values can be attributed to the change in vehicle classes and hence dynamic properties as well as the variations in the mixing layer lengths, which at larger values, have been shown to produce a quasi-steady behaviour of the aerodynamic loads. Although no specific experimental validation has been performed for the fastback geometry, the similarity in these values instills confidence in the simulation results.

The collective roll, pitch and heave motions still combine to produce a downward motion of the front windward corner, as shown in Figures 6.29, 6.30 and 6.31, however there are some differences in magnitude from the short gust. The maximum roll angle reached by the vehicle is much larger than in the short gust, approximately double in all cases. As with the yaw and lateral responses, the unsteady static method provides an over prediction of this roll response. Although the difference is small, approximately 0.2°, this is further evidence that the inclusion of motion (in this case roll motion) within the CFD simulation, has a damping influence on the overall vehicle response. The small magnitudes of the pitch angle and heave responses are comparable to the short

gust and thus imply that from these three motions, the vehicle is more susceptible to rolling during a crosswind event. The steady static pitch response seems to provide a reasonable average of the two unsteady methods, whereas for heave, this method's results suggest that the body is continually rising on the suspension system throughout the event. In comparison, the unsteady methods predict that after an initial peak in displacement, the body gradually returns to its initial position. From Figure 6.32, it can be seen that this is a direct result of the unsteady aerodynamic lift force.
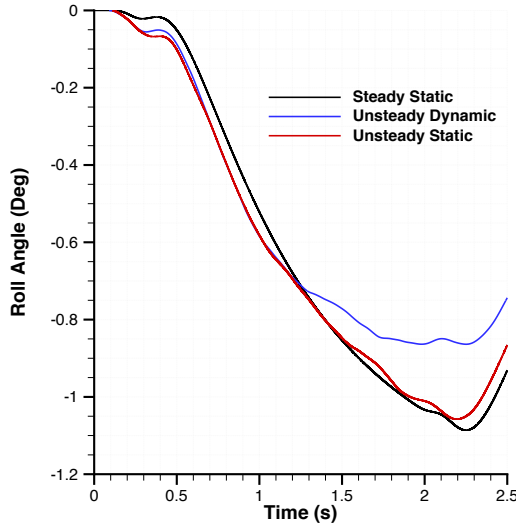
Figure 6.29: Long gust: Roll angle
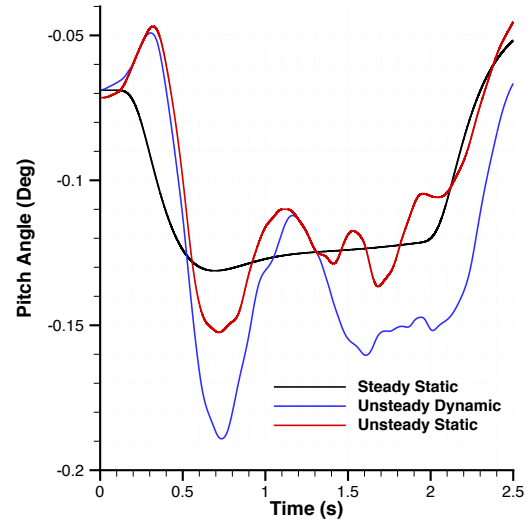
Figure 6.30: Long gust: Pitch angle
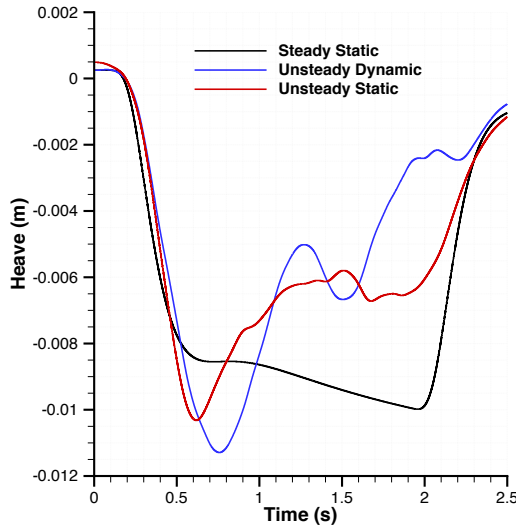
Figure 6.31: Long gust: Heave
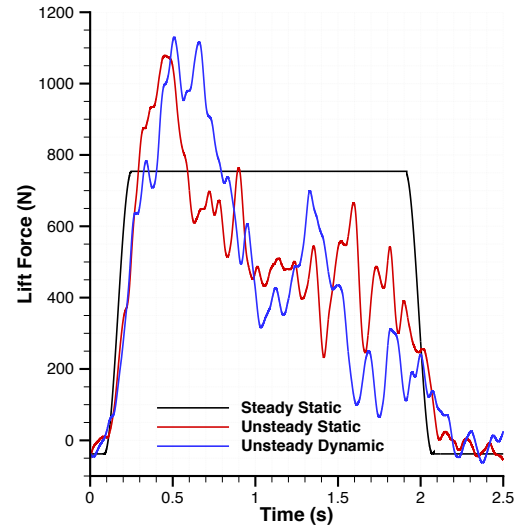
Figure 6.32: Long gust: Lift force

6.7.3 Computational Costs

The costs of running the methods (on 320 cores) are shown in Table 6.4. The steady static cost takes into account the time for two simulations, required as a minimum to generate the aerodynamic response. A speed up parameter, shown alongside the physical time, has been calculated by normalising the two one-way coupled costs by the fully coupled.

Table 6.4: Computational costs of coupling approaches.

	SS	US	UD
Short gust wall clock time (hrs)	24	36	121
Long gust wall clock time (hrs)	30	45	151
Speed up from unsteady dynamic approach	5.1	3.4	**1**

The addition of the moving overset grid approach increases the simulation time by approximately 3.4× over the unsteady static approach. This is a substantial increase from the 2.31× found in the oscillating Davis body simulations, Table 3.3, and provides a measure of the added cost when using more than one overset region in the domain. Over the steady static approach, this speed up is even more substantial, with the fully coupled simulation requiring a factor of 5.1× longer.

6.8 Summary

The results from the open loop manoeuvre, with no driver response, suggest that one-way coupled methods provide a reasonable estimate of the vehicle's response at significant reductions in computational cost, when subjected to both short (4**L**) and long (12**L**) crosswind events. The largest differences in the response between a one-way and fully coupled approach are a result of failing to including the vehicle's time accurate yaw angle and position whilst immersed in the gust. As the vehicle yaws during the crosswind region, the resultant flow velocity reduces, thus lowering the dynamic pres-

sure and consequently the aerodynamic yaw moment, providing a damping effect on the yaw displacement. The one way coupled methods do not include this effect, and thus exposes the vehicle to the maximum flow velocity throughout the event. This leads to over predictions in the values of vehicle yaw angle and lateral deviation. It is predicted that for an even longer event, the quality of the one way coupled response will deteriorate.

It is clear that yaw rotation and lateral translation are the dominant motions in response to a crosswind event with no driver input. With a realistic vehicle dynamics model, the stiffness of the suspension system and inertia of the body limit the pitch, roll and heave motions and do not appear to influence the dominant aerodynamic loads. For future fully coupled crosswind simulations, it seems appropriate to remove these motions from the simulation which will also offer reductions in computational expense.

It can also be seen that the steady static method introduces a time delay into the response, a result of failing to simulate the transient aerodynamic loads as the vehicle enters and exits the gust. In addition, the method inaccurately predicts the unsteady behaviour of the aerodynamic lift force throughout the event. An unsteady method captures the over shoot in the aerodynamic yaw moment which is consistent in magnitude with empirically calculated and experimentally measured values whilst also including the unsteady behaviour of the lift force. It is suggested that for future simulations of this particular test case, an unsteady static approach is used, as this method exposes the vehicle to the largest aerodynamic loads for the duration of the event, thus providing a *'worst case'* prediction of vehicle response. However, when accurate deviation values are required, or the gust no longer acts perpendicularly to the vehicle's initial path, the fully coupled approach is needed.

6.9   Results - Closed Loop

The fully coupled simulation method has also been applied to a closed loop vehicle dynamics system, with a driver in the loop. As already shown, the driver model has been developed using human steering angle data obtained through vehicle simulator

tests of the long crosswind event. The intention of the driver is to maintain their position within the lane. Using the model, the short and long crosswind simulations have been repeated to investigate the influence of a driver during both of these events. The length of the closed loop fully coupled simulations are consistent with the open loop simulations, 2 and 2.5 seconds respectively, however after this point, the vehicle dynamics simulation continues to run to a total time of 10 seconds. This simulation length captures the complete driver's response. As a result, the aerodynamic loads are assumed to be quasi-steady after the aerodynamic simulation has ended. This decision was based on the computational resources that would have been exhausted for a simulation of the complete length, but also the predicted minimal impact that the driver's input would have on the aerodynamics after leaving the gust.

6.9.1   Short Gust

For the short crosswind event, the effect of the driver can be seen in the vehicle's lateral deviation, shown in Figure 6.33. Unlike the open loop response, the driver is able to return the vehicle to its initial path, as intended. A delay in the lateral deviation when compared to the vehicle's yaw angle is consistent throughout the event. When the vehicle first returns to a 0° yaw angle after a positive peak of approximately 2°, the lateral deviation is not at its maximum. This delay is maintained at the next zero-crossing which does not coincide with the negative peak in position as the driver overshoots the initial path. This delay implies that in addition to yaw angle, a lateral slip contributes to the deviation.

The driver applies a steering input in an attempt to bring the vehicle back to its initial path. Figure 6.34 shows the steering wheel angle during and after the gust. By comparing this response to the vehicle's lateral deviation in Figure 6.33, it is clear that the driver is not explicitly responding to the position of the vehicle, as the peak steer angles occur well before the vehicle has reached the positive and negative extremes of lateral position. The driver actually responds to the vehicle's yaw motion. A negative steer angle of approximately 12° in magnitude is applied in an attempt to recover from the positive yaw angle that has developed as a result of the gust. This peak value is
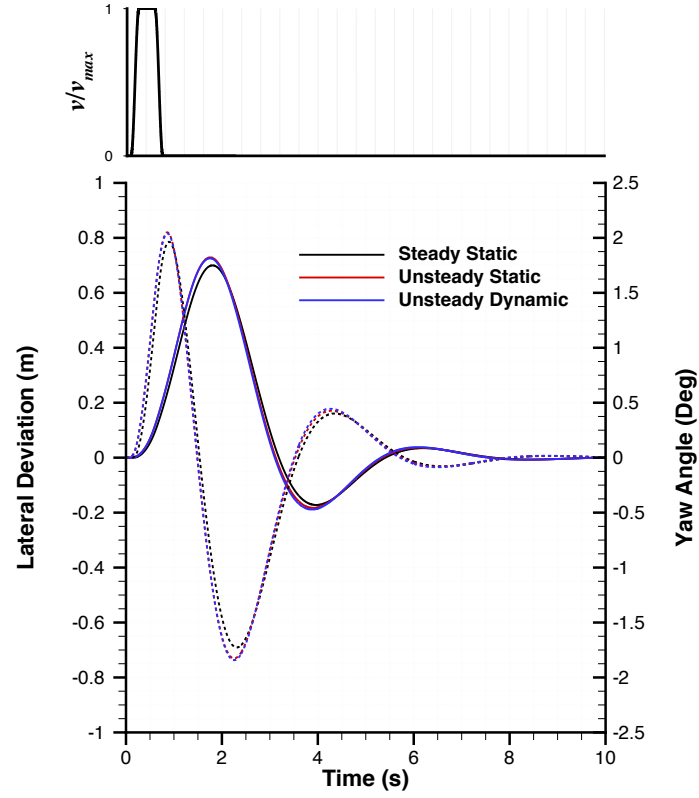
Figure 6.33: Short gust, closed loop: Lateral deviation and yaw angle (Dashed).

applied approximately 1 second after entering the gust and is delayed from the peak yaw angle by approximately 0.15 seconds. As a result the driver is still increasing the magnitude of their steer angle input when the yaw rate of the vehicle switches direction. Due to the length of the gust and the reaction time of the driver, Figure 6.34 clearly shows that the driver only begins to apply the maximum steering input after the crosswind has passed and this delay is responsible for the overshoot from the vehicle's initial path.

The total vehicle response is the sum of the vehicle's reactions due to the driver and due to the gust. The latter has already been obtained with the open loop simulations, thus the influence of driver can be calculated by subtracting the open loop response from the total response with a driver. This is shown in Figure 6.35 through the vehicle's yaw rate and clearly shows the delay in the driver's response. An ideal response would take the form of the anti-phase of the vehicle reactions due to the gust, however the delay in the driver's steer response shifts the vehicle reaction due to the driver. A measure
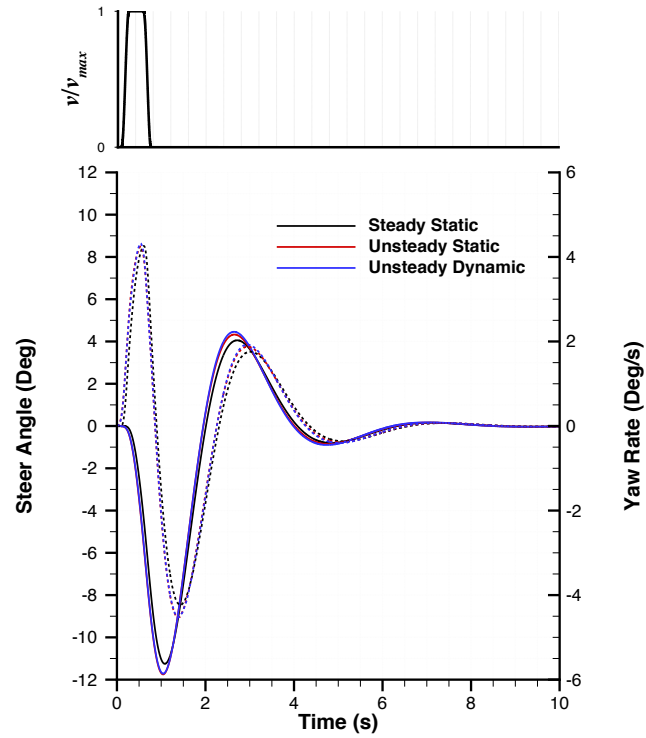
Figure 6.34: Short gust, closed loop: Steering wheel angle and yaw rate (Dashed).

of the quality of the driver's reactions can be calculated using the integral of the yaw rate's absolute value $|\dot{\beta}|$. This value represents the total yaw angle displacement of the vehicle, thus by calculating this value for the simulations with and without driver, the influence of the driver can be numerically quantified. A value of 3.69° for the open loop and 8.86° for closed loop implies that the driver intensifies the vehicle's yaw displacement by a factor of approximately 2.4.

6.9.2 Long Gust

For the long gust, the driver is still able to return the vehicle to its initial path as shown in Figure 6.36, but the time taken to recover is substantially longer than for the short gust. Again a delay in the lateral deviation when compared to the yaw angle of the vehicle indicates that lateral slip contributes to the vehicle's position. The driver's steering input is much more aggressive for this gust, as shown in Figure 6.37. A peak steering wheel angle of over 20° in magnitude is applied to oppose the growing vehicle
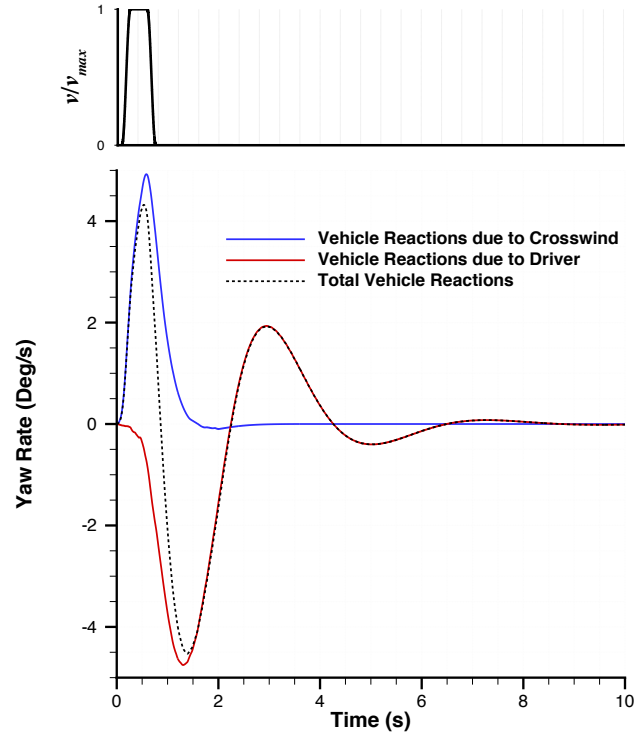
Figure 6.35: Short gust, closed loop: Vehicle reactions due to crosswind and driver.

yaw angle, however the rate at which this angle is applied is similar to the shorter gust. As a result, the delay between the steer angle and vehicle yaw rate responses is similar and an overshoot from the vehicle's initial path is still present.

Deconstructing the vehicle's yaw rate into the reactions due to the gust and due to the driver it is clear the driver's reactions are still unable to cancel out the vehicle reactions due to the gust, as shown in Figure 6.38. By the time the vehicle's yaw rate due to the gust is decreasing, the rate due to the driver's input is still increasing in the opposite direction. The direction of this steering angle is quickly reversed, however as was the case for the short gust, the delay in this switch causes the vehicle to over shoot its initial path.

Due to the longer event and larger steering input, the values of total yaw angle displacement are much larger: without the driver 14.17° and with the driver 18.05°. Despite these larger values, the factor by which the driver intensities the vehicle's response is reduced to 1.27. This is consistent with the work of Wagner and Wiedemann [53] who
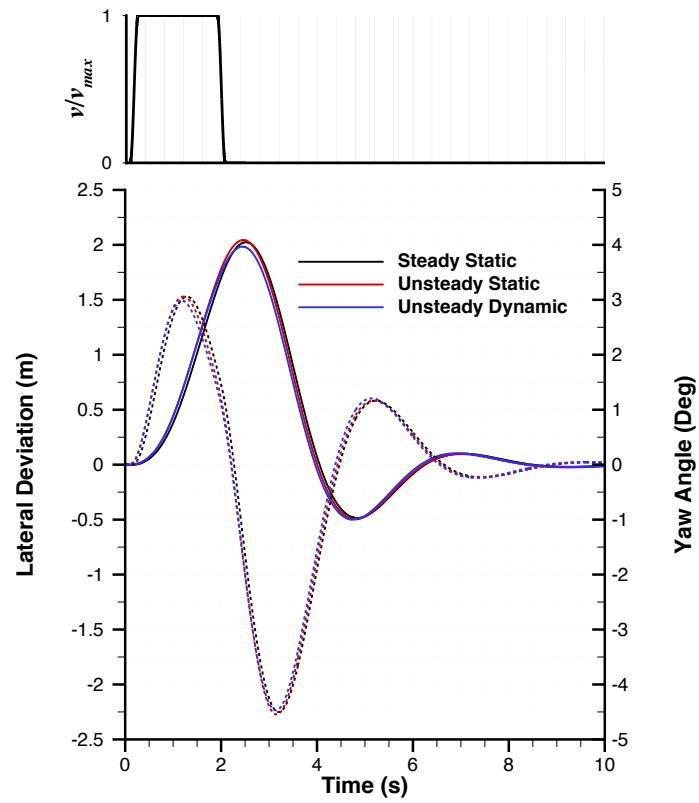
Figure 6.36: Long gust, closed loop: Lateral deviation and yaw angle (Dashed).
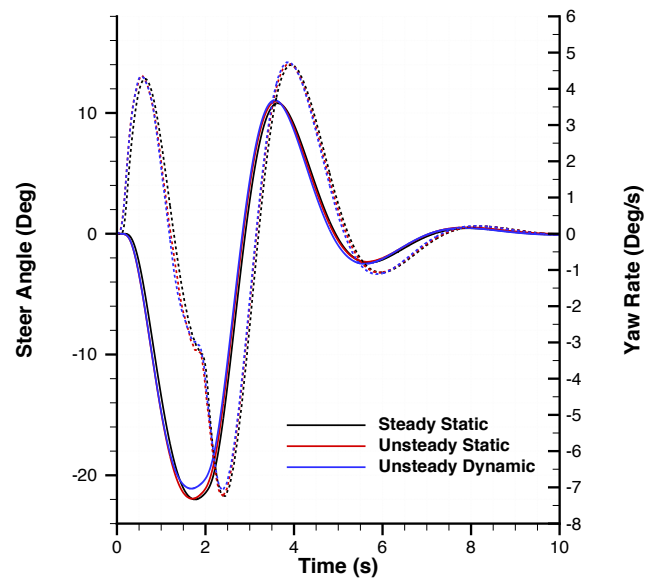
Figure 6.37: Long gust, closed loop: Steering wheel angle and yaw rate (Dashed).
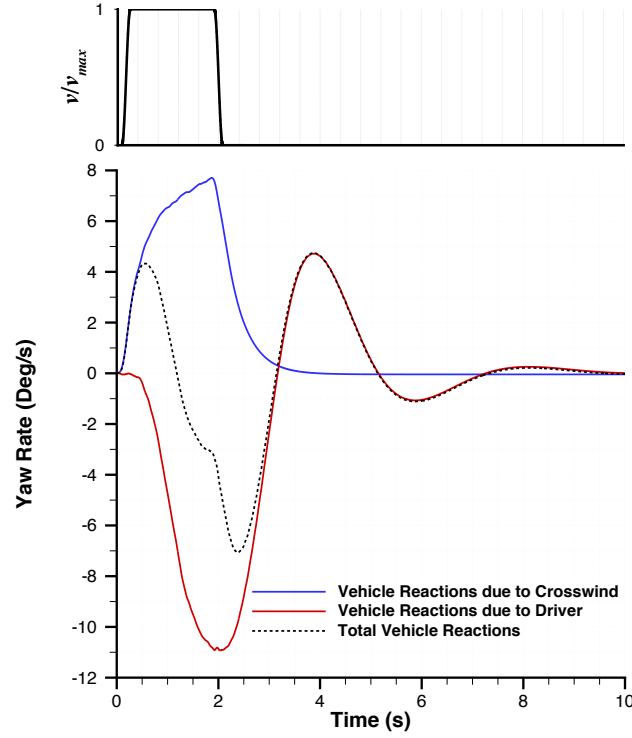
Figure 6.38: Long gust, closed loop: Vehicle reactions due to crosswind and driver.

showed that at the frequency of the short gust (1.5Hz) a driver amplifies the vehicle's reactions with the largest intensification factor, whereas at lower frequencies, such as the long gust (0.5Hz), the driver is able to compensate for the gust to a better extent.

6.9.3 The Influence of Coupling Approach on the Closed Loop Response

For both gusts, the choice of coupling approach has a minimal influence on the driver's and vehicle's responses. As shown in the open loop simulations, variations in the vehicle response are caused by the change in yaw angle and hence aerodynamic loads whilst immersed in the gust. As the driver's input is determined by the vehicle's response, the same will be true for the steering input. For the short gust, due to its length, the variation in vehicle response between the approaches was already minimal in the open loop results and with the addition of the driver, a smaller yaw angle is reached during this period. As a result, the choice of coupling approach has almost no effect on the driver's and vehicle's response for this gust event.

Similarly, for the longer gust, the driver's input reduces the yaw angle reached during the length of the gust. However, the maximum yaw angle reached during this period, 3°, is still large enough to introduce variations into the aerodynamic yaw moment, as shown in Figure 6.39.
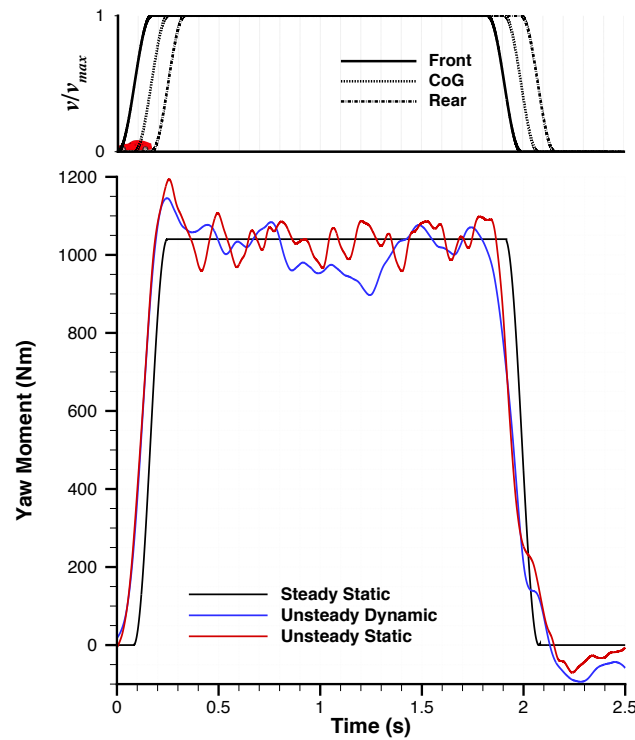
Figure 6.39: Long gust, closed loop: Yaw moment

At approximately 1.3 seconds, the yaw angle of the vehicle reduces the aerodynamic yaw moment by approximately 14% when compared to the steady static value. After this point, a reduction in the yaw angle as the driver returns the vehicle to its initial orientation, increases the aerodynamic yaw moment back towards the maximum loading. However this 'dip' in load is reflected in the steer angle input and lateral deviation, by a reduction of 4% and 3% respectively, from the unsteady static values. This maintains the conclusions of the open loop simulations that the one-way coupled approaches provide a worst case response, although with the addition of the driver, the magnitude of the difference between this worst case and the fully coupled response is reduced.

6.10   Summary

With the inclusion of the driver, it has been shown that the vehicle is able to return to its initial path. The time taken for this recovery is dependent on the length of the gust and it has been shown that for a gust of frequency 1.5Hz, a driver amplifies the vehicle's response. The delay in the driver's response causes the vehicle's yaw displacement to be increased by a factor of approximately 2.4 and this results in an over shoot from the vehicle's initial path. In contrast, for a longer gust of frequency 0.5Hz, the intensification factor of the driver's response on the yaw angle displacement is much lower, approximately 1.27, implying that they have a more positive influence on the vehicle's response.

The use of a fully coupled approach for the closed loop simulation is computationally expensive and does not justify the differences seen in the vehicle response over the one-way coupled methods. As shown in the open loop simulations, the largest variation between the approaches emerges from the difference in vehicle yaw angle whilst immersed in the gust. Due to the driver's steering input, this yaw angle does not reach the levels of the open loop simulations and thus is not large enough to promote significant variation into the aerodynamic loads and vehicle response.

CHAPTER 7

CONCLUSIONS

A fully-coupled, six degree of freedom system in which a vehicle's aerodynamics and dynamics can be assessed using simulation has been designed and evaluated against current, traditional methods.

In such a system, a vehicle's aerodynamics should, where possible, be simulated using a detached-eddy simulation methodology. It was shown through comparison to experimental wind tunnel data of a generic, simplified vehicle geometry, that a Reynolds-Averaged Navier-Stokes method with k-ω SST turbulence model is unable to capture the large levels of turbulent mixing in a vehicle's base wake, resulting in a much larger structure and consequently inaccurate force coefficients. It was felt that despite the large increase in computational time, with DES taking approximately 35 times longer than the RANS simulations to obtain a converged and sufficiently time-averaged prediction, the increase in expense justifies the improvements that are gained in flow physics prediction.

The overset grid technique was shown to be a suitable method of including moving geometry components within a CFD domain, such that a vehicle's dynamic response could be included in an aerodynamics simulation. This was achieved through simulation of experimental wind tunnel data in which a Davis body underwent a continuous oscillation in yaw angle. Although the large levels of flow hysteresis present in the experiment could not be reproduced at the specific reduced frequency ($K = 0.098$), it was felt that this was due to imperfections in the experiment, yawed onset flow or model imperfections, rather than the simulation method. This also agreed with the relationship of reduced frequency and flow unsteadiness published in literature. Flow

hysteresis was present in the simulation at a much larger frequency, ($K = 0.98$), due to delays in the formation and dissipation of the A pillar vortices.

An alternative technique of including motion using a sliding mesh showed minimal differences in side force coefficient behaviour, but ran in approximately 55% of the time taken for the overset grid approach. Despite this speed up, the technique can only be applied to motion with one degree of freedom, thus the method was not suitable for the six degree of freedom, fully coupled system.

The aerodynamic side of the system's architecture uses CD-Adpaco's STAR-CCM+ v10.04.009 and the dynamics model has been programmed in Simulink/MATLAB. Communication between software is performed using a collection of Java macros and a Level-2 MATLAB S-Function. The full set of aerodynamic forces and moments (Drag, Side Force, Lift, Roll, Pitch, Yaw) are sent to the dynamics model and the appropriate vehicle response is calculated. The three translational velocity components and three angular velocity components of the vehicle are then returned to the CFD simulation and the vehicle's position in the domain is updated. This data exchange takes place at every time step, or as desired.

The fully-coupled system was applied to the simulation of crosswind behaviour, but initially the influence of real world flow conditions on a vehicle's aerodynamics was investigated. It was found that the shear in the natural wind during such an event, a result of the atmospheric boundary layer, has a minimal effect on a vehicle's aerodynamic loadings, although this was only investigated for two very similar vehicle geometries (DrivAer model: fastback and estate) and a single, moderate flow yaw angle of 10°. Turbulence of 8% intensity on top of a sheared velocity profile has a much larger effect, decreasing the vehicle's side force and yaw moment coefficients but increasing the drag. Inspection of the flow around the vehicle revealed a reduction in the onset flow yaw angle and delay in flow separation from the rear corners and were suggested as sources for the variations in these aerodynamic loads. The stationary force and moment coefficient gradients suggested that the fastback geometry was more sensitive to crosswinds than the estate and that a steady, unsheared crosswind profile would provide the maximum aerodynamic loads relevant to vehicle stability.

With these conclusions, the fully coupled simulation was performed. The fastback geometry and steady, unsheared flow conditions were selected to provide the potential worst case conditions. Despite this, the results suggested that an unsteady, one-way coupled approach, in which the vehicle position is fixed in the CFD simulation, provides a reasonable prediction of the vehicle's fully coupled response. The realistic but large yaw inertia of the vehicle and high suspension stiffness prevents the vehicle reaching any large attitude or positional change whilst immersed in the gust, from which variations to the aerodynamic loads can arise. These vehicle properties also limited the roll, pitch and heave of the body, and the results suggested that these motions could be removed in favour of a less computationally intense simulation with only three degrees of freedom.

The largest variations between the coupling approaches were between the fully coupled and a steady, one-way coupled approach. Introduction of a time delay due to the loads acting through a single point, neglected any unsteady effects of the gust passing over the length of the vehicle and resulted in an overall under-prediction of the vehicle response.

For the current crosswind conditions, the unsteady, one-way coupled method provided the worst case response. This was due to a constant resultant flow velocity magnitude throughout the event. Whereas in the unsteady-dynamic event, the inclusion of the vehicle's yaw angle response led to reductions in the magnitude of this vector, thus lowering the dynamic pressure and aerodynamic forces.

These conclusions were maintained with the addition of a driver model, calibrated from real driver data recorded on a vehicle simulator. The driver's steering input reduced the vehicle's yaw angle growth whilst immersed in the gust, thus variations between the one-way and fully coupled methods were minimised even further. By comparing the vehicle response with and without a driver, the effectiveness of the steering input could be determined. It was shown that at a gust frequency of 1.5Hz, a driver intensifies the vehicle's yaw angle displacement to a greater extent when compared to the response during a longer gust of over three times the length. This was mainly due to a delay in the driver's initial reaction to the gust and is consistent with existing literature.

For the crosswind conditions simulated, which represent a severe and rare event, the computational cost of running a fully-coupled simulation does not justify the differences

between the one-way coupled vehicle response. A change in gust conditions or an alternative vehicle that is more sensitive to yaw motion, either through production of a larger aerodynamic yaw moment or lower body inertia, may widen the differences in dynamic response and support the use of the fully-coupled system.

It is suggested that in future applications, for example during a vehicle's design process, that an unsteady, one way coupled approach is taken to determine the effects of severe crosswinds on vehicle dynamics. This technique can be performed using the vast majority of commercial and open-source CFD codes and does not require any complex features, such as the overset grid method, which at present is not widely available. Should the results obtained using this approach suggest that the response of the vehicle will be significantly altered during the event, then the more computationally intense and complex fully coupled approach is an appealing tool that could be exploited.

REFERENCES

[1] ESDU, "Strong winds in the atmospheric boundary layer Part 1: hourly-mean wind speeds," Tech. Rep. 82026, Sept. 1982.

[2] I. Van der Hoven, "Power Spectrum of Horizontal Wind Speed in the Frequency Range from 0.0007 to 900 Cycles per Hour," *Journal of Meteorology*, vol. 14, pp. 160–164, Oct. 1957.

[3] I. Van der Hoven and H. Panofsky, "Spectra and cross-spectra of velocity components in the mesometeorological range," *Quarterly Journal of the Royal Meteorological Society*, vol. 81, pp. 603–606, 1955.

[4] K. R. Cooper and S. Watkins, "The Unsteady Wind Environment of Road Vehicles, Part One: A Review of the On-road Turbulent Wind Environment," in *SAE Technical Paper*, no. 2007-01-1236, Apr. 2007.

[5] H. Teunissen, "Characteristics of the Mean Wind and Turbulence in the Planetary Boundary Layer," Tech. Rep. 32, Institute for Aerospace Studies, Oct. 1970.

[6] S. Watkins, *Wind-Tunnel Modelling of Vehicle Aerodynamics: With Emphasis on Turbulent Wind Effects on Commercial Vehicle Drag.* PhD thesis, Victorian University of Technology R.M.I.T. Campus, Nov. 1990.

[7] C. Scruton, "A Review of Industrial Problems Related to Atmospheric Shear Flows," in *AGARD Conference Proceedings No. 48*, no. 23, 1969.

[8] L. Prandtl, "Über Flüssigkeitsbewegung bei sehr kleiner Reibung," in *3rd International Congress of Mathematicians*, (Heidelberg, Germany), 1904.

[9] R. G. J. Flay, *Structure of a Rural Atmospheric Boundary Layer Near the Ground.* PhD thesis, University of Canterbury, New Zealand, Nov. 1978.

[10] J. D. Holmes, *Wind Loading of Structures.* Taylor and Francis, 2 ed., 2007.

[11] C. L. Archer and M. Z. Jacobson, "Evaluation of global wind power," *Journal of Geophysical Research: Atmospheres*, vol. 110, no. D12, 2005.

[12] Department of Energy and Climate Change, "Average wind speed and deviations from the long term mean," Tech. Rep. ET 7.2, 2015 (accessed December, 2015).

[13] P. Sachs, *Wind Forces in Engineering.* Pergamon Press, 2 ed., 1978.

[14] BSi, "Load for buildings. Part 2. Code of practice for wind loads," Tech. Rep. BS 6399: Part 2, 1995.

[15] BSi, "Code of Basic data for the design of buildings - Chapter V: Loading - Part 2: Wind Loads," Tech. Rep. CP 3: Chapter V-2: 1972, 1972.

[16] R. Harris, "The nature of wind," in *Proceedings from Seminar: The Modern Design of Wind Sensitive Structures*, no. Paper 3, (London, UK), 1971.

[17] A. Davenport, "The relationship of wind structure to wind loading," in *Proceedings from National Physical Laboratory Conference: Wind Effects on Buildings and Structures*, no. Paper 2, (Teddington, UK), 1963.

[18] ESDU, "Strong winds in the atmospheric boundary layer Part 2: discrete gust speeds," Tech. Rep. 83045, Nov. 1983.

[19] ESDU, "Characteristics of atmospheric turbulence near the ground Part II: single point data for strong winds (neutral atmosphere)," Tech. Rep. 85020, Oct. 1985.

[20] A. Macklin, K. Garry, and J. Howell, "Comparing Static and Dynamic Testing Techniques for the Crosswind Sensitivity of Road Vehicles," in *SAE Technical Paper*, no. 960674, Feb. 1996.

[21] A. Lawson, D. B. Sims-Williams, and R. G. Dominy, "Effects of On-Road Turbulence on Vehicle Surface Pressures in the A-Pillar Region," *SAE International Journal of Passenger Cars - Mechanical Systems*, vol. 1, pp. 1–8, Apr. 2008.

[22] J. Wojciak, *Quantitative Analysis of Vehicle Aerodynamics during Crosswind Gusts.* PhD thesis, Technische Universtät München, Jan. 2012.

[23] P. Theissen, *Unsteady Vehicle Aerodynamics in Gusty Crosswind.* PhD thesis, Technische Universtät München, Jan. 2012.

[24] S. Watkins and J. W. Saunders, "Turbulence Experienced by Road Vehicles under Normal Driving Conditions," in *SAE Technical Paper*, no. 950997, Mar. 1995.

[25] J. Howell, "Real Environment for Vehicles on the Road," in *Euromotor - Progress in Vehicle Aerodynamics*, (Stuttgart, Germany), pp. 1–17, 2000.

[26] S. Wordley and J. W. Saunders, "On-road Turbulence," *SAE International Journal of Passenger Cars - Mechanical Systems*, vol. 1, pp. 1–20, Apr. 2008.

[27] S. Wordley and J. W. Saunders, "On-Road Turbulence: Part 2," in *SAE International Journal of Passenger Cars - Mechanical Systems*, pp. 111–137, Apr. 2009.

[28] B. R. McAuliffe, L. Belluz, and M. Belzile, "Measurement of the On-Road Turbulence Environment Experienced by Heavy Duty Vehicles," *SAE International Journal of Commercial Vehicles - Mechanical Systems*, vol. 7, pp. 685–702, Sept. 2014.

[29] J. W. Saunders and R. B. Mansour, "On-Road and Wind Tunnel Turbulence and its Measurement Using a Four-Hole Dynamic Probe Ahead of Several Cars," in *SAE Technical Paper*, no. 2000-01-0350, Mar. 2000.

[30] O. Mankowski, D. Sims-Williams, and R. Dominy, "A Wind Tunnel Simulation Facility for On-Road Transients," *SAE International Journal of Passenger Cars - Mechanical Systems*, vol. 7, pp. 1087–1095, Apr. 2014.

[31] B. R. McAuliffe, A. Wall, and G. Larose, "Simulation of Atmospheric Turbulence for Wind-Tunnel Tests on Full-Scale Light-Duty Vehicles," *SAE International Journal of Passenger Cars - Mechanical Systems*, vol. 9, pp. 583–591, Apr. 2016.

[32] B. R. McAuliffe and A. D'Auteuil, "A System for Simulating Road-Representative Atmospheric Turbulence for Ground Vehicles in a Large Wind Tunnel," *SAE International Journal of Passenger Cars - Mechanical Systems*, vol. 9, pp. 817–830, Apr. 2016.

[33] J. Howell, P. Newnham, and M. Passmore, "Effect of Free Stream Turbulence on Road Vehicle Aerodynamics," *FKFS - 6th Aerodynamic Conference 2007*, pp. 1–18, July 2007.

[34] P. Newnham, *The influence of turbulence on the aerodynamic optimisation of bluff body road vehicles.* PhD thesis, Loughborough University, May 2007.

[35] A. Cogotti, "Generation of a Controlled Level of Turbulence in the Pininfarina Wind Tunnel for the Measurement of Unsteady Aerodynamics and Aeroacoustics," in *SAE Technical Paper*, no. 2003-01-0430, Mar. 2003.

[36] H. Kobayashi and A. Hatanaka, "Active Generation of Wind Gust in a Two-Dimensional Wind Tunnel," *Journal of Wind Engineering and Industrial Aerodynamics*, vol. 41-44, pp. 959–970, 1992.

[37] A. Cogotti, "Update on the Pininfarina "Turbulence Generation System" and its effects on the Car Aerodynamics and Aeroacoustics," in *SAE Technical Paper*, no. 2004-01-0807, Mar. 2004.

[38] G. Carlino and A. Cogotti, "Simulation of Transient Phenomena with the Turbulence Generation System in the Pininfarina Wind Tunnel," in *SAE Technical Paper*, no. 2006-01-1031, Apr. 2006.

[39] P. Bearman and S. Mullarkey, "Aerodynamic Forces on Road Vehicles Due to Steady Side Winds and Gusts," in *Proceedings from Royal Aeronautical Society Vehicle Aerodynamics Conference*, (Loughborough, UK), 1994.

[40] M. Passmore, S. Richardson, and A. Imam, "An experimental study of unsteady vehicle aerodynamics," *Proceedings of the Institution of Mechanical Engineers, Part D: Journal of Automobile Engineering*, pp. 779–788, May 2009.

[41] D. Schröck, N. Widdecke, and J. Wiedemann, "Aerodynamics Response of a Vehicle Model to Turbulent Wind," in *Proceedings from 7th FKFS Conference*, (Stuttgart, Germany), Oct. 2009.

[42] R. Blumrich, N. Widdecke, J. Wiedemann, A. Michelbach, F. Wittmeier, and O. Beland, "New FKFS Technology at the Full-Scale Aeroacoustic Wind Tunnel of University of Stuttgart," *SAE International Journal of Passenger Cars - Mechanical Systems*, vol. 8, Apr. 2015.

[43] A. D'Hooge, L. Rebbeck, R. Palin, Q. Murphy, J. Gargoloff, and B. Duncan, "Application of Real-World Wind Conditions for Assessing Aerodynamic Drag

for On-Road Range Prediction," in *SAE Technical Paper*, no. 2015-01-1551, Apr. 2015.

[44] A. Gaylard, N. Oettle, B. Duncan, and J. I. Gargoloff, "Effect of Non-Uniform Flow Conditions on Vehicle Aerodynamic Performance," in *FKFS - 9th Aerodynamic Conference 2013*, (Stuttgart, Germany), pp. 63–78, Oct. 2013.

[45] A. P. Gaylard, N. Oettle, J. Gargoloff, and B. Duncan, "Evaluation of Non-Uniform Upstream Flow Effects on Vehicle Aerodynamics," *SAE International Journal of Passenger Cars - Mechanical Systems*, vol. 7, pp. 692–702, Apr. 2014.

[46] A. D'Hooge, R. Palin, L. Rebbeck, J. Gargoloff, and B. Duncan, "Alternative Simulation Methods for Assessing Aerodynamic Drag in Realistic Crosswind," *SAE International Journal of Passenger Cars - Mechanical Systems*, vol. 7, Apr. 2014.

[47] N. Oettle, D. B. Sims-Williams, R. G. Dominy, C. Darlington, C. Freeman, and P. Tindall, "The Effects of Unsteady On-Road Flow Conditions on Cabin Noise," in *SAE Technical Paper*, no. 2010-01-0289, Apr. 2010.

[48] N. Oettle, O. Mankowski, D. Sims-Williams, R. Dominy, C. Freeman, and A. Gaylard, "Assessment of a Vehicle's Transient Aerodynamic Response," in *SAE Technical Paper*, no. 2012-01-0449, Apr. 2012.

[49] N. Oettle, O. Mankowski, D. Sims-Williams, R. Dominy, and C. Freeman, "Evaluation of the Aerodynamic and Aeroacoustic Response of a Vehicle to Transient Flow Conditions," *SAE International Journal of Passenger Cars - Mechanical Systems*, vol. 6, pp. 389–402, Apr. 2013.

[50] A. Lawson, R. G. Dominy, D. B. Sims-Williams, and P. Mears, "A Comparison Between On-Road and Wind Tunnel Surface Pressure Measurements on a Mid-Sized Hatchback," in *SAE Technical Paper*, no. 2007-01-0898, Apr. 2007.

[51] N. Lindener, H. Miehling, A. Cogotti, F. Cogotti, and M. Maffei, "Aeroacoustic Measurements in Turbulent Flow on the Road and in the Wind Tunnel," in *SAE Technical Paper*, no. 2007-01-1551, Apr. 2007.

[52] C. Kounenis, D. Sims-Williams, R. Dominy, A. Berson, N. Oettle, and C. Freeman, "The Effects of Unsteady Flow Conditions on Vehicle in Cabin and External Noise Generation," in *SAE Technical Paper*, no. 2015-01-1555, Apr. 2015.

[53] A. Wagner and J. Wiedemann, "Crosswind Behavior in the Driver's Perspective," in *SAE Technical Paper*, no. 2002-01-0086, Mar. 2002.

[54] Applus IDIADA, "Crosswind Facility," tech. rep., accessed September 2015).

[55] J. Howell, "Experimental Results from a Small SUV Tested in the MIRA Crosswind Generator," in *Proceedings from MIRA International Vehicle Aerodynamics Conference*, (Birmingham, UK), Oct. 1996.

[56] R. Klein and J. Hogue, "Effects of Crosswinds on Vehicle Response-Full-Scale Tests and Analytical Predictions," in *SAE Technical Paper*, no. 800848, June 1980.

[57] R. Klein and H. Jex, "Development an Calibration of an Aerodynamic Disturbance Test Facility," in *SAE Technical Paper*, no. 800143, Mar. 1980.

[58] International Organization for Standardization, "Road Vehicles - Sensitivity to lateral wind - Open-loop test method using wind generator input," Tech. Rep. ISO 12021:2010, 2010.

[59] D. Stoll, T. Kuthada, J. Wiedemann, and T. Schütz, "Unsteady Aerodynamic Vehicle Properties of the DrivAer Model in the IVK Model Scale Wind Tunnel," in *Proceedings from 10th FKFS Conference*, (Stuttgart, Germany), Aug. 2015.

[60] S. Watkins, S. Toksoy, and S. J, "On the Generation of Tunnel Turbulence for Road Vehicles," in *11th Australasian Fluid Mechanics Conference*, (Hobart, Australia), pp. 223–226, Dec. 1992.

[61] F. N. Beauvais, "Transient Nature of Wind Gust Effects on an Automobile," in *SAE Technical Paper*, no. 670608, Feb. 1967.

[62] A. Ryan and R. G. Dominy, "The Aerodynamic Forces Induced on a Passenger Vehicle in Response to a Transient Cross-Wind Gust at a Relative Incidence of $30°$," in *SAE Technical Paper*, no. 980392, Feb. 1998.

198

REFERENCES

[63] R. G. Dominy and A. Ryan, "An Improved Wind Tunnel Configuration for the Investigation of Aerodynamic Cross Wind Gust Response," in *SAE Technical Paper*, no. 1999-01-0808, Mar. 1999.

[64] A. Ryan and R. G. Dominy, "Wake Surveys Behind a Passenger Car Subjected to a Transient Cross-Wind Gust," in *SAE Technical Paper*, no. 2000-01-0874, Mar. 2000.

[65] R. Volpe, A. Da Silva, V. Ferrand, and L. Le Moyne, "Experimental and Numerical Validation of a Wind Gust Facility," *ASME Journal of Fluids Engineering*, vol. 135, pp. 011106–1–9, Jan. 2013.

[66] R. Volpe, V. Ferrand, A. Da Silva, and L. Le Moyne, "Forces and flow structures evolution on a car body in a sudden crosswind," *Journal of Wind Engineering and Industrial Aerodynamics*, vol. 128, pp. 114–125, May 2014.

[67] M. Tsubokura, T. Nakashima, T. Ikenaga, K. Onishi, K. Kitoh, N. Oshima, and T. Kobayashi, "HPC-LES for the Prediction of Unsteady Aerodynamic Forces on a Vehicle in a Gusty Cross-flow Condition," in *SAE Technical Paper*, no. 2008-01-3001, Apr. 2008.

[68] T. Nakashima, M. Tsubokura, T. Ikenaga, and Y. Doi, "HPC-LES for Unsteady Aerodynamics of a Heavy Duty Truck in Wind Gust - 2nd report: Coupled Analysis with Vehicle Motion," in *SAE Technical Paper*, no. 2010-01-1021, Apr. 2010.

[69] M. Tsubokura and T. Nakashima, "Unsteady Aerodynamic Simulator for Road Vehicles Based on Large-Eddy Simulation," in *Proceedings from 8th MIRA International Vehicle Aerodynamics Conference*, (Grove, UK), Oct. 2010.

[70] T. Nakashima, M. Tsubokura, S. Matsuda, and Y. Doi, "Coupled Analysis of Unsteady Aerodynamics and 6DOF Motion of a Heavy Duty Truck in Strong Wind Gusts," in *29th AIAA Applied Aerodynamics Conference*, (Orlando, FL), pp. 1–11, June 2011.

[71] M. Tsubokura, Y. Ikawa, T. Nakashima, Y. Okada, T. Kamioka, and T. Nouzawa, "Unsteady Vehicle Aerodynamics during a Dynamic Steering Action: 2nd Report,

Numerical Analysis," *SAE International Journal of Passenger Cars - Mechanical Systems*, vol. 5, pp. 340–357, Apr. 2012.

[72] T. Nakashima, M. Tsubokura, M. Vázquez, H. Owen, and Y. Doi, "Coupled analysis of unsteady aerodynamics and vehicle motion of a road vehicle in windy conditions," *Computers and Fluids*, vol. 80, pp. 1–9, July 2013.

[73] J. Steger, F. Dougherty, and J. Benek, "A Chimera Grid Scheme," in *Proceedings from Applied Mechanics, Bioengineering and Fluids Engineering Conference*, (Houston, TX), pp. 59–69, 1983.

[74] W. Hucho and H. Emmelmann, "Theoretical Prediction of the Aerodynamic Derivatives of a Vehicle in Cross Wind Gusts," in *SAE Technical Paper*, no. 730232, Feb. 1973.

[75] T. Favre, *Aerodynamics simulations of ground vehicles in unsteady crosswind*. PhD thesis, KTH Engineering Sciences, Dec. 2011.

[76] H. Hemida and S. Krajnović, "Transient Simulation of the Aerodynamic Response of a Double-Deck Bus in Gusty Winds," *Journal of Fluids Engineering*, vol. 131, no. 3, pp. 1–10, 2009.

[77] A. Wood, M. Passmore, D. Forbes, D. Wood, and A. Gaylard, "Base Pressure and Flow-Field Measurements on a Generic SUV Model," *SAE International Journal of Passenger Cars - Mechanical Systems*, vol. 8, pp. 1–9, Apr. 2015.

[78] G. Johl, *The Design and Performance of a 1.9m × 1.3m Indraft Wind Tunnel*. PhD thesis, Loughborough University, Apr. 2010.

[79] G. Johl, M. Passmore, and P. Render, "Design Methodology and Performance of an Indraft Wind Tunnel," *The Aeronautical Journal*, pp. 465–473, Sept. 2004.

[80] F. Menter, "Zonal two-equation k-ω turbulence model for aerodynamic flows," in *24th Fluid Dynamics Conference*, (Orlando, FL), pp. 1–22, July 1993.

[81] N. Ashton and A. Revell, "Key factors in the use of DDES for the flow around a simplified car," *International Journal of Heat and Fluid Flow*, vol. 54, pp. 236–249, June 2015.

[82] N. Ashton, A. West, S. Lardeau, and A. Revell, "Assessment of RANS and DES methods for realistic automotive models," *Computers and Fluids*, vol. 128, pp. 1–15, Apr. 2016.

[83] S. R. Ahmed, G. Ramm, and G. Faltin, "Some Salient Features Of The Time-Averaged Ground Vehicle Wake," in *SAE Technical Paper*, no. 840300, Feb. 1984.

[84] G. K. Batchelor, *The Theory of Homogeneous Turbulence.* Cambridge University Press, 1953.

[85] J. Baden Fuller, *The unsteady aerodynamics of static and oscillating simple automotive bodies.* PhD thesis, Loughborough University, Aug. 2012.

[86] J. P. Davis, *Wind Tunnel Investigation of Road Vehicle Wakes.* PhD thesis, Imperial College of Science and Technology, University of London, Oct. 1982.

[87] J. Fuller and M. A. Passmore, "The importance of rear pillar geometry on fastback wake structures," *Journal of Wind Engineering and Industrial Aerodynamics*, vol. 125, pp. 111–120, Feb. 2014.

[88] E. Mercker, N. Breuer, H. Berneburg, and H. Emmelmann, "On the Aerodynamic Interference Due to the Rolling Wheels of Passenger Cars," in *SAE Technical Paper*, no. 910311, Feb. 1991.

[89] L. Axon, K. Garry, and J. Howell, "An Evaluation of CFD for Modelling the Flow Around Stationary and Rotating Isolated Wheels," in *SAE Technical Paper*, no. 980032, Feb. 1998.

[90] G. Wickern, K. Zwicker, and M. Pfadenhauer, "Rotating Wheels - Their Impact on Wind Tunnel Test Techniques and on Vehicle Drag Results," in *SAE Technical Paper*, no. 970133, Feb. 1997.

[91] A. Waschle, "The Influence of Rotating Wheels on Vehicle Aerodynamics - Numerical and Experimental Investigations," in *SAE Technical Paper*, no. 2007-01-0107, Apr. 2007.

[92] B. Duncan, S. Kandasamy, K. Sbeih, T. H. Lounsberry, and M. E. Gleason, "Further CFD Studies for Detailed Tires using Aerodynamics Simulation with Rolling Road Conditions," in *SAE Technical Paper*, no. 2010-01-0756, Apr. 2010.

[93] P. Mlinaric and S. Sebben, "Investigation of the Influence of Tyre Deflection and Tyre Contact Patch on CFD Predictions of Aerodynamic Forces on a Passenger Car," in *7th MIRA International Vehicle Aerodynamics Conference*, (Coventry, UK), pp. 312–323, Oct. 2008.

[94] S. Cyr, K.-D. Ih, and S.-H. Park, "Accurate Reproduction of Wind-Tunnel Results with CFD," in *SAE Technical Paper*, no. 2011-01-0158, Apr. 2011.

[95] C. Albukrek, P. Doddegowda, A. Ivaldi, J. Amodeo, and E. Bardoscia, "Unsteady Flow Analysis of a Formula Type Open Wheel Race Car in Cornering," in *SAE Technical Paper*, no. 2006-01-3661, Dec. 2006.

[96] B. Duncan and K. Golsch, "Characterization of Separated Turbulent Flow Regions in CFD Results for a Pontiac NASCAR Race Car," in *SAE Technical Paper*, pp. 1–39, Dec. 2004.

[97] S. Kandasamy, B. Duncan, H. Gau, F. Maroy, A. Belanger, N. Gruen, and S. Schäufele, "Aerodynamic Performance Assessment of BMW Validation Models using Computational Fluid Dynamics," in *SAE Technical Paper*, no. 2012-01-0297, Apr. 2012.

[98] C. Landstrom and L. Lofdahl, "Detailed Flow Studies in Close Proximity of Rotating Wheels on a Passenger Car," *SAE International Journal of Passenger Cars - Mechanical Systems*, vol. 2, pp. 861–874, Apr. 2009.

[99] S. Sebben and C. Landstrom, "Prediction of Aerodynamic Drag for Different Rim Designs Using Varied Wheel Modelling in CFD," in *8th FKFS Conference - Progress in Vehicle Aerodynamics and Thermal Management*, (Stuttgart, Germany), pp. 1–4, Sept. 2011.

[100] A. D'Hooge, R. B. Palin, S. Johnson, B. Duncan, and J. I. Gargoloff, "The Aerodynamic Development of the Tesla Model S - Part 2: Wheel Design Optimization," in *SAE Technical Paper*, no. 2012-01-0178, Apr. 2012.

[101] T. Hobeika, S. Sebben, and C. Landstrom, "Investigation of the Influence of Tyre Geometry on the Aerodynamics of Passenger Cars," *SAE International Journal of Passenger Cars - Mechanical Systems*, vol. 6, pp. 316–325, May 2013.

[102] C. Landstrom, T. Walker, L. Christoffersen, and L. Lofdahl, "Influences of Different Front and Rear Wheel Designs on Aerodynamic Drag of a Sedan Type Passenger Car," in *SAE Technical Paper*, no. 2011-01-0165, Apr. 2011.

[103] C. Landstrom, S. Sebben, and L. Lofdahl, "Effects of Wheel Orientation on Predicted Flow Field and forces when modelling rotating wheels using CFD," in *8th MIRA International Vehicle Aerodynamics Conference*, (Grove, UK), pp. 1–9, Oct. 2010.

[104] S. Koitrand, L. Lofdahl, S. Rehnberg, and A. Gaylard, "A Computational Investigation of Ground Simulation for a Saloon Car," *SAE International Journal of Commercial Vehicles*, vol. 7, pp. 111–123, Apr. 2014.

[105] M. Tsubokura, T. Nakashima, K. Kitoh, Y. Sasaki, N. Oshima, and T. Kobayashi, "Development of an Unsteady Aerodynamic Simulator Using Large-Eddy Simulation Based on High-Performance Computing Technique," *SAE International Journal of Passenger Cars - Mechanical Systems*, vol. 2, pp. 168–178, Jan. 2009.

[106] K. Okumura and T. Kuriyama, "Transient Aerodynamic Simulation in Crosswind and Passing an Automobile," in *SAE Technical Paper*, no. 970404, Feb. 1997.

[107] D. Uystepruyst and S. Krajnović, "Numerical simulation of the transient aerodynamic phenomena induced by passing manoeuvres," *Journal of Wind Engineering and Industrial Aerodynamics*, vol. 114, pp. 62–71, Feb. 2013.

[108] R. J. Corin, L. He, and R. G. Dominy, "A CFD investigation into the transient aerodynamic forces on overtaking road vehicle models," *Journal of Wind Engineering and Industrial Aerodynamics*, vol. 96, pp. 1390–1411, May 2008.

[109] J. P. Dean, J. D. Clifton, D. J. Bodkin, and J. C. Ratcliff, "High Resolution CFD Simulations of Manoeuvering Aircraft Using the CREATE-AV/Kestrel Solver," in *49th AIAA Aerospace Sciences Meeting*, (Orlando, Florida), pp. 1–22, Jan. 2011.

[110] S. Morton, T. A. Eymann, D. R. McDaniel, D. R. Sears, B. Tillman, and T. R. Tuckey, "Rigid and Maneuvering Results with Control Surface and 6DoF Motion for Kestrel v2," in *49th AIAA Aerospace Sciences Meeting*, (Orlando, Florida), pp. 1–20, Jan. 2011.

[111] S. Y. Cheng, M. Tsubokura, T. Nakashima, T. Nouzawa, and Y. Okada, "A numerical analysis of transient flow past road vehicles subjected to pitching oscillation," *Journal of Wind Engineering and Industrial Aerodynamics*, vol. 99, pp. 511–522, Apr. 2011.

[112] M. Tsubokura, S. Y. Cheng, T. Nakashima, Y. Okada, and T. Nouzawa, "Simulation and Analysis of Effects of Dynamic Pitching for Idealized Sedan-Type Vehicle Models," in *SAE Technical Paper*, no. 2011-01-0153, Apr. 2011.

[113] T. Kawamura and A. Ogawa, "Effect of Unsteady Lift Force on Vehicle Dynamics in Heave and Pitch Motion," in *SAE Technical Paper*, no. 2014-01-0576, Apr. 2014.

[114] M. Kawakami, N. Sato, P. Aschwanden, J. Mueller, Y. Kato, M. Nakagawa, and E. Ono, "Validation and Modeling of Transient Aerodynamic Loads Acting on a Simplified Passenger Car Model in Sinusoidal Motion," in *SAE International Journal of Passenger Cars - Mechanical Systems*, pp. 324–339, May 2012.

[115] William M. Chan, "Overset grid technology development at NASA Ames Research Center," *Computers and Fluids*, vol. 38, pp. 496–503, Mar. 2009.

[116] P. Buning, I. Chiu, S. Obayashi, Y. Rizk, and J. Steger, "Numerical simulations of the integrated space shuttle vehicle in ascent," in *AIAA Paper*, no. 1988-4359, 1988.

[117] I. Chiu, R. Pletcher, and J. Steger, "On Computations of the Integrated Space Shuttle Flowfield Using Overset Grids," Tech. Rep. NASA-DR-186927, July 1990.

[118] R. Meakin and N. Suhs, "Unsteady aerodynamics simulation of multiple bodies in relative motion," in *AIAA Paper*, no. 1989-1996, 1989.

[119] R. Gomez, D. Vicker, S. Rogers, M. Aftosmis, William M. Chan, R. Meakin, and S. Murman, "STS-107 Investigation Ascent CFD Support," in *34th AIAA Fluid Dynamics Conference*, (Portland, Oregon), pp. 1–15, July 2004.

[120] B. C. Peters, M. Uddin, J. Bain, A. Curley, and M. Henry, "Simulating DrivAer with Structured Finite Difference Overset Grids," in *SAE Technical Paper*, no. 2015-01-1536, Apr. 2015.

[121] L. Carbonne, N. Winkler, and G. Efraimsson, "Use of Full Coupling of Aerodynamics and Vehicle Dynamics for Numerical Simulation of the Crosswind Stability of Ground Vehicles," *SAE International Journal of Commercial Vehicles*, vol. 9, pp. 359–370, Sept. 2016.

[122] N. Winkler, L. Drugge, A. S. Trigell, and G. Efraimsson, "Coupling aerodynamics to vehicle dynamics in transient crosswinds including a driver model," *Computers and Fluids*, vol. 138, pp. 26–34, Oct. 2016.

[123] S. Mansor, *Estimation of Bluff Body Transient Aerodynamic Loads Using an Oscillating Model Rig*. PhD thesis, Loughborough University, Apr. 2006.

[124] D. Sims-Williams, "Cross Winds and Transients: Reality, Simulation and Effects," *SAE International Journal of Passenger Cars - Mechanical Systems*, vol. 4, pp. 172–183, Apr. 2011.

[125] G. Pavia, M. Passmore, and A. Gaylard, "Influence of Short Rear End Tapers on the Unsteady Base Pressure of a Simplified Ground Vehicles," in *SAE Technical Paper*, no. 2016-01-1590, Apr. 2016.

[126] A. Perry, G. Pavia, and M. Passmore, "Influence of short rear end tapers on the wake of a simplified square-back vehicle: wake topology and rear drag," *Experiments in Fluids*, vol. 57, pp. 1–17, Oct. 2016.

[127] A. I. Heft, T. Indinger, and N. A. Adams, "Introduction of a New Realistic Generic Car Model for Aerodynamic Investigations," in *SAE Technical Paper*, no. 2012-01-0168, Apr. 2012.

[128] N. Jarrin, S. Benamadouche, D. Laurence, and R. Prosser, "A synthetic-eddy-method for generating inflow conditions for large eddy simulations," *International Journal of Heat and Fluid Flow,*, vol. 27, pp. 585–593, Aug. 2006.

[129] N. Ashton and A. Revell, "Comparison of RANS and DES Methods for the DrivAer Automotive Body," in *SAE Technical Paper*, no. 2015-01-1538, Apr. 2015.

[130] H. Kawamata, S. Kuroda, S. Tanaka, and M. Oshima, "Improvement of Practical Electric Consumption by Drag Reducing under Cross Wind," in *SAE Technical Paper*, no. 2016-01-1626, Apr. 2016.

[131] J. Howell and G. Le Good, "The Influence of Aerodynamics Lift on High Speed Stability," in *SAE Technical Paper*, no. 1999-01-0651, Mar. 1999.

[132] A. Wagner, *Ein Verfahren zur Vorhersage und Bewertung der Fahrerreaktion bei Seitenwind.* PhD thesis, Universität Stuttgart, 2003.

[133] M. Tsubokura, N. Yamada, S. Kitayama, T. Nakashima, and K. Kitoh, "Effects of Body Shapes on Unsteady Aerodynamics of Road Vehicles in a Gusty Crosswind," in *28th AIAA Applied Aerodynamics Conference*, (Chicago, IL), pp. 1–9, June 2010.

[134] M. Tsubokura, T. Nakashima, M. Kitayama, Y. Ikawa, D. H. Doh, and T. Kobayashi, "Large eddy simulation on the unsteady aerodynamic response of a road vehicle in transient crosswinds," *International Journal of Heat and Fluid Flow*, vol. 31, pp. 1075–1086, July 2010.

[135] R. Demuth and P. Buck, "Numerical Investigations on the Unsteady Aerodynamics of Road Vehicles Under Gusty Weather Conditions," in *6th MIRA International Vehicle Aerodynamics Conference*, (Gaydon, UK), pp. 48–60, Oct. 2006.

[136] D. Wieser, H.-J. Schmidt, S. Müller, C. Strangfeld, C. Nayeri, and C. Paschereit, "Experimental Comparison of the Aerodynamic Behaviour of Fastback and Notchback DrivAer Models," *SAE International Journal of Passenger Cars - Mechanical Systems*, vol. 7, pp. 682–691, Apr. 2014.

[137] M. Best, "A Simple Realistic Driver Model," in *11th International Symposium on Advanced Vehicle Control AVEC' 12*, (Seoul, Korea), Sept. 2012.

[138] SAE International, "Surface Vehicle Recommended Practice: Vehicle Dynamics Terminology," Tech. Rep. J670, 2008.

[139] SAE International, "Surface Vehicle Recommended Practice: Vehicle Aerodynamics Terminology," Tech. Rep. J1594, 2010.